Microwave Properties

of Carbon Powders

A thesis submitted in fulfilment of the requirement for the degree of Doctor of Philosophy

By

Fatma Shkal

School of Engineering - Cardiff University

UK -2018

DECLARATION AND STATEMENTS

DECLARATION

This work has not previously been accepted in substance for any degree and is not concurrently submitted in candidature for any degree.

Signed ……………………….…... (candidate) Date………..……….

STATEMENT 1

This thesis is being submitted in partial fulfilment of the requirements for the degree of Doctor of Philosophy (PhD).

Signed ……………………….…. (Candidate) Date………..……….

STATEMENT 2

This thesis is the result of my own independent work/investigation, except where otherwise stated. Other sources are acknowledged by explicit references.

Signed ……………………….… (candidate) Date………..……….

STATEMENT 3

I hereby give consent for my thesis, if accepted, to be available for photocopying and inter-library loan, and for the title and summary to be made available to outside organisations.

Signed ……………………….… (candidate) Date………..……….

ABSTRACT

Microwave techniques have been used in many applications due to the simplicity of the associated construction and use. They provide several advantages in contrast with traditional methods, including fast (almost instantaneous) measurements and their non-destructive nature, at least at low microwave power levels. Moreover, microwave methods provide an accurate and sensitive measurements of dielectric properties of carbon powders (in sp^2 form) due to their strong interactions with microwave electric fields.

The contributions to the state-of-the-art provided by the work presented in this thesis are novel applications of the microwave cavity and coaxial probe methods to differentiate between the types of carbon materials of industrial relevance by characterization of their dielectric properties. Measurements are typically carried out between 10 MHz to 10 GHz for the coaxial probe method, and between 2.5 GHz to 10 GHz for the cavity method, also as a function of temperature up to 150 ^{0}C.

The results of this thesis show that microwave methods are sufficient to differentiate carbons materials by measuring the complex permittivity under different conditions. The industrial relevance arises from being able to identify different types of carbons in two groups: one for blast furnace dust, which is crucial to quantify the utilization of coal injected in the furnace and determine the efficiency of coal injection; the other for activated carbons, which are highly porous structures used for applications such as carbon dioxide capture in fossil fuel combustion

Dielectric properties of different carbons (quantified by their complex permittivities) shown in this thesis are measured in-situ as frequency-dependent and temperature-dependent quantities and are different for different types of carbonaceous materials in the two groups of powders. Hence, the impact of this work is the realisation of simple and easy to use test methods that are robust enough to be applied in an industrial setting.

ACKNOWLEDGEMENTS

First and foremost, I thank the Almighty Allah for showering his infinite bounties and grace upon me to complete my Ph.D. study.

I would like to offer my most sincere thanks to my supervisor, Professor Adrian Porch for the opportunity to work with such an exciting field. I am grateful for his counsel and he has my lasting admiration. I must also thank him for all suggestions, explanations, and improvements in the writing of this thesis.

My thanks go to Doctor Julian Steer at the Cardiff School of Engineering for his assistance in providing the blast furnace dust samples. I must also thank him for all his suggestions, explanations.

My thanks go to Doctor Susana Garcia Lopez and her team at Heriot Watt School of Engineering & Physical Sciences for their assistance in providing the activated carbon samples.

My thanks go to Duncan Muir at the Cardiff School of Earth and Ocean Sciences for his assistance in the SEM characterizations.

I acknowledge the financial support of Libyan government. Thank you also to my friends and colleagues whose enlightening conversations has informed and enthused me throughout my studies.

This research would not be possible without the help of many people. I wish to express my gratitude to them all for their contributions. Many thanks to the technicians in the electrical/electronic workshop, mechanical workshop, and the IT group in the School of Engineering for their help and cooperation.

This work would not have been possible without the love and patience from my friend Mabrouka and my cousin Noor and her husband Masoud, whose unfaltering support and encouragement have been invaluable.

Finally, and not least, I would like to give my deepest thanks to my parents and family for supporting me spiritually throughout my studies.

PUBLICATIONS

1. Fatma Shkal, Susana Garcia Lopez, Daniel Slocombe, Adrian Porch, "Microwave Characterization of Activated Carbons." Journal of Computer and Communications, 2017. 6(01): p. 112

2. Céline Shepherd, Emina Hadzifejzovic , Fatma Shkal, Kerstin Jurkschat, Jonathan Moghal, Emily M. Parker, Montree Sawangphruk, Daniel R. Slocombe, John S. Foord, Mark G. Moloney., "New Routes to Functionalize Carbon Black for Polypropylene Nanocomposites". Langmuir, 2016. 2016. 32(31): p. 7917-7928.

3. Fatma Shkal, Julian Steer, Adrian Porch, "Microwave Techniques to Differentiate the Types of Carbon." accepted to the Eurpean Conference on Feul and Enrgy research and its Applications (12th ECCRIA).

TABLE OF CONTENTS

Table of Contents

LIST OF FIGURES

LIST OF TABLES

LIST OF ABBREVIATIONS

XX

AC = Activated Carbon

BFD = Blast Furnace Dust

ISM = Industrial, Scientific and Medical frequency

IUPAC = International Union of Pure and Applied Chemistry

MUT = Materials Under Test

PSA= Pressure Swing Adsorption

SEM = Scanning Electron Microscopy

TGA = Thermogravimetric Analyser/Analysis

TSA= Temperature Swing Adsorption

Chapter 1 Introduction and Thesis Summary

It is important to develop reliable test methods in characterization of carbon materials to replacing and improving the existing technologies. Microwave resonators can provide very accurate characterization of carbon materials due to the sensitivity of carbonaceous materials to the microwave electric field component. However, resonators provide the measurements at the discrete set of resonant frequencies, but a broadband coaxial probe has the ability to provide the measurements over a range of frequencies, although with a much lower sensitivity.

This thesis focuses on microwave techniques used in the characterization of different types of carbons. The original contributions are proposed to provide new test methods to quantify and differentiate between these carbonaceous materials.

Microwave cavity perturbation has been used to characterise and differentiate two groups of carbonaceous materials. The first group is activated carbons, produced from different precursors and different treatments such as ammoxidation and ammonia heat treatment. The other group is of carbons in blast furnace dust, such as coke, coal or partially burnt chars.

The broadband coaxial probe was also used to determine the frequency-dependent permittivity for both groups over range of frequencies from 10 MHz to above 10 GHz. In addition, the cylindrical cavity at 2.5 GHz was used for the measurement of the temperature-dependent dielectric properties of both groups of carbon materials, to investigate their microwave complex permittivity as functions of temperature.

1.1 Project Aims

The aims of this project were to develop and use microwave systems that could be used to differentiate the types of carbon materials. Cylindrical cavity resonators (at the ISM frequency of approximately 2.5 GHz) and coaxial probes were used for dielectric property investigation of the carbon samples and used to differentiate them. The main sets of experiments were as follows:

➢ Microwave techniques to measure the dielectric properties of different carbon materials.

➢ Frequency-dependent dielectric properties of carbon materials.

➢ Temperature-dependent dielectric properties of carbon materials.

1.2   Thesis Outline

The thesis is composed of the following chapters:

Chapter 1 - Introduction and Thesis Summary

This chapter presents a general introduction, the main project aims, and the thesis outline.

Chapter 2 – Literature Survey

This chapter gives a background on the carbon materials studied in this thesis, their properties, and presents a literature survey on the use of microwave techniques for measuring the dielectric properties of materials, with focusing on carbonaceous materials. Some examples from the literature related to microwave cavities and other microwave measurement techniques are presented for selected applications.

Chapter 3 - **Modelling, Design and Methods**

This chapter presents a review of the theory of microwave techniques, the design of the microwave systems used in this research and the simulation of both types of microwave applicators that have been used for the dielectric property measurements. This includes the design fundamentals and simulation of the cylindrical cavity resonator and coaxial probe.

Chapter 4 - Microwave cavity for dielectric characterization

Measurement of complex permittivity of different types of activated carbons, produced from different precursors, using the microwave cavity system are presented. Additionally, the main different forms of carbon contained in blast furnace dust (BFD) are also presented. The results show the effectiveness of the microwave cavity technique as a simple method to characterise and differentiate between activated carbons and the main components in BFD using dielectric properties only, without the need for more sophisticated materials analysis.

Chapter 5 - Frequency-dependent dielectric properties

This chapter presents the results of using a multimode cavity and open-ended coaxial probe for frequency-dependent dielectric characterisation of carbon materials. The microwave cavity excited in different TM modes was used for complex permittivity measurements at the discrete set of resonant frequencies. The open ended coaxial probe technique was also used to investigate dielectric properties of different types of carbon over a wider range of frequencies from 10MHz to 20GHz, to support the spot 2.5 GHz results presented in Chapter 4.

Chapter 6 - Temperature-dependent dielectric properties

The microwave cavity perturbation method was used for the temperature-dependent dielectric characterisation of carbons. The whole cavity system (plus sample) was placed inside a controlled laboratory oven to change the ambient temperature. This was to study the absorption/desorption of species from activated carbon (in particular), such as moisture.

Chapter 7 - Conclusions and future work

The main conclusions of the work are summarized in this chapter and some recommendations are presented for future work.

1.3   Main original contributions

The main contributions presented in this thesis are summarised as:

- New use of the microwave cavity and coaxial probe methods to characterize the dielectric properties of activated carbon samples.
- First demonstration of microwave methods to differentiate the main components of blast furnace dust.
- First in-situ dielectric characterization of activated carbons as a function to temperature to study the absorption/desorption processes.

Chapter 2 Literature Survey

The historical development of microwave engineering in the latter half of the 20th century has led to the introduction of many new methods which can be applied in numerous industrial and biological applications. Most traditional microwave/RF applications are in communication systems such as wireless and radar systems, but now also in medical and environment applications [1, 2].

This chapter presents the most common microwave techniques, relevant for the characterization and applications of carbonaceous materials. Activated carbons and other different forms of carbons contained in blast furnace dust will be the focus of this thesis. Activated carbon materials, their applications, production, and the regeneration of activated carbon will be introduced in Section 2.1. Section 2.2 reviews blast furnace dust. Chemical aspects of carbon will be outlined in Sections 2.3 and 2.4. Finally, the chapter concludes with Section 2.5, comprising a review of microwave measurement techniques and the associated advantages/disadvantages of each technique.

2.1 Activated Carbons

"Activated carbon" is a generic terminology referred to carbonaceous materials of very large surface area and highly porous microstructures. In general, the activated carbon samples have pore volumes of about 0.2ml/g, and the surface area is approximately in the range 400 - 2000 m^2/g; subsequently, they have inherently low densities, which is less than 0.4 g/cm^3 [3-5].

Activated carbon (AC) materials can be generally manufactured from different organic materials, such as biomass, coal, wood, sawdust, coconut shell, peach or apricot stones and waste materials, after which the activation process is carried out. The activation process can be physical or chemical. In physical activation, a char is exposed to steam, CO_2, or air at high temperatures. In chemical activation, some activating elements are introduced during the carbonization process, such as zinc chloride ($ZnCl_2$), phosphoric acid (H_3PO_4), potassium hydroxide (KOH). The mixture of the chemical agents and the AC is heated at temperatures ranging from 340ºC to 780ºC. Adding these chemicals to AC provides products with high porosity. The advantages of chemical

activation are the higher production volumes, lower temperature of activation, less activation time and higher development of porosity; among the disadvantages are the high costs of the activating agents and the need to perform an additional washing stage to remove the chemical agent [6, 7].

Activated carbon materials have many industrial applications, especially in the purification of gases and water technologies, but they have limited adsorption capacity. Therefore, it is preferable to regenerate any exhausted activated carbon instead of disposing of it, to minimize the cost of production of fresh material. Moreover, materials regeneration will reduce the hazards of pollutants on the environment which result from increased waste. The world-wide necessity to capture and store carbon dioxide from, for example, the combustion of fossil fuels in particular, has increased greatly in the last few years [8-10].

2.1.1   Types of activated carbon

There are many types of activated carbon materials available commercially, in both granular and powdered forms, and are used for water purification by surface adsorption of the dissolved organics and contaminant species from water and wastewaters due to their highly porous structure. Granular activated carbon has a typical average particle size ("diameter") of about 0.2 mm, and can be manufactured from hard organic starting materials such as almond and coconut shell. Powdered activated carbon can be easily obtained from the granular form by grinding. Fibres and activated carbon cloths are other different forms of activated carbon, which can be woven to form a flexible, thin "fabric." Figure 2.1 illustrates these different forms of activated carbons [11-13].

Granular Activated Carbon (GAC)

Broken GAC   Shaped GAC

Powdered Activated Carbon (PAC)
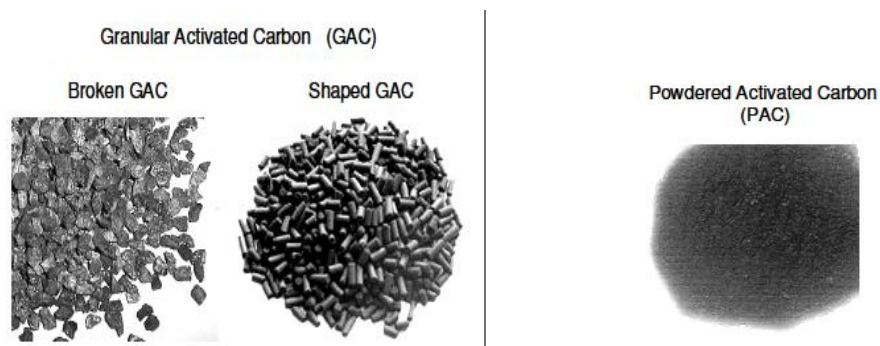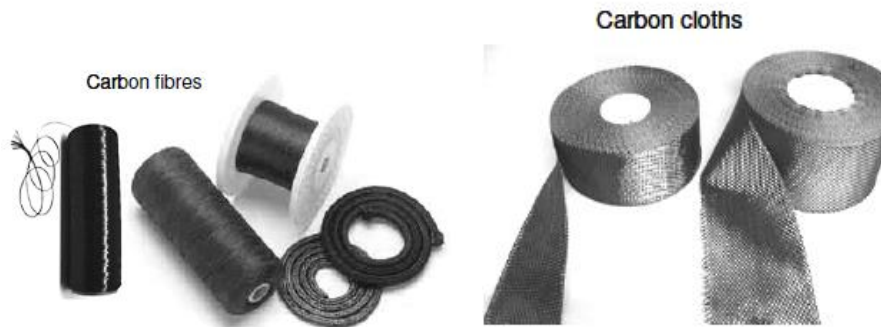
Figure 2-1 Types of activated carbons[13]

2.1.2 Applications of activated carbons

As already mentioned, activated carbon has many industrial and chemical applications. It is used in capture and storage technologies such as storage carbon dioxide. It is also used to determine and remove volatile organic pollutants. For example, activated carbon used to purify water from the liquid phase pollutants.

The different size of pores in AC should be considered for the specific application, as the AC adsorbs molecules from both liquid and gaseous phases, which depends on their surface area, their shape, pore size, and surface chemical characteristics. These properties specify the quality of AC and are directly the result of the nature of precursors and the type of the production method and the temperature of production.

In adsorption from the gas phase, mainly microporous carbon is used, whereas mesoporous carbon is applied in liquid phase processes. Applications of mesoporous activated carbons include: drinking water purification, waste-water treatment, sweetener decolourization, food, and chemical processing. On the other hand, microporous carbons are used for solvent recovery, gasoline emission control, cigarette filters and for industrial emission gas treatment [7, 8, 14, 15].

2.1.3 Production of activated carbon

Activated carbon materials are produced from different organic materials such as coconut and almond shell, biomass, and waste materials. The manufacturing methods can be divided into two main processes: carbonization and activation [6]. Figure 2-2 shows the typical life cycle of activated carbons.
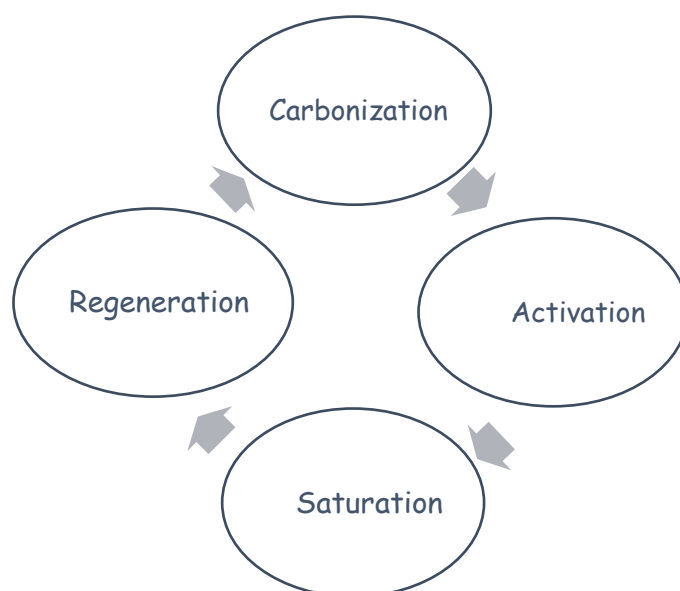
Figure 2-2 Production of activated carbon

2.1.3.1 Carbonization

In this process, the raw materials are treated under elevated temperatures to reduce the volatile content in the raw materials in order to convert it to a suitable form for activation.

After the carbonization stage, most of the non-carbon elements such as hydrogen and oxygen are first removed in gaseous form by pyrolytic decomposition of the raw material and the released atoms of elementary carbon are grouped into organized crystallographic formation known as elementary graphitic crystallites.

Carbonization of biomass material starts above 170ºC and it is almost completed around 500ºC- 600ºC. The rate of pyrolysis is considerably affected by the moisture content of the starting material. Additional important factors are uniform heating of the furnace and the temperature of carbonization, which must not be very high.

In the simple carbonization product, the common arrangement of the crystallites is irregular, so that free gaps remain between them. However, as a result of deposition and decomposition of tarry materials, these gaps are filled (or at least blocked) by disorganized (amorphous) carbon. The resulting carbonized product has small adsorption capacity. Apparently, at least for carbonization at lower temperatures, part of the formed tar remains in the pores between the crystallites and on their surface. Such carbonized materials can then be partially activated by removing the tarry products by heating them in a stream of an inert gas, or by extracting them with a suitable solvent, or by a chemical reaction [16].

2.1.3.2   Activation

Carbonized materials are activated to produce activated carbons with enhanced porous structure. The activation can be thermal or chemical. Thermal activation can be executed by treating the carbonized materials with passing steam, air, or carbon dioxide at high temperatures in the range approximately between 600 ℃ –and 900 ℃, resulting in the chemical processes listed in equations (2-1) – (2-4) below [4].

$$C + O_2 \rightarrow CO_2 \qquad\qquad (2\text{-}1)$$

$$2C + O_2 \rightarrow 2CO \qquad\qquad (2\text{-}2)$$

$$C + H_2O \leftrightarrow H_2 + CO \qquad\qquad (2\text{-}3)$$

$$C + CO_2 \leftrightarrow 2CO \qquad\qquad (2\text{-}4)$$
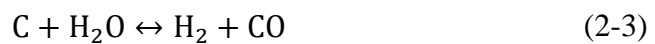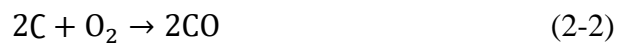
The chemical activation process can be executed by adding some additional chemicals such as zinc chloride, phosphoric acid, and potassium hydroxide. This process is also carried out at high temperatures, approximately between 400 ℃ and 800 ℃ [6].

2.1.4   Structure of activated carbons

Activated carbon is similar to graphite in terms of composition, both consisting of an array of hexagonal rings of carbon, noting that activated carbon rings are irregular and incomplete, especially at the edges. The random distribution of activated carbon rings leads to the presence of holes of different sizes and shapes. The surface area of one gram of activated carbon (the sum of the surface areas of the pores) reaches 1000 m^2.

In addition, the absence of activated carbon rings at the edges leads to the presence of certain atomic groups on the surface, which in turn determines the chemical nature of the AC surface (acidic, base, neutral). It is noted that the nature of raw material used in the preparation of AC, as well as the activation method, are the most important factors affecting the type and quantity of surface groups [16].

Micro-crystallites of AC are formed during carbonization of the raw materials, then free valence electrons are produced during the activation process; these electrons are very reactive. Additionally, the formation of interior vacancies in the microcrystalline structures can be affected by the presence of impurities and process conditions. The only difference between the graphite structure and that of AC is that the latter is the harder of the two [17].

The porous structure of AC can contain some of different non-homogeneous atoms such as oxygen and hydrogen. Some AC materials can also contain different amounts of minerals (sometimes denoted as ash content). The AC composition depends on the nature of the raw material used as the precursor. The porous structure of AC is considered as the main physical property that characterizes them. This is formed by pores of different sizes which as shown in **Figure 2-3** which, according to IUPAC recommendations [18], can be classified into three major groups:

- Micropores with a pore width of less than 2 nm.
- Mesopores with widths from 2 to 50 nm.
- Macropores with a pore width larger than 50 nm [13, 19].
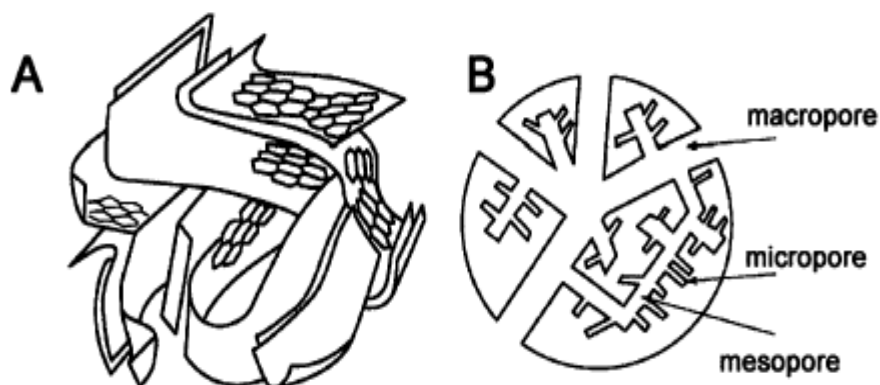
Figure 2-3 Three-dimensional and two-dimensional structures of activated carbon [20]

2.1.5   Microwave characterization of activated carbons

Most carbonaceous materials have a common characteristic of being highly absorbing of microwave energy, mostly as a result of their interaction with the microwave electric field, and so can be quantified and characterized by their dielectric properties. This absorption of microwave energy will result in intense, volumetric heating of the samples if the microwave electric field (i.e. microwave power) is high [7, 14].

The relative permittivity of the material ε_r is used to quantify a material's response (via its polarization) to an applied electric field. At microwave frequencies this is considered a complex quantity; its real part ε_r' is related to the material polarization (i.e. stored energy), whilst its imaginary part ε_r'' is related to energy loss. Their ratio $\tan\delta = \varepsilon_r''/\varepsilon_r'$ is known as the material's loss tangent and is the usual figure of merit used to compare the power dissipation between different dielectric materials at microwave frequencies. Therefore, it is necessary to measure the complex permittivity of any material to quantify its interaction with a microwave electric field, especially its ability to be heated by microwaves [6, 14, 21].

A number of studies attempted to measure the complex permittivity of AC at microwave frequencies [14, 21-27]. The AC samples were produced from coconut shell and were investigated using broadband measurements over a frequency range between 0.2 to 26 GHz at different temperatures. The samples were prepared as fine powders with particle size from 710 µm to 1500µm. They were heated at 180˚C for 72 hours to ensure that there was no absorption of additional chemical species, such as water. These studies concluded that most AC materials have a susceptibility to being heated by microwave radiation in the range of frequencies between 0.9 and 6 GHz, which is allowed by their high values of loss tangent. This frequency range includes the main industrial, scientific, and medical microwave ranges (at about 0.9, 2.45 and 5.7 GHz). It was also concluded, unsurprisingly, that the complex permittivity of AC materials depended on the frequency and temperature [14]. Permittivities of three AC samples of different origin were measured using a coaxial dielectric probe over the frequency range from 0.2 to 26 GHz at temperature range between 22ºC and 190 ºC. There were obeserved differences in permittivity of AC samples owing to the variations in the carbonaceous raw material (i.e. peat, coal, and

coconut shell) and variations in the activation method and pre-activation treatments; the complex permittivity of coconut shell AC is shown in figure 2.4 [14, 21].
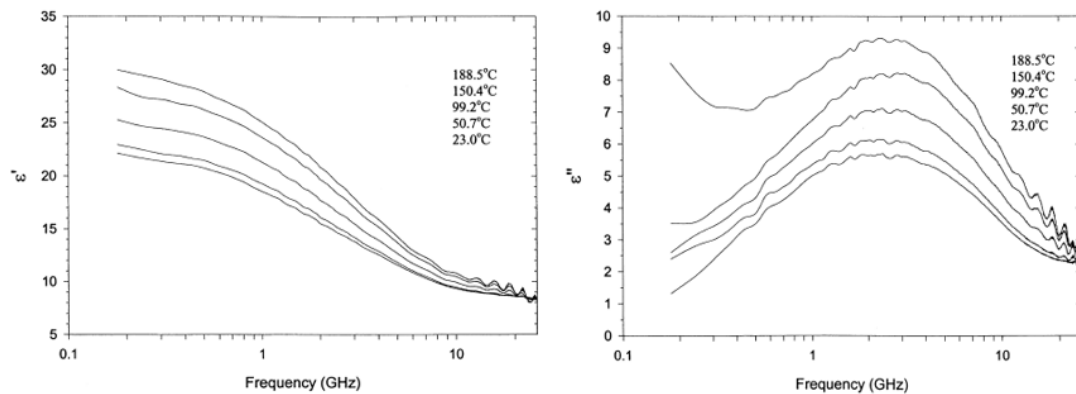
Figure 2-4 Complex permittivities of activated carbon from coconut shell. ε' and ε'' values increase monotonically with temperature from 23ºC to 188.5ºC [21]

Some cruder studies used domestic microwave ovens to measure the microwave absorption of activated carbons, at different power level, irradiation times, and different particle sizes/masses of the samples. The microwave absorption characteristics of activated carbon, coke, and different types of coal were measured by calorimetry at different microwave power levels, irradiation times, and masses of the materials. As the particle size of samples increases, the microwave absorption characteristics of the sample were also found to increase. Additionally, as the irradiation time and power level both increase, the microwave energy absorbed by AC were also found to increase [26]. The use of microwave ovens for the microwave heating of samples is an obvious one, but it is worth pointing out that it is fraught with problems. Firstly, the microwave electric field distribution within the oven space is not known precisely and will change when the sample is introduced. This leads to unpredictable heating rates. Secondly, neither the frequency nor the power level of the magnetron power supply can be changed, so heating rates cannot be controlled easily. Far preferable is the use of a single mode microwave cavity with (amplified) solid state power source, over which there is full knowledge of the electric field level and full control of the microwave power dose.

Microwave heating can be used as pyrolysis method to produce fuels from biomass such as switchgrass. To achieve this, the measurement of the dielectric properties is an essential step in the design of the microwave heating system. The dielectric properties of the materials are expected to change with temperature when the materials

are heated by microwaves, therefore, it is important to investigate this effect. Many factors can vary the dielectric properties during pyrolysis process, such as the existence of water, the decomposition of volatile material, the change in weight and density, and the transformation process of biomass into carbonaceous material. It has been found that there was a decrease in the permittivity through the drying and pyrolysis processes, as might be expected owing to the high permittivity of water (of both its real and imaginary parts). However, the permittivity sharply increased in char region; the transformation of phase to carbonaceous char could be the main reason behind this sudden rise in dielectric properties [27].

2.1.6   Regeneration of activated carbons

Microwave heating technology has been utilized for the regeneration of AC in recent years. For example, microwave heating was used to release CO_2 from AC materials at two different temperatures (70˚C and 130˚C), and the results were compared with conventional methods, in which a commercial tubular oven was used. The materials used in this study were commercially-available AC which was produced from coconut shell. The study concluded that the microwave heating offers the fastest rate of releasing CO_2 from samples, at a rate 3-4 times faster when compared with conventional oven heating, as shown in **Figure 2-5** [8].
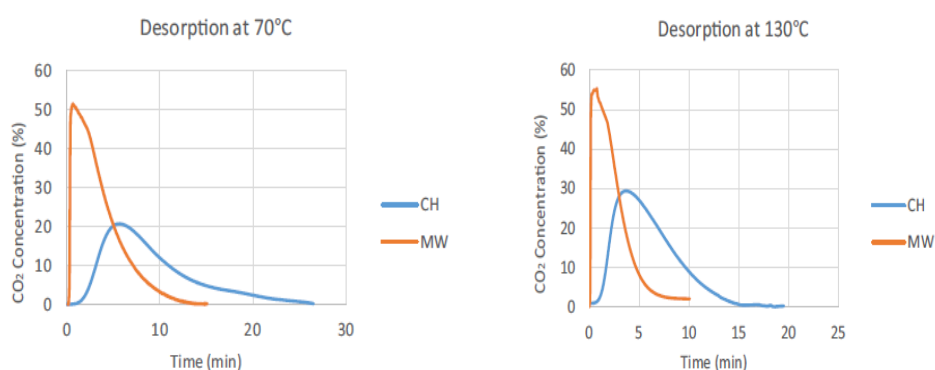
Figure 2-5 Comparison between microwave and conventional heating desorption of carbon dioxide at 70˚C and 130˚C [8]

In these experiments, an electrical oven and a single mode microwave cavity (operating at 2.45GHz) were used to regenerate AC which was saturated by phenol, at 850 ℃. The study concluded that, when comparing microwave heating with

conventional heating, the regeneration process time was 9 times shorter, taking only 4 minutes compared to 37 minutes when a conventional oven was used. Moreover, the porous structure of regenerated AC was efficiently preserved [11].

2.1.7   Advantages of microwave regeneration

Using microwave heating to recycle exhausted AC has many benefits, including the ability to be repeated multiple times and its speed of regeneration compared to traditional methods; hence, it is more efficient than traditional approaches in that it uses less total energy. Moreover, microwave methods have been demonstrated to retain the original porous structure of the starting AC material, actually with an apparent increase in total surface area when using microwave heating to regenerate the AC. Ania et al. [10] concluded that mesoporosity of the AC samples which were treated using microwaves were about 20% larger than the samples treated in an electric furnace. Meanwhile, microporosity was found to become higher in AC samples treated with microwaves. This result occurs mainly when treatment is carried out under an inert N_2 atmosphere, whilst providing an oxidizing atmosphere during the treatment gives rise to an increase of mesoporosity, due to partial gasification of the activated carbon [11]. Additionally, the adsorption performance and capacity of materials has been found to be improved when using microwave heating compared to conventional methods [8, 11, 14, 19, 28-30]. Figure **2-6** shows a comparison of the adsorption capacity of AC and the regenerated samples when saturated with phenol, between microwave and conventional electric furnace recycling to compare the effect of the different heating mechanisms on the adsorptive capacities of the regenerated AC [11].
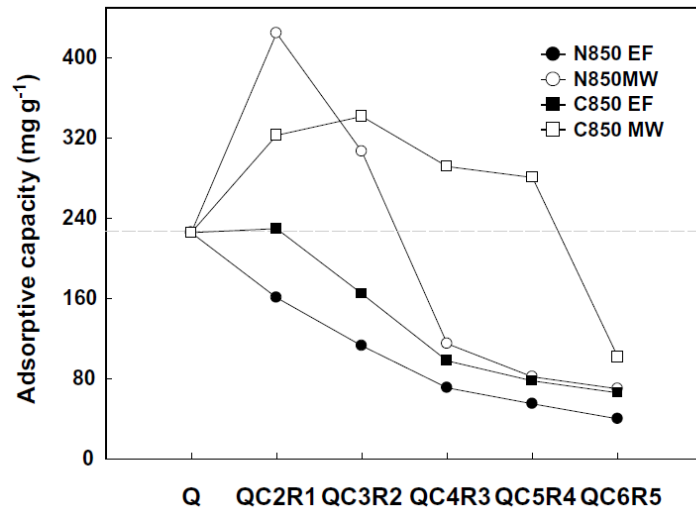
Figure 2-6 Adsorptive capacities of phenol after various cycles of regeneration in electric furnace (EF) and microwave (MW) furnaces. horizontal axis show the samples of AC, labelled as CiRi where Ci the cycles of saturation and Ri the number of regenerations [11]

2.2 Blast furnace dust

Carbonaceous materials found in blast furnace dust can be categorized into three types: namely, char, coke, and coal, but the predictable quantity of coal is low. Both char and soot result from very rapid pyrolysis of coal [31].

Coke, which is a high-carbon product, is usually produced by destructive distillation of coal, coke has a simple composition, consisting mainly of carbon with some mineral materials and small amounts of hydrogen, sulphur and oxygen [32]. On the other hand, coke has a very complex structure, with a different size of pores and wall and shapes as well as cracks. The coke walls consist of different textures which have various microscopic properties and vary in optical anisotropy depending on the rank and type of coal in the coal mix used [33].

One of the usual processes in modern blast furnace ironmaking is the injection of powdery coal. The main purpose of this is to reduce the consumption of coke (per ton) during hot metal production, which is usually referred to as coke rate. The monitoring of the combustion of injected coal is not possible as the process occurs within an extremely hot and completely closed environment. Currently, the level of combustion of the injected, pulverised coal can be obtained from indirect analysis of the particles loaded in the top gap of the furnace, and from the dust collected at the end of the

process. The combustion efficiency characteristic of the furnace can be demonstrated by the quantification of the types and amounts of the different carbon materials in the blast furnace dust (BFD), especially for materials resulting from pulverised coal injection. However, such quantification is a major challenge, as the origin and the type of the resulting carbon materials cannot be identified using a chemical analysis of carbon. Although, BFD has high levels of carbonaceous material resulting from loaded coke, distinguishing between the carbonaceous materials produced from loaded coke and combustion remainders is not simple because both have the same chemical characteristics. In addition, detection of small amounts of pulverised coal injection residues in BFD is very challenging because BFD also contains a large amount of non-carbonaceous materials, such as iron ore. Thermogravimetric analysis (TGA) can be adapted for the quantitative analysis of BFD to differentiate the different types of carbon [31, 34], but realistic alternatives are scarce.

For these reasons, in this research, microwave techniques were proposed for a simpler, more practical differentiation of carbonaceous materials in blast furnace dust based on their dielectric property measurement. The simplicity of this method also means that it could be deployed in-situ at the combustion site.

2.2.1 Synthesis and characterization of blast furnace dust

Blast furnace dust is one of the most important solid industrial wastes and it contains many key components. Carbon is the most common component contained with high concentration. Such carbonaceous materials are prospective materials for recycling as fuels or agents for thermochemical transformation or mineralogy.

To transfer carbonaceous materials in BFD into waste gas, they are gasified and the two major resultant gases - methane and hydrogen – are collected to be used as fuels. The main factors affecting the efficiency of the combustion and gasification processes are the physical and chemical properties of the carbons contained in the BFD. Therefore, differentiation of types of BFD carbons is necessary for their recycling as fuels or reducing agents. Existing typical techniques for differentiation include:

- Chemical analysis methods: the carbonaceous materials contained unused coal, char, and coke.

- X-ray diffraction techniques, in combination with chemical analysis, as a standard procedure to identify and differentiate the char and coke structures.

- Raman spectroscopy, which is used to determine the proportion of char and coke and the degree of graphitization for carbonaceous materials.[35]

2.2.2 Microwave characterization of carbons in blast furnace dust

A number of studies show the potential of the use of microwaves as a non-invasive tool to differentiate types of carbons [14, 21, 22, 25, 26]. Microwave complex permittivity, which contains information about both the polarization and absorption characteristics, of different types of carbon can be measured and used to distinguish between coke and other types of coal, which could also contain different quantities of carbon, moisture, volatile materials and ash. Different carbonaceous materials have been shown to yield significant differences in their microwave absorption, with coke being the best absorber [26].

Published results have demonstrated the variations of the microwave complex permittivities of different types of carbons with different properties and chemical compositions, with measurements carried out in the range of X-band frequencies (8.2 to 12.4 GHz) and more generally in the frequency range between 1 and 10 GHz. It has been found that the permittivity values of coals are considerably smaller than for graphite and carbon black. As shown in Figure **2-7**, the complex permittivity of three graphite (AT-No.5, artificial graphite and pure carbon) and one carbon black samples were measured. The real part ε_r' was found to decrease with increasing frequency, limiting to a close to constant value above 6.5 GHz. The imaginary (i.e. loss) ε_r'' values also decrease with increasing frequency in the similar way as the ε_r' values [22].

Marland et al. [33] attempted to use microwave cylindrical cavity resonator for dielectric permittivity measurements of UK coals with different coal rank and different minerals contents at three frequencies (0.165, 1.413 and 2.216GHz). They concluded that the permittivities of coals decrease with coal rank and depend (as one would expect) on the moisture and mineral contents; they also change with both temperature and frequency. The results summarized in Table 2-1. The dielectric properties of coals

can change with frequency, decrease with increasing frequencies to and approach a constant value above 6.5 GHz. as shown in Figure 2-7 [36].
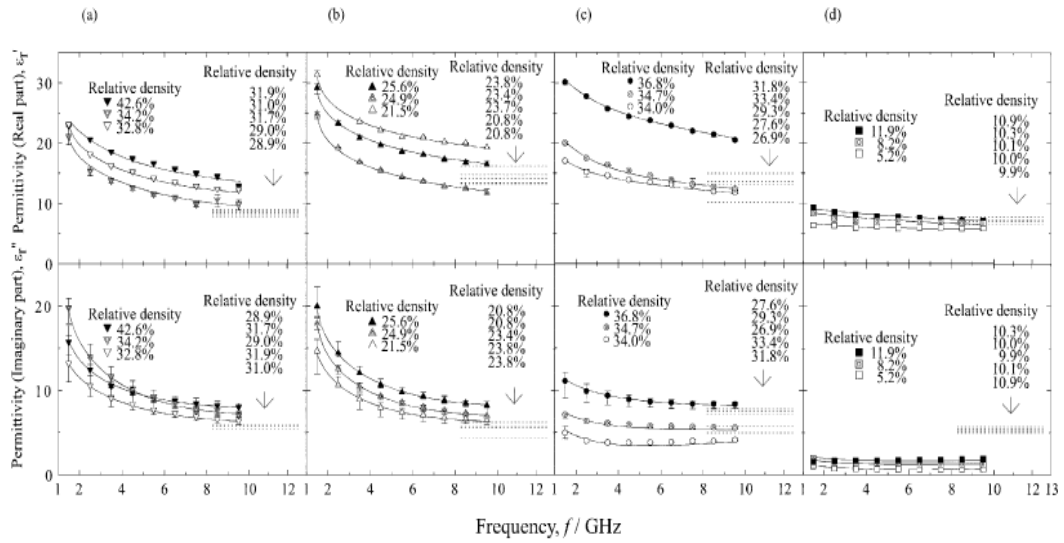
Figure 2-7 Frequency dependency of relative complex permittivity (εr' and εr") for the graphite and carbon black samples: (a) AT-No.5, (b) artificial graphite, (c) pure carbon, and (d) carbon black [22]

Table 2-1 dielectric properties of coals at different frequencies, all at 60^{0}C [36]

coal	0.615 GHZ		1.413 GHZ		2.216 GHZ	
	ε_r'	ε_r''	ε_r'	ε_r''	ε_r'	ε_r''
F-1	2.91	0.6130	2.89	0.1433	2.93	0.1657
F-2	2.47	0.0443	2.46	0.0402	2.49	0.0539
F-3	2.30	0.0543	2.31	0.0534	2.34	0.0818
F-4	2.80	0.1951	2.75	0.1810	2.77	0.2087
F-5	2.40	0.1380	2.34	0.1317	2.32	0.1389
F-6	2.88	0.191	2.84	0.1489	2.86	0.1564
F-7	2.50	0.1150	2.45	0.1188	2.45	0.1252
F-8	3.63	0.3792	2.52	0.3191	3.51	0.3153
P-1	2.94	0.2161	2.84	0.1893	2.87	0.1848
P-2	1.62	0.0873	1.61	0.0772	1.62	0.0772
P-3	2.89	0.1929	2.80	0.1768	2.84	0.1684
P-4	2.27	0.0740	2.24	0.0560	2.28	0.0658
P-5	2.66	0.1401	2.65	0.1186	2.69	0.1274
P-6	2.42	0.1623	2.39	0.0803	2.44	0.0914
P-7	2.62	0.1055	2.55	0.0783	2.58	0.0906

2.3 The surface chemistry of activated carbon

Activated carbon is an effective adsorbent for the removal of dissolved organic substances from waters and wastewaters. The physicochemical nature of the surface of carbon is an important factor in the adsorption process and should be considered in selection or preparation of carbons for specific applications. The surface of any activated carbon is comprised in part of residual electron- and ion exchange functional groups, connected by electron-conducting bond systems. The nature of these functional groups is determined to a large extent by the method of activation, as well as by the type of raw material from which the carbon is prepared. With the existence of electron- and ion-exchange groups at the surface of carbon, it is reasonable to expect that electrolytes in solution may interact with the carbon to influence its behaviour as an adsorbent. In fact, such interactions could considerably affect the overall adsorption process under certain conditions, possibly effecting changes in the process which may be put to good advantage to achieve higher efficiency or enhanced effectiveness for the removal of pollutants [37].

Although there is little direct information available on the structure of activated carbon, much can be derived from existing data on the structure of carbon black. Very little chemical difference exists between these two substances, and the only apparent physical difference is that the carbon black has much less internal surface area [37].
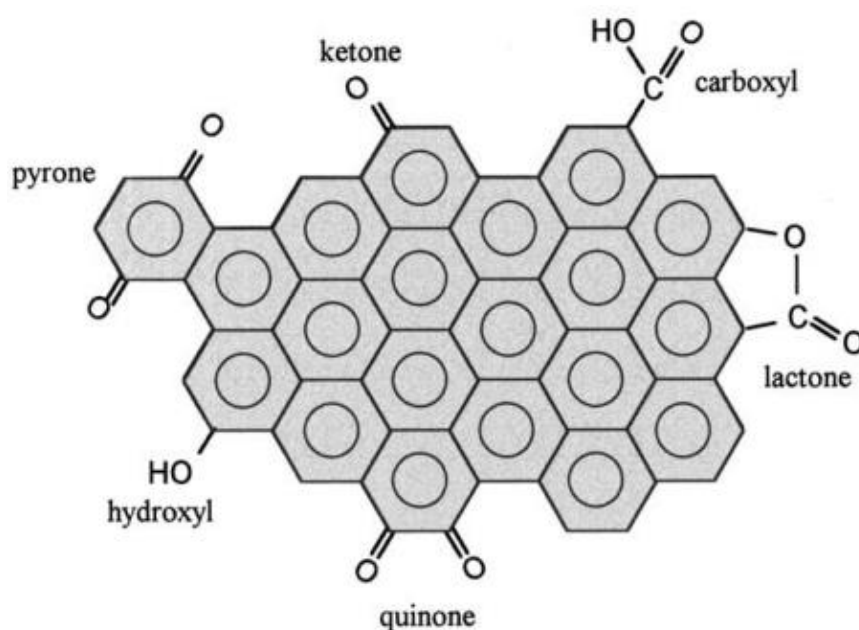
Figure 2-8 surface chemistry of carbon black [38]

The surface chemistry of carbon plays an important role because of its high reactivity. In the field of carbonaceous materials, the surface chemistry usually refers to the chemical nature and properties of their surface (being made up of unpaired electrons) and of the type, quantity, and bonding of various heteroatoms, especially oxygen. These are bonded to the carbon skeleton and form the same surface functional groups as those typically found in aromatic compounds. Such groups may be acidic groups (i.e. carboxyls, lactones, and phenols) and basic groups (i.e. pyrones, chromenes, ethers, and carbonyls). Also, the delocalized p-electrons of carbon's basal planes are basic sites. Moreover, activated carbon has reducing ability due to oxygen functional groups such as phenolic, lactone, carbonyl, and quinone [39].

The behaviour of carbonaceous materials in catalysis depends on their surface properties, which in turn are determined by their structure. The structure of the porous carbons used in catalysis is graphitic; thus, there are unsaturated carbon atoms at the edges of the graphene layers and in basal plane defects that can easily react with oxygen, water, or nitrogen compounds, originating in surface groups such as those represented schematically in **Figure 2-9**. These groups can be used to anchor catalysts or catalyst precursors, or for subsequent functionalization; in addition, they may be active sites for specific catalytic reactions.
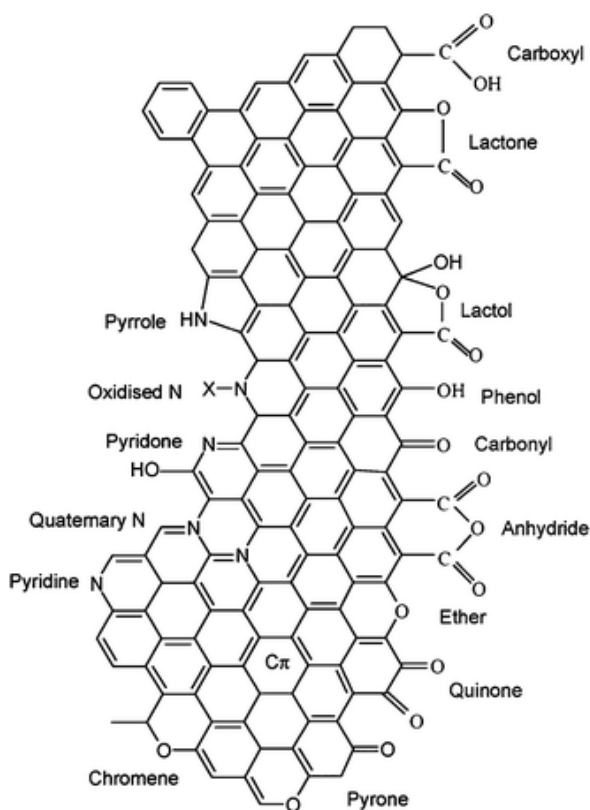
Figure 2-9 Nitrogen and oxygen surface groups on carbon. [40]

Among the oxygenated groups, carboxylic acids and anhydrides, lactones, lactols, and phenols, are acidic, while carbonyl and ether groups are neutral or may form basic structures (quinone, chromene, and pyrone groups). The nitrogen groups include pyridine (N-6), pyrrole, or pyridone (N-5), and oxidised nitrogen (NX) at the edges, and quaternary nitrogen (N-Q) incorporated into the graphene structure. The nitrogen atoms provide additional electrons, inducing surface basicity and enhanced catalytic activity in oxidation reactions. The acidic surface properties are caused by the presence of carboxyl groups (also in the form of their cyclic anhydrides), lactones, or lactols as shown in **Figure 2-10**, and hydroxyl groups of phenolic character [40, 41].
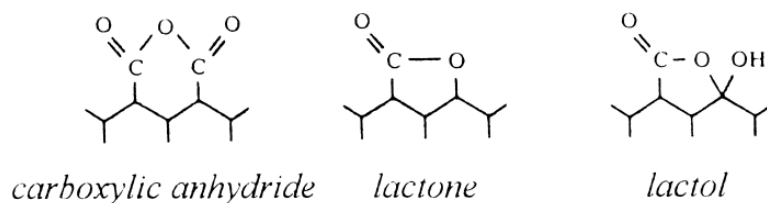
Figure 2-10 some possible surface groups [41]

2.4   Bonding in carbon

Molecular bonding behaviour has a large influence on the structure of a material and its chemical and physical properties. Carbon atoms bond themselves are not in form of identical molecular orbitals, they actually are in form of hybridized orbitals. In the following sections, the term hybridization is explained in this context and the influence on the properties is described using the examples of graphite and diamond. Pure carbon has many allotropes with markedly different crystal structures which reveal also very different material properties, originating from the particular type of bonding between carbon atoms.

The normal bonding behaviour of molecular orbitals involves the bonding of the same kind of orbital. Two s-orbitals or two similar p-orbitals bind together in an antibonding and bonding way, depending on the sign of the orbital. Carbon atoms form bonds by the mixing (i.e. hybridization) of different orbitals, namely s- and p-orbitals. Also a mixture of s-, p- and d-orbitals is possible, but is less important for combining carbon orbitals only [42]. In the next section, the resulting sp^3 and sp^2 hybridization will be explained in detail.

2.4.1 Sp^3 Hybridization

A carbon atom contains six electrons which occupy the following electron configuration: $(1s)^2 (2s)^2 (2p)^2$. In the ground state there are two unpaired electrons in the outer shell, so that one could assume the ability to bind only two additional molecules. Because of the small energy difference between the 2s- and the 2p-states, it is easily possible to excite one electron from the 2s state into the 2p-state. In the presence of an external perturbation, such as a nearby atom such as hydrogen, the energy difference is overcome. This results in a mixed state formed out of one s-orbital and three p-orbitals (namely p_x, p_y and p_z). Four new hybrid orbitals are formed. The direction of the orbitals and also the centre of mass are determined by the specific contributions of the p-orbitals and the s-orbital. A combination of the hybrid orbitals produces a tetrahedral assembly with the centre of masses in the corners shown in **Figure 2-11**. This is called sp^3 hybridization, and accounts for the highly symmetric bonding found in the diamond form of carbon, which accounts for many of its remarkable material properties (e.g. hardness, strength, and stiffness).
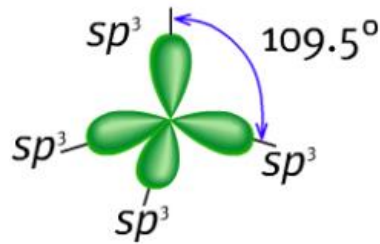
Figure 2-11 sp^3 -hybrid orbital [42]

The characteristic angle between the hybrid orbitals in the sp^3 -configuration is 109.5°. Assembling many different sp^3 - hybridized carbon atoms within a single crystal, one achieves the typical diamond structure as shown in **Figure 2-12**. The unique properties of diamond are now even more understandable. Due to the three-dimensional sp^3 – structure, the binding strength between neighbouring carbon atoms is equal for each atom and very strong. Diamond has a wide bandgap of about 5 eV and so its electrical conductivity is very low (it can be considered to be almost an ideal dielectric material); as a consequence, its microwave absorption is also very low (it has a very small loss tangent at microwave frequencies). Furthermore, the transparent appearance of diamond is associated with the wide bandgap, so that electrons cannot be excited out of the valence band into the conduction band with wavelengths in the optical range.
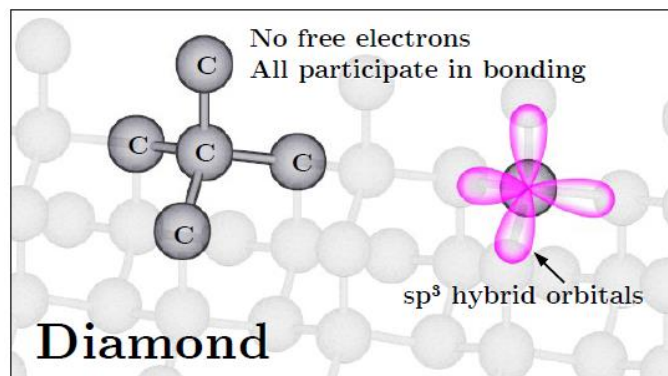
Figure 2-12 the crystal structure of diamond, whose bonds are fully sp^3 hybridized [43]

2.4.2 Sp^2 Hybridization

Sp^2 Hybridization is the combination of one s-orbitals with only two p- orbitals, namely p$_x$ and p$_y$. They contribute to form a planar assembly, as shown in **Figure 2-13**, with a characteristic angle of 120° between the hybrid orbitals, thus forming a so-called

σ-bond. The additional p_z-orbital is perpendicular to the sp^2 hybrid orbitals and forms a so-called π-bond.
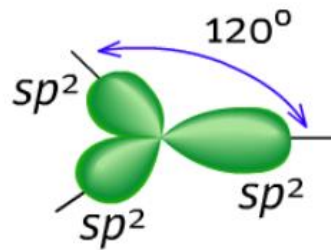
Figure 2-13 sp3 -hybrid orbital [42]

A typical example of a sp^2 hybridized crystal structure is graphite, shown in **Figure 2-14**. It consists of parallel carbon layers. Within a single layer, the planar sp^2 hybrid orbitals align themselves as in Figure 2-8 to form a structure with strong binding. Between the layers the π-orbitals give rise to weak Van-der-Waals forces, allowing the layers to slide over each other. As a result, graphite is very soft and is thus used in pencils. Conversely, a single layer (known as graphene) is the stiffest material known. The band structure of graphite is such that it can be described as a semimetal. The connection of valence and conduction bands allows easy electron excitation into the conduction band, independent of the wavelength, so that graphite is a very good electrical conductor over a broad range of frequencies and is optically opaque.
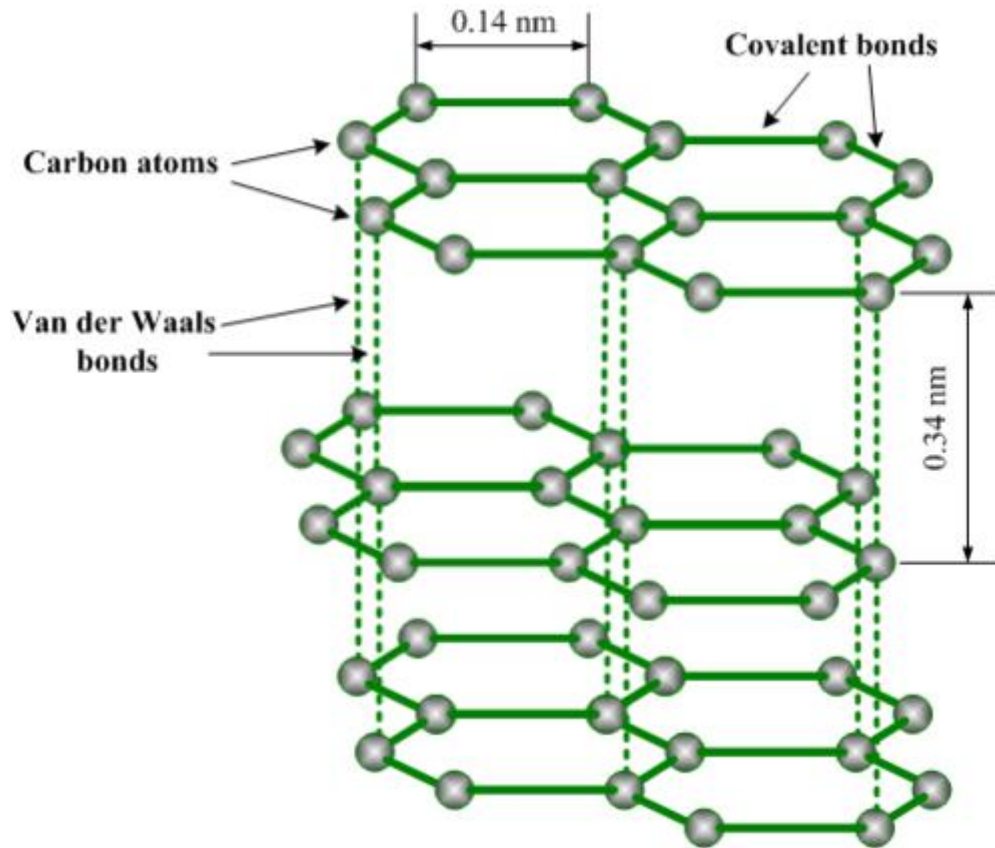
Figure 2-14 Crystal structure of graphite.

2.5 Microwave measurement techniques

Over the past three decades, measurements of dielectric properties of materials using microwave techniques has received much attention. This has been especially so for the non- destructive characterisation of materials used in passive device applications, including sensors.

Microwave measurement techniques are generally divided into two main categories, resonant and non-resonant methods. The measurement methods used for dielectric measurement in this work are cavity resonator and coaxial probe methods, which will be described in more detail below.

2.5.1 Non-resonant techniques

Transmission/Reflection techniques are used for measurements of the real part of the complex permittivity of both high and low loss materials over a broad range of

frequencies. However, these methods do not have adequate resolution to measure the imaginary part of the permittivity, and so have limited use for materials with low loss tangents. The transmission/ reflection techniques have two basic types. One method depends on measuring the complex S-parameters S_{11} and S_{21} (i.e. voltage reflection and transmission coefficients, respectively), which are then used to calculate the dielectric property via a suitable inversion process; this is called a distributed impedance technique and is used for frequencies typically above about 0.1 GHz). The other method (typically used for frequencies less than about 0.1 GHz) is a lumped impedance technique which is based on circuit theory, which essentially involves the direct measurement of capacitance. Both of these methods require precise knowledge of the electric field and its uniformity in the vicinity of the sample under test; indeed, the inversion analysis is simplified by assuming the electric field is uniform within the sample, an approximation which is valid for a suitable design of sample test fixture [44-46].

2.5.1.1   Transmission line method (Waveguide)

In this method, a specified length of sample is filled inside an enclosed section of transmission line prior to measuring the reflected and transmitted signals. In spite of this method being more accurate than the coaxial probe reflectance method (more of which below), it has a narrower range of frequencies (especially when using waveguide fixtures). Furthermore, the sample preparation is more difficult, since the sample should fit within the fixture tightly, with no gaps which would form material boundaries between the materials and hence affect the electric field component normal to these boundaries [47, 48].

A microwave network analyser (purchased from major microwave instrument suppliers such as Keysight and Rohde & Schwarz) can be used to measure the S-parameters to obtain permittivity (and, indeed, permeability when magnetic) of the sample filling the transmission line test fixture.

In this T/R technique waveguides are often used at higher frequencies (e.g. above 10 GHz) and coaxial lines are preferable at lower frequencies. Waveguide test fixtures can be rectangular or circular waveguides and the mode of transmission depends on the aspect ratio of the test structure [49]. In practice, rectangular waveguide operating

in the TE_{01} mode is most common, since for circular waveguide the dominant TE_{11} mode is degenerate (comprising in practice of two orthogonal modes propagating at the same frequency).
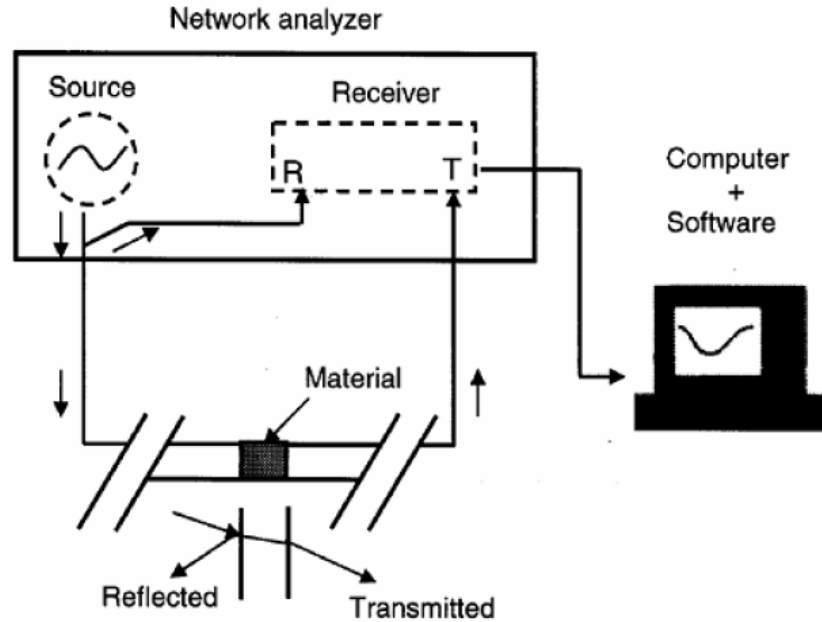
Figure 2-15 Measurement using transmission/reflection method with a waveguide [50]

A coaxial line has been presented in [51] as a tool for microwave permittivity measurements of two elastomeric matrixes differing in their chemical nature. According to the study, it has been found that the interface polarization, relaxation processes, and the distribution of absorption active filler can be affected by the type of matrices, and are reflected in the permittivity values measured [51].

Figure 2-16 and Figure 2-17 show the dielectric constant (ε_r) of nitrile butadiene rubber (NBR) and natural rubber (NR) based composites as a function of frequency and filler amount. As the frequency and amount of filler increased, the values of the dielectric constant increased. For both matrices, the effect is more noticeable at higher filler amounts. The overall values of the dielectric constant of NBR based composites are higher than those for NR based ones. The main reason of this behaviour is in the

polarity of the two matrixes (the nitrile matrix is very polar while the natural rubber is non-polar) [51].
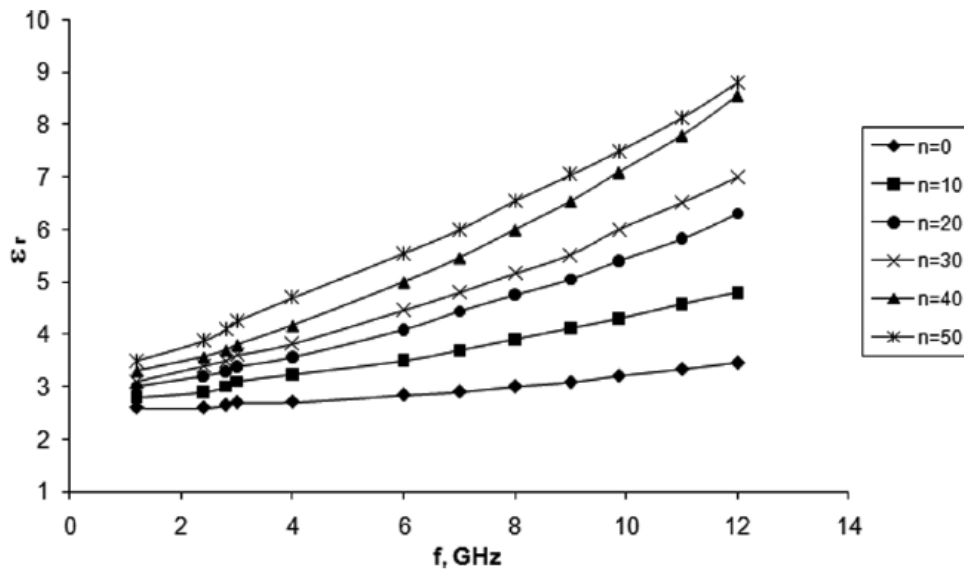
Figure 2-16 Dependency of dielectric permittivity on the frequency and filler amount for composites based on NBR [51]
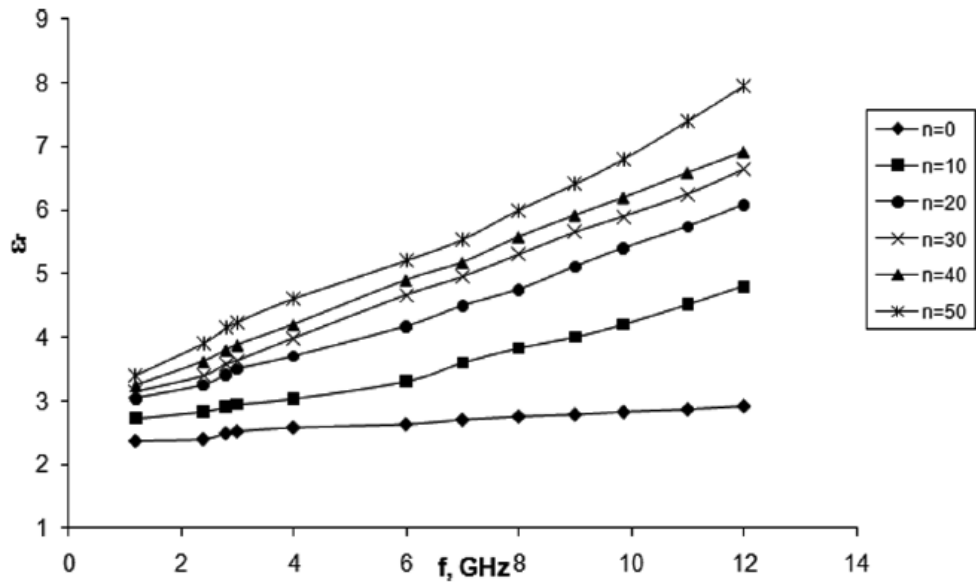
Figure 2-17 Dependency of dielectric permittivity on the frequency and filler amount for composites based on NR [51]

2.5.1.2   Coaxial probe method

The coaxial probe method is basically an adaption of the transmission line method in that only reflected signals from the sample are measured. The sample is simply fixed at the open circuit termination of the cable. For this reason, an electric field interacts with the sample so that the method is only suitable for dielectric property measurement (and not for simultaneous magnetic property measurement).

In this method, the flat surface of a solid sample is in contact with the tip of the coaxial probe, or the coaxial probe is dipped into a liquid sample; it is very important to ensure that there is no gap between the probe tip and the sample, as this is difficult to model in the inversion analysis to extract complex permittivity, and so the method works best for flat, homogeneous samples. The method is easy in that no special machining of the sample is needed, other than the presentation of a flat surface, and can be used over a very broad band of frequencies (typically 100 MHz–110 GHz, the upper frequency dependent on the diameter of the coaxial aperture at the open circuit end of the probe). As previously mentioned, the method has limited accuracy, especially for low loss materials. The coaxial probe used in the experiments in this thesis was specially adapted from a miniature connector (in this case, a K-connector) to increase the bandwidth of operation. The probe and its analysis are discussed in more detail in Chapter 3.

In the case of solid sample measurements, the coaxial probe with a flat flange is preferable for use, to make the resulting inversion analysis to calculate complex permittivity easier. In the case of liquid and semi-solid samples, such as biological and food materials, flange-free open-ended coaxial line probes have been used for broadband measurements of permittivity but require careful calibration [47]. The error related to the coaxial probe measurement method is related to the density of the sample, the contact between the sample and the end of the probe, and the conductivity between the particles in the case of the powder samples. This method is not suitable in the case of granular samples, owing to the random nature of the contacts between the grains, especially if they are of size which is comparable to the characteristic fall-off of electric field from the end of the probe [47].

The open ended coaxial probe has been used for the last 40 years or so. One of the [52] first reports in the literature is by Stuchly and Stuchly in 1982, who used it to

measure the dielectric properties of biological materials [50, 52]. Over the years the method has been improved involving refined geometries, inversion procedures, and experimental calibration. The calibration reference planes for the coaxial probe are established using well known reference materials using Short-Open-Load (SOL) techniques [47, 49]. SOL calibration is based on shorts, opens, and loads as calibration standards, with each component behaviour being specified in advance using data or models. As the behaviours of all standards are well known, measuring them with the network analyser provides the opportunity to define all of the error terms. The load behaviour mainly determines the directivity terms. Together, the short and open mainly determine source match and reflection tracking [53].

The coaxial probe has electrical field lines both inside the probe and a fringing field which spills out at the end. The probe is basically an open-ended coaxial line consisting of a centre conductor surrounded by a dielectric material and an outer conductor. A schematic of the measurement set-up is shown in Figure 2-18.
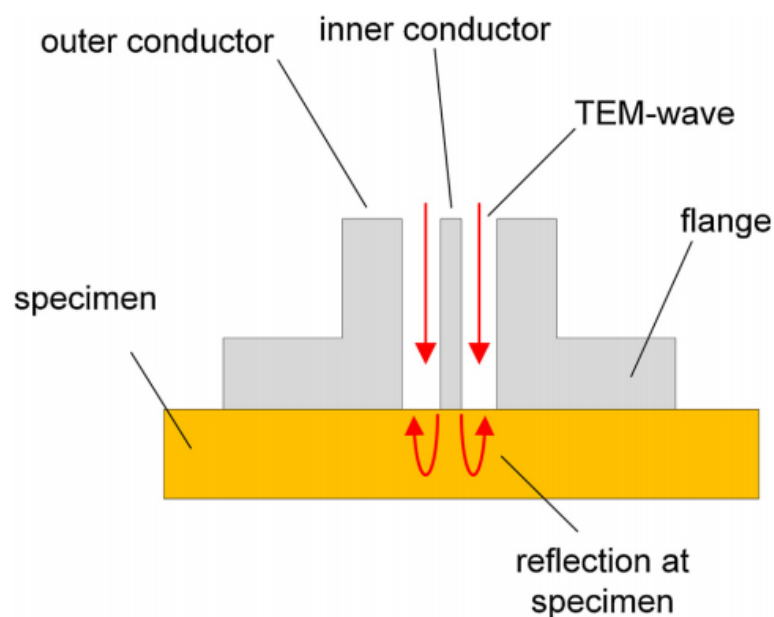
Figure 2-18 Schematic of the measuring procedure using an open-ended coaxial probe [54]

The open-ended coaxial probe has been used for dielectric measurement of oil palm shell and oil palm shell char in the frequency ranging between 0.5 and 20GHz at room temperature for the elemental identification of biomass. The dielectric properties of oil palm shell and oil palm shell char are found to be largely dependent upon the microwave frequency. This would be a suggest using microwaves for thermal

treatment of biomass, as an efficient, fast and volumetric method of heating to convert biomass to bio oil and other products [55, 56].

2.5.1.3 Free space method

In this method, two antennas (a transmitter and receiver) antennas are used to measure the phase shift of a signal with and without a sample placed in the line-of-sight path. The sample is usually in sheet-form, and the electric field of the transmitted signal is oriented parallel to the sample, to make the inversion analysis simple and to negate the need for depolarisation factors. The sample does not require any special preparation, other than its careful orientation and it should be of sheet like nature; thus the method is convenient, especially for high temperature measurements since the sample is isolated from the test fixtures, and for inhomogeneous dielectric materials since there is no requirement for special sample preparation.

Additionally, this technique may be preferable for continuous monitoring and control in industrial applications. For example, moisture content determination and density measurement can be carried out using free space methods and the measurement of permittivity can be achieved accurately over a broadband of frequencies by this technique [47, 49]. **Figure 2-19** shows a typical configuration of a free-space measurement setup. The system consists of a vector network analyser, antennas, cables, and computer software to collect S parameters and invert them into complex permittivity values. The antennas are usually horn-type and are fed with a TE_{01} waveguide, giving electric field polarisation in the flat plane of the sample. Whilst the method is inherently broad-band, the bandwidth is limited to a specific waveguide band by the use of waveguide antennas.

As mentioned, this method assumes that a uniform plane wave is normally incident on the flat surface of a homogenous material, and that the planar sample has infinite extent laterally [47, 57], thus neglecting any diffraction effects at the edges of the sample. To obtain accurate results some other factors should be taken in account: namely, the type of radiating elements, the design of the sample holder, the sample geometry (especially thickness and its uniformity) and the sample location between the two radiating elements. This method is contactless, non-destructive, and is appropriate for high frequency measurements; it is also possible to use low frequencies although this

is limited by practical sample size, owing to the large size of the antennas required [48, 50].
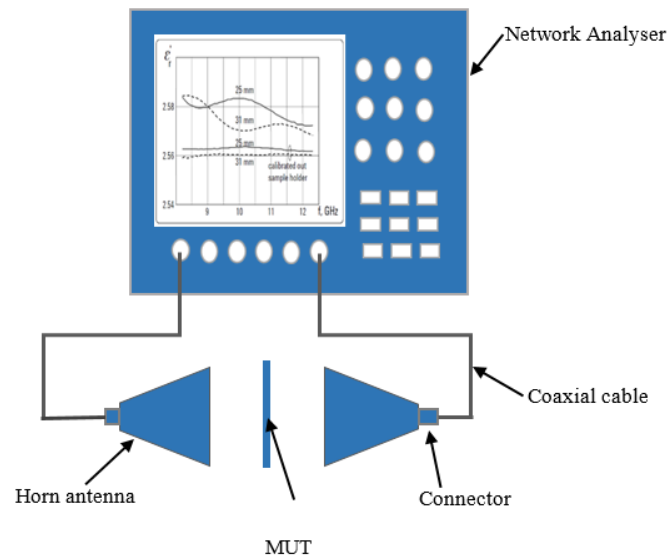
Figure 2-19 Schematic diagram of measurement system for the free space method using a pair of lens antennas

The dielectric properties of two types of Chinese coals have been measured using the free space method in the low-terahertz (THz) frequency range between 75 GHz to 110 GHz [58]. the two types of coals are bituminous and anthracite. They have different properties. Bituminous coals have lower fixed carbon and higher volatile matter than anthracite. They are also having different physical properties, Bituminous coal appears shiny and smooth, but it actually has layers. Whilst, Anthracite coal is a hard, brittle, and black lustrous coal, often referred to as hard coal, containing a high percentage of fixed carbon and a low percentage of volatile matter. It is found that the dielectric properties for both coals (bituminous and anthracite) decrease considerably with increasing frequency, as shown in Figure 2-20. The anthracite coals exhibit higher real and imaginary permittivity values compared with bituminous coals. The imaginary part of the permittivity of the coal samples exhibits a more significantly decreasing trend in the frequency range from 90 GHz to 110 GHz compared with frequencies below 90 GHz. It is also notable that dielectric properties of some coal samples depends on the moisture content For example, in Figure 2-20(a), dielectric constant of sample E is much higher than sample C owing to their relative moisture contents he moisture contents (9.45% for E, compared with 2.47% for C). However,

the differences in dielectric properties of other bituminous samples is not clear because of the uncertainty in their moisture contents [58].
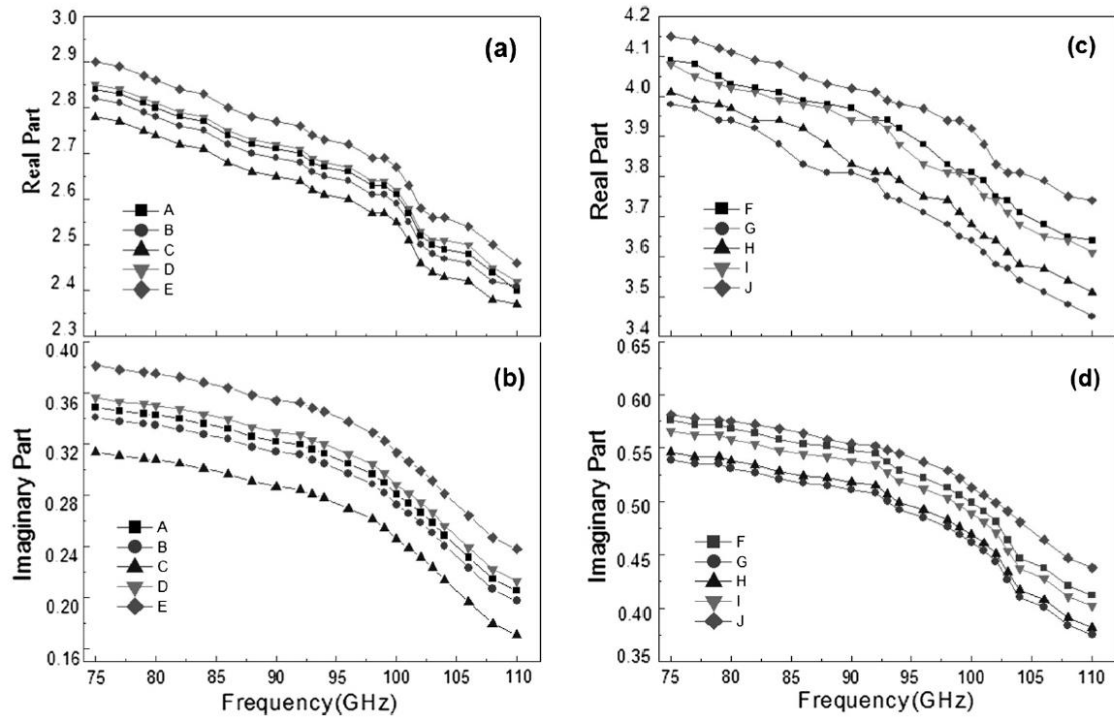
Figure 2-20 Variations of the dielectric permittivity with frequency for coals: (a) real part, (b) imaginary part of bituminous coal samples, (c) real part and (d) imaginary part of anthracite coal samples [58]

2.5.2   Resonance techniques

Resonance techniques typically have greater utility in measuring low loss materials. This is owing to the ability to measure very small changes in resonance bandwidth (or, equivalently, quality factor Q) associated with the presence of a sample. Since for dielectric property measurement the sample is immersed in the electric field of the cavity, there is no issue with sample contact (as with the coaxial probe), though one has to take care about the orientation of the electric field relative to the sample [59]. Resonant techniques can use one microwave port, but generally 2-port measurements of the S-parameters are performed.

Though similar in principle to the free space R/T method, measurements of dielectric properties of materials by resonant methods are more accurate than these reflection/ transmission methods, especially for dielectric loss. A disadvantage is that

measurement can only be accomplished at the (discrete) resonant frequencies allowed by the resonances of the host system, whereas in the transmission/ reflection methods the measurements can be obtained over a range of frequencies, though in practice this range is not that broad owing to the restrictions imposed by the waveguide band used [44-46].

2.5.2.1   Cavity Resonators

Microwave cavity resonators are used in many applications in the heating and drying of materials in industrial applications, such as the paper and food industries [44, 60] . The main advantages of using microwaves instead of traditional processes of heating is that microwave heating (via its electric field in most instances of water-containing materials) is fast, volumetric (as the penetration depth can be very large, from cm to m scales) and can be designed to be highly efficient [60, 61].

Waveguide-type resonators (usually called "cavity" resonators) are more superior to circuit-type (i.e. lumped element) resonators since their quality factor can reach several thousands, compared to a few hundred at most for circuits; the main reason for this is the higher operational frequency of cavity resonators, coupled with the fact that the electromagnetic fields are distributed over a larger volume (strictly, a higher volume to surface area ratio), both of which lead to higher Q. For this reason, lumped element resonators are not suitable for some applications such as spectroscopy and accurate tuning applications [62].

Microwave cavities will be used in this thesis to measure the complex relative permittivity of carbon samples. In this process, cavity perturbation analysis is used to calculate the complex permittivity from measurements of the resonant frequency shift and the change of quality factor on inserting the samples into the electric field of the cavity resonator[44, 63]. Perturbation theory and analysis will be discussed in detail in Chapter 3. The accuracy of the results of cavity resonator measurements depends on several factors. The most important is the quality factor, a high value of which is needed for measurements of dielectric loss, especially for low loss and/or small volume samples [64].

Levcheva et al. [65], presented a new method of using a cylindrical host cavity in its TE_{011} mode, proposed to measure complex permittivity of different states of low loss

dielectric materials: foams, layers, and thin sheets. When the resonator was filled with foam materials, exact solutions for resonator's fields were used for calculations. In the case of thin disk specimen, which is placed centrally in the resonator, the perturbation method was used to extract its complex permittivity [65].

In [66] a cylindrical cavity resonator was used to measure the dielectric constant and loss tangent of five different types of biomass generated from the Malaysian agricultural industry (oil palm shell, empty fruit bunch, rice husk, and coconut shell) and wood (sawdust) based industry. The measurements were made at the frequencies of 397 MHz, 912 MHz, 1429 MHz, 1948 MHz, 2466 MHz, and 2986 MHz using a cavity perturbation method in the temperature range between room temperature up to around 700 °C. This study could be the basis of design and simulate a microwave biomass processing system with selective frequency for large scale application [66].

Microwave cavity resonators were used to investigate the microwave dielectric properties of switchgrass and hay during the process of simultaneous heating. The relative dielectric constant, loss factor, and tangent loss of the hay were measured at 915 and 2450 MHz frequencies from room temperature to around 700 ^{0}C and under nitrogen (N$_2$) environment, as shown in **Figure 2-21**. The heating process can be divided into three different phases, namely drying, pyrolysis, and char region. The dielectric permittivity decreased during the drying and pyrolysis stages, but increased dramatically in the char region, indicating the strong microwave absorption capability of the char. This could be due to the transformation of biomass material into carbonaceous material, continuous change in weight and density, or the release of moisture and volatile matter. Hence, the dielectric properties tend to change with temperature and material characteristics. Models can also be developed for the dielectric properties that can be helpful to design and simulate microwave systems for biofuel and bio-product applications [67].
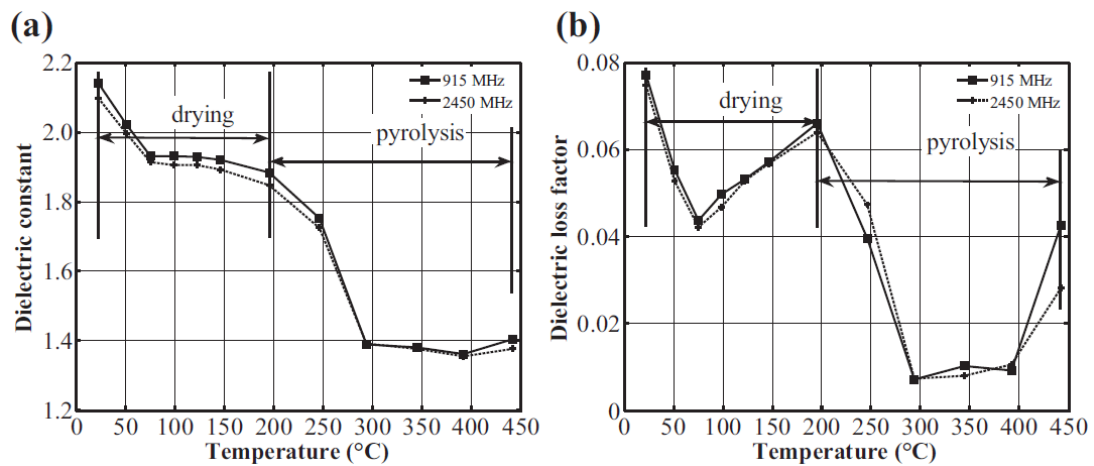
Figure 2-21 Dielectric properties of hay vs. temperature under nitrogen environment at 915 MHz and 2450 MHz with initial density of 0.76 ± 0.05 g/cc; (a) relative dielectric constant and (b) relative loss factor [67]

Microwave cavity resonators were used to investigate the dielectric properties of corn stover (i.e. the remains of stalks, leaves, and cobs after the corn harvest) during its thermal decomposition. The results confirm that the ability of corn stover to absorb microwaves is poor in in the pyrolysis stage but high in the char stage [27, 67, 68].

Cavity resonators were also used to measure the dielectric properties of oil shale at 2470 and 912 MHz to investigate effects of organic content, temperature, and moisture content on the microwave heating efficiency. [69] One of the factors that limits the use of microwave heating as a convenient technology for the extraction of organic material from oil shales is an insufficient means of obtaining accurate dielectric property data [69].

2.5.2.2   Dielectric Resonators

A dielectric resonator (DR) is constructed of cylindrical or rectangular shape and is made up of low loss and dielectric material surrounded by a metallic cavity, which preserves a high Q (as much as 100000 at room temperature and frequencies below 5 GHz). Dielectric constant, Q factor, and temperature coefficient of the resonant frequency are the most significant properties of materials for DRs. In general, DRs are smaller, lower in cost and weight compared with an air-spaced cavity of the same resonant frequency made wholly from aluminium or copper. Microwaves can easily be coupled into the resonator by installing probe antennas or small loops through the

walls of the outer metal shield. Dielectric resonators can be utilized for dielectric property measurements as for air-spaced rectangular or cylindrical cavity resonators, with a suitably designed sampled space (e.g. a gap between two dielectrics, or an axial hole) [2]. Dielectric resonators have become common resonant components of microwave filters and oscillators owing to their compact size and low loss (i.e. high Q) [2].

The split-post dielectric resonator (SPDR) has now become a well-established technique for measurements of the dielectric properties of low loss dielectric materials, thin films and wide bandgap semiconductors that are difficult to measure by other techniques. It is a highly accurate method for measuring the complex permittivity. The SPDR technique was used to measure complex permittivity of single crystal standard reference dielectric materials in frequency range 1.4–5.5 GHz to compare the results with well-known dielectric properties previously measured by other techniques [70]. The results show that split post resonators can be used to measure permittivity with uncertainty about 0.3%. The SPDR has also been used for measurements of the complex permittivity of dielectric and ferrite laminar specimens at a frequency range 1-12 GHz. Single crystals quartz was used as the standard reference material since it has an accurately determined permittivity and very low dielectric losses to assess the SPDR for the uncertainty of permittivity; this study demonstrates well the use of the SPDR for accurate and convenient measurements of dielectric properties at frequencies 20-25 GHz [70-72]. The geometry for the split dielectric resonators is shown in Figure 2-22, showing clearly the sample space.
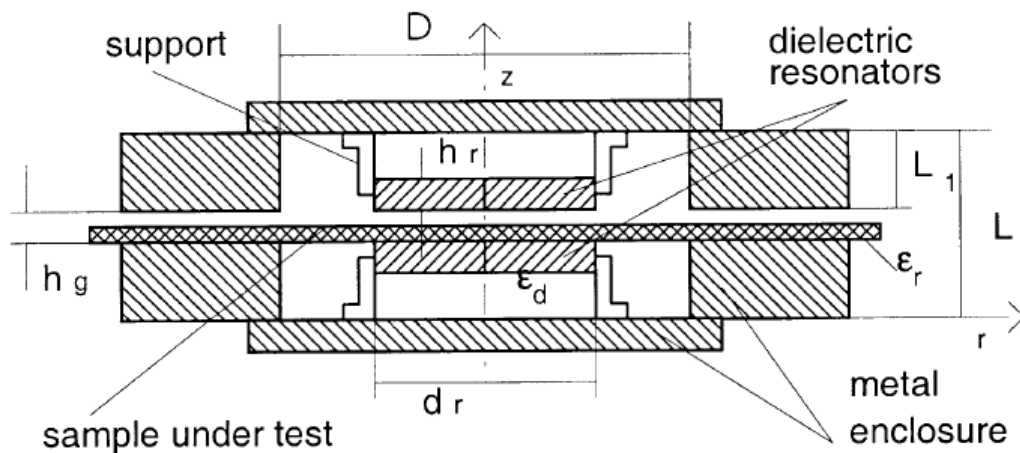
Figure 2-22 Schematic diagram of a split dielectric resonator fixture [70]

2.5.2.3   Microstrip Ring Resonator

There are many microwave circuits that use microstrip ring resonators, such as filters, oscillators, mixers, couplers and antennas. Their attractiveness is due to their compact and planar design, and also compatibility with integrated circuit technology. Microstrip ring resonator structure can be used more to measure dielectric constant and loss factor of materials (especially thin films or flat substrates) at broadband frequencies using their harmonics, rather than using many different ring resonators individually. A microstrip ring resonator consists of printed microstrip on a solid substrate, as shown in Figure 2-23 [73-75]. Such resonators have been very useful for accurate measurements of the complex permittivities of liquids in a microfluidic environment, for "lab-on-chip" applications.
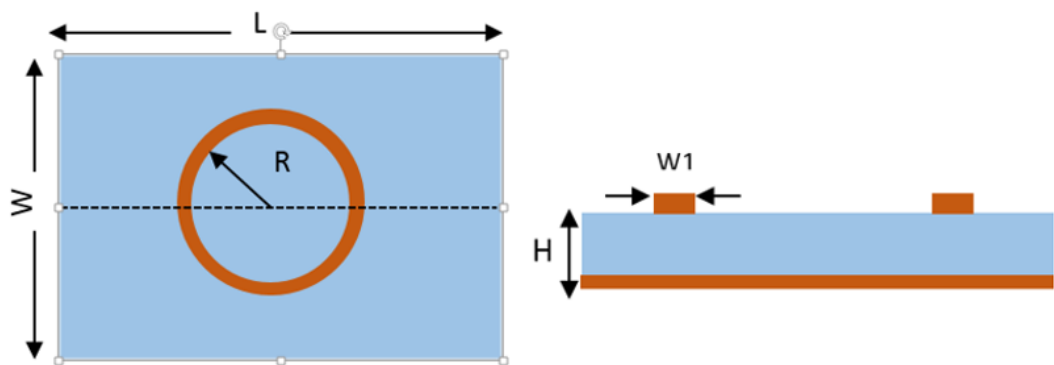
Figure 2-23 Microstrip and ring resonator

Dielectric properties of some common liquids (such as hexane, chloroform, methanol, ethanol, and water) have been measured using a new double split-ring resonator (DSRR) with two gaps, which is shown in **Figure 2-24**. The samples were filled inside two types of tubes (quartz and PFA tubes). Perturbation theory was used to extract the dielectric properties of samples from the shift in resonant frequency and change in the quality factor [76, 77].
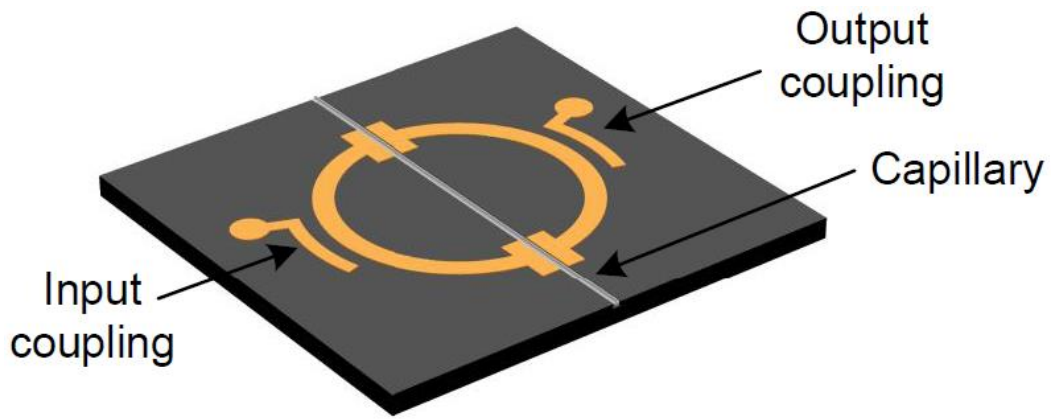
Figure 2-24 Schematic of DSRR microfluidic sensor [76]

resonator sensitivity is limited at high permittivity by the effects of depolarization, but for low permittivity gives very accurate results for small changes in the permittivity of liquids. From Figure **2-25** and Figure **2-26** it is clear that water caused the largest resonant frequency shift, while the minimum shift was caused by hexane, which is consistent with their known dielectric properties [76, 77].
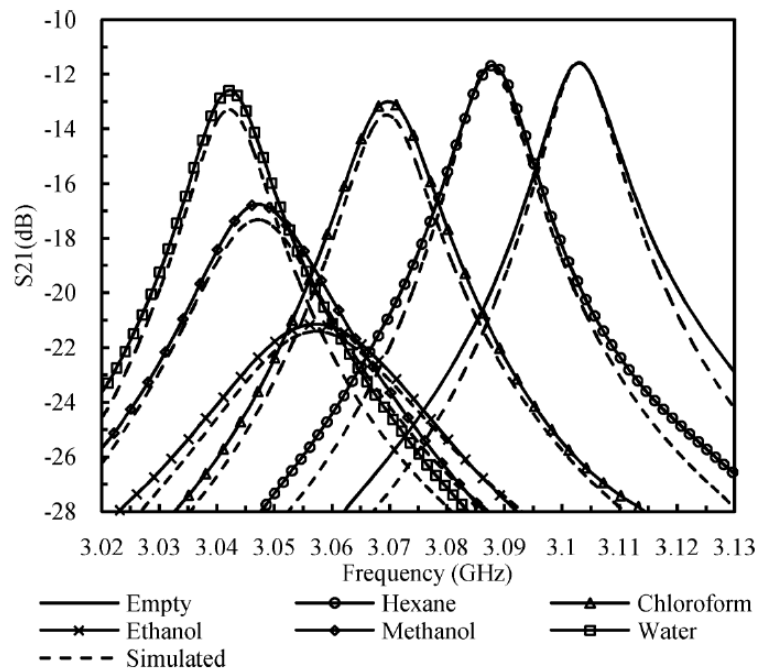
Figure 2-25 $|S_{21}|$ of the sensor using a quartz tube: simulated results by COMSOL Multiphysics Software (dotted lines) and measured results (solid lines and symbols) [77]
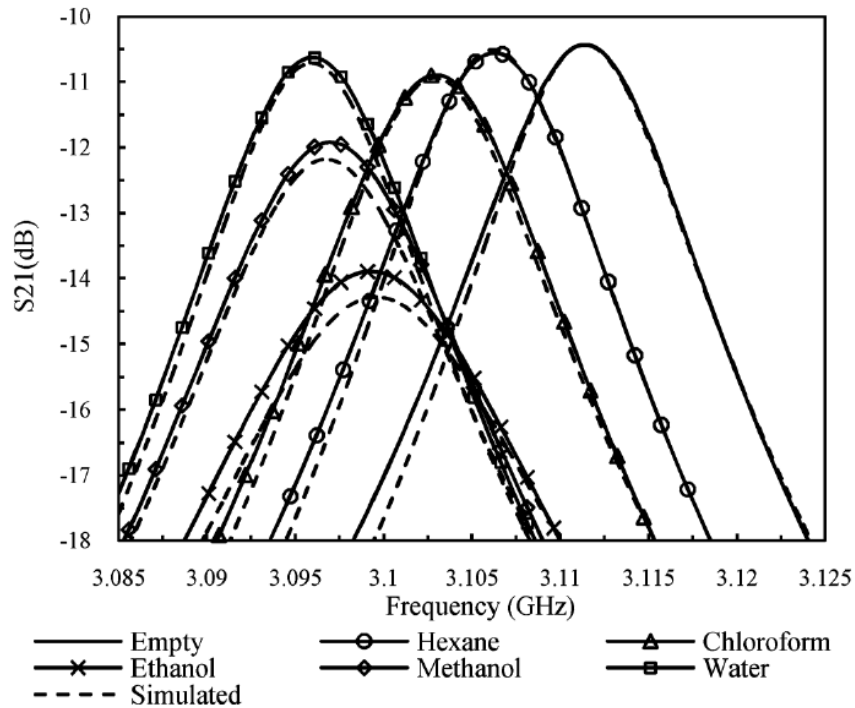
Figure 2-26 $|S_{21}|$ of the sensor using PFA tube: simulated results by COMSOL Multiphysics Software (dotted lines) and measured results (solid lines and symbols) [77]

2.6 Microwave techniques for this research

In this thesis, the microwave cavity system and broadband coaxial probe technique are used for dielectric properties measurements. There are many practical reasons to choose these techniques such as simplicity of construction, non-destructive nature, non-contacting (for the cavity system) and high accuracy. The summary of the microwave systems used in this thesis can be outlined as follows.

The microwave cavity system was used in measurements of the microwave permittivity of the final product of activated carbons produced from different precursors and different forms of carbonaceous materials contained in blast furnace dust (Chapter 4).

The microwave broadband coaxial probe, together with a new method of preparing samples, is used in frequency dependent microwave dielectric permittivity measurements of activated carbons and the different carbonaceous materials which are found in blast furnace dust (Chapter 5).

The microwave cavity system has been incorporated into an oven, with procedures to calibrate temperature errors, and is thus used in temperature dependent microwave dielectric permittivity measurements of activated carbons and blast furnace dust (Chapter 6).

Chapter 3 Modelling, Design and Methods

3.1 Introduction

This chapter reviews the theoretical basis of the design microwave applicators (i.e. low power sensors and high-power cavities) that have been used in this research, and presents the modelling and design of these applicators for their use in dielectric characterization and heating. Dielectric theory is introduced in section 3.2. The fundamentals of cylindrical cavities and cavity perturbation theory are presented in sections 3.3 and 3.4, respectively. In section 3.5, a review of coaxial probe techniques that have been used to measure dielectric properties are presented. Modelling and design of cavity resonators and the coaxial probe are presented in sections 3.6 and 3.7, respectively.

3.2 Dielectric theory

The dielectric material response to an electric field at microwave frequencies can be modelled using a relative complex permittivity which is consists of two parts real and imaginary. The real part ε' quantifies the stored energy in the material under the applied electric field, whilst the imaginary part ε'' quantifies the energy loss within the material. The permittivity can be normalized to that of free space using $\varepsilon' = \varepsilon_0 \varepsilon_r'$ and $\varepsilon'' = \varepsilon_0 \varepsilon_r''$; ε_r'' is called loss factor and the loss tangent can be calculated using ε_r'' and ε_r' as follows:

$$tan\,\delta = \frac{\varepsilon_r''}{\varepsilon_r'} \tag{3-1}$$

The effects of electric field on an arbitrary material can be modelled by combing dielectric and conductive effects via a complex current density $\bar{J} = (\sigma + j\omega\varepsilon)E$. Thus electric currents have two components: conduction current due to the free charges in the material, and displacement current which is produced by the oscillating applied electric field [78].

When the electric field is applied to a dielectric material, displacement of positive and negative charges will occur. This reaction of the material is called polarization, which depends generally on the material type and the frequency of the electric field, shown

in **Figure 3-1**. In general, the polarization can be divided to four types: space charge polarization, polarization by dipole alignment, ionic polarization, and electronic polarization.
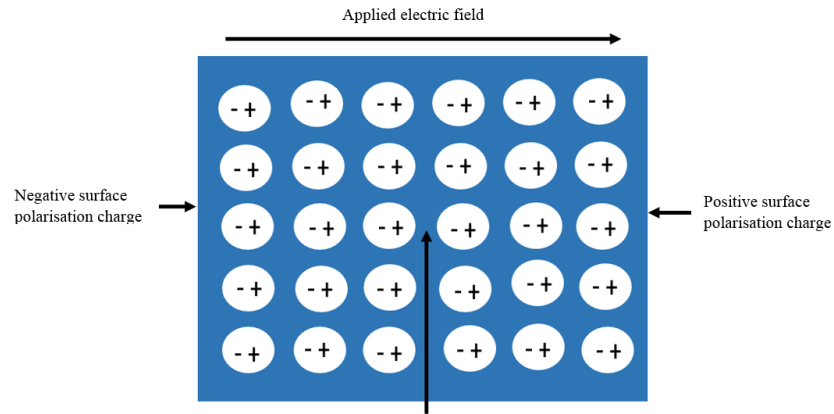
Figure 3-1 the polarisation of a dielectric material when placed in a uniform electric field.

3.2.1   Space charge polarization

When the electric field is applied to a material containing free electrons, these free electronic accumulate on the material boundaries. This action results in a separation of charges which polarizes the material and is an essential mechanism in semiconductors.

3.2.2   Polarization by dipole alignment

Some materials have a permanent electric dipole moment, such the water, which means that charges within the molecule are always separated even in absence of electric field, owing to the electrochemical characteristics of the inherent atoms. With no applied electric field, the dipoles inside the material are randomly oriented and so electrically cancel each other. The existence of an electric field makes the dipoles rearrange to align with the direction of electric field, giving rise to a strong polarization, called orientational polarization.

3.2.3   Ionic polarization

Ionic polarisation occurs in crystalline solids, where applying an electric field gives strong polarisation by displacing the positive and negative ions from their position in the molecule. When an electric field is applied to a molecule, the positive charges are displaced along the field, while the negative charges are displaced in a direction opposite to that of the field. Ionic polarizability occurs in materials that exhibit ionic bonding, such as sodium chloride [79].

3.2.4   Quantification of polarization and depolarization effects

The electrons surrounding the nucleus of each atom within a material will be displaced by an applied electric field, thus causing a dipole moment.
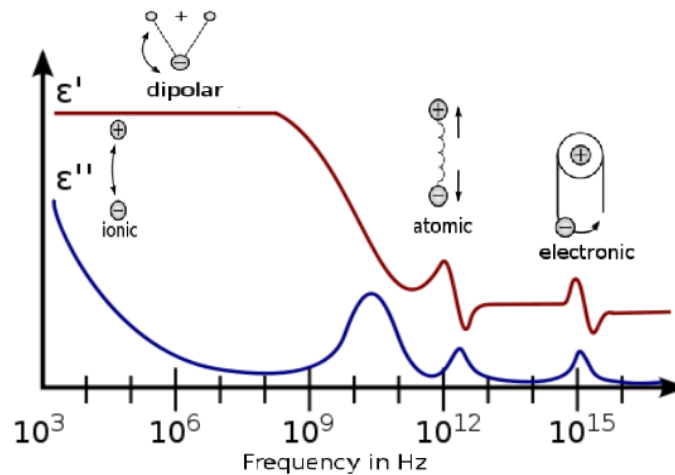
Figure 3-2 Dielectric constant and loss dispersion of dielectric materials against frequency [79]

When an electric field E_0 is applied to a dielectric material, the interaction between the material and field is described by the material's relative permittivity ε_r. The polarization per unit volume P is directly proportional to the internal electric field E_{in} and it can be expressed as:

$$P = (\varepsilon_r - 1)\varepsilon_0 E_{in} \equiv \chi_e \varepsilon_0 E_{in} \qquad (3\text{-}2)$$

where $\chi_e = (\varepsilon_r - 1)$ is a dimensionless quantity called the electric susceptibility of the dielectric; it describes how strongly a dielectric will polarize when placed in an applied E_0 field. Losses can be considered by writing ε as the complex quantity $\varepsilon_r =$

$\varepsilon' - j\varepsilon''$ the quantity $(\varepsilon' - 1)$ is proportional to the material's polarization and ε'' to the power dissipation.

The magnitude of the internal electric field can be expressed as following:

$$E_{in} = \frac{E_0}{1 + N\chi_e} \tag{3-3}$$

By substituting $\chi_e = (\varepsilon_r - 1)$ in the above,

$$E_{in} \approx \frac{E_0}{1 + N(\varepsilon_r - 1)} \tag{3-4}$$

where N is a dimensionless number called the depolarization factor, which depends on the object's shape and the direction of the applied field [80-82].

Assuming a uniform internal electric field and an external field consisting of the applied field plus a dipole term, the depolarization factor for a cylindrical shape is

1. $N \approx$ zero, when the applied electric field is parallel to the axis of a long cylinder, or in the plane of a thin sheet of large 2D surface area. So, the internal electric field is approximately equal to the applied electric field $E_{in} \approx E_0$ as shown in **Figure 3-3** (a).

2. $N = 1/2$, when the applied electric field is perpendicular to the axis of a long cylinder. So, the internal electric field is reduced to $E_{in} \approx \frac{2E_0}{1 + \varepsilon_r}$ as shown in **Figure 3-3** (b). i.e. the magnitude of internal electric field is much smaller than applied field E_0 when the relative permittivity $\varepsilon \gg 1$.
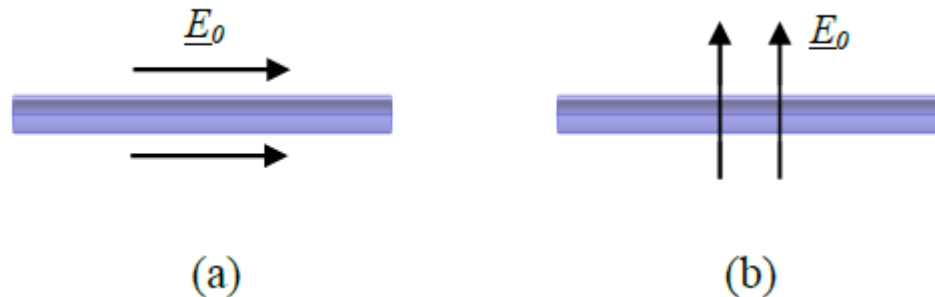
Figure 3-3 The depolarization effects in dielectric cylindrical shape. (a) Cylindrical sample in parallel, non-depolarising configuration, and (b) Cylindrical sample in perpendicular, depolarising configuration.

Therefore, it is desirable to apply and electric field E along the long dimension of the material sample in applications that require the maximum internal electric field inside the material. Only in these instances is there maximum polarisation, and so maximum interaction between the applied electric field and the sample [83].

3.2.5   Penetration Depth

The penetration depth, D_p, the depth to which the field penetrates to $1/e \approx 37\%$ of its surface value, is a measure of the depth of microwave penetration in a dielectric material. It is mathematically defined as[84]:

$$D_\rho = \frac{\lambda_0}{2\pi(2\varepsilon')^{1/2}} \left\{ \left[1 + \left(\frac{\varepsilon''}{\varepsilon'} \right)^2 \right]^{1/2} - 1 \right\}^{-1/2} \qquad (3\text{-}5)$$

where λ is the free space wavelength of incident radiation. From (3-5), the penetration depth increases with an increase in the wavelength or a decrease in the frequency. The penetration depth is also approximately inversely proportional to the values of ε' and ε''.

Due to the short wavelength of microwaves (of the order of centimetres), they penetrate quite deeply within non-metals, so keeping the resonator perturbation principle preserved. Accordingly, the volumetric material properties can be deduced, e.g. moisture content, since microwaves are not restricted to the surface of the tested material [84-86]. **Table 3-1** shows the relative permittivity (real part) of selected materials and the field penetration depth at a frequency of 3 GHz

Table 3-1 values of penetration depth for some dielectric materials

Material	T [ºC]	ε_r	D_p [m]
Water	25	76.7	0.023
Ice	-12	3.20	19.77
Polystyrene	25	2.55	60.42
Teflon	22	2.10	146.44
Table salt	25	2.26	32.62
Fused quartz	25	3.78	246.91

Taking the opposite extreme of a weakly conducting dielectric, the skin depth δ of a good conductor is expressed as

$$\delta = \sqrt{\frac{2}{\omega\mu\sigma}} = \sqrt{\frac{2\rho}{\omega\mu}} \tag{3-6}$$

where μ is the permeability of the material in H/m, $\mu = \mu_0\mu_r$, σ is the conductivity in S/m and ρ is the resistivity in Ωm. The skin depth according to (3-7) is a function of three variables; conductivity (or resistivity), permeability, and frequency of operation. Since $\mu_r \approx 1$ for most metals, the skin depth can be re-written as:

$$\delta = \sqrt{\frac{2}{\omega\mu_0\sigma}} = \sqrt{\frac{2\rho}{\omega\mu_0}} \tag{3-7}$$

At microwave frequencies, the skin depth for good conductors is extremely small (around 1μm), and so a very thin coating of a good conductor such as gold or silver is necessary to realize low-loss microwave components [2, 87].

3.2.6   Effect of electronic conductivity on microwave loss

Conductivity introduces an energy loss mechanism owing to the scattering of mobile charges in an applied electric field. This introduces a characteristic term in the imaginary permittivity which is inversely proportional to frequency and directly proportional to the conductivity, as shown in (3-8).

$$\varepsilon = \varepsilon' - j\varepsilon'' \tag{3-8}$$

$$\varepsilon'' = \varepsilon_d'' + \varepsilon_\sigma'' = \varepsilon_d'' + \frac{\sigma}{\varepsilon_0\omega} \tag{3-9}$$

The subscripts d and s stand for contributions due to the lattice of a material and electronic conduction, respectively. At low frequencies, ε is dominated by the influence of conductivity, while the variation of permittivity in the microwave range is mainly caused by lattice (dipolar) relaxation effects. At microwave frequencies, dipolar polarization is dominant at lower frequencies while electronic and atomic polarizations are dominant at higher frequencies. For electrolytes, the latter is related to the ionic concentration of solutions (i.e. their conductivity) which is also then inversely dependent on frequency.

3.2.7   Dielectric Relaxation

Relaxation of a dielectric is a phenomenon that normally happens immediately after removing the applied electric field, the charges take a finite time to return to their natural positions. The time which is taken by material's charges to return to their normal order is called the relaxation time [60, 88].

There are different relaxation models for dielectrics, such as that of Debye, leading to the Cole-Cole equations [80]. Debye's theory shows the relation between complex permittivity and relaxation time, namely, as the relaxation time increases, the permittivity decreases. Debye's equation can be expressed as follows:

$$\varepsilon = \varepsilon' - j\varepsilon'' = \varepsilon_\infty + \frac{\varepsilon_s - \varepsilon_\infty}{1 + j\omega\tau} \qquad (3\text{-}10)$$

Therefore, the real and imaginary parts can be separated as follows:

$$\varepsilon' = \varepsilon_\infty + \frac{\varepsilon_s - \varepsilon_\infty}{1 + j(\omega\tau)^2} \quad , \quad \varepsilon'' = \frac{(\varepsilon_s - \varepsilon_\infty)\omega\tau}{1 + j(\omega\tau)^2} \qquad (3\text{-}11)$$

where ε_∞ is the permittivity at high frequency (infinity), ε_s is the permittivity at low frequency (static), ω is the angular frequency and τ is the relaxation time (a constant).

Practically, liquids and solids tend to have more extended distributions for permittivity than the Debye equation shows because of the different origins of the relaxation phenomenon, and also given the fact that the materials might have a relaxation spectrum. This can be demonstrated mathematically by adding the empirical exponent parameter α to the Debye equation, as in the following form [60, 89].

$$\varepsilon = \varepsilon_\infty + \frac{\varepsilon_s - \varepsilon_\infty}{1 + (j\omega\tau)^{1-\alpha}} \qquad (3\text{-}12)$$

The constant α is related to τ and has values in the crange $0 \leq \alpha < 1$. When $\alpha = 0$ there is only a single relaxation time; when the value of α increases the relaxation time is distributed over broader range [90].
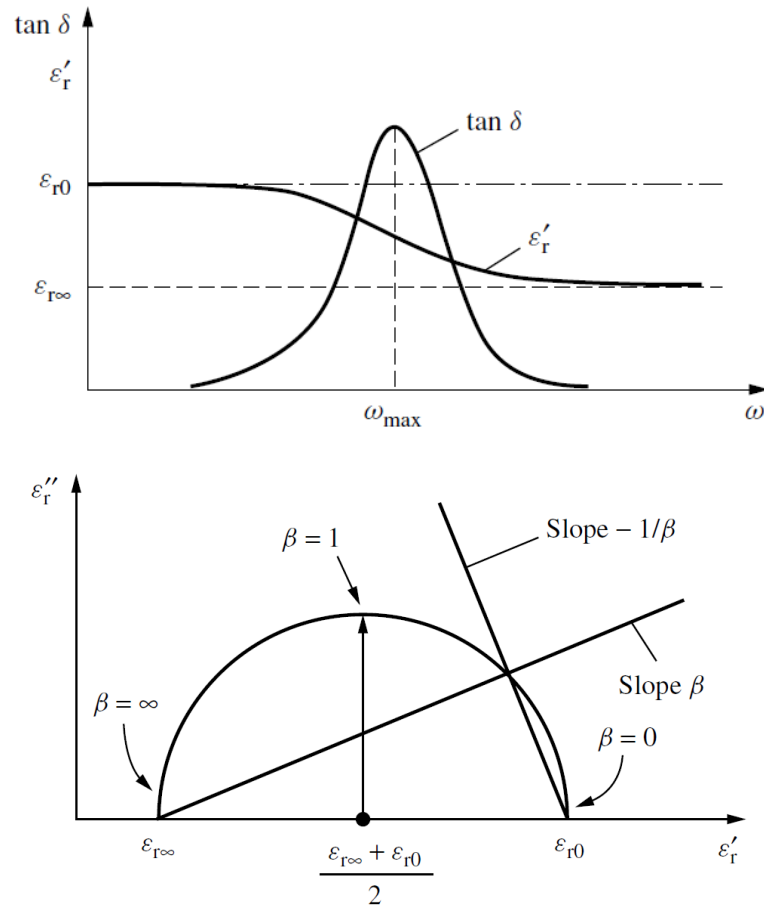
Figure 3-4 Debye and Cole-Cole Diagrams [90]

3.3 Fundamentals of cylindrical cavities

Cylindrical cavity resonators can be fabricated from circular waveguides with short circuits at both ends to enclose the fields within it. There is a standing electromagnetic wave associated with every resonant frequency, which is called a mode. Quite generally, a cavity with any shape supports a series of resonant frequencies (modes), the number of which is determined approximately by the following formula

$$N = \frac{8\pi}{3c^3} V f^3$$

(3-13)

where V is the volume of the cavity, c is the velocity of electromagnetic wave in the dielectric filling the cavity, and f is the frequency [64].

Resonant modes occur when the electric and magnetic fields form standing waves, with resonant frequencies which depend on the internal dimensions of the cavity and dielectric properties of the material contained within the cavity. The transverse electric (TE) and transverse magnetic (TM) are the two types of modes which exist in a cavity with only metal walls.

The TE modes in cylindrical cavity of radius (*a*) and length (*d*) and the propagation constant of the TE_{nml} mode can be expressed as:

$$E_t = E(\rho, \phi)(A^+ e^{-j\beta_{nm}z} + A^- e^{+j\beta_{nm}z})e^{j\omega t} \tag{3-14}$$

$$\beta_{nm} = \sqrt{k^2 - \left(\frac{p'_{nm}}{a}\right)^2} \tag{3-15}$$

where $k = \omega\sqrt{\mu\epsilon}$. Applying the field boundary conditions ($E_t = 0$ at $z = 0$ and d) leads to the conditions $A^+ = -A^-$ and $A^+ \sin\beta_{nm}d = l\pi$, for l=0, 1, 2, 3 . . . where l is the integer number of half-guide wavelengths along the cavity length. The resonant frequency of the TE_{nml} mode can be written as in equation(3-16) [2].

$$f_{nml} = \frac{c}{2\pi\sqrt{\mu_r\varepsilon_r}}\sqrt{\left(\frac{p'_{nm}}{a}\right)^2 + \left(\frac{l\pi}{d}\right)^2} \tag{3-16}$$

The propagation constant and resonant frequency of the TM_{nml} mode is [2]

$$\beta_{nm} = \sqrt{k^2 - \left(\frac{p_{nm}}{a}\right)^2} \tag{3-17}$$

$$f_{nml} = \frac{c}{2\pi\sqrt{\mu_r\varepsilon_r}}\sqrt{\left(\frac{p_{nm}}{a}\right)^2 + \left(\frac{l\pi}{d}\right)^2} \tag{3-18}$$

The parameters introduced in these equations are as follows:

f_{nml} is the operation frequency of the cylindrical cavity resonator.

c is the speed of light in vacuum, i.e. 3×10^8 m/s

μ_r is the relative permeability of the material inside the cylindrical cavity resonator

ε_r is the relative permittivity of the material inside the cylindrical cavity resonator

The values of p_{nm} and p'_{nm} are listed below in **Table 3-2** and Table 3.3 respectively [2].

Table 3-2 Values of p_{nm}

	m = 1	2	3
n = 0	2.4048	5.5201	8.6537
1	3.8317	7.0156	10.1735
2	5.1356	8.4172	11.6198

Table 3-3 Values of p'_{nm}

	m = 1	2	3
n = 0	3.8317	7.0156	10.1735
1	1.8412	5.3314	8.5363
2	3.0542	6.7061	9.9695

3.3.1   Mode chart

A mode chart relates the frequencies of each mode to the dimensions of the cavity, in this case a cylinder. Either of (3.14) and (3.16) above may be written as:

$$(fa)^2 = A + Bl^2 \left(\frac{a}{d}\right)^2$$

(3-19)

where f is the resonant frequency and A, B are constants depending on the mode [91].

When designing cylindrical cavity resonators for materials measurement by cavity perturbation, it is important to ensure that there is no degeneracy, which means that no modes have the same resonant frequency. The problem is to minimize the effects of competing modes without any degrading the main mode [91], in our case TM_{010}. **Figure 3-5** shows a mode chart for the lower order resonant modes of a cylindrical cavity. This chart is useful for the design of cylindrical cavity resonators, as it shows what modes can be excited at a given frequency for a given cavity size.
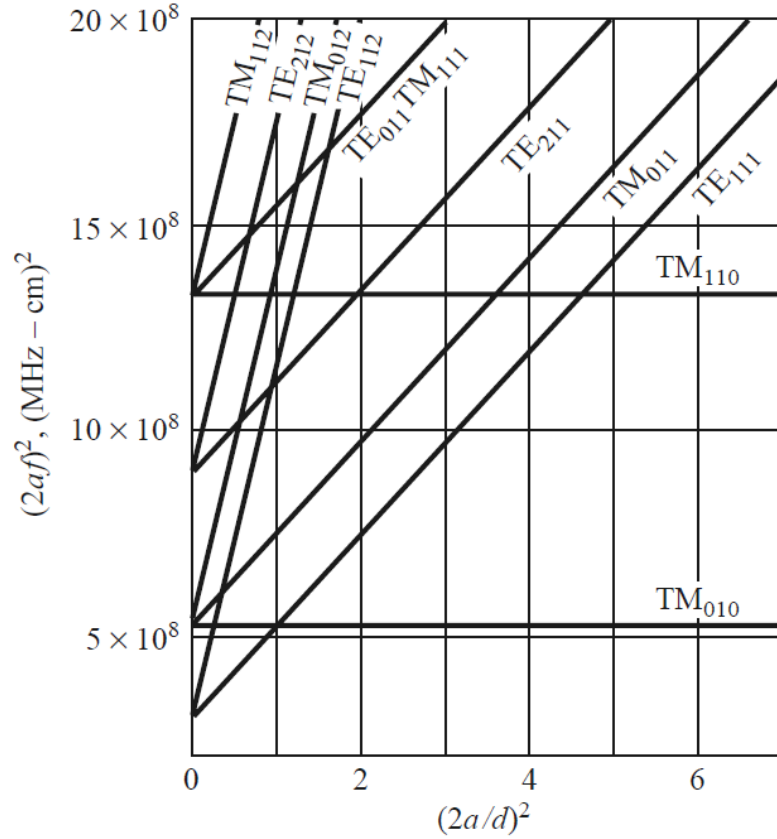
Figure 3-5 Resonant mode chart for a cylindrical cavity [2]

3.3.2 Quality factor

The quality factor is the ratio of the stored energy and the energy losses per cycle in the metal walls of the cavity, which is defined as

$$Q = \frac{2\pi f \ (energy \ stored \ in \ the \ cavity)}{power \ lost} = \omega_0 \frac{u}{p_{loss}} \qquad (3\text{-}20)$$

Q represents the quality factor without any load (external circuits), ω_0 is the angular resonant frequency. When a cavity resonator is connected to external circuits, which have their own effective quality factor Q_{ext} since the coupling effectively causes a leakage (i.e. loss) of energy, the total, measured quality factor Q_t becomes as in (3-21).

$$\frac{1}{Q_t} = \frac{1}{Q} + \frac{1}{Q_{ext}} \ and \ Q_t = \frac{f_0}{\Delta f} \qquad (3\text{-}21)$$

where f_0 is the centre frequency, Δf is the shift of resonant frequency.

3.3.3 Coupling of cavity resonators (excitation)

Excitation of cavity resonators is achieved by its coupling to an external circuit which provides a stimulus [58]. The coupling of resonators to external circuits through transmission lines or waveguides depends on the type of resonator and its applications [2]. There are some common methods used for coupling cavity resonators, which will be summarised below.

3.3.3.1 Coupling probe

In this coupling technique, the coaxial cable or wire antenna which feeds the cavity can be extended into the cavity. Its length should be small compared to the wavelength to make its input impedance equivalent to an open circuit [64]. and its position should be chosen according to required type of coupling and the matching of impedance [62]. Such a probe placed along the direction of maximum electric field [92] couples to the cavity's electric field; for this reason, this type of coupling is also called capacitive coupling.
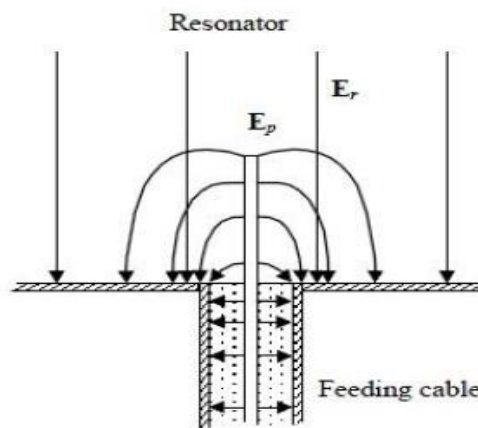
Figure 3-6 The coupling probe [93]

3.3.3.2 Coupling loop

To achieve coupling using a current carrying loop, the coaxial line which feeds the cavity should be extended, bent and grounded on the cavity wall. Again, its size should be small compared to the wavelength to make its input impedance equivalent to a short circuit. To achieve optimum coupling the loop should be placed where the magnetic

field has a high value and is oriented so that its direction is perpendicular to the plane of the loop [64, 94]. The loop couples to the magnetic field via the linking of magnetic flux between it and the cavity, and so this type of coupling is also called inductive coupling.
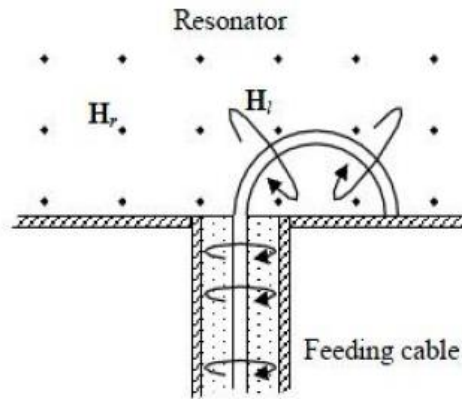
Figure 3-7 The coupling loop [93]

3.3.3.3   Aperture coupling

To connect a cavity to a waveguide circuit, a small hole or aperture is used. The electric and magnetic fields will penetrate through the hole to couple to the cavity [64].
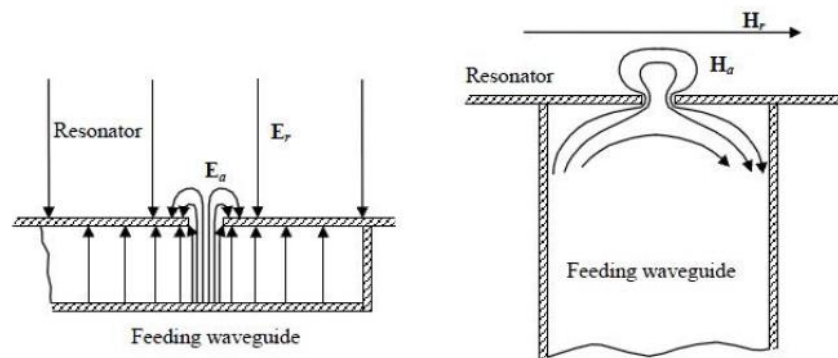
Figure 3-8 Aperture coupling, electric and magnetic [93]

3.3.3.4   Coupling Coefficient

The required level of coupling between the resonator and the external circuits depends on the application. The coupling coefficient is the measure of the strength of the coupling between the resonator and feed line. Maximum power transfer between the

53

resonator and a feed line can be achieved by matching them at the resonant frequency; the resonator is then said to be critically coupled to the feed. These concepts can be understood by considering the series resonant circuit shown in **Figure 3-9** [2].
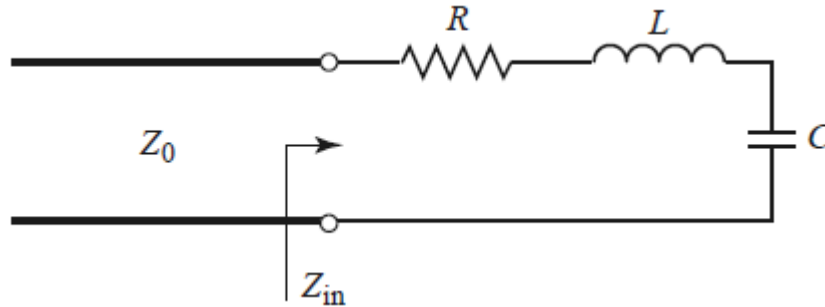
Figure 3-9 A series resonant circuit coupled to a feedline [2]

The input impedance near resonance of the series resonant circuit of **Figure 3-9** is given by

$$Z_{in} = R + j2L\Delta\omega = R + j\frac{2RQ_0\Delta\omega}{\omega_0} \tag{3-22}$$

The unloaded Q is

$$Q_0 = \frac{\omega L}{R} \tag{3-23}$$

At resonance, $\Delta\omega = 0$, so the input impedance is $Z_{in} = R$. In order to match the resonator to the input line we must have:

$$R = Z_0 \tag{3-24}$$

In this case the unloaded Q is:

$$Q_0 = \frac{\omega_0 L}{Z_0} \tag{3-25}$$

The external Q is:

$$Q_e = \frac{\omega_0 L}{Z_0} = Q_0 \tag{3-26}$$

The coupling parameter k is related to the total loaded quality factor Q_t and unloaded quality factor Q_0 is given by

$$k = \left[\frac{Q_t - Q_0}{Q_t + Q_0}\right] \tag{3-27}$$

The higher the value of loaded Q, the lower the value of the coupling parameter. The coupling coefficient g is defined to be

$$g = \frac{Q_0}{Q_{ext}}$$
(3-28)

Both the coupling parameter k and coupling coefficient g should be low to obtain higher loaded quality factor [95]. In the following discussion we will refer to the coupling coefficient g (rather than k).

There are three cases of coupling levels, which are:

- Under coupling when $g < 1$
- Critically coupling $g = 1$ (resonator is matched to its input line)
- Over coupling $g < 1$

3.3.4 Network analyser and scattering parameters

Scattering parameters can be measured using a network analyser at different frequencies. A network analyser mainly consists of a source, used to generate a known signal, and receiver used to determine changes to this signal caused by the material-under-test. They are capable of measuring transmitted (S_{21}) and reflected (S_{11}) signals, expressed as voltage transmission or reflection coefficients. Equations defining the full set of four scattering parameters of a two port network (e.g. a two port cavity) are expressed in (3-29) to (3-32).

$$S_{11(forward)} = \frac{reflected}{incident} = \frac{b_1}{a_1}\Big|_{a_2=0}$$
(3-29)

$$S_{21(forward)} = \frac{transmitted}{incident} = \frac{b_2}{a_1}\Big|_{a_2=0}$$
(3-30)

$$S_{22(reverse)} = \frac{reflected}{incident} = \frac{b_2}{a_2}\Big|_{a_1=0}$$
(3-31)

$$S_{12(reverse)} = \frac{tranmitted}{incident} = \frac{b_1}{a_2}\Big|_{a_1=0}$$
(3-32)

where a_1, a_2, b_1, and b_2 can be voltage or current. The relationship between the incident wave [a] and reflected wave [b] are normally represented by the scattering matrix, as shown in (3-33):

$$\begin{bmatrix} b_1 \\ b_2 \end{bmatrix} = \begin{bmatrix} S_{11} & S_{12} \\ S_{21} & S_{22} \end{bmatrix} \begin{bmatrix} a_1 \\ a_2 \end{bmatrix}$$

(3-33)
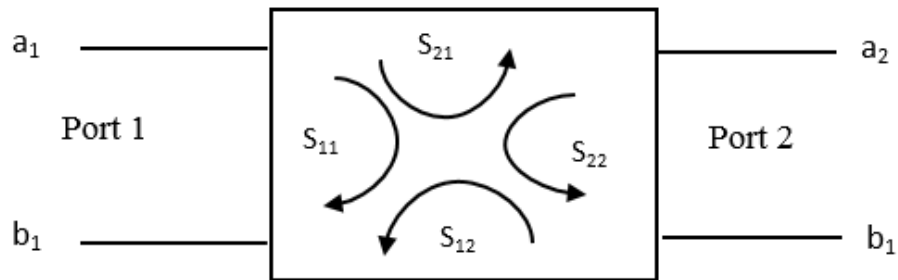
Figure 3-10 Two port network

3.3.5 Equivalent circuits of cavity resonators

Microwave cavity resonators can be represented by equivalent series or parallel RLC resonant circuits, which are shown in **Figure 3-11**. Input impedance/admittance, power loss, stored magnetic energy, stored electric energy, resonant frequency, unloaded Q, and external Q for series or parallel RLC resonant circuits are briefly summarized in **Table 3-4**.
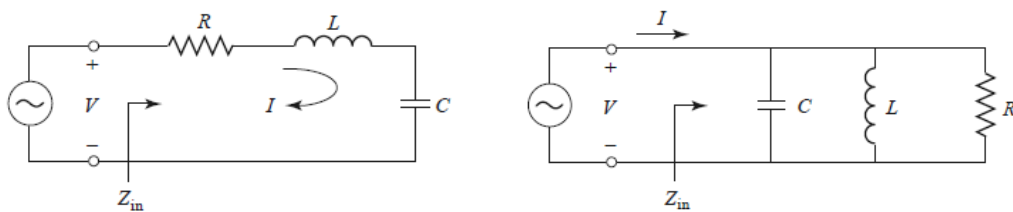
Figure 3-11 series and parallel *RLC* equivalent circuits of resonator [2]

Table 3-4 Summary of formulae for Series and Parallel Resonators [2]

Quantity	Series circuit	Parallel circuit
Input impedance/admittance	$Z_{in} = R + j\omega L - j\dfrac{1}{\omega C}$ $\approx R + j\dfrac{2RQ_0\Delta\omega}{\omega_0}$	$Y_{in} = \dfrac{1}{R} + j\omega C - j\dfrac{1}{\omega L}$ $\approx \dfrac{1}{R} + j\dfrac{2Q_0\Delta\omega}{R\omega_0}$

Power loss	$P_{loss} = \dfrac{1}{2}|I|^2 R$	$P_{loss} = \dfrac{1}{2}\dfrac{|V|^2}{R}$
Stored magnetic energy	$w_m = \dfrac{1}{4}|I|^2 L$	$w_m = \dfrac{1}{4}|V|^2\dfrac{1}{\omega^2 L}$
Stored electric energy	$w_e = \dfrac{1}{4}|I|^2\dfrac{1}{\omega^2 C}$	$w_e = \dfrac{1}{4}|V|^2 C$
Resonant frequency	$\omega_0 = \dfrac{1}{\sqrt{LC}}$	$\omega_0 = \dfrac{1}{\sqrt{LC}}$
Unloaded Q	$Q_0 = \dfrac{\omega_0 L}{R} = \dfrac{1}{\omega_0 RC}$	$Q_0 = \omega_0 RC = \dfrac{R}{\omega_0 L}$
External Q	$Q_e = \dfrac{\omega_0 L}{RL}$	$Q_e = \dfrac{RL}{\omega_0 L}$

3.4   Cavity perturbation theory

The perturbation of resonant cavities may be achieved by changes in the stored energy or power dissipated, which give rise to changes in resonant frequency and Q factor, respectively. Perturbations can be realized by making one of the ends of cavity walls movable (shape perturbations), or by the introduction of small pieces of dielectric or ferromagnetic material (material perturbations). In the case of dielectric measurements, the second way is applied. Cavity perturbation measurements can be highly accurate and are particularly advantageous in the determination of relative permittivity of dielectrics with small loss tangents. Perturbation techniques permit the measurement of dielectric samples of small sizes and various shapes. The most convenient of sample shapes for easy analysis are spheres, rods, discs, and slabs/sheets [96].

Cavity perturbation methods are used to determine the complex permittivity, in which a sample of material is inserted into the cavity and the resulting perturbations measured, as illustrated in **Figure 3-12**. In the cavity perturbation technique, it is necessary to use a small sample to ensure that the changes in the fields will be small in the vicinity of the sample [63]. The accuracy of the results of the measurements depends on several factors. The most important is the quality factor Q of the cavity resonator, where a high Q value is required to obtain accurate results [97].
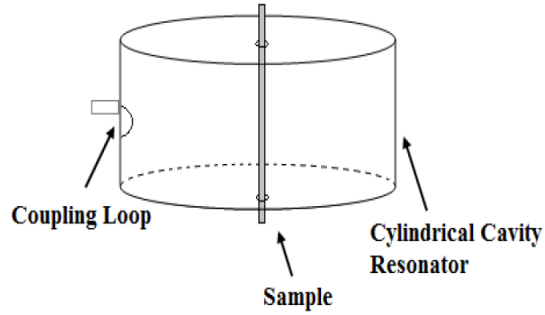
Figure 3-12 A dielectric material, in the form of a thin rod, measured using a cylindrical host cavity resonator [64]

The cavity's material perturbations are considered as a means of measuring material properties by analysis of the shift in the (complex) resonant frequency when the dielectric material sample is inserted into the cavity [2, 64].
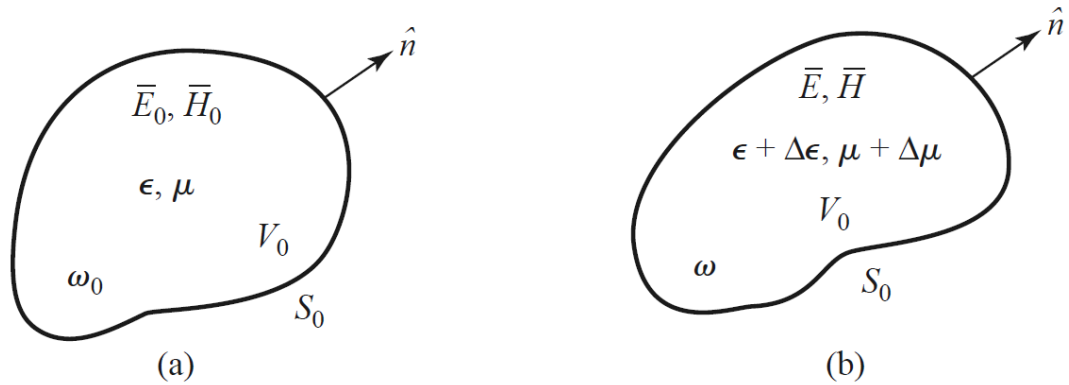
Figure 3-13 a resonant cavity perturbed by a changing in the permittivity or permeability of the materials in the cavity. (a) Original cavity. (b) Perturbed cavity [2]

We assume that the material inside the cavity resonator has permittivity ε and permeability μ. The subscript "0" is used to denote the resonant frequency and EM fields of the cavity before the perturbation. Maxwell's time-dependent equations can then be written as

$$\nabla \times \overline{E_0} = -j\omega_0 \mu \overline{H_0} \tag{3-34}$$

$$\nabla \times \overline{H_0} = j\omega_0 \epsilon \overline{E_0} \tag{3-35}$$

$$\nabla \times \overline{E} = -j\omega(\mu + \Delta\mu)\overline{H} \tag{3-36}$$

$$\nabla \times \overline{H} = j\omega(\epsilon + \Delta\epsilon)\overline{E} \tag{3-37}$$

where $\Delta\epsilon$ and $\Delta\mu$ are the changes in permittivity and permeability [98].

We next take the scalar product of the conjugate of (3-34) with $\bar{H}$, and the scalar product of (3-35) with $\overline{E_0^*}$. Subtracting the results and using the vector identity $\nabla.(\bar{A} \times \bar{B}) = \bar{B}.\nabla \times \bar{A} - \overline{\bar{A}.\nabla \times \bar{B}}$ gives

$$\nabla \cdot \left(\overline{E_0^*} \times \bar{H}\right) = j\omega_0\mu\bar{H} \cdot \overline{H_0^*} - j\omega(\epsilon + \Delta\epsilon)\overline{E_0^*} \cdot \bar{E} \qquad (3\text{-}38)$$

Repeating the same procedures on (3-35) and (3-36), we obtain (3-39)

$$\nabla \cdot \left(\bar{E} \times \overline{H_0^*}\right) = -j\omega_0(\mu + \Delta\mu)\overline{H_0^*} \cdot \bar{H} - j\omega_0\overline{E_0^*} \cdot \bar{E} \qquad (3\text{-}39)$$

By adding (3-38) and (3-39), integrating over the volume V_0, and applying the divergence theorem we get

$$\int_{v_0} \nabla \cdot \left(\overline{E_0^*} \times \bar{H} + \bar{E} \times \overline{H_0^*}\right)dv = \int_{s_0}\left(\overline{E_0^*} \times \bar{H} + \bar{E} \times \overline{H_0^*}\right).ds$$
$$= j\int_{v_0}\left\{[\omega_0\epsilon - \omega(\epsilon + \Delta\epsilon)]\overline{E_0^*}.\bar{E} + [\omega_0\mu - \omega(\mu\Delta\mu)]\overline{H_0^*}.\bar{H}\right\}dv \qquad (3\text{-}40)$$

As long as $\hat{n} \times \bar{E} = 0$, the integrals over the cavity surfaces give zero, hence.

$$\frac{\omega - \omega_0}{\omega} = \frac{-\iiint \left(\Delta\epsilon\bar{E}.\overline{E_0^*} + \Delta\mu\bar{H}.\overline{H_0^*}\right)dv}{\iiint \left(\epsilon\bar{E}.\overline{E_0^*} + \mu\bar{H}.\overline{H_0^*}\right)dv} \qquad (3\text{-}41)$$

Assuming $\Delta\epsilon$ and $\Delta\mu$ are very small, $\bar{E}$ and $\bar{H}$ can be approximated by $\overline{E_0}$ and $\overline{H_0}$; i.e. the unperturbed fields. Thus

$$\frac{\omega - \omega_0}{\omega_0} = \frac{-\iiint \left(\Delta\epsilon|\bar{E}_0|^2 + \Delta\mu|\bar{H}_0|^2\right)dv}{\iiint \left(\epsilon|\bar{E}_0|^2 + \mu|\bar{H}_0|^2\right)dv} \qquad (3\text{-}42)$$

From equation (3-12) and (3-18), it is clear that the resonant frequency will reduce in proportion to increases in ε and μ. Equation (3-42) determines the change in centre frequency of a resonator when a sample is inserted inside it.
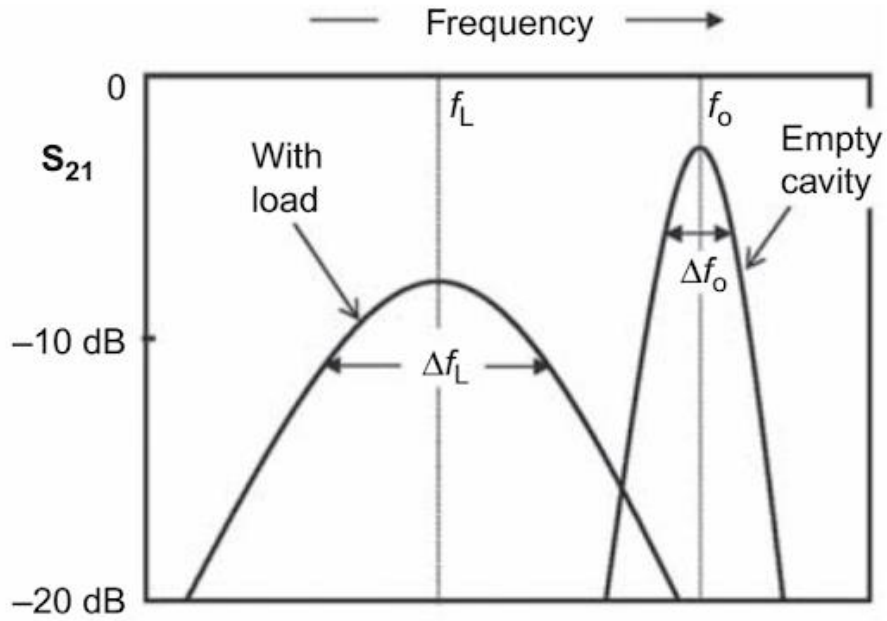
Figure 3-14 Typical S21 spectra, for the empty cavity and with the load (sample) [99]

The TM$_{010}$ mode usually has the lowest resonant frequency in a cylindrical cavity, given by

$$f_0 = \frac{p_{01}}{2\pi a \sqrt{\mu_0 \varepsilon_0}} \qquad (3\text{-}43)$$

here $\mu_0 = 4\pi \times 10^{-7}$ H/m and $\varepsilon_0 = 8.85 \times 10^{-12}$ F/m are permeability and permittivity of free space, respectively, and $p_{01} = 2.405$, i.e. the first root of the Bessel function of first type and zero order.

The quality factor of the empty TM$_{010}$ cylindrical cavity can be written as:

$$Q_0 = \frac{\eta}{R_s} \frac{p_{01}}{2\left(\frac{a}{d} + 1\right)} \qquad (3\text{-}44)$$

where $\eta = 377\Omega$ is the impedance of free space and R$_s$ is the surface resistance of the metal of the cavity construction.

For the TM$_{010}$ mode, the perturbation calculations of real and imaginary parts of the complex permittivity can be simply derived using two following formulas below:

$$\varepsilon'_r = 2J_1^2(P_{01}) \frac{\Delta f}{f_0} \frac{a_c^2}{a_s^2} \qquad (3\text{-}45)$$

60

$$\varepsilon_r'' = J_1^2(P_{01})\Delta\left(\frac{1}{Q_l}\right)\frac{a_c^2}{a_s^2} \qquad (3\text{-}46)$$

where $\Delta f = f_c - f_{c'}$, $\Delta\left(\frac{1}{Q_l}\right) = \frac{1}{Q_s} - \frac{1}{Q_0}$, f_0 is centre frequency of empty cavity, f_s is centre frequency of loaded cavity with sample (as shown in **Figure 3-14** (Q_0 is the quality factor of empty cavity, Q_s is the quality factor of loaded cavity, a_c is the radius of the cavity, a_s is the radius of the (cylindrical) sample, $J_1(x)$ is the first order Bessel function of the first type, with $J_1(p_{01}) = 0.52$ with $p_{01} = 2.405$ [100].

3.5   Modelling and design of the cylindrical cavity resonator

The cavity is constructed from three pieces of aluminium, as shown in **Figure 3-15**. Aluminium is chosen as it has a high electrical conductivity and is reasonably priced compared to copper. The inner radius of the cavity is 46 mm and the inner height is 40 mm. The cavity is fabricated of an open cylinder of aluminium placed between two aluminium plates which are held in tightly using steel bolts to ensure a good electrical connection for high Q of TM modes. Coaxial SMA connectors (of the probe type for capacitive coupling) are used for external coupling of the cavity. The cavity was designed with an axial hole of radius 5 mm for sample insertion.
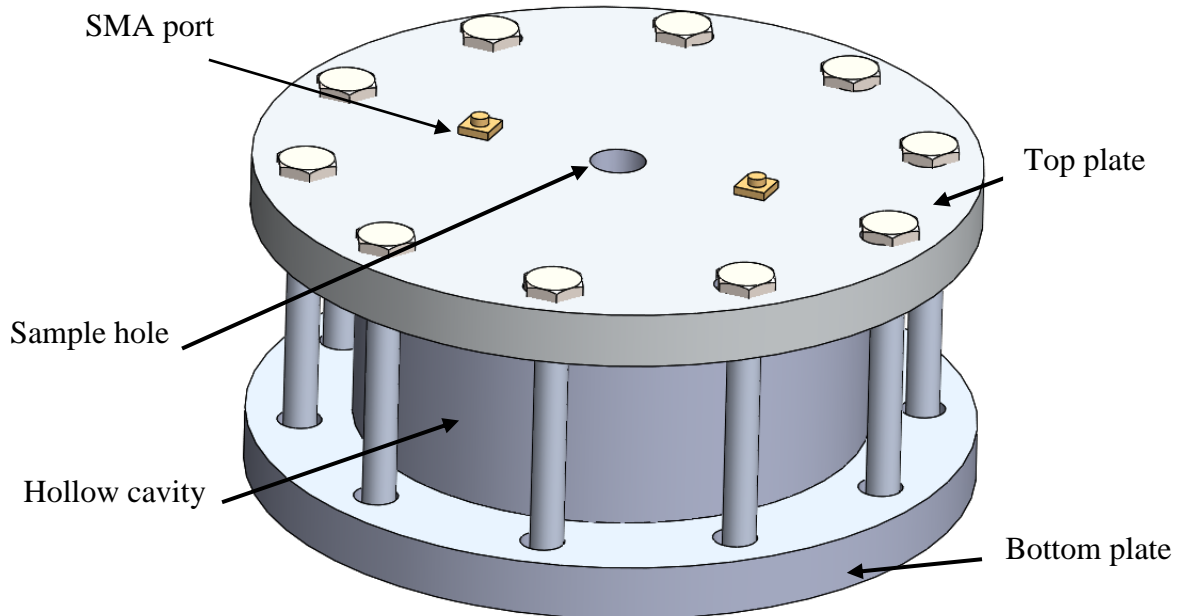
Figure 3-15 Cavity system set-up.

The cavity system is used to measure the dielectric properties of the sample, which is filled in quartz tubes and centred in the cavity. This cavity resonator was designed to work with $TM_{010,}$ TM_{020} modes at 2.5GHz and 5.7GHz, respectively. It is also possible to use this cavity with many other modes at different frequencies for broadband dielectric properties measurements, such as TM_{011}, TM_{021}, $TM_{012,}$ and TM_{022} at frequencies of 4.502GHz, 6.843GHz, 7.899GHz, and 9.432 GHz, respectively. COMSOL Multiphysics® 4.4 was used to implement simulations of the cylindrical cavity for its microwave fields, and the electric and magnetic field distribution of some of these modes are shown in **Figure 3-16**.
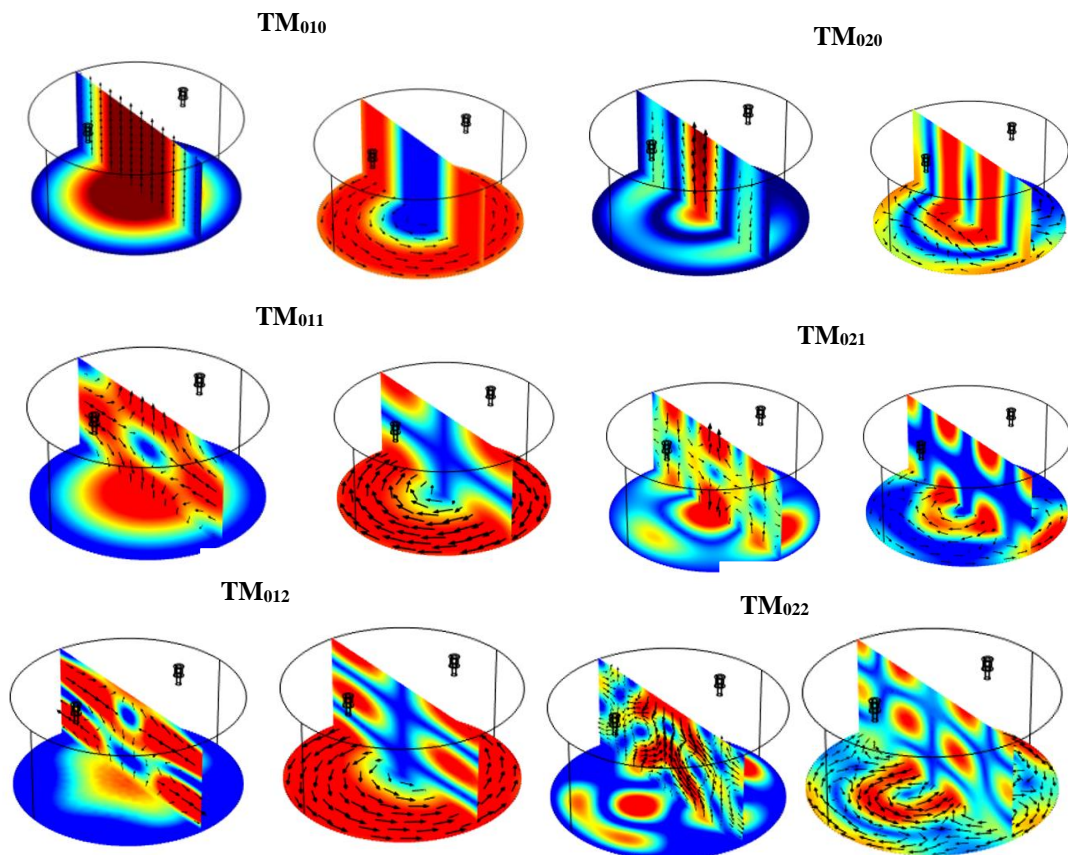
Figure 3-16 COMSOL Simulation of some TM modes. Electric and magnetic field distributions.

3.6 Fundamentals of the coaxial probe technique

The coaxial probe technique is used to measure the broadband dielectric properties of materials in many industrial and medical applications. This method is based on the fact that the reflection coefficient of an open ended coaxial line depends on the dielectric

parameters of the material which terminates it. To calculate the dielectric parameters from the measured reflection coefficient it is necessary to use an equivalent circuit of an open-ended coaxial line. To determine the values of the elements in this equivalent circuit, a calibration using materials with known dielectric properties is done [101].

The open ended coaxial probe technique has the advantages of simple construction and commercial availability of many types of coaxial lines. The limitation of the coaxial probe technique is related to the sample shape and size, which should be thick and large enough to locating all fields inside the materials; the thickness should be at least four times the aperture diameter [99]. Sources of measurement error arise from the air gap between the probe and the sample, and air pockets within the sample itself. The sample surface should be flat and fit perfectly aligned with the probe for accurate measurements [99].

The coaxial probe has electrical field lines both inside the probe and a fringing field at its end. The probe is nothing more than a centre conductor surrounded by a dielectric material and an outer conductor, basically an open-ended coaxial line as shown in **Figure 3-17**.
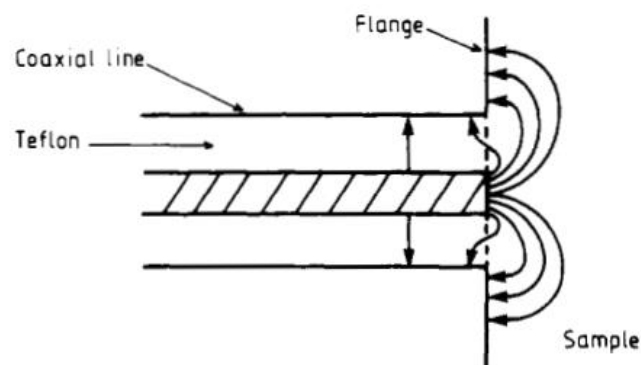
Figure 3-17 Open-circuit coaxial line sample measurement configuration [102]

When a signal is transmitted to the probe's end, the sample is seen as a load. The fringing field interacts with the sample, where it displaces the ions and charge carriers. This energy causes a reflection coefficient at the aperture plane, $\Gamma(\omega, \varepsilon)$, that is measured as S_{11} by a vector network analyser (VNA) at the measurement calibration plane.

$\Gamma(\omega, \varepsilon)$ is a complex value, dependent on the permittivity of the sample and the angular frequency at which the reflection was measured. With $\Gamma(\omega, \varepsilon)$ known, the characteristic admittance of the load may be calculated by

$$Y_L(\omega, \varepsilon) = Y_0 \frac{1 - \Gamma(\omega, \varepsilon)}{1 + \Gamma(\omega, \varepsilon)} \tag{3-47}$$

where Y_0 is the probe's characteristic admittance. With $Y_L(\omega,\varepsilon)$ calculated, complex permittivity ε may be found from (3-47) by using an appropriate inversion process

$$Y_L(\omega, \varepsilon) = j\omega C_1 + jA\omega^3 \varepsilon^2 + B\omega^4 \varepsilon^{2.5} \tag{3-48}$$

where A and B are constants dependent on the dimensions of the aperture.

The complex permittivity of the samples can be extracted using a capacitive model which is shown in **Figure 3-18**. The complex permittivity can be calculated from measured reflected coefficient S_{11} from the reflected signal using (3-50).
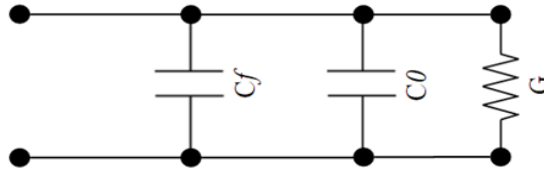
Figure 3-18 Equivalent circuit of an open-ended coaxial probe

When a dielectric sample with complex relative permittivity is connected to the probe, the equivalent capacitance will be changed and therefore the complex reflection coefficient at the measurement plane (measured by the network analyser) is given by (3-49).

$$s_{11}^* = s_{11}e^{j\theta} = \frac{1 + j\omega Z_0(\varepsilon_r C_0 + C_f)}{1 - j\omega Z_0(\varepsilon_r C_0 + C_f)} \tag{3-49}$$

where Z_0 is the characteristic impedance of the coaxial line (here 50Ω), C_0 is the capacitance of the probe terminated in free space, C_f is the fringing capacitance, ω is the angular frequency, θ is the phase associated with the electrical length of the coaxial probe and ε is the complex permittivity of the sample. The complex relative permittivity can be derived using (3-50).

$$\varepsilon_r = \frac{1 - S_{11}^*}{j\omega z_0 C_0(1 + S_{11}^*)} \frac{C_f}{C_0} \tag{3-50}$$

The two unknown capacitances can be calculated by measuring material with known permittivity, such as water [103-106].

3.7 Modelling and design of coaxial probe

The microwave broadband coaxial probe is designed for dielectric measurements over the low to high GHz region. It operates by measuring reflected scattering parameters when the sample is attached to the open ended of coaxial probe, where the electromagnetic fields (here, specifically the electric field) interact with the material under test. Complex permittivity can be accurately measured using open-ended coaxial probes by adding a finite conductor flange at the probe's aperture. This can be used for a more accurate formulation for extracting permittivity from the measurements [107].

Measurement of complex permittivity by using a probe with a flange significantly improves the performance of the probe in contrast with measurement using probe without a flange, since the standard coaxial aperture models require a flange (mathematically, a conducting, infinite half plane).

The aperture of the probe used in this research has an active region which has an outer diameter of 1.6 mm with an inner conductor with a diameter of 0.3 mm, as shown in Figure **3-19**. The simulation results of a COMSOL model of the coaxial probe used in this research.
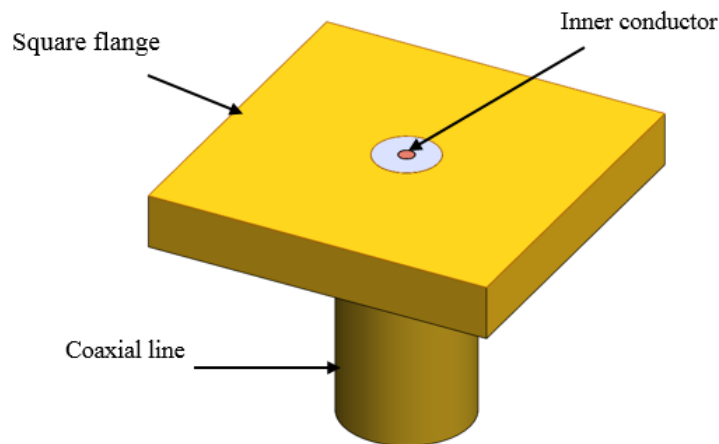
Figure 3-19 Square flange coaxial flat probe. The flange improves the performance of the probe because the flange model more closely represents the model of an infinite ground plane.
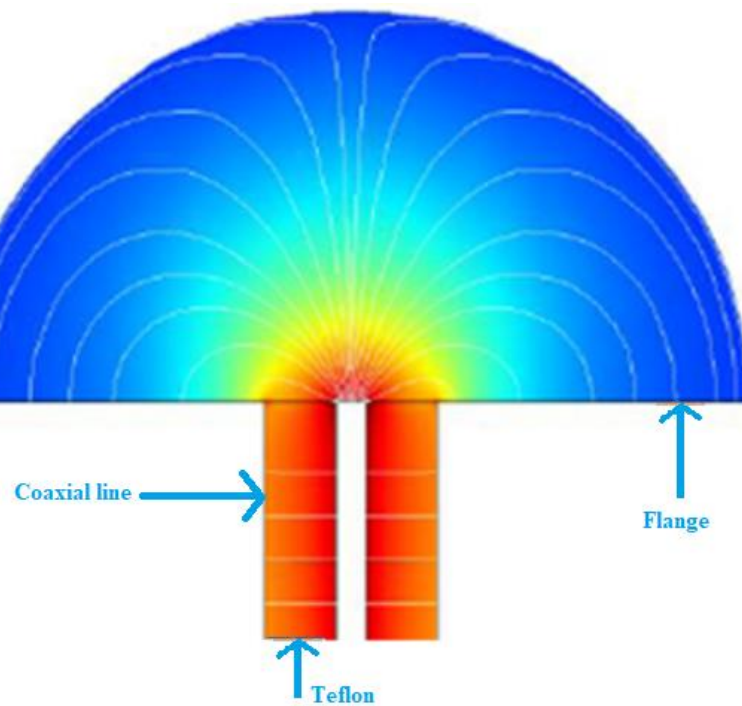
Figure 3-20 COMSOL model of the coaxial probe. Electric field distribution, the active sample region of the probe is at the tip of the probe where the E-field evanescently disperses into the air atmosphere, the colours are for illustrative purpose only (red is being high)

3.8   Errors and calibration

There are three types of errors, namely systematic, drift and random errors. Systematic errors are those such as frequency response, directivity, and load match, and are the resultant of deficiencies in the measurement devices and most of them are invariant with time. Systematic errors can be determined and mostly eliminated through a calibration process, and mathematically removed during the measurement procedures. Drift errors are due to the changing the ambient or experimental conditions and require a stable environment in terms of temperature and humidity to be eliminated.

Random errors are unpredictable and can be caused by the internal noise of the instrument, connectors, adapters, and cables. Such errors can be minimized by making repeatable measurements and calculating the average values.

3.8.1   Network analyser calibration

It is important to calibrate the network analyser before any measurements to minimize the systematic measurement uncertainty referred to above. A mathematical technique called vector error correction can be used to provide very accurate measurements. This method depends on measuring known electrical standards to quantify the errors and their effects can be mathematically removed from the following measurements.

3.8.2   Cavity measurement system calibration

The systematic errors in the cavity measurements are due to different reasons. Firstly, the existence of the sample hole in the cavity can add some errors to the measurements due to the distortion in the fields inside the cavity; this will have an impact on the resonant frequency, which introduce an error into the measured dielectric properties of the MUT. The error produced by the sample hole can be analytically corrected. Secondly, changing the ambient conditions in terms of temperature and humidity can also affect the measurements, but these can be minimized by working in stable environment [108].

The most important cause of errors in cavity measurement is sample preparation, which overwhelms any error associated with the accuracy of measuring the frequency shift and quality factor. Sample preparation errors can be minimised by trying to prepare several samples identically and performing a suitable statistical analysis on the end results.

3.8.3   Coaxial probe measurement calibration

The calibration of the network analyser for coaxial probe measurements is a very important step to obtain an accurate measurement and minimize the imperfections of network analyser. Full one port calibration was done by the standard Agilent 85052D calibration kit using the SOLT technique to the plane of the SMA connector. It is simple and can be done once for every set of measurements. Moreover, it can be done for a broad range of frequencies.

In the SOLT technique, the behaviours of all standard are known, and the error can be defined by measuring the standards with network analyser. The load behaviour largely

sets the directivity terms. Together, the short and open largely determine source match and reflection tracking.

Shorts can be defined by an S-parameter file or a model consisting of a transmission line length and a frequency-dependent inductance.

Opens can be defined by an S-parameter file or a model consisting of a transmission line length and a frequency-dependent capacitance.

Loads can be defined by an S-parameter file or a model consisting of a transmission line length, a shunt capacitance, a resistance, and a series inductance.

Chapter 4 Microwave cavity for dielectric characterization

4.1   Introduction

Arising from the need to differentiate the types of carbons, a microwave cavity system was used as a test method to characterise different types of carbons by measuring the dielectric complex permittivity.   This chapter focuses on dielectric property measurements of two different groups of carbons, namely, activated carbons and carbonaceous materials contained in blast furnace dust. Significant dielectric contrasts between various samples have been measured in both groups.

The technique is based on measuring changes in the resonant frequency and quality factor of the cavity before and after the sample under test is inserted inside the cavity using a vector network analyser, as described in detail theoretically in Chapter 3.

The microwave cavity perturbation method was used to measure the dielectric properties of six different types of activated carbons, to assess the effects of the production technique on their dielectric properties, and the effects of impregnation with some adsorbates such as Ammonia (NH_3).   The different types of carbons contained in blast furnace dust, namely coke, coal or partially burnt char, have been characterized also. The differentiation of these types of carbons in blast furnace dust is important to quantify the utilization of coal injected in the furnace and to determine the efficiency of coal injection.

4.2   Measurement system

The experimental implementation of the dielectric complex permittivity measurement system is described in this section. A cylindrical cavity is connected to a Keysight PNA N5232A network analyser system to measure the voltage transmission coefficient, S_{21}, in the frequency domain, and to record the change in centre frequency and quality factor when the sample inserted inside the cavity.

The material under test is inserted vertically through an axial hole (of diameter 5 mm), since the electric field is at a maximum along the axis in the TM_{010} mode. The cavity has an internal radius of 46 mm and length 40 mm, giving a resonant frequency of the

empty cavity in the TM_{010} mode of approximately 2.5 GHz, reducing to around 2.45 GHz when filled with sample (i.e. within the relevant ISM band). The length is chosen to be not so short as to reduce the quality factor Q too much, but not too long as to allow the mode TE_{111} to interfere with the TM_{010} mode. The measured Q of the empty cavity in the TM010 mode is around 8000. This is lower than the "book value" of around 12000 for aluminium since aluminium alloy is used in the fabrication, and imperfections in the surface (such as roughness and dislocations) will increase the surface resistance, hence reducing Q. The measured value of 8000 is deemed acceptable for cavity perturbation. Therefore, on insertion of an axial sample, the centre frequency will be shifted downwards, and the quality factor will reduced for the TM_{010} mode, as explained in section 3.4.

Figure **4-1** shows the COMSOL simulation results for the electric (E) and the magnetic (H) fields, showing a 3D view in (a) and (b), side view in (c) and (d), for the mode TM_{010}. The operating resonant frequency is 2.498 GHz for the dimensions listed above.

(a)

(b)

(c)

(d)
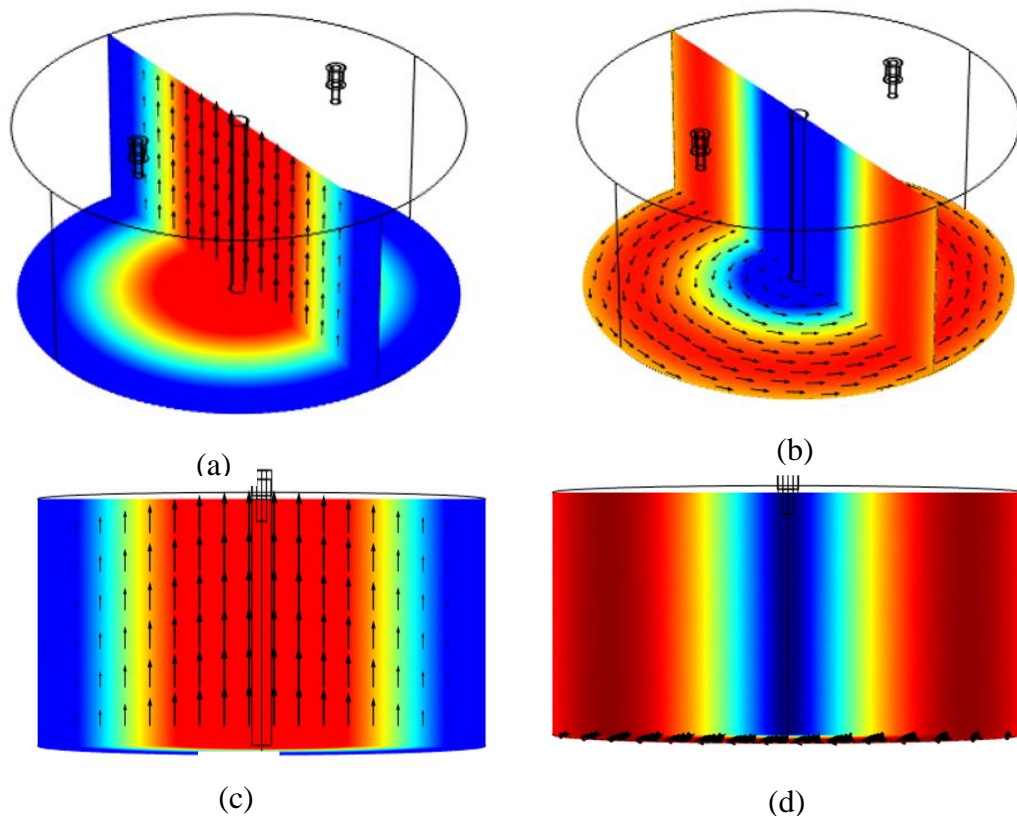
Figure 4-1 COMSOL simulation of the cylindrical cavity resonator TM_{010}, showing the electric ((a)) and (c)) and magnetic ((b) and (d)) field distribution.

Figure 4-2 presents the COMOSL simulation S$_{21}$ for the cylindrical cavity resonator before and after a filled tube inserted is inside the cavity (the outer diameter of the tube is 2 mm and inner diameter is 1.2 mm and is filled with water, $\varepsilon_r = 78$).
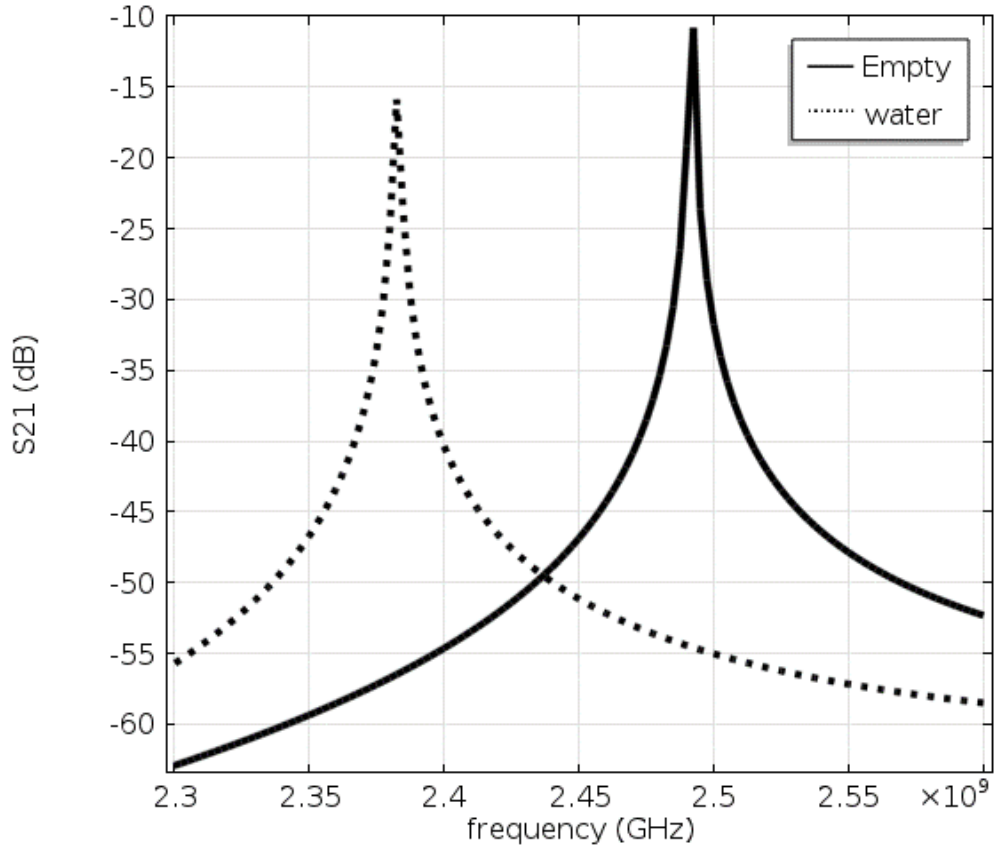
Figure 4-2 COMSOL simulation of the resonant traces of the TM$_{010}$ mode when empty and when sample-loaded. Insertion the sample reduces the resonant frequency from 2.4925GHz to 2.3875GHz and increases the bandwidth from 1.2MHz to 6.33MHz, dependent on the complex permittivity of the sample.

The real and imaginary values of the complex permittivity can be extracted from the change in both resonant frequency and quality factor using the equations (4-1) and (4-2). These are derived from the cavity perturbation equations (3-45) and (3-46) for a sample along the axis of the cavity, with its length placed parallel to the electric field (as for the TM$_{010}$ mode) [100].

$$\varepsilon' - 1 = \left(\frac{f_0 - f_s}{f_0}\right)\left(\frac{2V_{eff}}{V_s}\right) \tag{4-1}$$

$$\varepsilon'' = \Delta\left(\frac{1}{Q}\right)\left(\frac{V_{eff}}{V_s}\right) \tag{4-2}$$

where f_0 and f_s are the resonant frequencies without and with sample, respectively, Vs is the sample volume within the cavity and V_{eff} is the effective cavity volume. This latter quantity is the effective space filled by the electric field energy, and for the TM_{010} mode can be shown to be about 26.9% of the cylinder volume [100].

A photograph of the microwave cavity system and its supporting/auxiliary systems, based on the information from the literature review, is seen in **Figure 4-3**.

For all of the experiments, powdered samples were filled in quartz tubes with inner and outer diameter of 2.0 mm and 2.4 mm, respectively. The TM_{010} mode at 2.498GHz was used, with the sample tube centred in the cavity using open SMA connector, as shown in **Figure 4-3**. Error introduced due to the finger prints on the quartz tube while loading the samples investigated by measuring clean empty tube and tube with lots of finger prints on. That is shown in Figure 4-4. It is clear that, the finger prints on the tube is negligible.
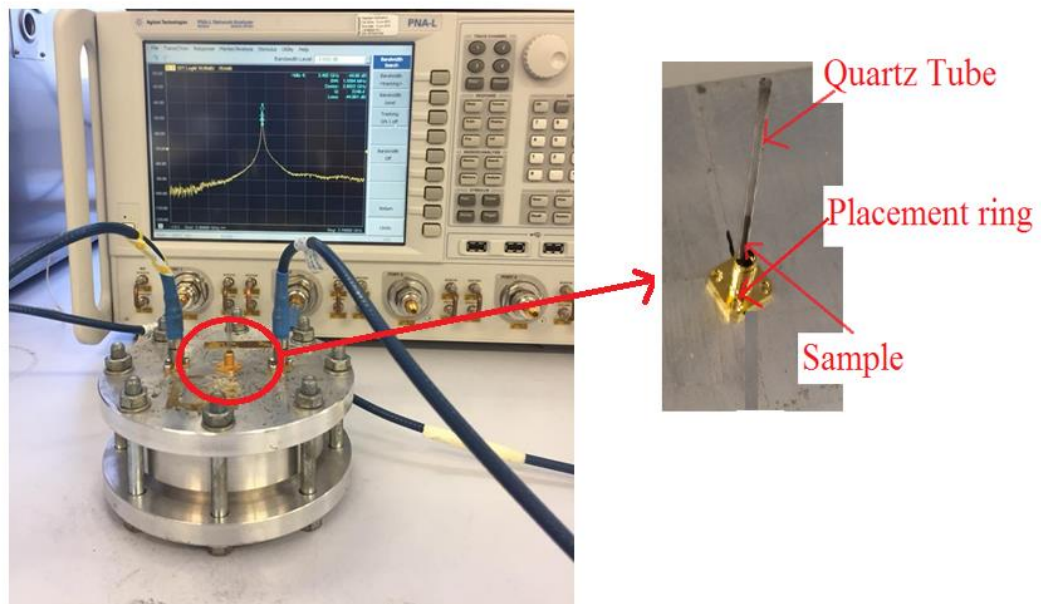
Figure 4-3 Photographs of the experiment set-up for cavity perturbation measurement.
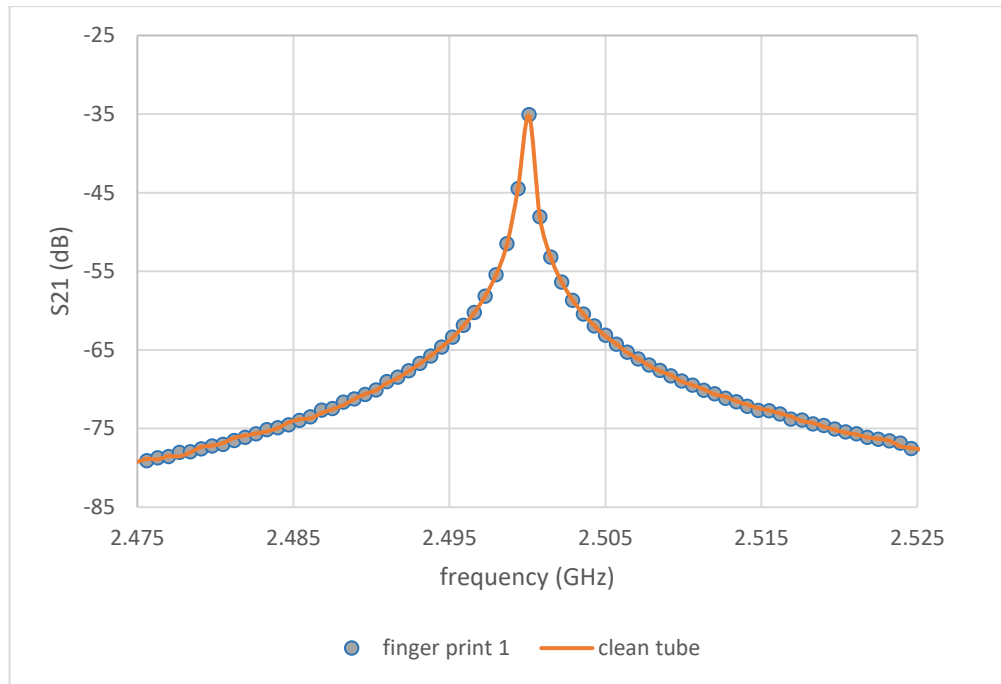
Figure 4-4 the resonant traces of the TM010 mode when clean quartz tube and tube with finger prints loaded to the cavity. The finger prints have negligible affects.

4.3 Materials

Different types of carbons were selected for this study and all samples were classified into two groups. Group 1 comprised commercial activated carbon, which was produced from different predecessors and selected to assess any dependence of dielectric properties on the raw materials that have been used in their production. These were provided by Heriot Watt University, under the product name NORIT GCN3070, listed in Table **4-1**. A modified microwave oven and a conventional oven were used for heating the activated carbon samples[15]. Group 2 comprised different forms of carbon contained in blast furnace dust, namely, coke, coal, and char to quantify coke, coal or partially burnt chars contained in the dust, as listed in

Table **4-2**. Additionally, three lab-made carbon samples were also measured. The lab-made samples contained different weight concentrations of coal, char, and coke, to resemble the composition of blast furnace dust. These samples are listed in

Table **4-3**.

Table 4-1 Group 1 carbon materials.

Material	Label	Description
Norit GCN 3070	AC1	Coconut shell based granular AC
MW	AC2	Norit after 25 Microwave (MW) heating cycle
CH	AC3	Norit after 25 Conventional heating (CH) cycle
GKOS	AC4	Ground olive stone derived activated carbon (AC)
GKOS-N800	AC5	GKOS with 800^0C treated NH_3 impregnation
Calgon BLP	AC6	Bituminous coal based granular activated carbon (GAC)

Table 4-2 Group 2 carbon materials.

Material	Label	size classification	oxygen: carbon ratio	residence time of oxygen
Ground coke	coke	-	-	-
PM coal-1	coal-1	100% < 1mm	5	60ms
PM coal-2	coal-2	100% < 1mm	5	35ms
PM coal-3	coal-3	100% < 1mm	5	35ms
PM coal-4	coal-4	100% < 1mm	14	700ms
PM coal-5	coal-5	100% <1mm 50% > 250 µm	5	35ms

Table 4-3 Lab-made samples

Material	Label	Description
Char 80%	Char 80%	Labe-made sample has 80% char, 10% coal, and 10% coke, by weight.
Coke 80%	Coke 80%	Labe-made sample has 10% char, 10% coal, and 80% coke, by weight.

Coal 80%	Coal 80%	Labe-made sample has 10% char, 80% coal, and 10% coke, by weight.

The Group 1 samples of activated carbon were formed from different particle sizes. They were crushed using a mortar and pestle, and then sieved by 63µ Lab sieve to be approximately 60µm size, as illustrated schematically in **Figure 4-5**.

granular AC → powdered AC

Figure 4-5 Grinding the granular activated carbon to powder

The sample powders were poured into quartz tubes (outer and inner diameters of 2.4 mm and 2.0 mm respectively) and left to settle on a vibrating stage for 10 minutes. Quartz was chosen as a tube material as it has very low dielectric loss and thus minimal effect on the unloaded centre frequency and bandwidth. To minimise the errors, multiple samples are prepared in the same way and measured using the cavity.

4.4   Dielectric properties measurements of activated carbons

The real and imaginary parts of the complex permittivity are shown in **Figure 4-6** and **Figure 4-7**, which illustrate the average values of the measurements of complex permittivity of Group 1 activated carbon samples. The dielectric properties of activated carbons have been presented in the 3rd International Conference on Microwave and Terahertz Technology (ICMTT 2018) [109].

The same measurements were repeated at least 10 times for each sample, so that mean values (and standard deviation of the mean) can be estimated reliably for each sample.

Figure 4-6 shows that the dielectric constant (i.e. real values of the complex permittivity) of the samples for all activated carbons are significantly different. The small errors are associated with the small differences in sample volumes each time a

powder sample is loaded into the cavity (since they are powders, with random packing nature, and all tubes have a volume size distribution giving an error of about 2%).

It is clear that the sample AC6, which is produced from bituminous coal, has the highest values of real permittivity, around 14.14. Samples AC1, AC2 and AC3 are the same activated carbon which is produced from coconut shell, samples AC2 and AC3 are treated with microwave and conventional heating, respectively; both have values of real permittivity that are approximately similar to AC1. The dielectric constant of AC5, which was produced from ground olive stone with 800ºC and treated with NH_3 impregnation, is approximately double that of the real permittivity of AC4, derived from ground olive stone.

Figure 4-7 show the dielectric loss factor (i.e. imaginary value of the complex permittivity) of all activated carbon samples. It is clear that the values are again significantly different. The sample AC6, again, has the highest value of 9.57. Samples AC1, AC2 and AC3 have slightly different values. The dielectric loss factor of AC5, produced from ground olive stone with 800ºC treated NH_3 impregnation, is approximately double the dielectric loss factor of AC4, derived from ground olive stone.
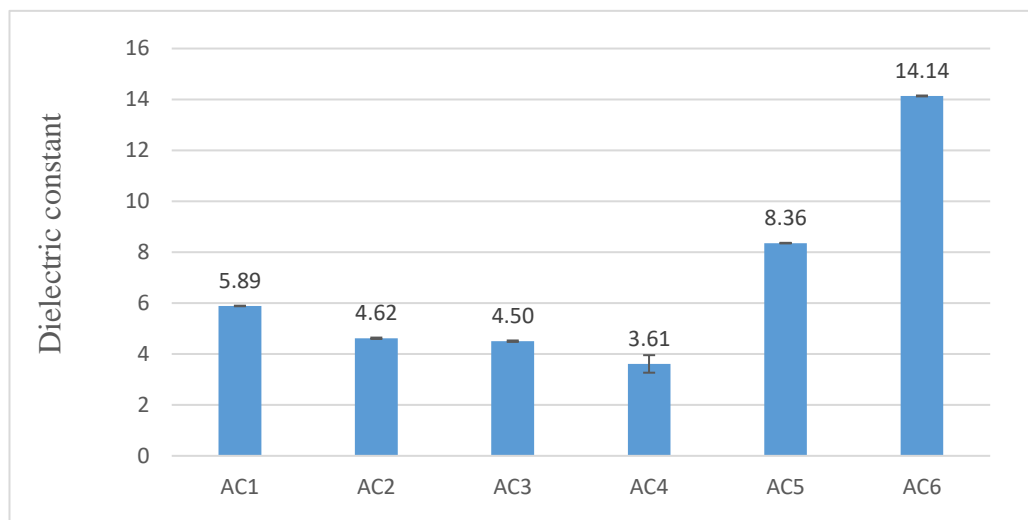
Figure 4-6 Dielectric constant of activated carbon samples. The typical standard error is ±0.02, which in most cases is too small to observe.
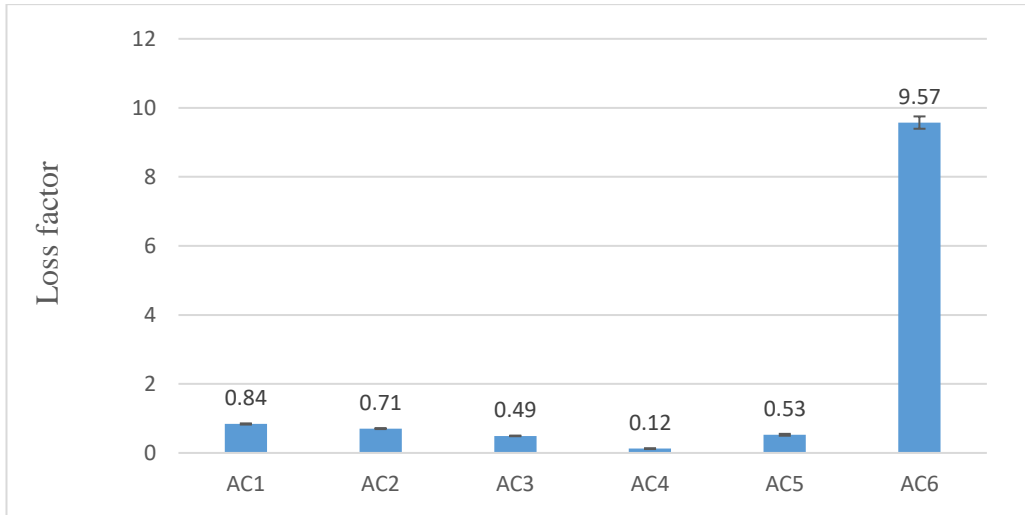
Figure 4-7 Dielectric loss factor of activated carbon samples. The typical standard error is ±0.0027, which in most cases is too small to observe.

4.5   Dielectric properties of carbons in blast furnace dust

The real and imaginary parts of the complex permittivity of different types of carbon are shown in **Figure 4-8** and **Figure 4-9**, respectively. The average values of the measurements of complex permittivity of Group 2, comprising different forms of carbon contained in blast furnace dust, are illustrated. These figures show that the dielectric constant and loss factor of all samples are different and depend on the coal type.

Figure 4-8 and **Figure 4-9** clearly show that the coke has highest values of dielectric constant and dielectric loss factor. The dielectric constant and loss factor of Coal-3 is at least 2.5 times that of other types of coals.

The real and imaginary parts of the complex permittivity of the three lab–made blast furnace samples are shown in **Figure 4-10** and **Figure 4-11**. From these it is clear that the samples containing the highest weight concentration of coke and char have higher complex permittivity than the sample with highest weight concentration of coal.
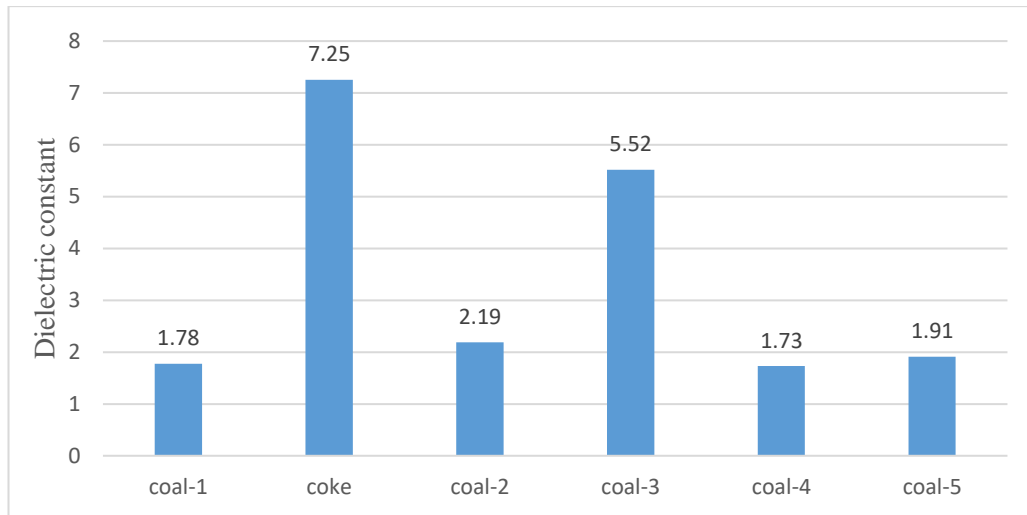
Figure 4-8 Dielectric constant of different carbon samples. The typical standard error is ±0.03, which in most cases is too small to observe.
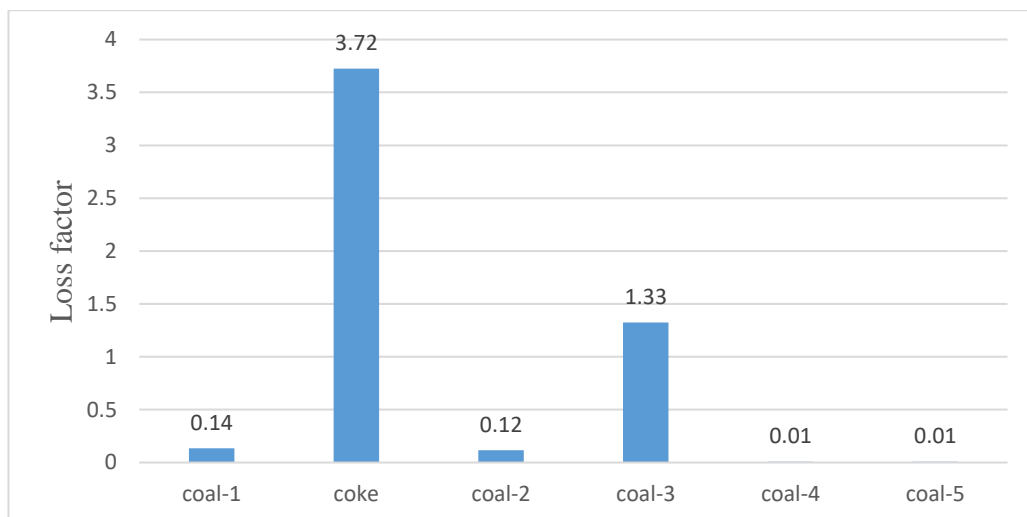
Figure 4-9 Dielectric loss factor of different carbon samples. The typical standard error is ±0.03, which in most cases is too small to observe.
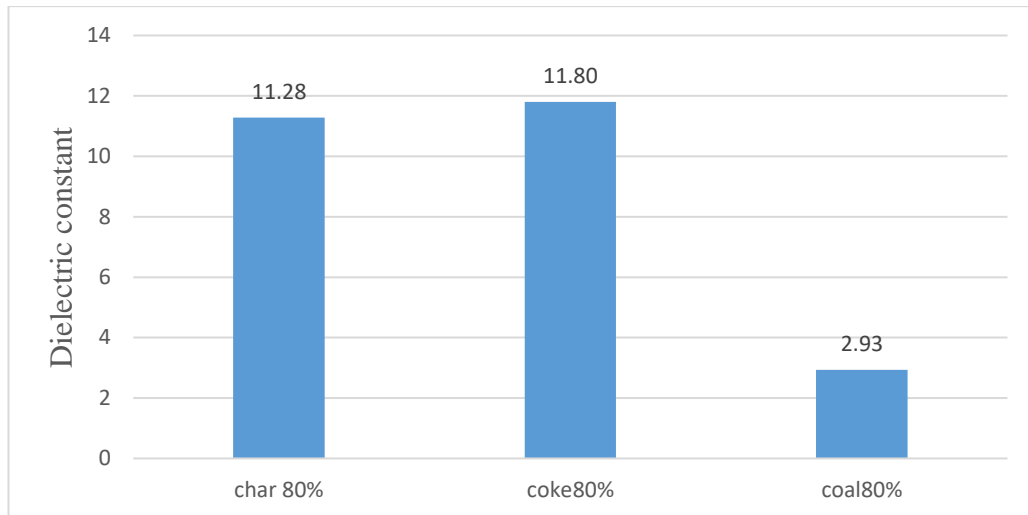
Figure 4-10 Dielectric constant of lab-made carbon samples. The typical standard error is ±0.01, which in most cases is too small to observe.
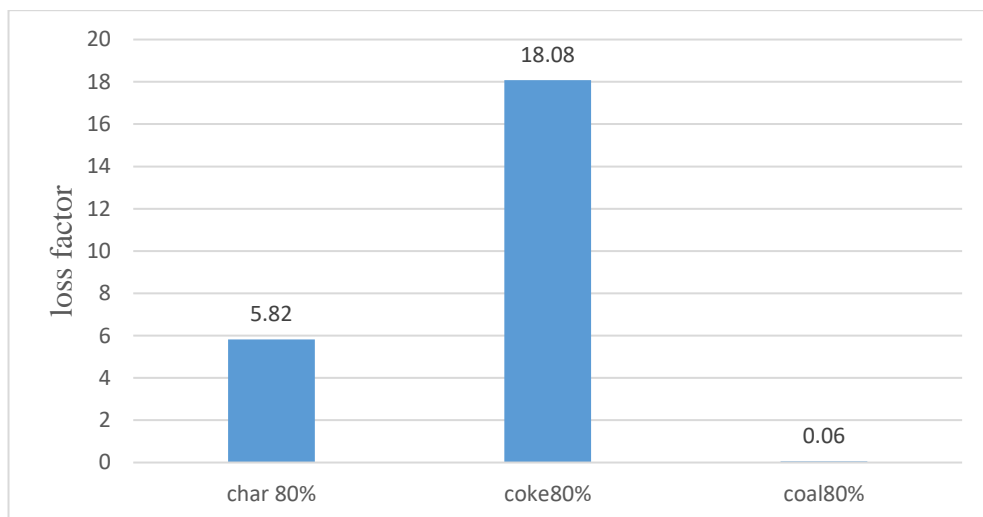
Figure 4-11 Dielectric loss factor of lab-made carbon samples. The typical standard error is ±0.024, which in most cases is too small to observe.

4.6   Conclusions

This chapter has presented the principles of cavity perturbation applied to measurements of the complex permittivity of different types of carbon materials at frequency of around 2.5 GHz using a cylindrical host cavity operating in its TM_{010} mode.

It can be concluded that the dielectric properties of activated carbons change depending on the raw materials that have been used in their production; for example, AC6, which was produced from bituminous coal, has the highest dielectric constant and loss factor, at values of 14.1 and 9.6, respectively. It is also noticed that the both AC2 and AC3 samples, which were pre-heated using conventional heating and microwave heating, respectively, have approximately the same complex permittivities.

In addition, the different types of carbons contained in blast furnace dust have different dielectric properties, where the coke and coal-3 have highest dielectric constants at approximately 7.25 and 5.5, respectively. They also have the highest dielectric loss factors at 3.7 and 1.3, respectively. As coke is generally made by heating coal in the absence of air, the loss of the volatile components and restructuring of the carbon may increase. As a consequence of that the conductivity increases due to increasing electron mobility. As temperatures continue to increase the mobility of electrons and level of free charge per unit volume increases.

For the lab-made blast furnace dust, the samples contained different weight contribution of coke, coal, and char. The sample that contained the highest amount of coke had highest dielectric constant and loss factor, at approximately 11.8 and 18.07, respectively.

The importance of these measurements and the variant dielectric properties of carbon samples would mean that microwave cavity technique can be simply used to differentiate activated carbons and carbons contained in blast furnace dust. This is a completely new way of assessing this complex material and could open up an important on-site diagnostic for all industrial applications involving blast furnaces.

Chapter 5 Frequency-dependent dielectric properties

A microwave cavity offers several TM modes which can be used for complex permittivity measurements over a range of frequencies, from 2.5 GHz up to about 10 GHz, which may provide more complete information than results at the single TM_{010} resonant frequency (around 2.5 GHz for the measurements presented here). Using a microwave cavity system to measure the frequency-dependent complex permittivity of different types of carbons is both practical and simple, at least in terms of the preparation the samples. Moreover, due to its high sensitivity, it is more accurate compared to other techniques.

An open-ended coaxial probe technique was also used to investigate dielectric properties of different types of carbon over a much wider range of frequencies, from 10 MHz to 20 GHz. Although the coaxial probe is broadband, it has lower accuracy compared with the cavity method, especially for loss measurements. It is also prone to large error, so coaxial measurements need to be repeated many times to assess such errors; this is especially so for inhomogeneous samples.

This chapter focuses on the frequency-dependent dielectric properties measurements of two different groups of carbons. Activated carbons and carbonaceous materials contained in BFD (blast furnace dust), i.e. Groups 1 and 2, respectively, identified in Chapter 4. Significant contrasts between various samples have been measured in both groups.

5.1   Multiple modes cavity system

Microwave complex permittivity can be measured over a range of frequencies using a cavity (the same cavity used in the previous chapter) by exciting multiple TM modes which have frequencies calculated using (3-18) and listed in **Table 5-1**. The samples were mixed with silica to minimize the effects of the inter-grain conductivity between the particles of the powder, so that the intrinsic loss properties are characterised. It should be noted that, by definition, all of these TM modes provide an electric field parallel to an axial sample.

Table 5-1 Resonant frequencies (in GHz) of the various TM modes used here.

mode	Calculated	Simulated	Measured
TM_{010}	2.494	2.500	2.501
TM_{011}	4.502	4.521	4.532
TM_{020}	5.729	5.734	5.746
TM_{021}	6.843	6.875	6.891
TM_{012}	7.899	7.931	7.946

The broadband measurements of complex permittivity of different types of carbons are shown in Figure **5-1** and Figure **5-2**. There are obvious differences in the dielectric constant and dielectric loss factor that depend on the type of carbons. Coke has the highest values for the TM_{010} and TM_{011} modes, and coal-3 (char) has the highest values at TM_{020} and TM_{021} modes. From **Figure 5-6** it can be seen that some modes such as TM_{010}, TM_{011} are more convenient to differentiate types of carbon.

Other coals have only slightly different dielectric behaviours, as shown in **Figure 5-1** and **Figure 5-2**, but it is still sufficient to use these measurements to distinguish between the different types of carbon. For example, to identify these different types of carbons, the TM_{021} mode can be used sufficiently for measuring the dielectric constant and the TM_{010} mode can be also used for measuring dielectric loss factor.

The three lab-made samples that contained different weight concentrations of coal, char, and coke were also measured using multimode cavity system. From **Figure 5-5** and **Figure 5-6**, it obvious that the TM_{021} and TM_{010} modes, alone, are sufficient to distinguish between these samples.
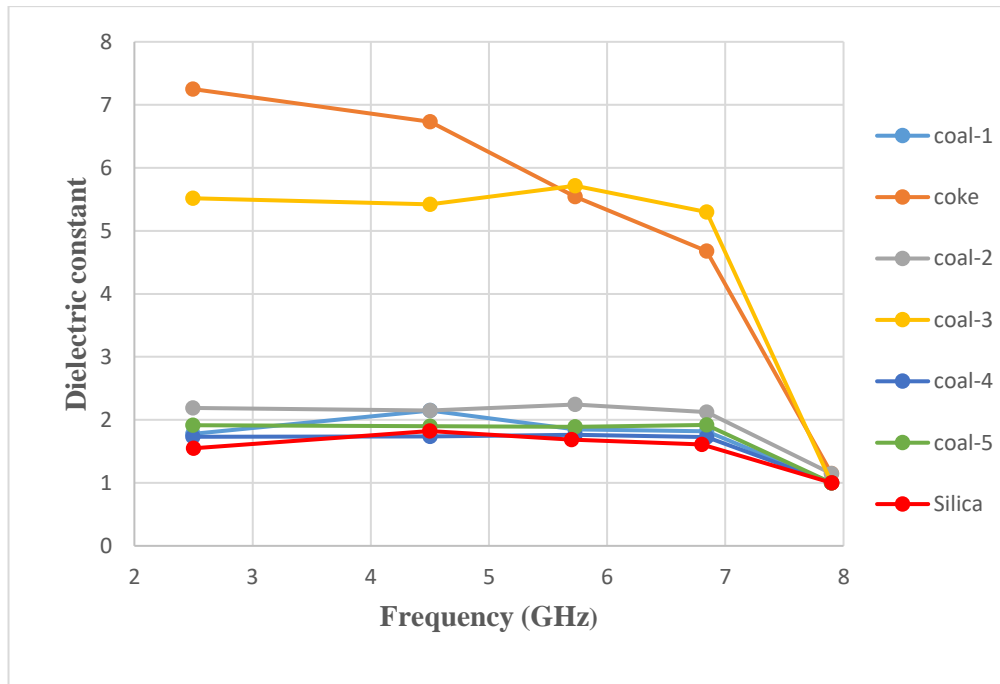
Figure 5-1 Real components of complex permittivity of different types of carbons
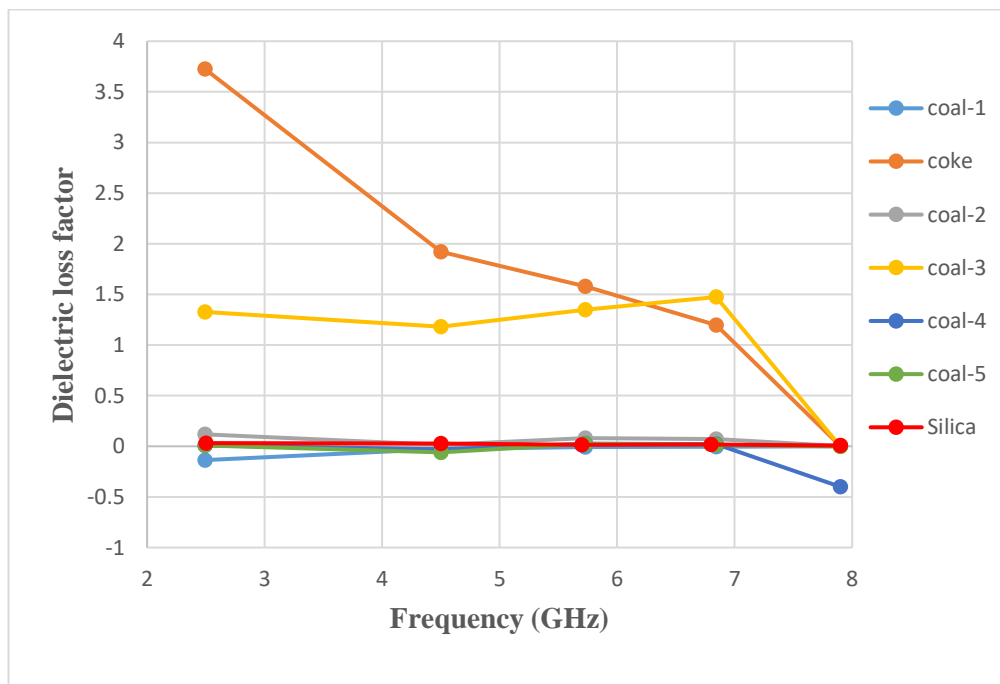
Figure 5-2 Imaginary components of complex permittivity of different types of carbons
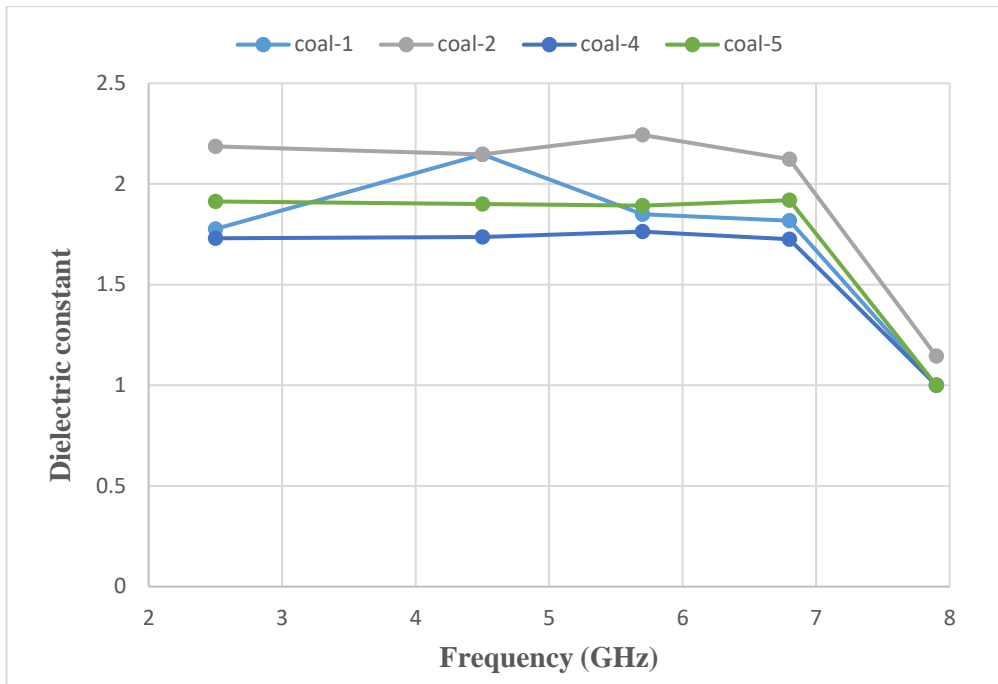
Figure 5-3 Real components of complex permittivity of different types of coals
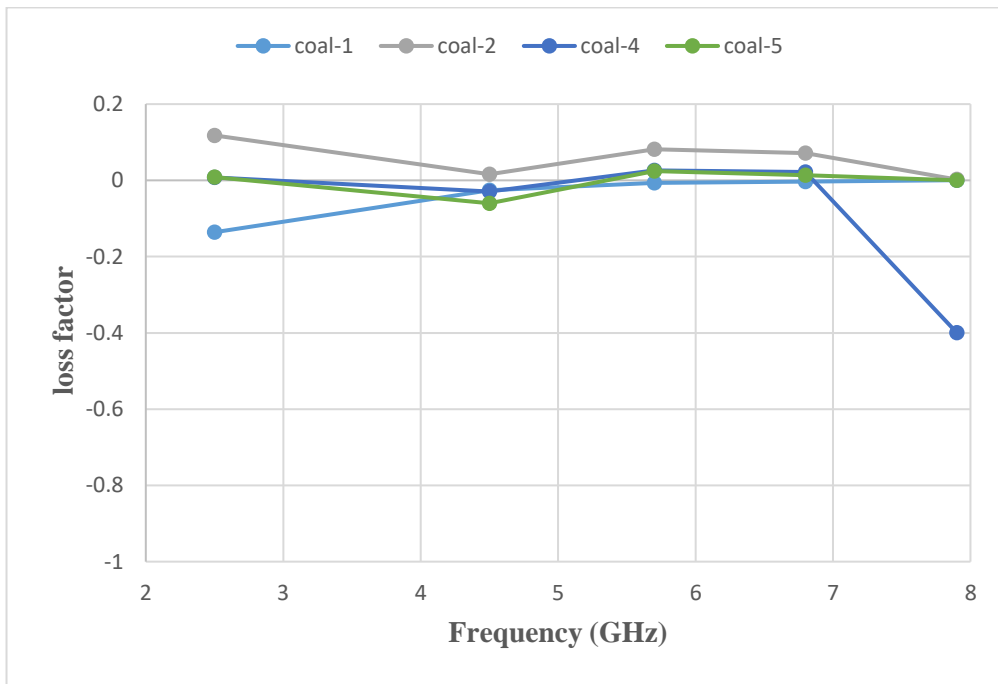
Figure 5-4 Imaginary components of complex permittivity of different types of coals
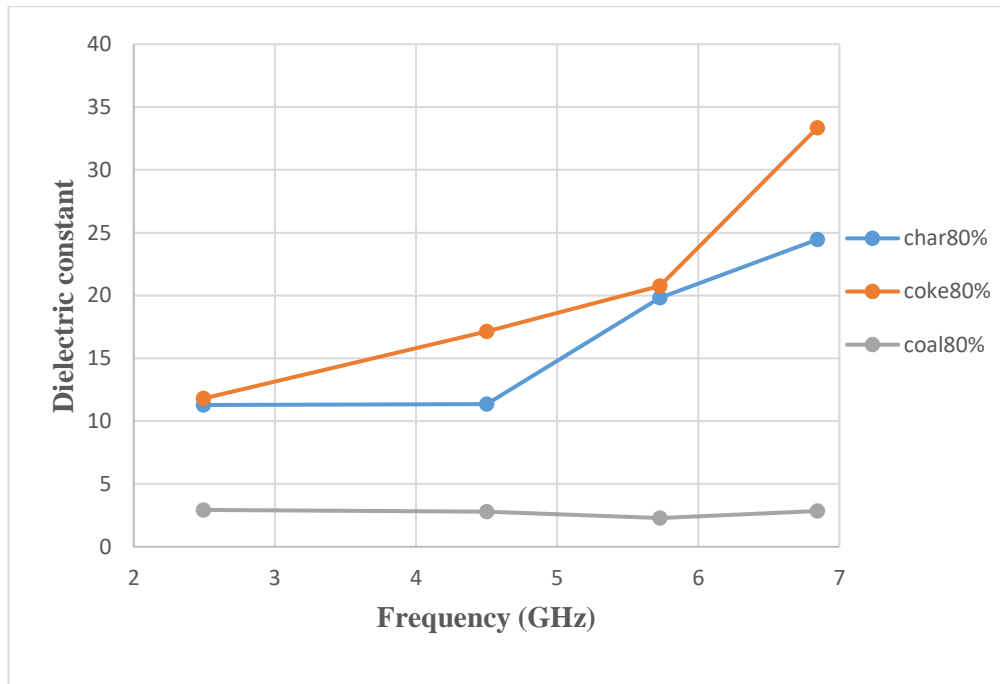
Figure 5-5 Real components of complex permittivity of lab-made samples
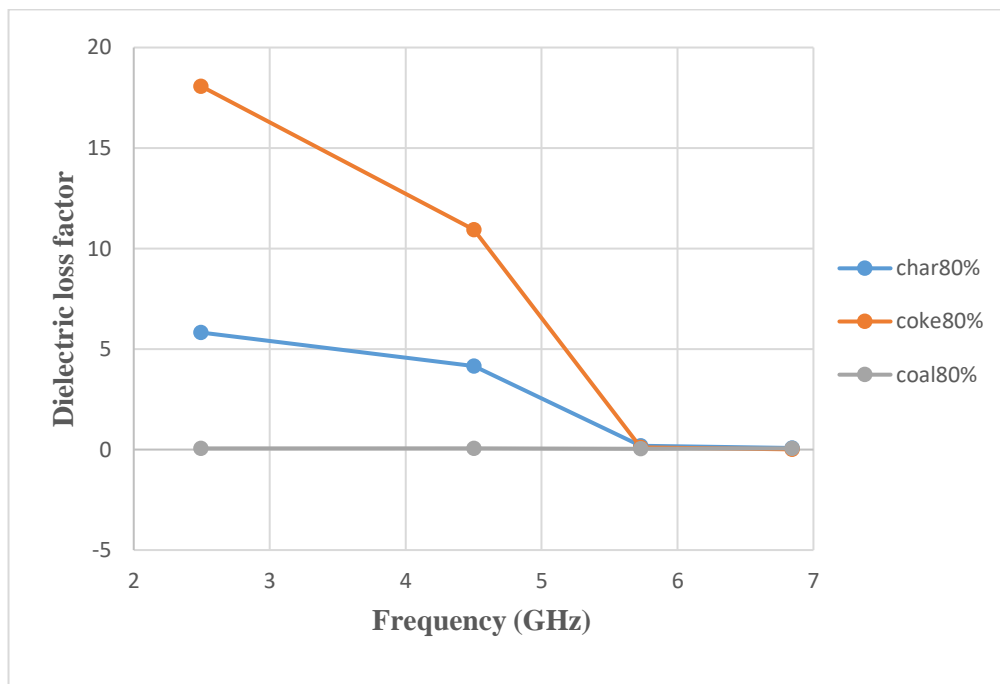
Figure 5-6 Imaginary components of complex permittivity of lab-made samples

5.2 Open-ended coaxial probe system

The coaxial probe technique is used to measure the dielectric properties of material over a broad, continuous range of frequencies. The samples were in granular from,

being activated carbon which was produced from coconut shell provided by Heriot Watt University (the product name is NORIT GCN3070). The samples were introduced to the probe in two different forms. Firstly, the measurements started with powdered samples. Secondly, the powdered samples were mixed with silicone rubber in different mixing ratios. The powders were formed by grinding the sample using a mortar and pestle, followed by sieving using a 63µ Lab sieve to approximately 60µm size.

The samples were pressed onto the top of the coaxial probe using the system shown in **Figure 5-7** to ensure that there is good contact between the sample and probe.
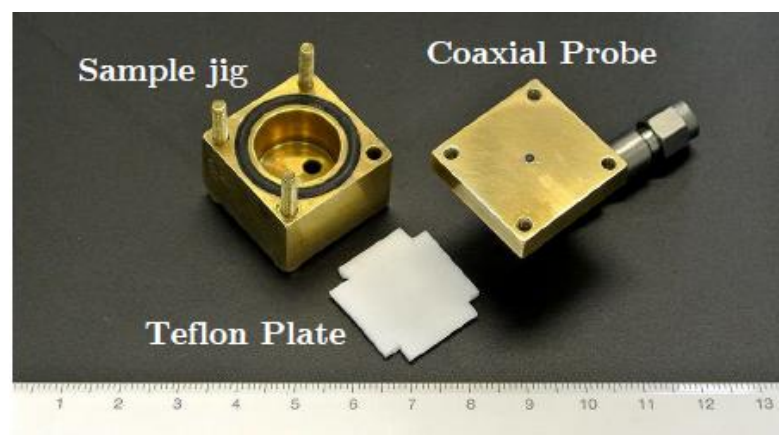
Figure 5-7 coaxial probe and sample fixture. Sample is placed on the top of the probe, while S11 is measured using a PNA network analyser and controlled by a LabVIEW program [43]

The measurements were carried out using coaxial flat probe with square flange which was connected to the Agilent PNA-L vector network analyser, after a standard short-open-load calibration process done using an Agilent 85052D calibration Kit.

5.3 Dielectric properties of powdered activated carbons

It was found during the analysis of the resulting data that the data values varied considerably over the fifty sets of measurement of activated carbon and ten sets of measurement of three lab-made carbon samples (containing different weight concentration of coal, char and coke). These differences have a likely origin in the random electrical contacts that occur between the powder grains, which cause connective paths which also could affect the capacitance (and hence "dielectric constant") at these high frequencies. The array of contacts is different each time the

powdered sample is pressed onto the coaxial aperture of the probe. As shown in **Figure 5-8** and **Figure 5-9**, the real and imaginary parts of complex permittivity of the activated carbon sample (Norit GCN3070) deceased with frequency. The real and imaginary parts of complex permittivity are shown below, for char80% (in **Figure 5-10** and **Figure 5-11**) for coke80% (in Figure 5-12 and **Figure 5-13**), and for coal (in **Figure 5-14** and **Figure 5-15**). Both parts of complex permittivity also deceased with frequency. It is clear that there is large level of systematic uncertainty in the measurement data. The measurement data show large variations in the lower frequency region, while in the higher frequency region the data becomes more stable; this is also likely to be owing to percolation paths between particles, which are more prevalent at lower frequencies as they become shorted out at higher frequencies owing to the parallel capacitance between powder particles.

It is clear from **Figure 5-9** and **Figure 5-11** that, at low frequencies, the dielectric loss is dominated by the electronic conductivity, as described in (3.10). These log-log graphs in this limit exhibit a straight-line behaviour with a gradient of -1. This is the classic indication of electronic conduction through the inverse proportionality of the dielectric loss term with frequency. The size of this term varies with conductivity and for the range of values here is 0.1 to 1.0 S/m for AC, to over 100 S/m for char. This is most likely due to the contacts between grains causing conducting percolation paths.
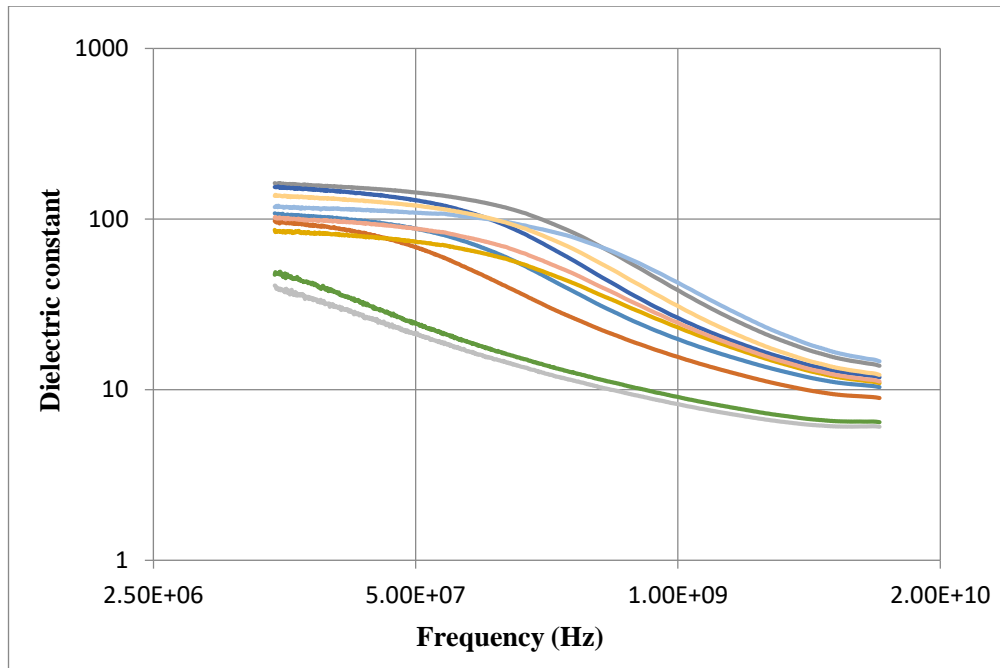
Figure 5-8 real component of the complex permittivity of powdered activated carbon (Norit GCN3070) for 10 independent measurements
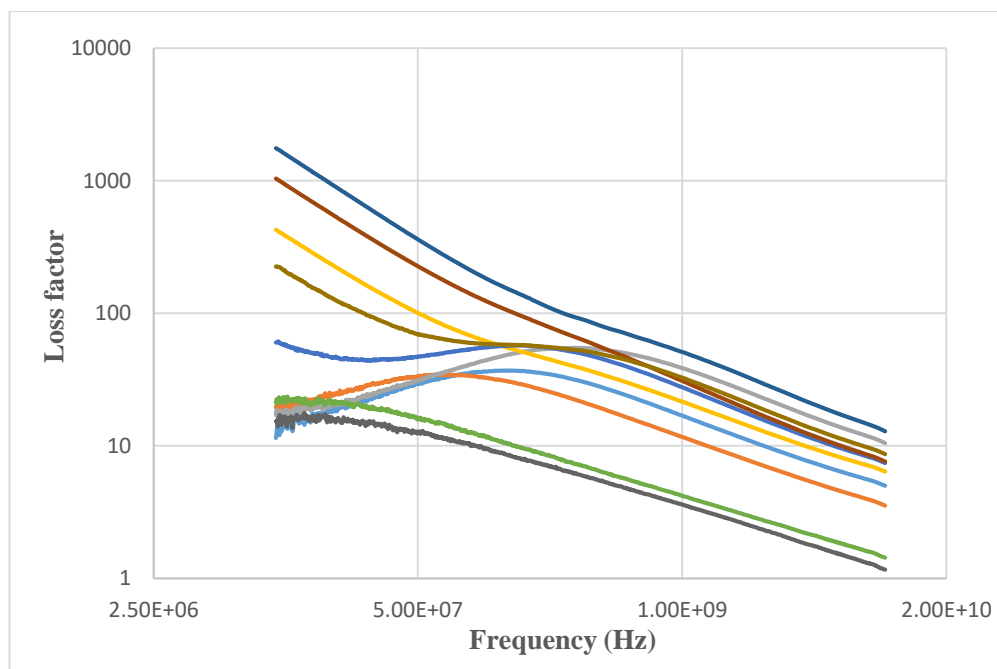
Figure 5-9 imaginary component of the complex permittivity of powdered activated carbon (Norit GCN3070) for 10 independent measurements

From **Figure 5-8** and **Figure 5-9** and the negative slope with increasing frequency emerges in both real and imaginary parts, this decrease in loss with frequency is because of either free electron conductivity or space-charge polarisation, both of which are mechanisms related to conduction. Free electron conductivity appears in the losses

with a 1/f dependence. Space-charge polarisation appears in both the real and imaginary parts of permittivity. This mechanism can therefore be identified by a decrease in both the real and imaginary parts as frequency increases

Figure 5-10 Real component of complex permittivity of Char 80% for 10 independent measurements

Figure 5-11 Imaginary component of complex permittivity of Char 80% for 10 independent measurements

Figure 5-12 Real component of the complex permittivity of Coke 80% for 10 independent measurements

Figure 5-13 Imaginary component of the complex permittivity of Coke 80% for 10 independent measurements

Figure 5-14 Real component of the complex permittivity of Coal 80% for 10 independent
measurements

Figure 5-15 Imaginary components of the complex permittivity of Coal 80% for 10
independent measurements

5.4   Dielectric properties of carbon mixed with silicone rubber

To avoid the large level of uncertainty resulting from the conductivity between the powder particles, which align differently each time a powdered sample is placed on the aperture of the probe, the samples were mixed with silicone rubber to both fix their positions and separate them, thus reducing the density of inter-grain contacts. It is easy to cut the resulting composites and perform dielectric property measurement.

Dielectric properties of powdered activated carbons and silicone rubber mixtures were measured in the frequency range of 10 MHz to 20 GHz using the coaxial probe technique. The measurements demonstrate that the dielectric permittivity of the activated carbon changes according to the volume fraction of activated carbon in the mixtures. Both the dielectric constant and dielectric loss factor increased with increasing proportion of activated carbon.

Silicone rubber with high and hardness of 27 Shore A[1] was purchased from MB Fibreglass, Northern Ireland. The activated carbon was produced from coconut shell and was provided by Heriot Watt University (product name NORIT GCN3070). In addition, some carbonaceous materials produced in the combustion laboratory at Cardiff's School of Engineering were also measured.

The samples were prepared as mixtures of silicone rubber with different amounts of powdered activated carbon to avoid the variability and uncertainty resulting from the conductivity between the powder particles. Fifteen samples with three different contents of activated carbon were prepared at mass ratios of silicone: carbon of 2:1, 4:1 and 8:1. The preparation of sample starting by mixing the two parts of silicone and hardener, then the powder was added to the mixture and was mixed thoroughly. The mixtures needed 6 - 8 hours at 25° to cure.

The experiments of the silicone rubber composites were divided into two stages. Firstly, measuring the pure silicone rubber to investigate the errors resulting of the air bubbles, which appear owing to the mixing of the silicone with the hardener.

---

[1] Shore Hardness is measured using a *durometer gauge*, which uses a spring loaded steel rod to compress the surface of the sample and provide a reading. A reading of 0 Shore describes the maximum possible indentation of the rod into the specimen, and 100 Shore indicates almost no indentation al all or a very high resistance to indentation. Shore A is for rubber, soft plastic and polyurethane. See appendix A.

Secondly, the samples were prepared as mixtures of silicone with different contents of powdered activated carbon.

5.4.1 Dielectric properties of activated carbon composites

Figure 5-16 and Figure **5-17** show the dielectric constant and loss factor of silicone rubber samples as function of frequency for five samples of silicone rubber. Each sample was measured at least fifteen times. The average was calculated for each sample and these are represented in **Figure 5-16** and Figure **5-17**. The microwave measurements show that all the five samples approximately have the same dielectric response, and the error resulting from the mixing process is too small to indicate. Thus, the air bubbles resulting of mixing the silicone with the hardener catalyst do not affect the permittivity measurements. Additionally, it shows that in the lower frequency region the dielectric constant fluctuated up to 100 MHz; however, in the higher frequency region the dielectric constant remains approximately constant up to around 5 GHz. **Figure 5-16** and Figure **5-17** represents the variation of dielectric loss factor, which fluctuates at MHz frequencies and then increases with increasing frequency in the GHz region.

Figure 5-18 and Figure **5-19** and show the dielectric constant and loss factor measurements of activated carbon samples, which were mixed with silicone rubber in the ratio of 4:1, and **Figure 5-20** and **Figure 5-21** show the dielectric constant and loss factor measurements of activated carbon samples which were mixed with silicone rubber in the ratio of 8:1. Five sample of each ratio were prepared at different times with separate mixing. The measurements show that the samples of each ratio have approximately the same microwave dielectric response, and the error resulting from the mixing process is too small to indicate.

The microwave measurements in Figure **5-22** and Figure **5-23**and show that the dielectric constant and dielectric loss factor change according to the content of activated carbon in the mixture. It has been found that increasing the content of activated carbon leads to an increase in both the relative permittivity and dielectric loss factor.
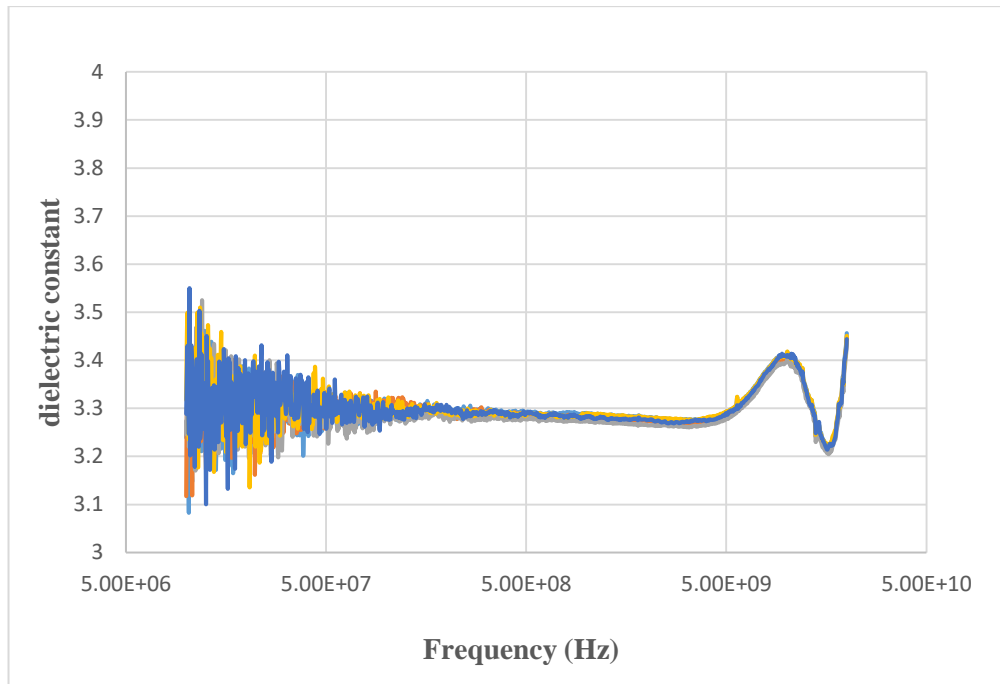
Figure 5-16 Real components of complex permittivity of Silicone rubber for 5 samples.
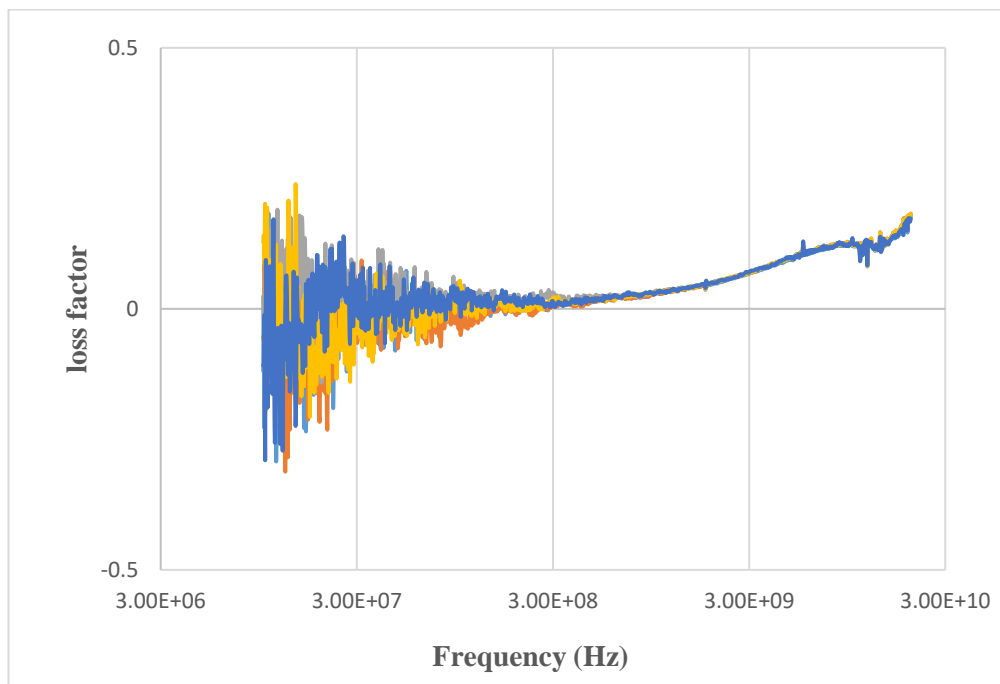
Figure 5-17 Imaginary components of complex permittivity of Silicone rubber for 5 samples.
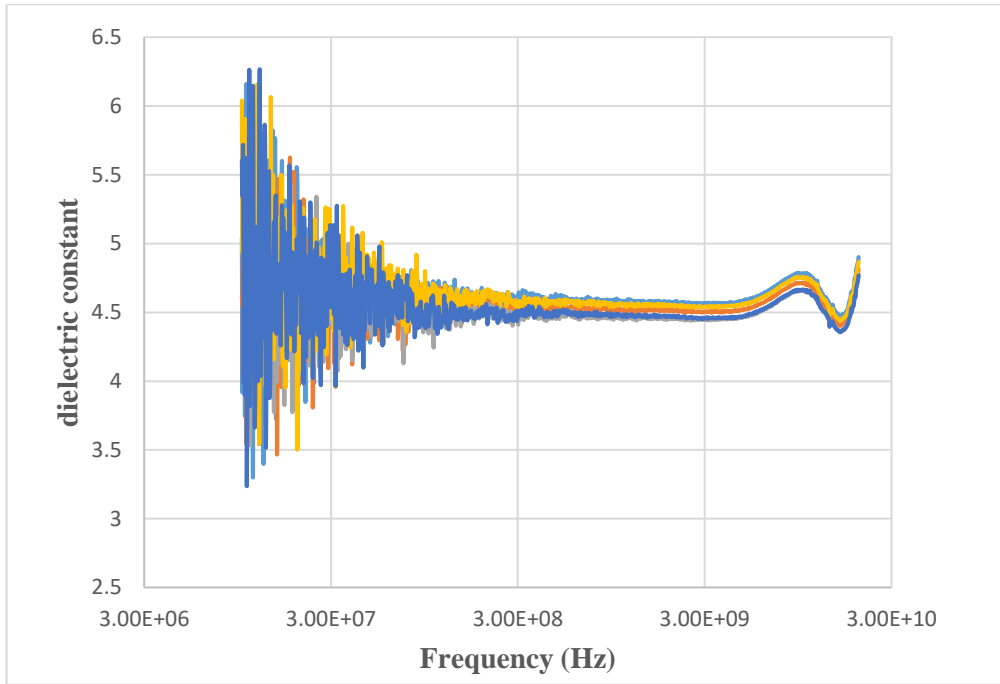
Figure 5-18 Real component of complex permittivity of 4:1 for 5 samples
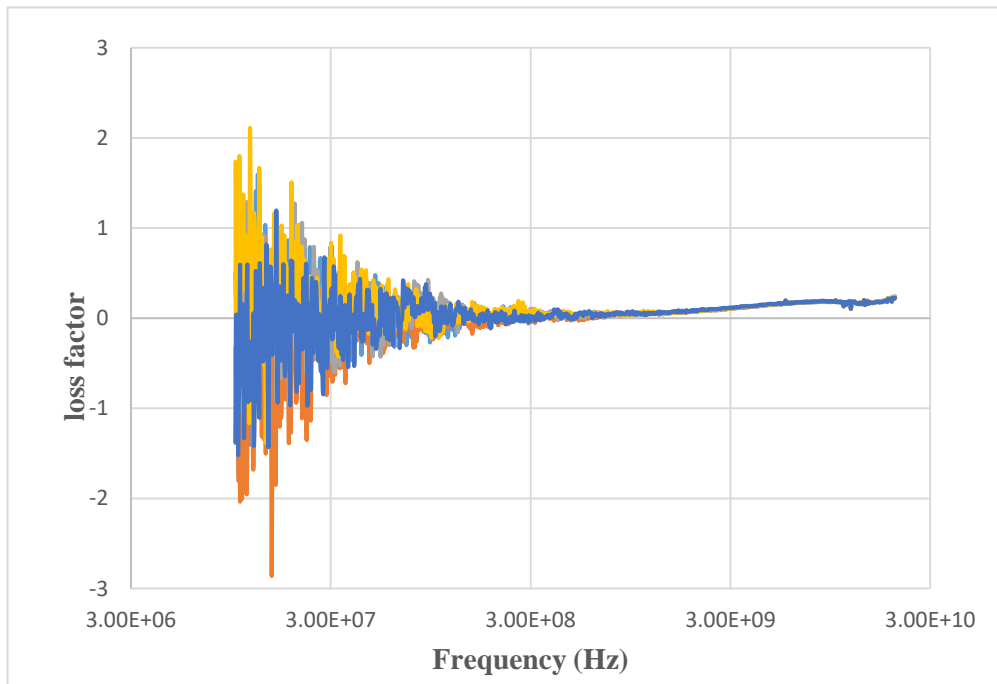
Figure 5-19 Real and imaginary component of complex permittivity of 4:1 for 5 samples
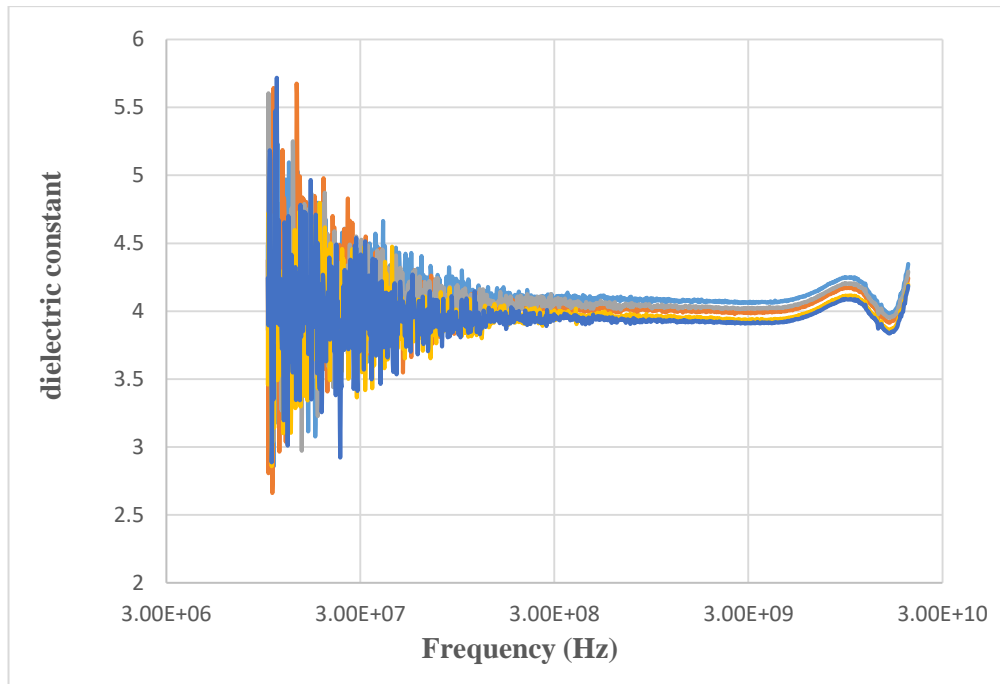
Figure 5-20 Real component of complex permittivity of 8:1 for 5 samples
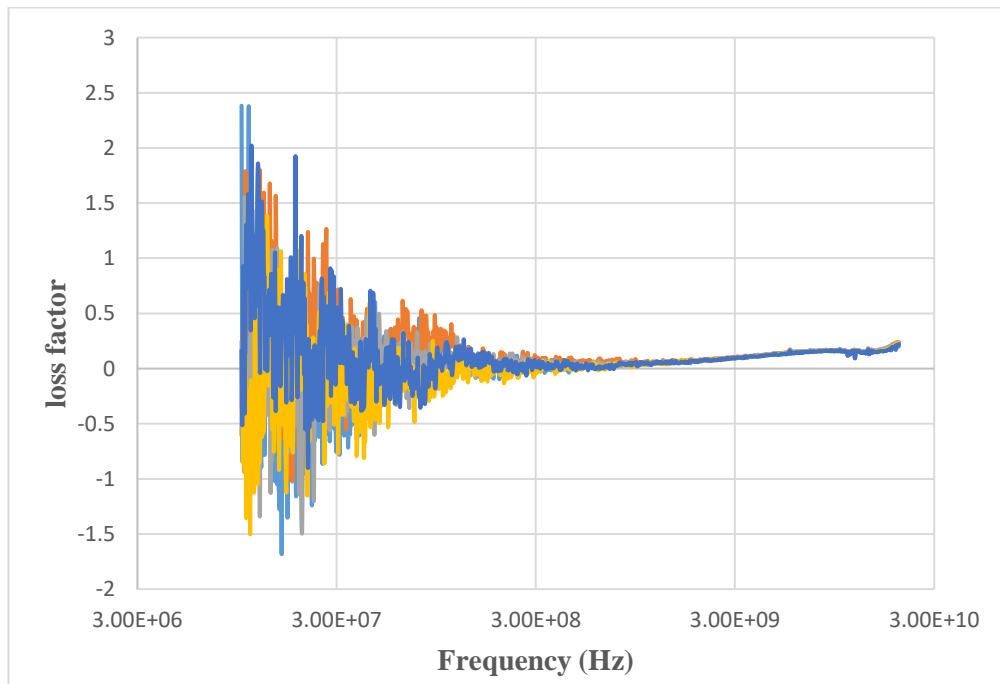
Figure 5-21 Imaginary component of complex permittivity of 8:1 for 5 samples
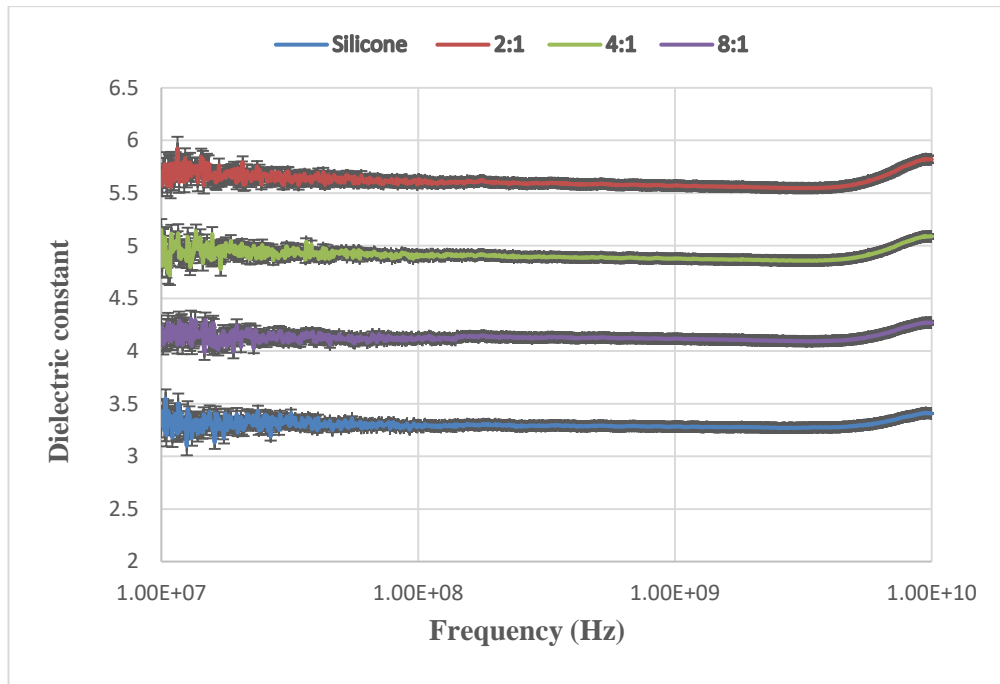
Figure 5-22 Real component of complex permittivity
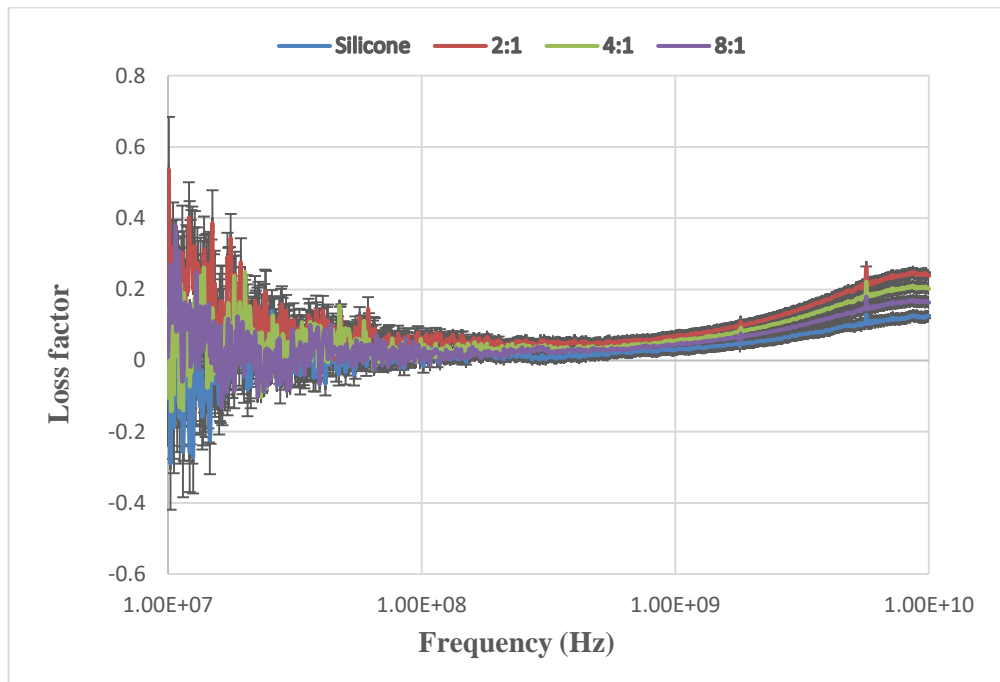
Figure 5-23 Imaginary component of complex permittivity

5.4.2   Dielectric properties of carbons contained in blast furnace dust

The complex permittivity results of all three samples (coke, coal-3, and coal-5) are shown in **Figure 5-24**, Figure **5-25**, **Figure 5-26**, Figure **5-27**, **Figure 5-28** and Figure **5-29**, respectively, over the frequency range of 0.1–10 GHz. The figures demonstrate

the changes in the real part (ε') and imaginary part (ε'') of the complex permittivity of all three samples vs frequency. With frequency increasing from 0.1 to 10 GHz, the real part of complex permittivity is almost unvarying; it is approximately constant in the frequency range between 0.1 GHz and 6.6 GHz, with average values of 5.7, 4.2, and 2.25 for coke, coal-3, and coal-5, respectively. Over the frequency range between 6.6 GHz and 10 GHz, the real part of complex permittivity slightly increases.

The imaginary part of the complex permittivity slightly decreases in the frequency range between 0.1 GHz and 1 GHz, and above this frequency, the decrease in the imaginary part of complex permittivity for all three samples becomes relatively higher. Comparison between the real and imaginary parts of the three samples is shown in **Figure 5-30** and **Figure 5-31**. It is clear that coke has highest value of ε', and coal-3 has a value of ε' compared with coal-5. All three samples have approximately the same values of ε'' over the frequency range of 0.1 to 0.55 GHz, with the variations in the ε'' value between coke and coal-3 and coal-5 becoming more obvious at higher frequencies. The variations between measurement sets are low compared to the variations when the measurements were done in the case of when the sample is introduced to the probe as a raw powder. All three samples: coke, coal 3, and coal 5 have different contents of moisture and minerals which affects their dielectric properties. Coke has highest average value s of dielectric constant, this might be because the high carbon and low impurities contents.
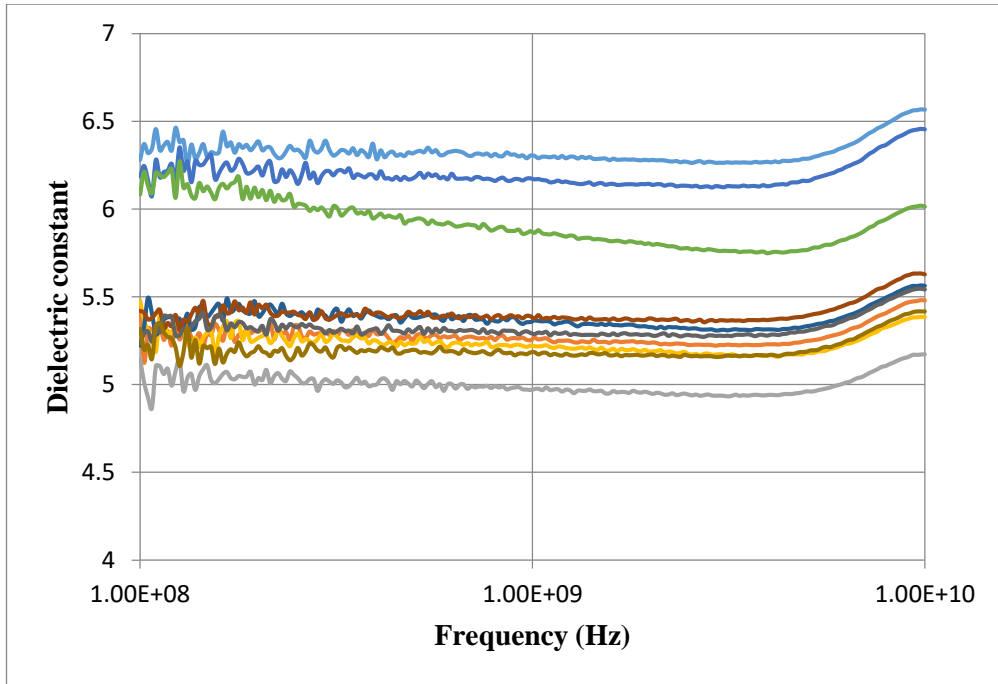
Figure 5-24 Real components of complex permittivity of coke for 10 independent
measurements
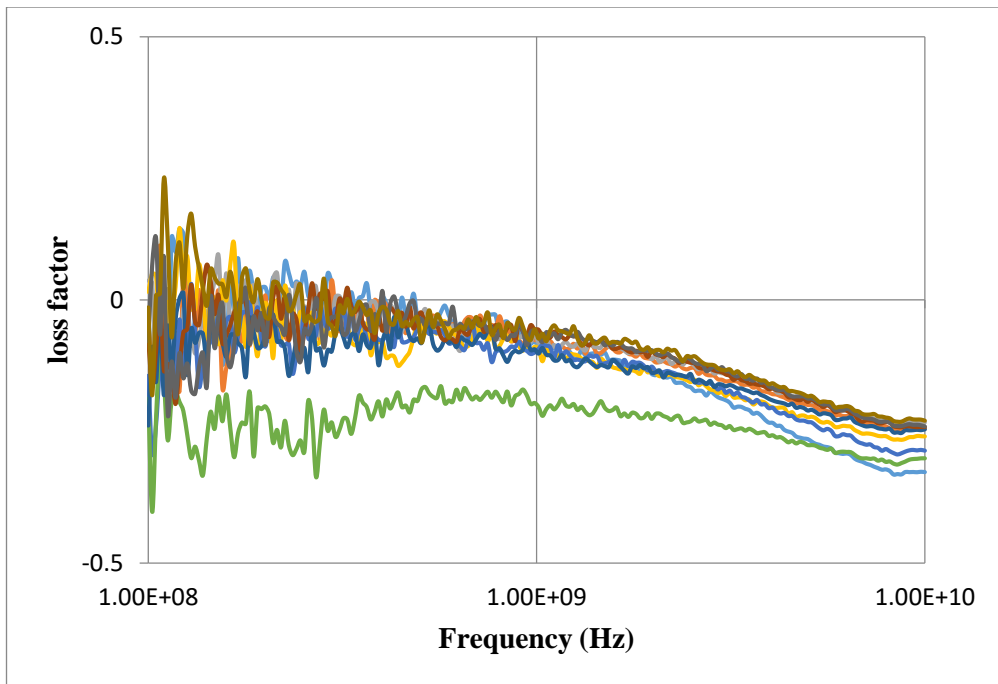
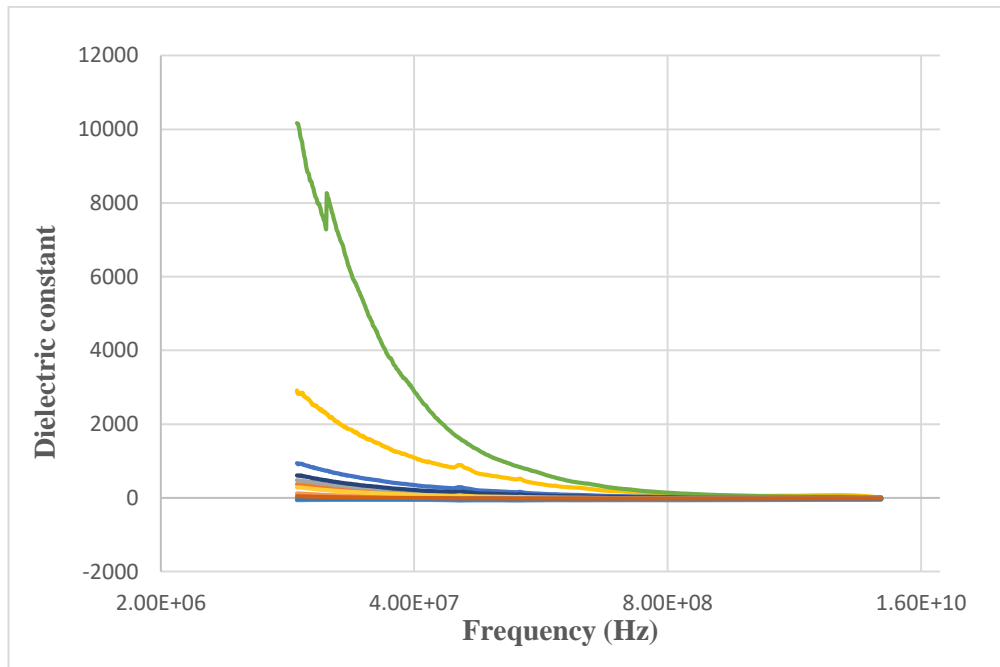Figure 5-25 Imaginary components of complex permittivity of coke for 10 independent
measurements
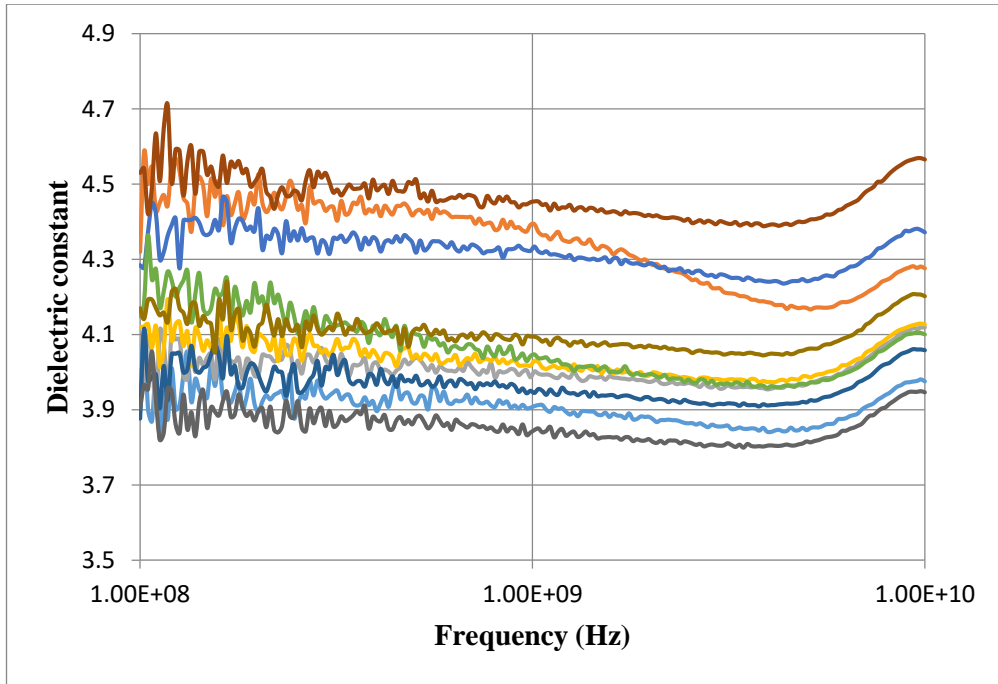
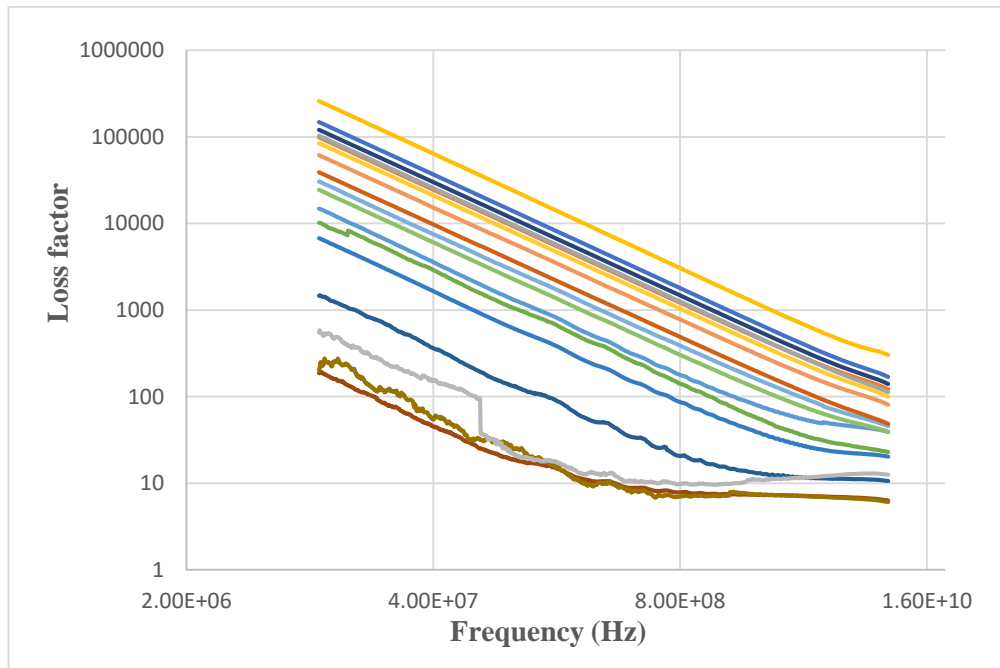Figure 5-26 Real component of complex permittivity of coal 3 for 10 independent measurements

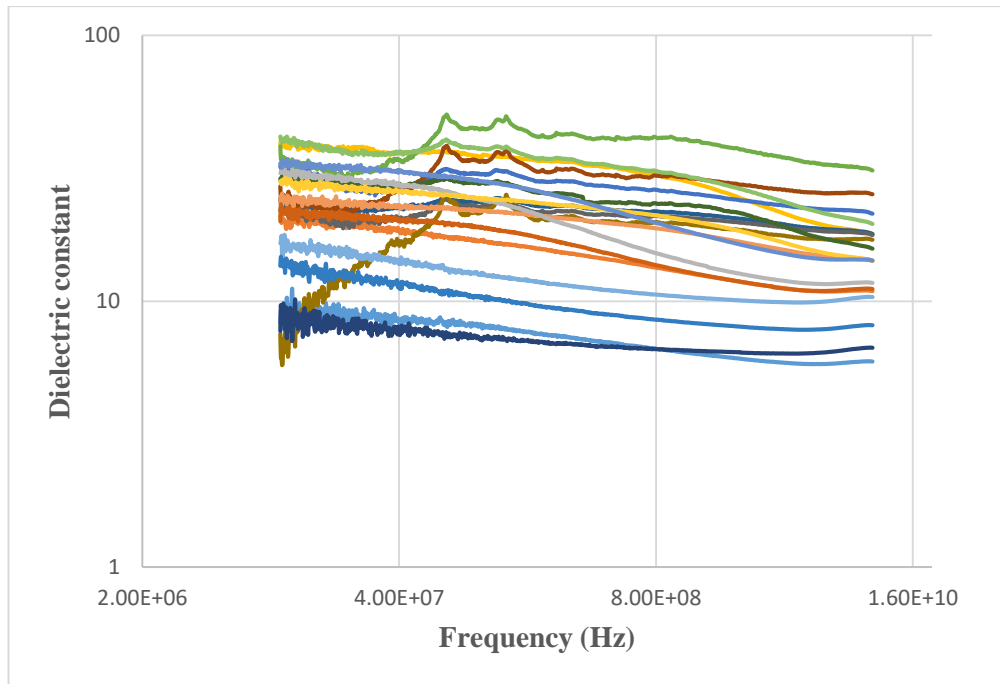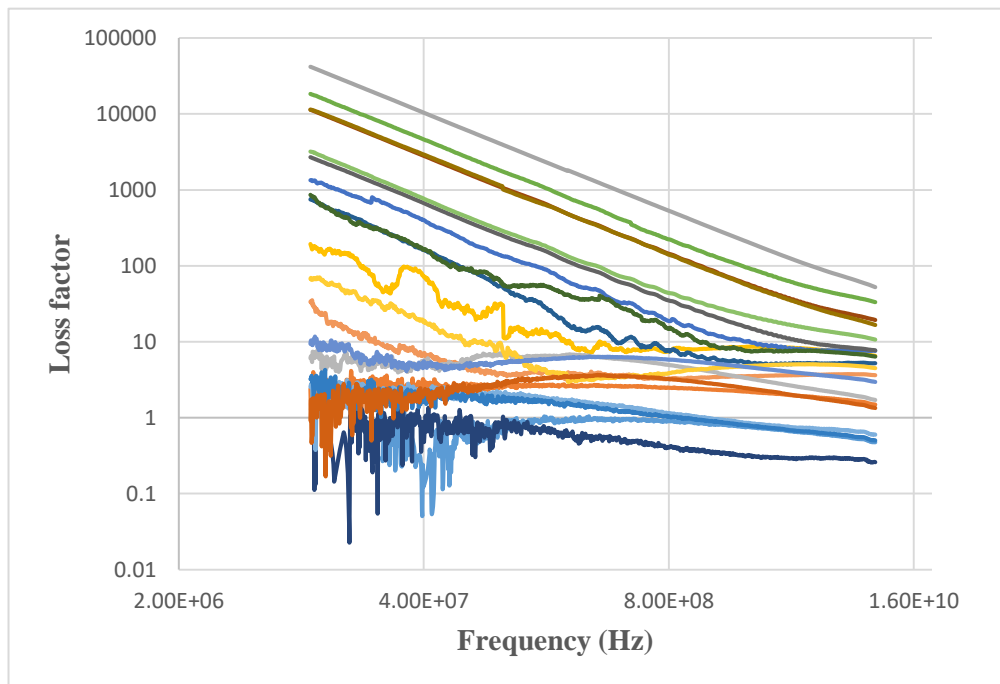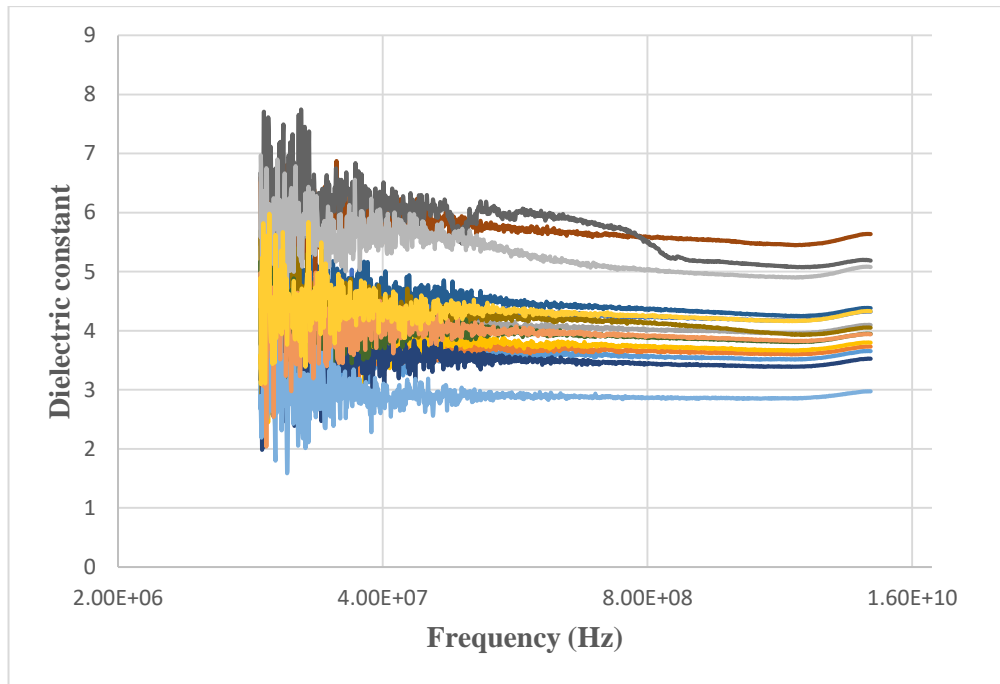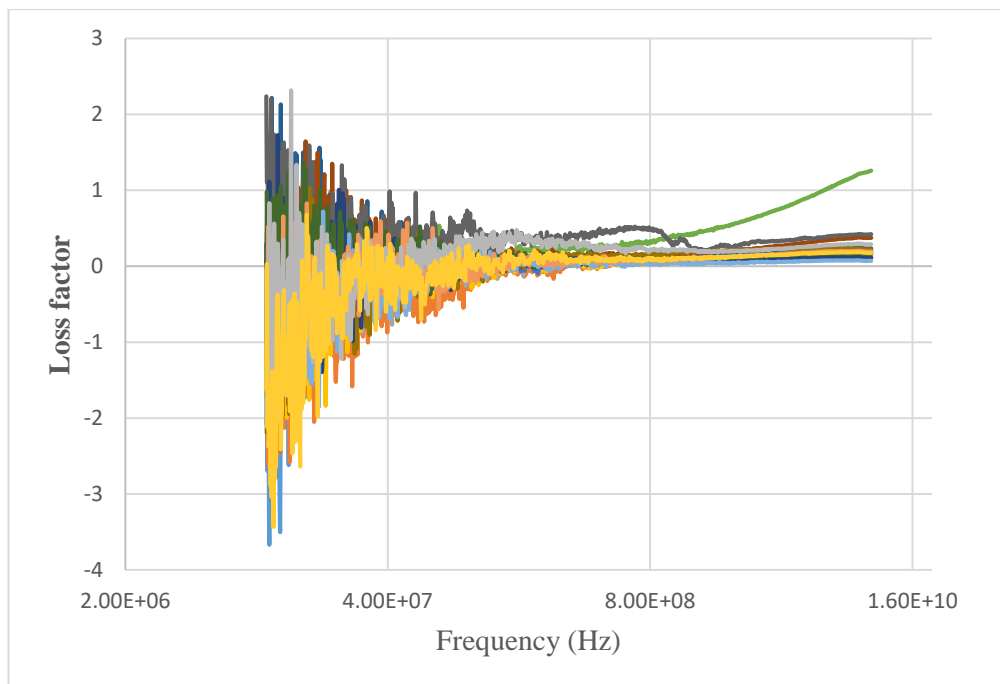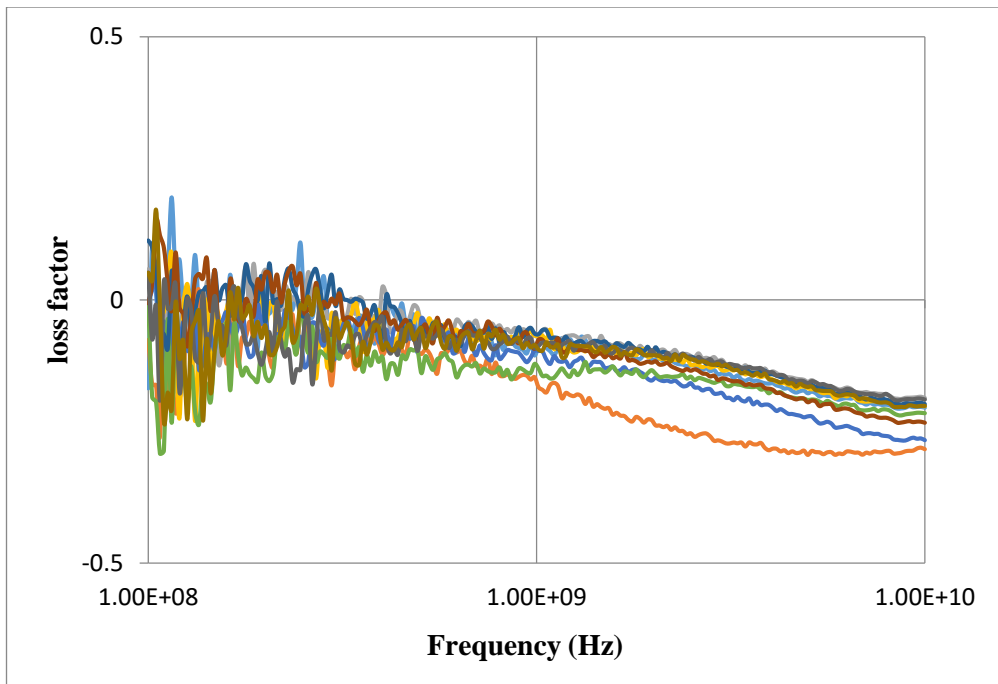Figure 5-27 Imaginary component of complex permittivity of coal 3 for 10 independent measurements
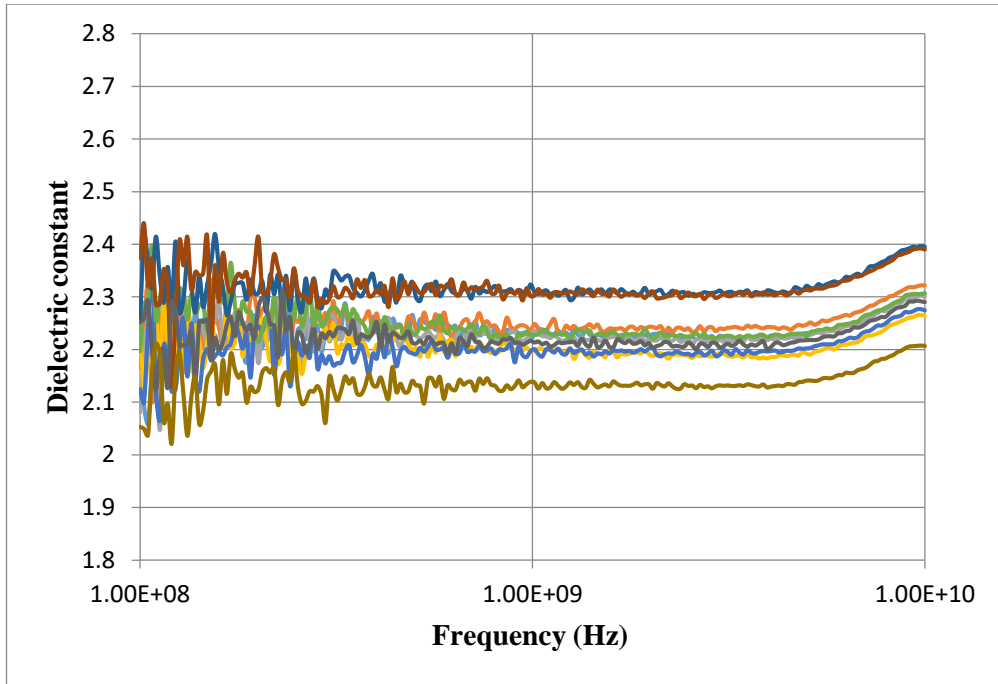
Figure 5-28 Real component of complex permittivity of coal 5 for 10 independent
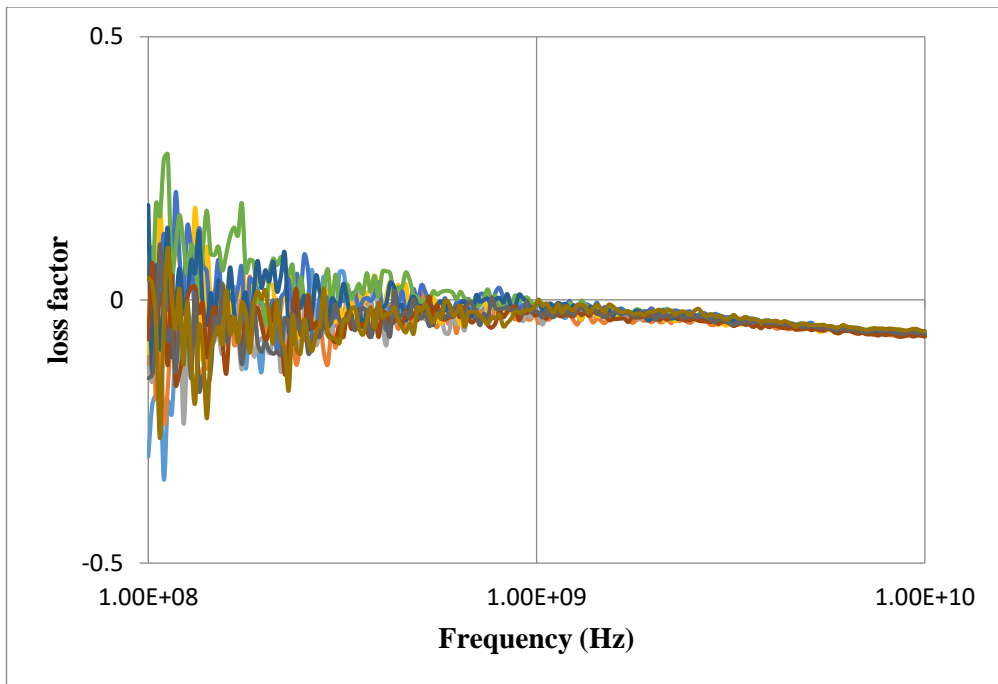
measurements

Figure 5-29Imaginary component of complex permittivity of coal 5 for 10 independent

measurements
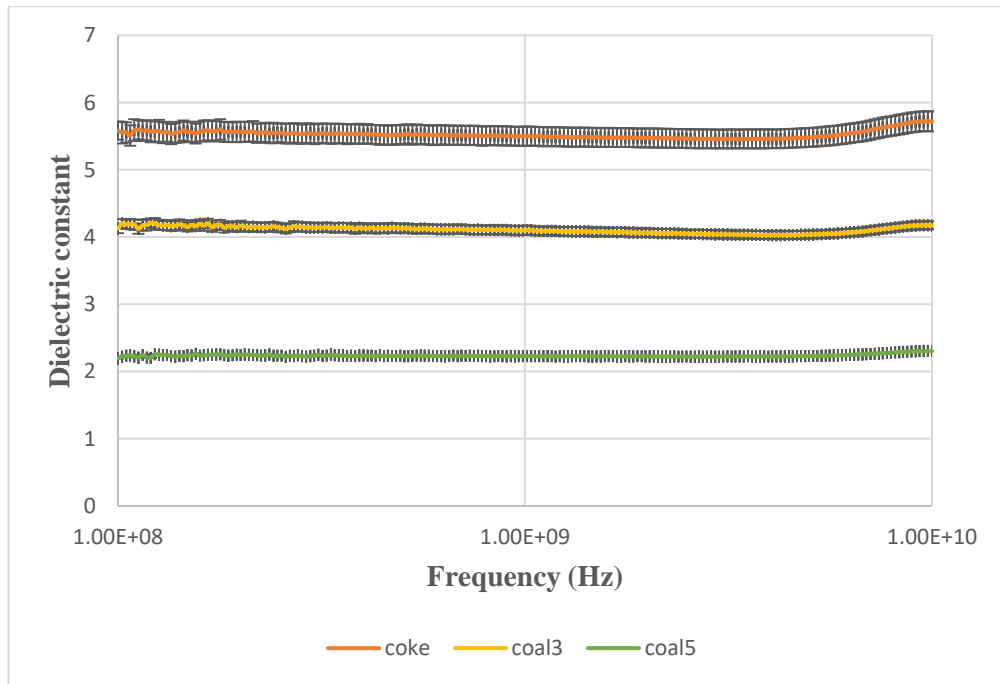
Figure 5-30 Real components of complex permittivity for three different types of carbon
samples
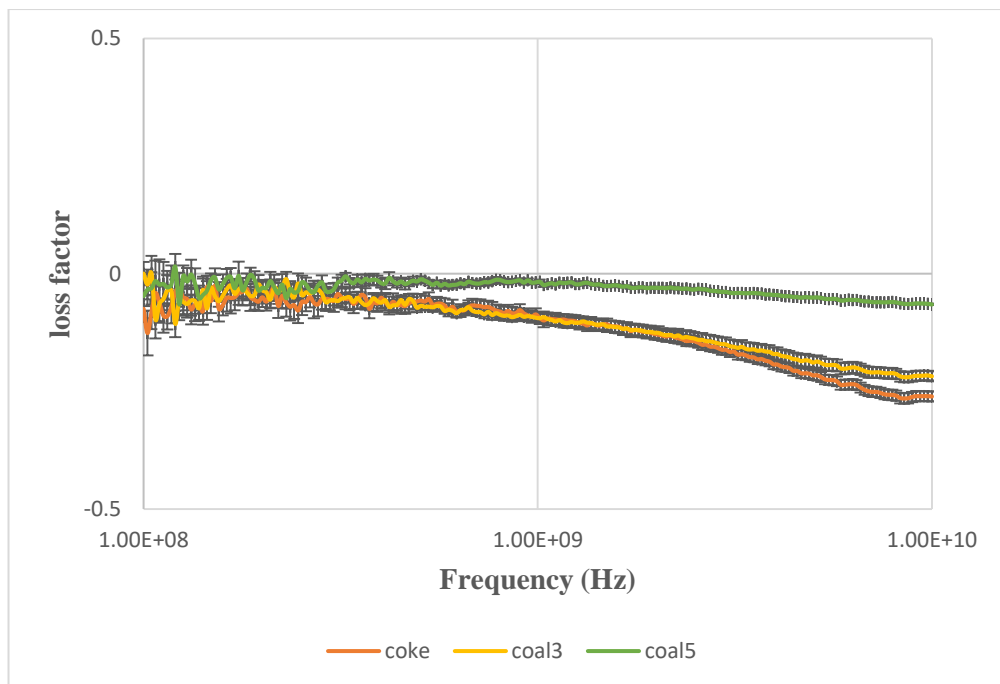
Figure 5-31 Imaginary components of complex permittivity for three different types of
carbon samples

5.5   Conclusion

The microwave dielectric properties of activated carbon/ silicone rubber mixtures were investigated over the frequency range 10 MHz to 20 GHz using a coaxial probe with increasing content of activated carbon within a silicone host.

The preparation methods of samples by dispersion of AC in silicone rubber have a strong impact on the properties of the resulting samples, at a same activated carbon loading, considerable improvement in the dielectric measurement with regard to the error. Mixing powders with silicone rubber decrease finite conductivity between the grains.

The results showed increases in dielectric constant and dielectric loss with increasing mass fraction of activated carbon in the sample. The results also show that the dielectric constant of all samples highly fluctuated in the region of frequencies between 10 MHz to 100 MHz this can be related to the phase change, whereas above 100 MHz it becomes approximately constant.

The same procedures and techniques were used for measuring the dielectric properties of three different types of carbonaceous materials contained in blast furnace dust over the frequency range 10 MHz to 10 GHz. The results show that the dielectric properties of the samples are influenced with increasing frequency, especially in the higher GHz region. The dielectric constant increase and the losses decrease with increasing frequency.

This study shows that multimode microwave cavity system can be used to estimate the microwave dielectric properties of carbon materials contained in BFD in the 2 to 10 GHz range. Some modes are more satisfied to differentiate these types of coal and coke, such as TM_{010}. In general, dielectric properties of the samples decrease as the frequency increased.

In conclusion, it is has been demonstrated that both the multimode cavity and open-ended coaxial probe methods are appropriate to be used as test methods for identifying and differentiating the different types of carbons based on the frequency dependence of their dielectric properties. The broadband coaxial technique is shown to be repeatable and accurate and a clear frequency dependence occurs for both real and imaginary parts of permittivity.

Chapter 6 Temperature-Dependent Dielectric Properties

Owing to their application in, for example, carbon dioxide capture, it is necessary to characterise the dielectric properties of activated carbon over a variable temperature range, typically to around 150^0C. Measuring temperature-dependent dielectric properties of activated carbons may be advantageous in the thermal treatment of activated carbons and in the thermal regeneration of saturated activated carbon.

In blast furnace dust (BFD), the dielectric properties of different types of carbon need to be characterised as a function of temperature to allow the real time monitoring of complex permittivity to differentiate the types of carbon. This is important to quantify the utilization of coal injected in the furnace and to determine the efficiency of coal injection.

The temperature dependent properties of two groups of carbon materials, activated carbons and the three different coal-based constituents contained in BFD, were measured using the TM_{010} microwave cavity technique at frequency of 2.498 GHz in the temperature range 30 ^{0}C to 150 ^{0}C.

6.1 Measurement system

In this chapter, the cavity perturbation technique is used for temperature dependent dielectric properties measurements. In this technique, which is detailed in Chapter 3, a sample of material is inserted (via a quartz sample tube) into the cavity and the resulting perturbations are measured.

A change in the ambient temperature of the cavity will cause a change in the resonant frequency, due to the thermal expansion of the cavity which causes change in the cavity dimensions, radius (a) and height (d). The thermal expansion coefficient α of the aluminium metal making up the cavity can be used to describe these changes. Therefore, the assumption that the volume of the cavity is fixed is not valid in the case of changing temperature. The perturbation equations (3-46) and (3-47) are valid in the case of the sample size being small compared to the cavity size. Therefore, any change in the cavity size due to temperature variation must be included in the calculations. This imposes systematic errors on the real part of the permittivity, in particular, as changes in frequency due to cavity dimension changes may be wrongly interpreted as

being due to changes in sample dielectric property, if perturbation analysis is performed without correction.

In this section, nodal modes are introduced, which were used for temperature correction measurements. Nodal cavity modes are those which have no electric fields in the centre of frequency and are therefore unaffected by the presence of the sample. The electric and magnetic distributions of some nodal modes for the "standard" cavity, with 40 mm radius and 46 mm height, are shown **Figure 6-1**.

The simplest way to obtain the temperature correction is to subtract the fractional frequency shift of nodal modes such as TM_{310} (of frequency 6.61 GHz) from the fractional shift of the measurement mode TM_{010} (of nominal frequency of approximately 2.5 GHz) [43, 110, 111]. The justification of this is analysis is based on the fact that the resonant frequency of any TM_{nm0} mode depends only on radius, so that when temperature changes by an amount ΔT

$$f_0 = \frac{c}{2\pi a} p_{nm} \tag{6-1}$$

$$a = a_0(1 + \alpha T) \quad \rightarrow \quad \frac{\Delta f_0}{f_0} = -\frac{\Delta a}{a} = -\alpha \Delta T \tag{6-2}$$

where p_{nm} are the zeros of $J_n(x) = 0$. This means that the fractional frequency shift, for a given change in temperature, is the same for all TM_{mn0} modes, dependent only on the thermal expansion coefficient α of the material making up the cavity. This includes measurement modes such as TM_{010}, and nodal modes such as TM_{310}, allowing for the part of the frequency shift due to temperature change of the cavity to be subtracted from the frequency shift of the cavity plus sample, to provide unambiguous values of the temperature dependent permittivity of the sample, free from systematic temperature error.
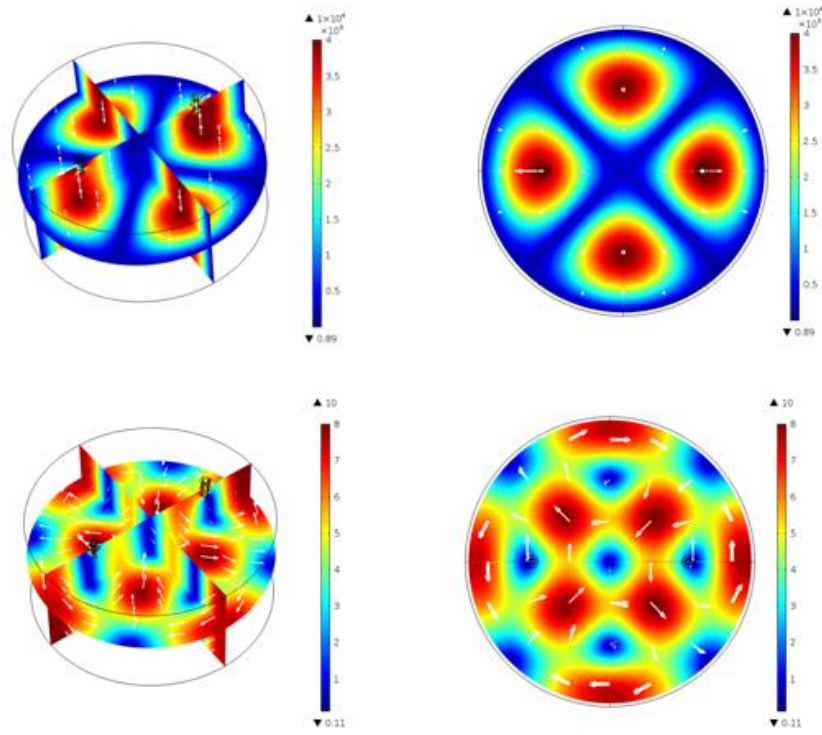
Figure 6-1 Distributions of electric (top) and magnetic (bottom) fields of the nodal mode
TM_{210} at 5.33 GHz
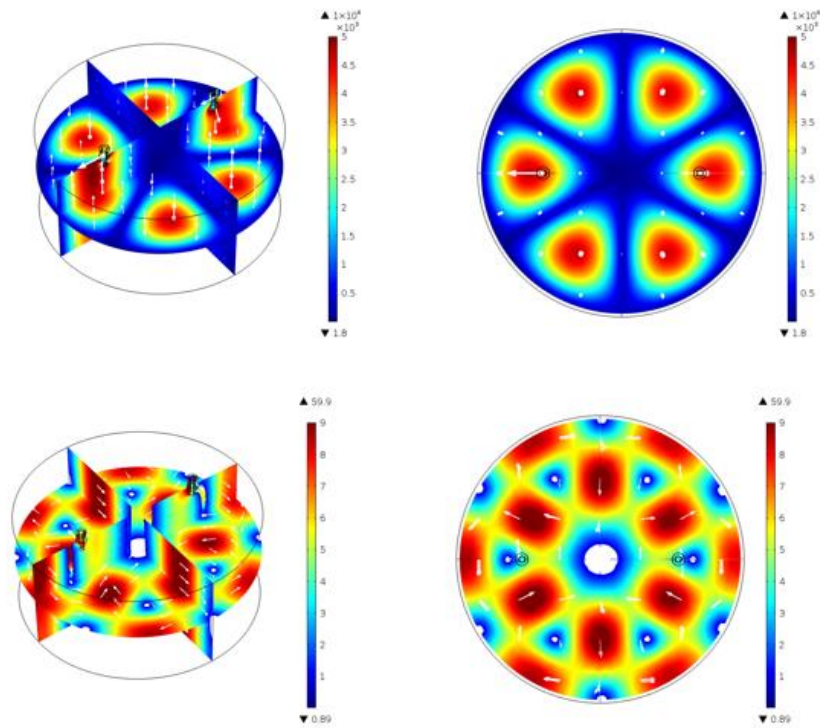
Figure 6-2 Distributions of the electric (top) and magnetic (bottom) fields of the nodal mode
TM_{310} at 6.61 GHz

Thus, the simplest way to obtain the temperature correction using a nodal mode is to subtract the fractional frequency shift of the nodal mode (such as TM_{210} and TM_{310}) from the measurement mode TM_{010} [43, 110, 112].

This process is shown quantitatively below, where the subscript "u" denotes the fractional frequency shift with temperature of the unperturbed cavity. Through cavity perturbation, the change in permittivity with respect to a reference temperature can be expressed as following:

$$\frac{\Delta f_s(T)}{f_s(0)} = \left[\frac{\Delta f_{010,s}(T)}{f_{010,s}(0)} - \frac{\Delta f_{m10,s}(T)}{f_{m10,s}(0)}\right] \tag{6-3}$$

$$- \left[\frac{\Delta f_{010,u}(T)}{f_{010,u}(0)} - \frac{\Delta f_{m10,u}(T)}{f_{m10,u}(0)}\right]$$

$$\varepsilon_1(T) \simeq -2\left[\frac{f_s(T) - f_0(0)}{f_0(0)}\right]\frac{V_c}{V_s}G_{nmp} + 1 \tag{6-4}$$

$$\varepsilon_2(T) \simeq -2\left[\frac{1}{Q_s(T)} - \frac{1}{Q_0(0)}\right]\frac{V_c}{V_s}G_{nmp} \tag{6-5}$$

The nodal mode TM_{310} is used for temperature correction in the experiments presented here as it is not perturbed by a sample placed along its axis; both electric and magnetic fields are zero in this location. In the case of the use of the standard cavity with radius of 40 mm and height of 46 mm, TM_{310} occurs at resonant frequent of 6.61 GHz (since $p_{31} = 6.380$). Applying (6-4) and (6-5) to calculate the corrected temperature dependent dielectric constant and loss factor.

For the temperature dependent experiments the cavity (loaded with a sample) was placed inside a Memmert UF30 laboratory oven, as shown in **Figure 6-3**. The change in the resonant frequency and bandwidth were recorded using a custom LabVIEW program. Temperature was measured using resistance temperature detector PT100 RTDs provided by Omega, interfaced to a National Instruments C-DAQ. At each temperature, the magnitude of the voltage transmission coefficient S_{21} was measured in the frequency domain with a PNA-L network analyser N5232A to obtain the resonant frequency and quality factor Q.

Figure 6-3 Photograph of the bench-top experimental assembly for cavity measurements. The cavity is put inside a computer-controlled oven and connected to a network analyser under control of a LabVIEW program.

6.2　Materials

The materials were again in the two groups comprising (1) three commercial samples of activated carbon which were provided by Heriot Watt University, and (2) different types of carbon contained in blast furnace dust (coke, coal, and char) produced in the combustion laboratory at Cardiff School of Engineering. The commercial activated carbon (NORIT GCN3070, labelled here as CN), was treated in two different ways to produce another two modified activated carbon samples: CN800 and CNO300, to enhance their adsorption capacity by modifying their surface area. CN800 was CN which was treated with gaseous ammonia at 800 ℃; it was placed in a vertical quartz tube in a furnace after drying at 100℃ for 12h under nitrogen flow for 30 min., after which the temperature was increased to 800℃ and the flow changed from nitrogen to ammonia (known as amination treatment). CNO300 had the same treatment except of that instead of flow of ammonia, the flow was a mixture of ammonia and air at a ratio of 1:2, held for 2h (known as ammoxidation treatment). As a result, CN800 and CNO300 were different in terms of both chemical composition, texture, and hence the adsorption capacity. The ultimate analysis of the activated carbon samples is elemental analysis of the activated carbons at various carbonization temperatures. The ultimate analysis of carbons involves determination of the weight percent carbon as

well as sulfur, nitrogen, and oxygen (usually estimated by difference). The results of ultimate analysis of activated carbon samples are presented in **Table 6-1**[113, 114].

Table 6-1 Ultimate analysis of the activated carbon samples[113, 114]

Sample	pH$_{pzc}$	Ultimate analysis (wt%, daf)			
		C	H	N	O
CN	2.8	82.9	3	0.4	13.7
CN800	8.9	88.7	0.7	6.3	4.3
CNO300	6.1	75.0	2.0	9.2	13.8

For the carbon samples contained in BFD, the samples were mixed with silica powder to dilute the sample volume and reduce the effects of the conductivity between the particles of the powder, which was previously found to give random, erratic results.

Table 6-2 Properties of coal samples

Material	Label	size classification	oxygen: carbon ratio	residence time of oxygen (inside blast furnace)
Ground coke	coke	-	-	-
PM coal-3	coal-3	100% < 1mm	5	35ms
PM coal-5	coal-5	100% <1mm 50% > 250 μ	5	35ms

6.3   Temperature-dependent dielectric properties of activated carbon

Activated carbon samples (CN, CN800, and CNO300) were measured for their temperature dependent dielectric properties. Four samples of each material have been measured; two samples were pre-dried at 110ºC for 12h and the other two measured without any pre-drying. The temperature- dependent complex permittivity of the activated carbon samples are shown in Figure 6-4 to Figure **6-9**, at a nominal frequency of 2.45 GHz over the temperature range between 30º C to 150ºC. The dielectric constant of CN, CN800, and CNO300 is seen to decrease considerably between 110ºC and 150ºC. This is unlikely to be due to moisture removal. The dielectric loss factor exhibits a different trend, with a significant decrease for the CN, CN800, and CNO300

being obvious between 110ºC and 150ºC. At the temperature between 80ºC and 100ºC, the dielectric constant of the samples decreases. This is most likely due to moisture removal, since water is highly polar, and such water removal may also change the volume and density of the samples. In the temperature range from 30ºC to 80ºC there is some increase in the dielectric constant, which is most pronounced for CNO300. The origin of this effect is likely to be the natural temperature dependence of the permittivity of the host carbon lattice.

There are some striking variations observed in the temperature range between 110ºC and 150ºC, where the dielectric constant and dielectric loss factor of some samples rise suddenly at a temperature 120 ° C, and then dramatically decreases. These features are associated with the powder being ejected from the sample tube, most likely as a dramatic release of some adsorbed species. The chemical surface of the samples might also cause influence on the dielectric properties of the sample; the end result of such an explosive ejection of powder is shown in **Figure 6-10**.

Figure 6-4 Real component of complex permittivity vs. temperature of CN

Figure 6-5 Imaginary component of complex permittivity vs. temperature of CN

Figure 6-6 Real component of complex permittivity vs. temperature of CN800

Figure 6-7 Imaginary component of complex permittivity vs. temperature of CN800

Figure 6-8 Real component of complex permittivity vs. temperature of CNO300

Figure 6-9 Imaginary component of complex permittivity vs. temperature of CNO300
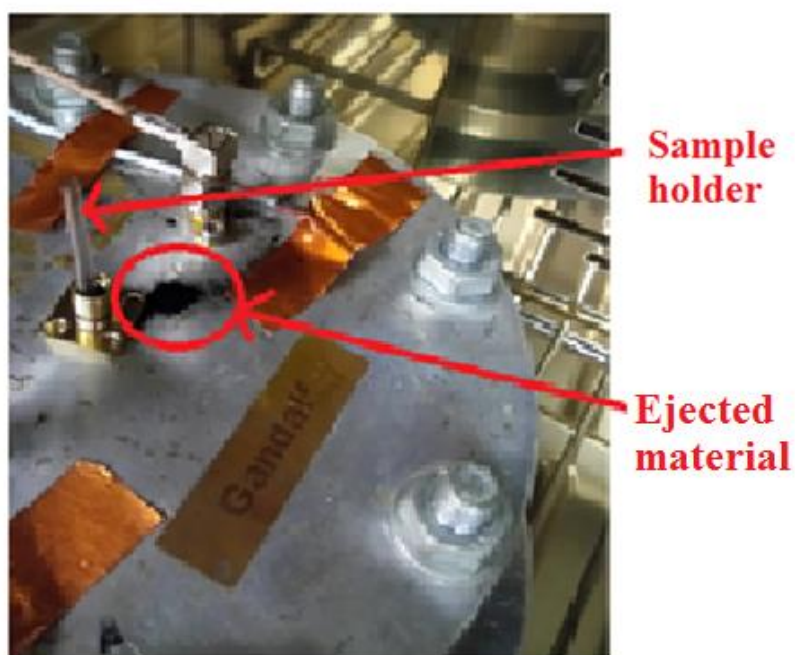
Figure 6-10 Photograph of the ejected materials after first heating cycle

To investigate further the dielectric responses of the samples of activated carbons labelled as CN and CN800, as in Figure 6-4 to Figure **6-7**, some extra measurements have been carried out. Firstly, the dielectric properties of the samples were measured over three heating cycles. **Figure 6-11** shows the dielectric constant of the CN sample as a function of temperature measured over three heating cycles. It is clear that the

second and third measurements are approximately identical, where the peak that occurs between 80º C and 100º C might be ascribed to the removal of moisture. Note that the dielectric constant of the CN sample over the first heating cycle has slightly different values from those of the second and third heating cycles, suggesting the initial irreversible removal of adsorbed species. The dielectric loss factor of the CN sample is shown in **Figure 6-12**. Again, the first cycle has different behaviour and higher overall values, and at temperature above 100ºC it increases then dramatically and suddenly) decreases above 120ºC. This discontinuity in gradient is not seen in the dielectric constant. The second and third heating cycle of CN yield similar results, indicating the general trend of the dielectric loss factor decreasing with increasing temperature.
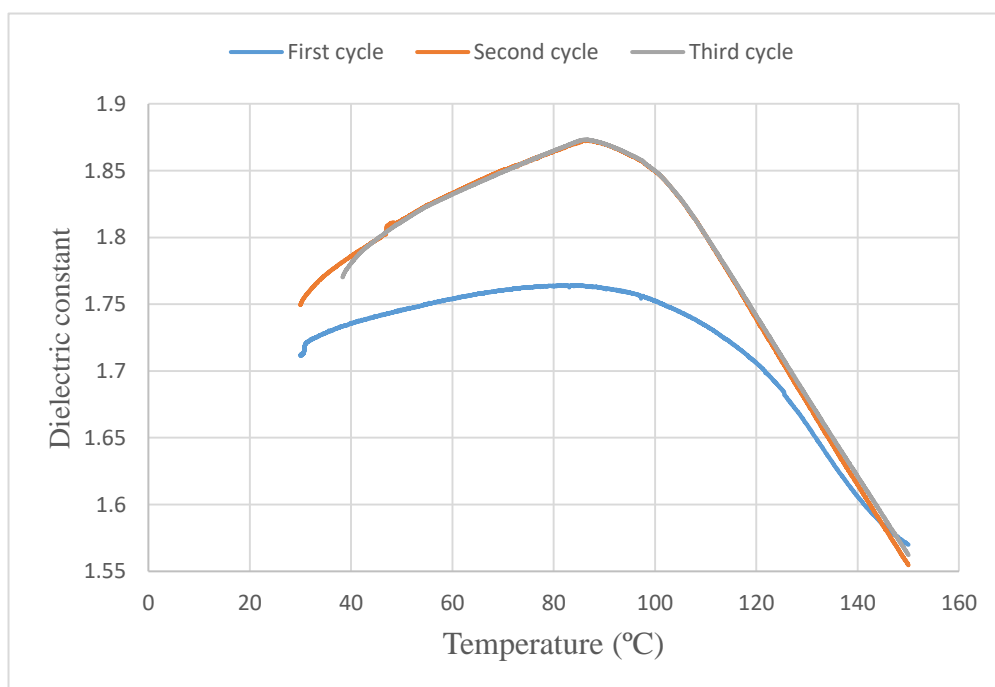
Figure 6-11 Real component of complex permittivity vs. temperature of CN
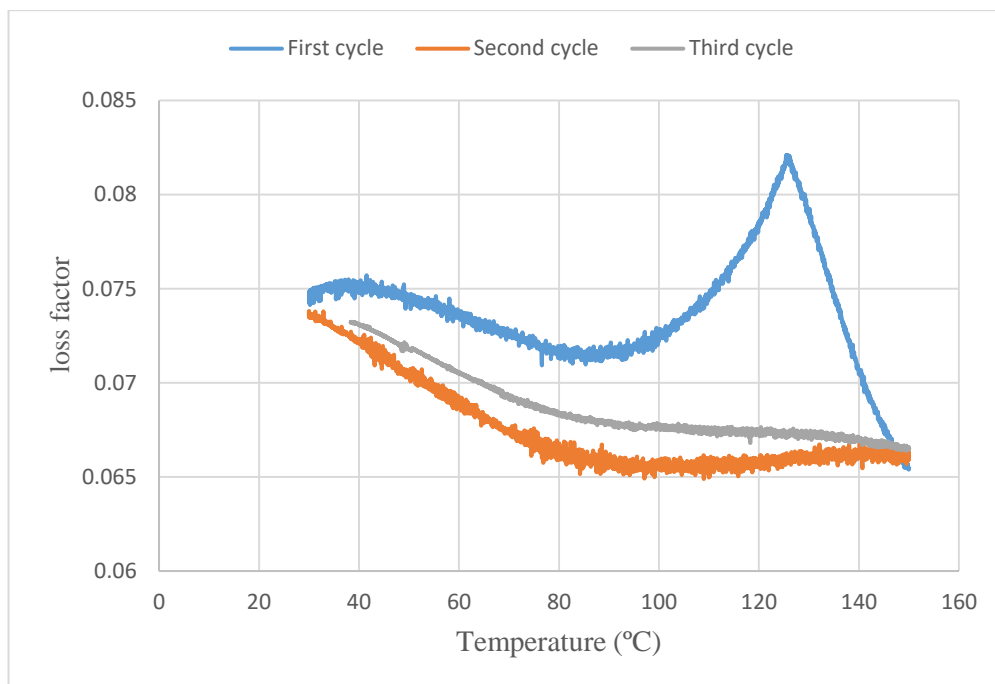
Figure 6-12 Imaginary component of complex permittivity vs. temperature of CN

Real and imaginary parts of measured complex permittivity of the CN800 sample are shown in **Figure 6-13** and **Figure 6-14**, respectively. For dielectric constant, the values peak between 80º C and 100º C for the first and second heating cycles, similar to the CN sample, while during the first heating cycle the dielectric constant slightly increases up to 120ºC, above which it dramatically decreases. The dielectric loss factor of the CN800 sample exhibits different behaviour and higher values through the first heating cycle, and above a temperature of 120ºC it dramatically increases before decreased above 130ºC. The second and third heating cycles of the CN sample show that the dielectric loss factor gradually decreases with increasing temperature.
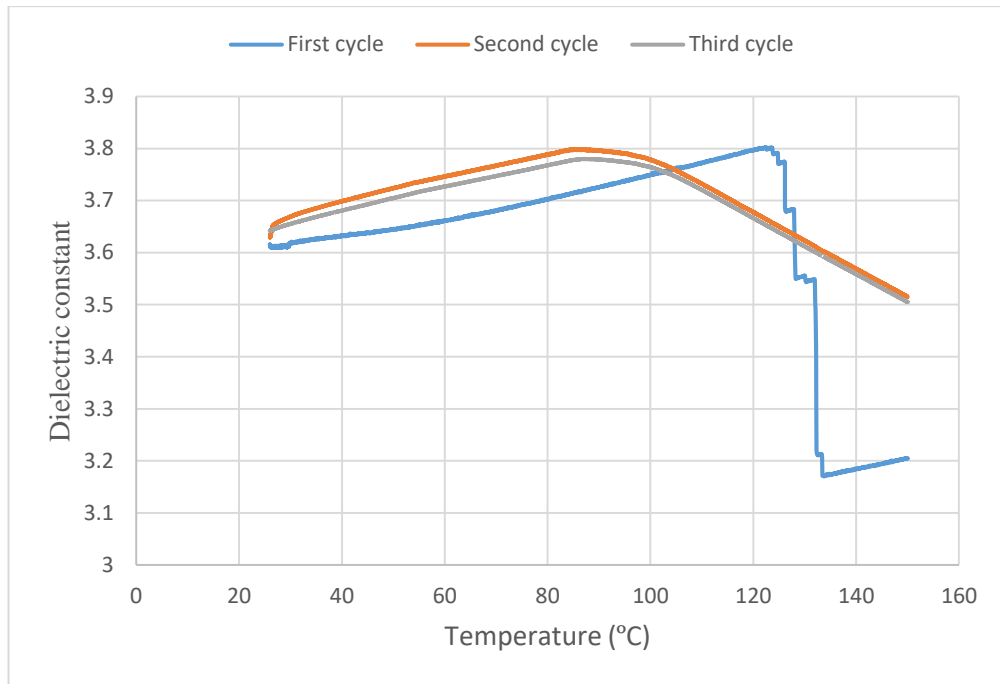
Figure 6-13 Real component of complex permittivity vs. temperature of CN800
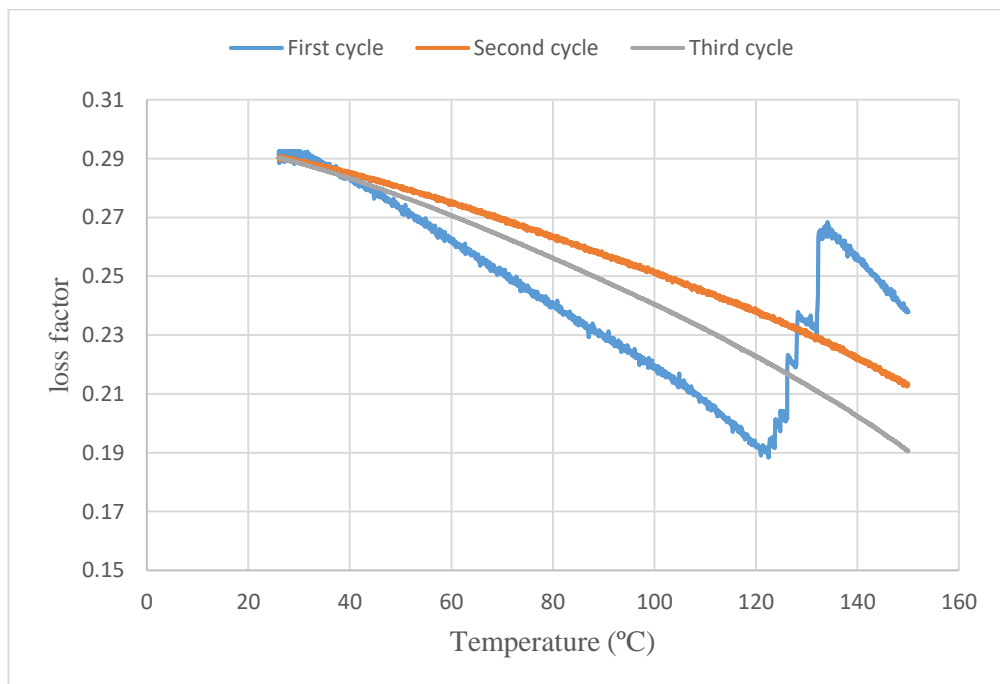
Figure 6-14 Imaginary component of complex permittivity vs. temperature of CN800

6.3.1 Scanning Electron Microscopy (SEM)

Scanning Electron Microscopy of the activated samples was used to obtain high-resolution imaging and analysis of sub-micron features in the powder materials. One

of the motivations was to evaluate any differences in powder microstructure that may have occurred as a result of the sudden (explosive) events reported in the previous section. The images were obtained using a FEI SEM-EDX instrument XL30 ESEM FEG at 512x384 resolution in back scattered and secondary electron detection modes.

In this set-up, the particles were first coated with carbon to make them conductive. As the samples were fine powder, they needed to be fixed firmly to a specimen holder substrate so that they will not contaminate the SEM specimen chamber. By dispersing the powder on the clean surface and pressing the sample holder down onto the powder, and trapping the excess away.

The figures below illustrate the surface morphology of the original activated carbon samples, CN, CN800, and CNO300, before and after the microwave experiments, at x500 and x2000 magnifications. There was no clear difference between Figure **6-15**, activated carbon samples before experiments, and Figure **6-16**, activated carbon samples after experiments.
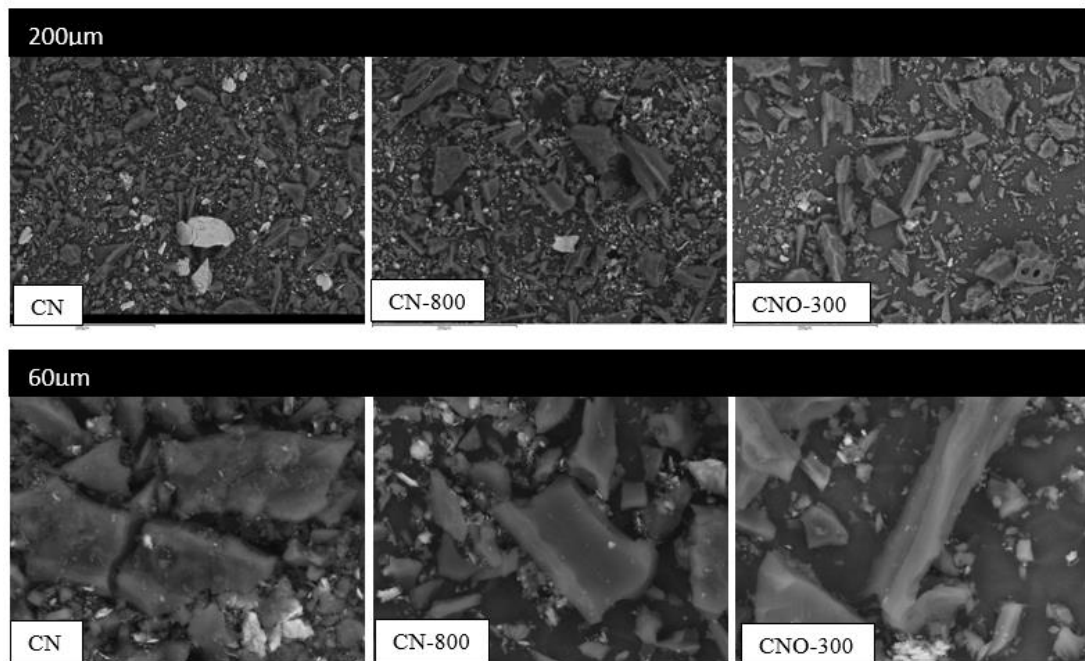
Figure 6-15 SEM photograph of activated carbon samples before heating, the scale is shown at 200µm and 60µm.
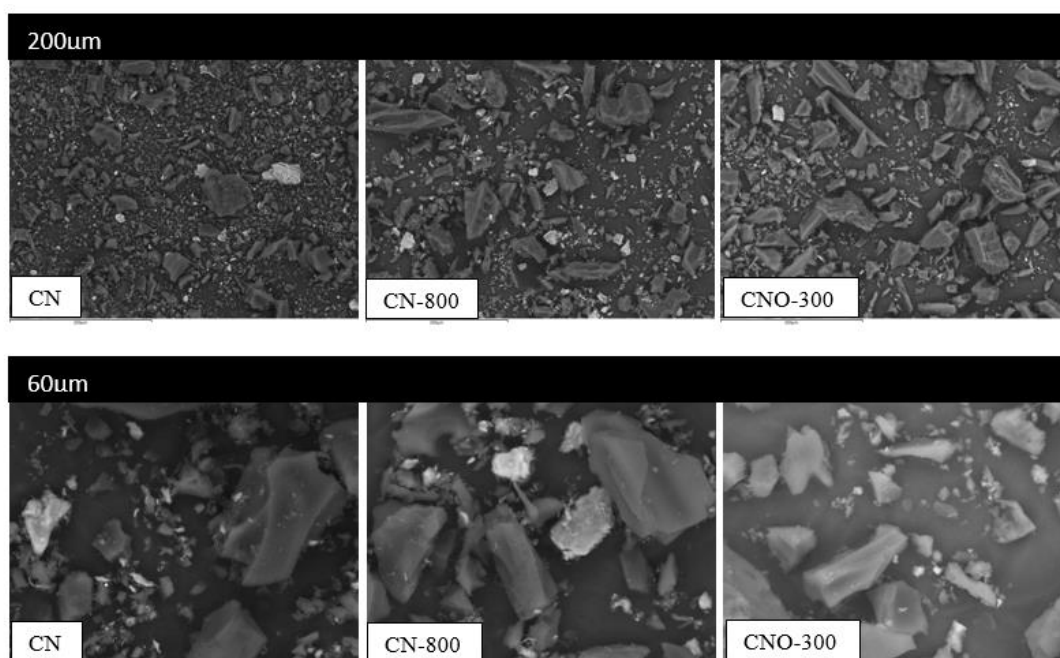
Figure 6-16 SEM photograph of activated carbon samples after heating, the scale is shown at 200µm and 60µm.

Thermogravimetric and differential scanning calorimetry techniques were applied to the activated carbon sample using a Mettler-Toledo TGA/DSC 3+ thermal Analyser. Experiments were performed under air and samples (~12 mg) were loaded in a sample pan. The samples was heated from 30−150ºC at a ramp rate of 10 °C min−1. The CN, CN800, and CNO300 samples showed a similar weight loss, 0.3−1.0%, in the temperature range 20−150 °C, due to degassing and volatilization of water or residual solvents. In the 50−150 °C temperature range, Figure **6-17** shows higher weight loss for the CNO300 samples compared to pristine CN and this might attributed to thermal decomposition. Unlike for the microwave measurements, no sudden changes are observed at specific temperatures.
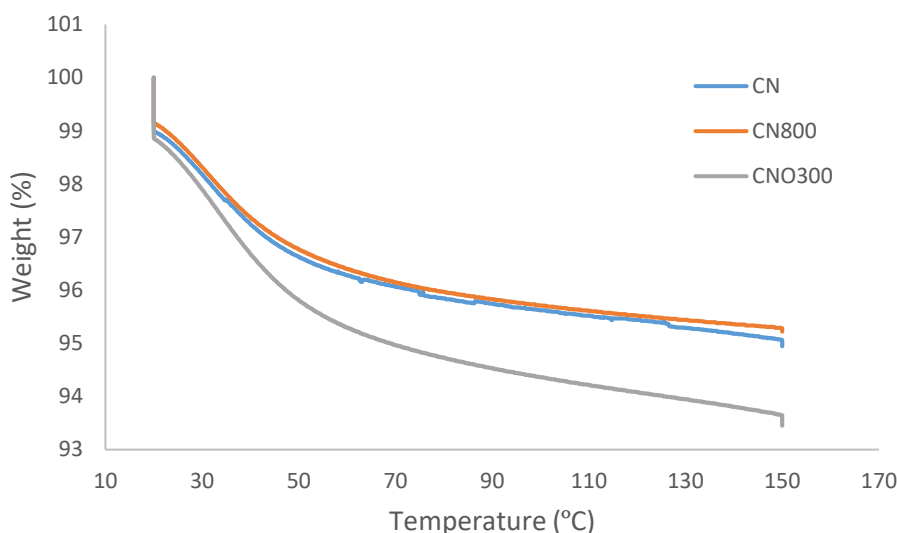
Figure 6-17 Thermogravimetric analysis of activated carbon samples

6.4   Temperature-dependent dielectric properties of BFD

Three different carbon samples (coke, coal-3, and coal-5) were measured and the dielectric properties of samples of each material have been calculated. The samples were pre-dried at 110ºC for 2h, then mixed with fine silica at weight ratio 50:50 to reduce the effects of the percolation conductivity due to inter-grain contacts, then filled in the standard quartz tubes to be ready for measurements.   The temperature-dependent complex permittivity of carbon samples are shown in **Figure 6-18** to **Figure 6-25**, over the range of temperature between 30º C to 150ºC. The dielectric constant of coke shown in **Figure 6-18** increases almost linearly with temperature, from 30 to 100ºC while the dielectric loss factor shown in **Figure 6-19** decreases approximately linearly with temperature. The dielectric constant was found to increase from 7.328 to about 8.1. The increased phenomenon coincides with an increase in electrical conductivity and is successively associated with an increase in carbon content due to devolatilization which is the removal of volatile substances from a solid. It could be that long baking times might affect the crystallization process and coke formation.
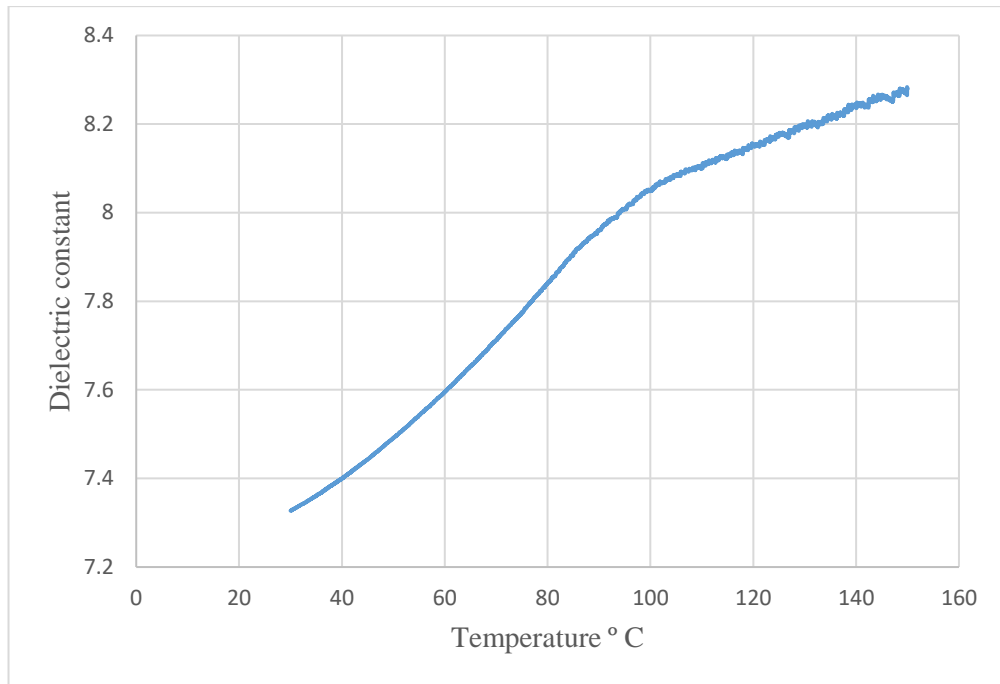
Figure 6-18 Real component of complex permittivity vs. temperature of coke
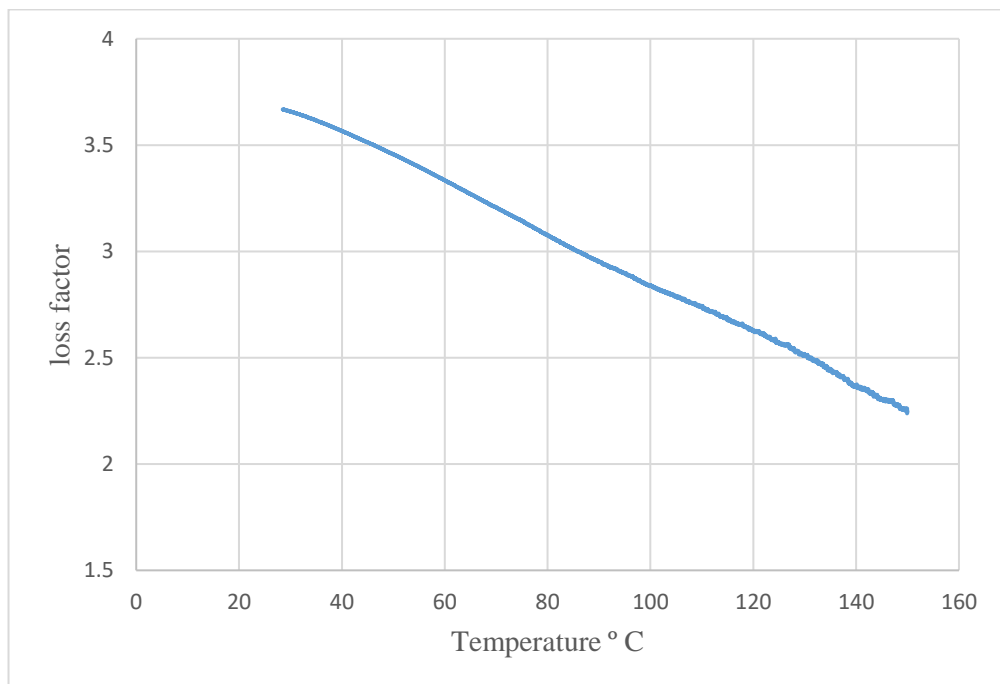
Figure 6-19 Imaginary component of complex permittivity vs. temperature of coke

The dielectric constant data of coal-3, shown in **Figure 6-20**, and coal-5, shown in **Figure 6-22**, exhibit similar behaviour to that observed by Marland et al. and to the dielectric constant for the CNO300, shown in **Figure 6-8**, in that the dielectric constant decreases considerably between 80ºC and 150ºC. The reduction in dielectric constant that occurs over this temperature range has been previously correlated with the coal

drying.[36], but in the experiments reported here the sample was pre-dried. The dielectric loss factor of coal-3 shown in **Figure 6-21** decreases with temperature, while conversely it slightly increases for coal-5, shown in **Figure 6-23**. In general, it can be conclude that, though dielectric properties of coal samples have similar behaviour with temperature, using cavity perturbation techniques is effective method to differentiate the different types of carbon as shown in **Figure 6-24** and **Figure 6-25**; there are clear differences in both the values of dielectric constant and dielectric loss factor.
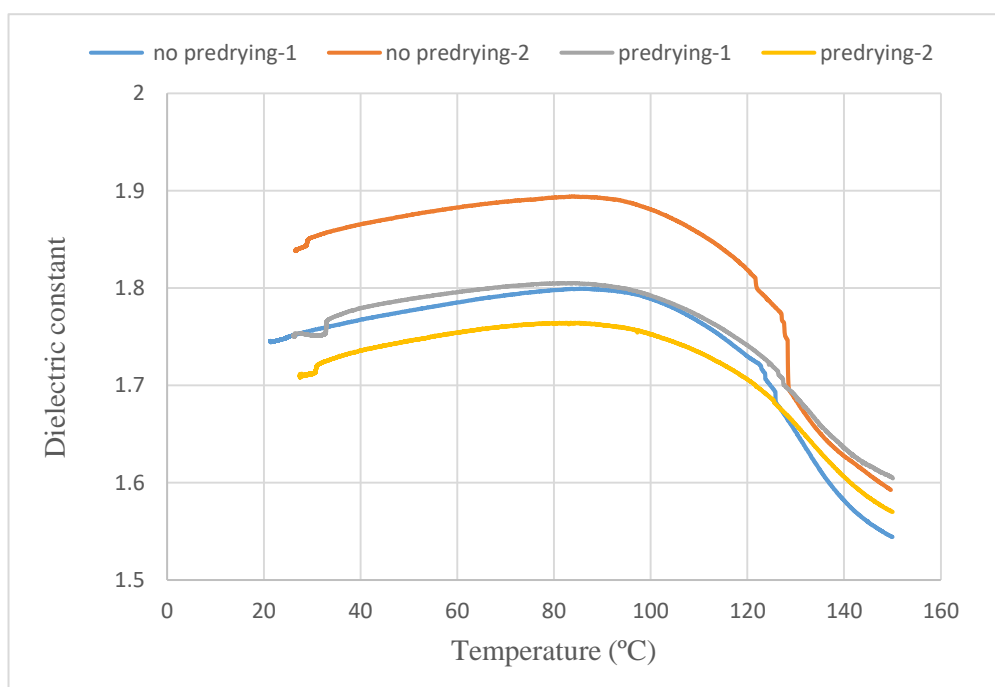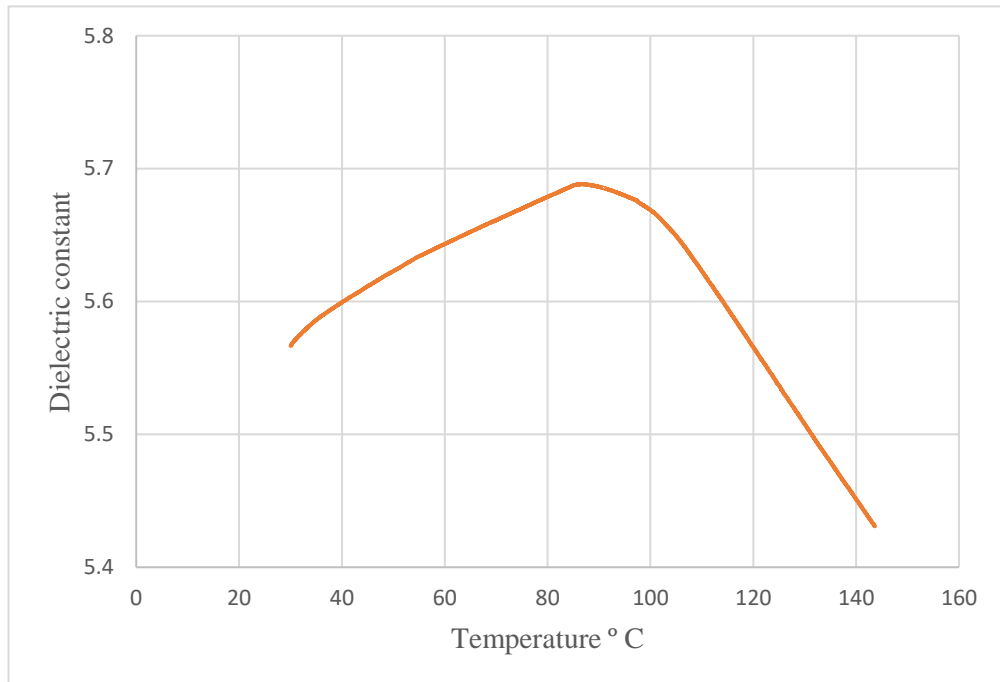

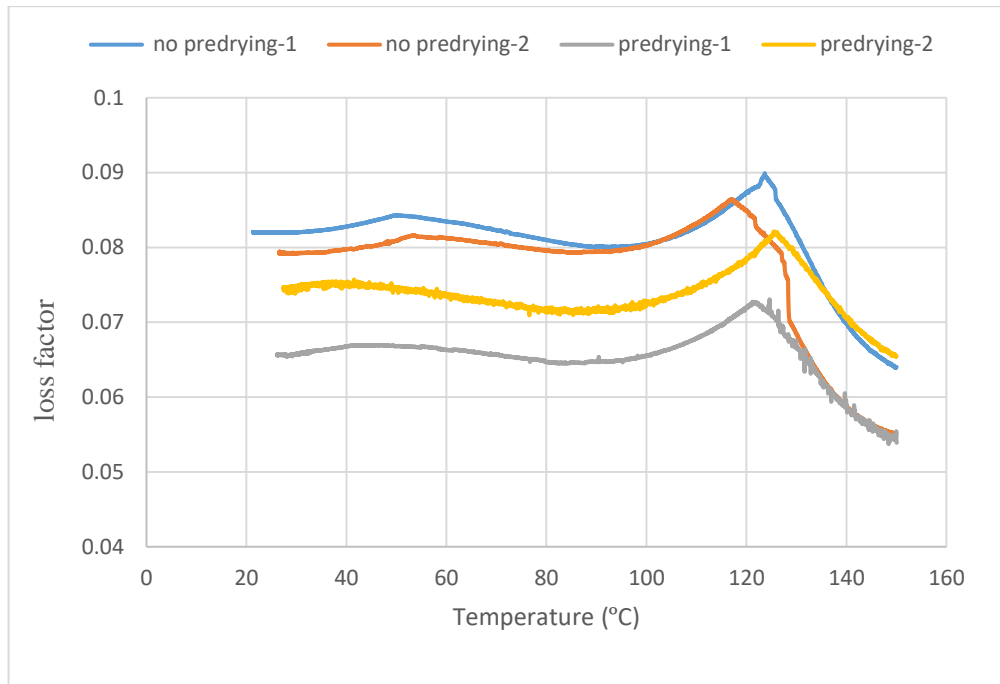Figure 6-20 Real component of complex permittivity vs. temperature of coal 3
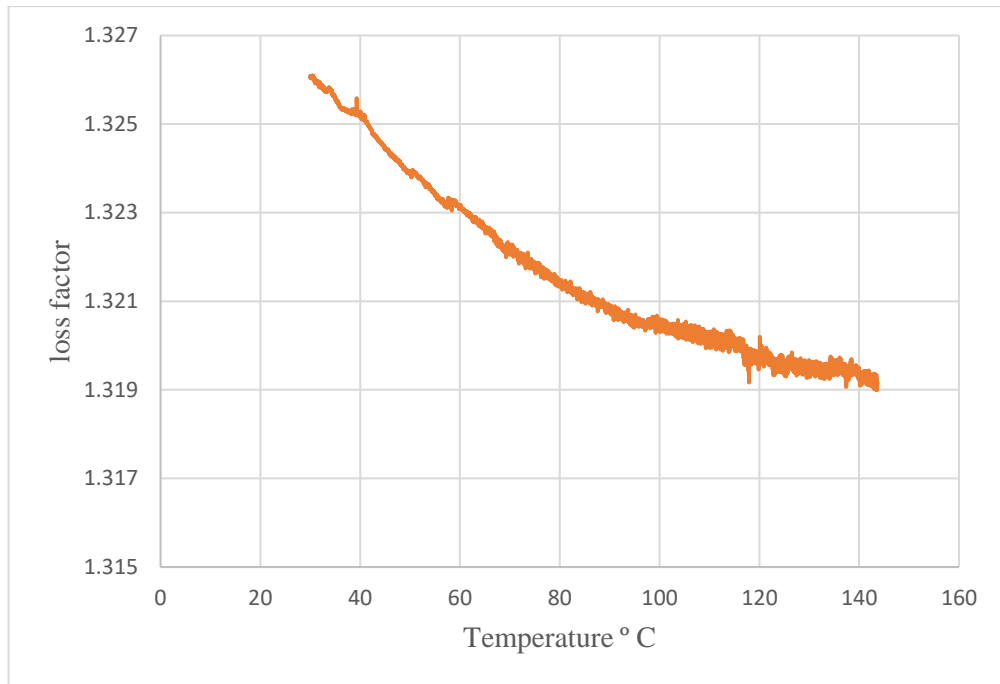
Figure 6-21 Imaginary component of complex permittivity vs. temperature of coal 3
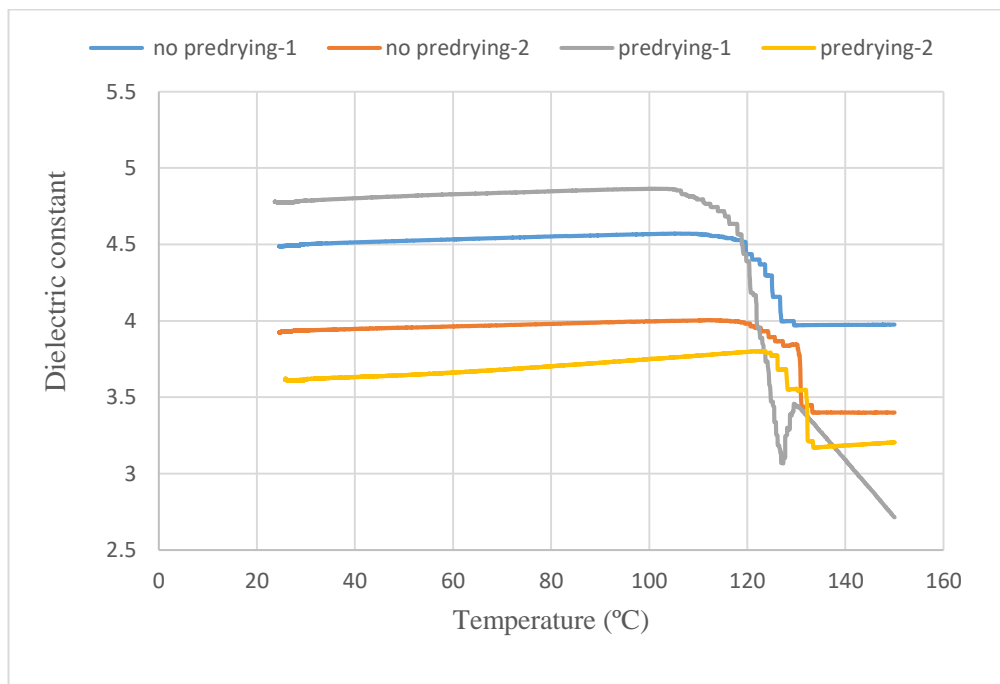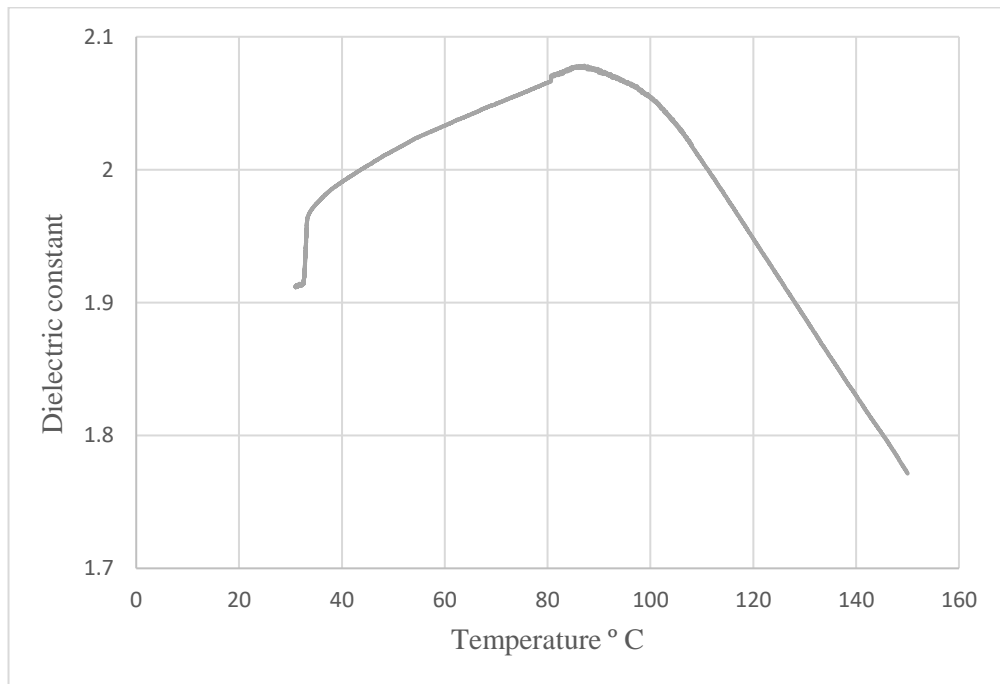

Figure 6-22 Real component of complex permittivity vs. temperature of coal 5
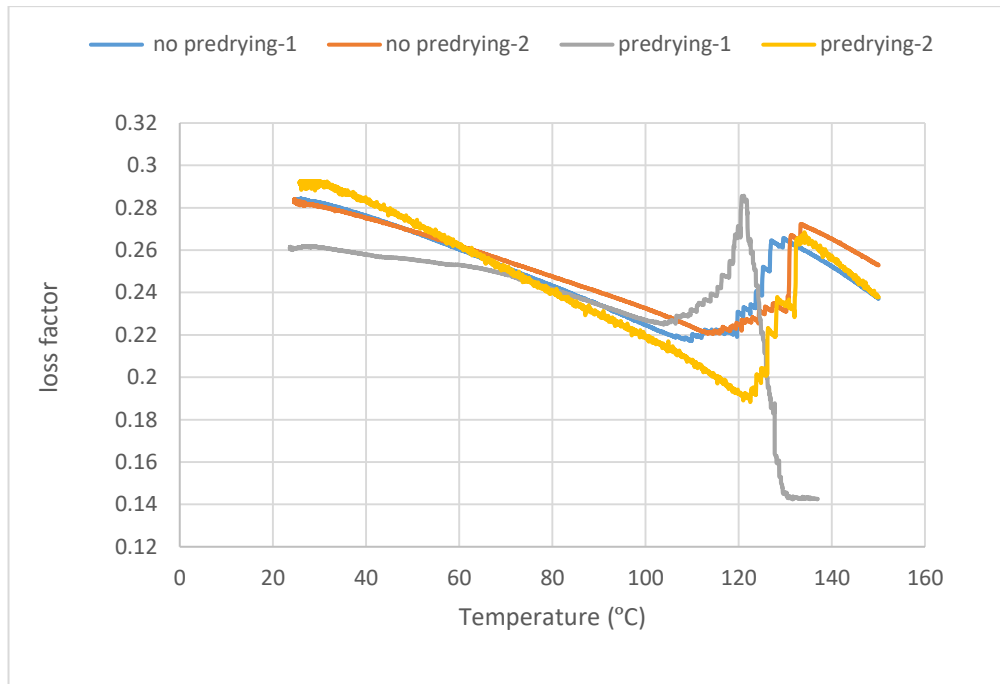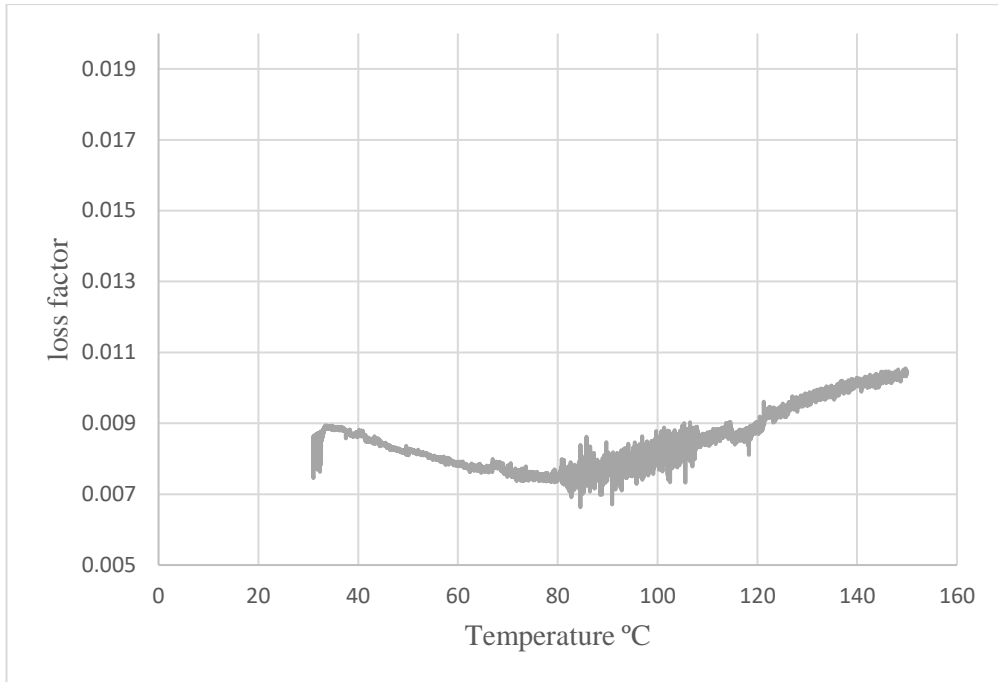
Figure 6-23 Imaginary component of complex permittivity vs. temperature of coal 5
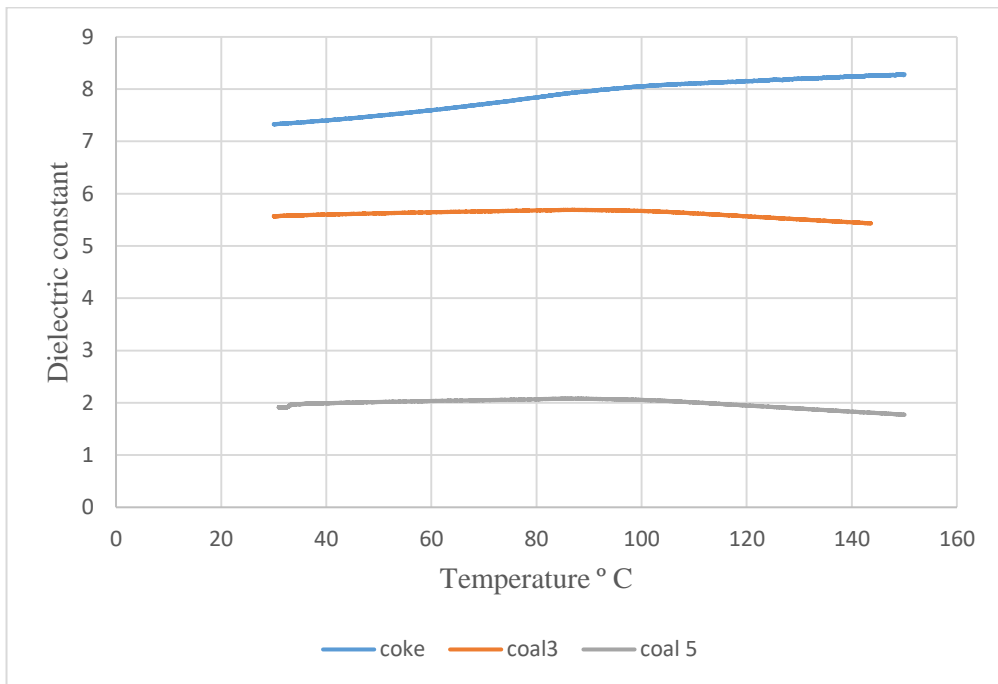
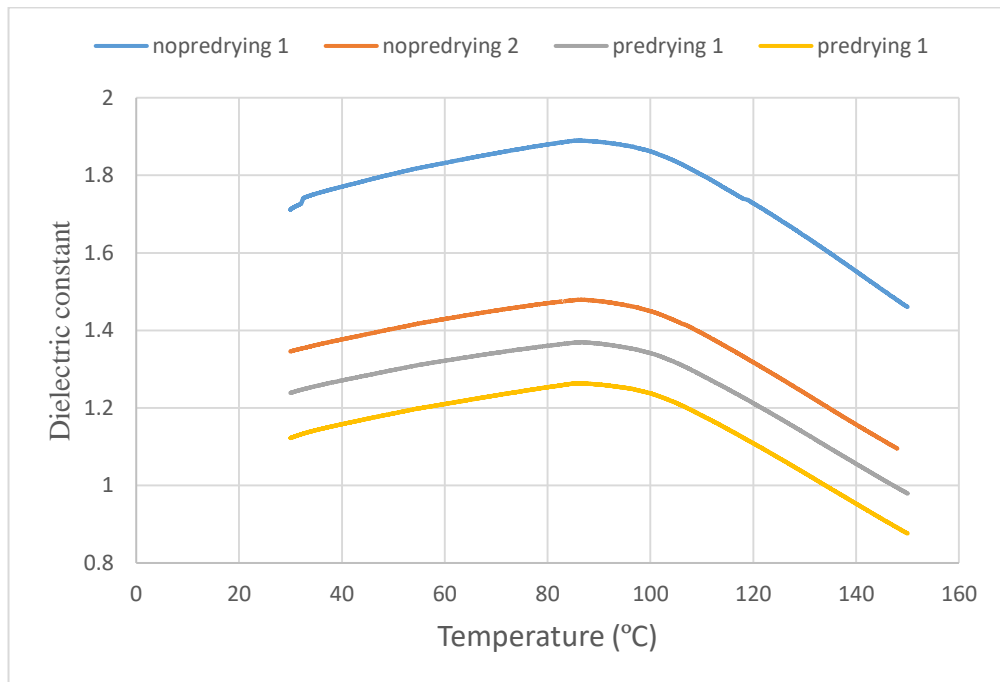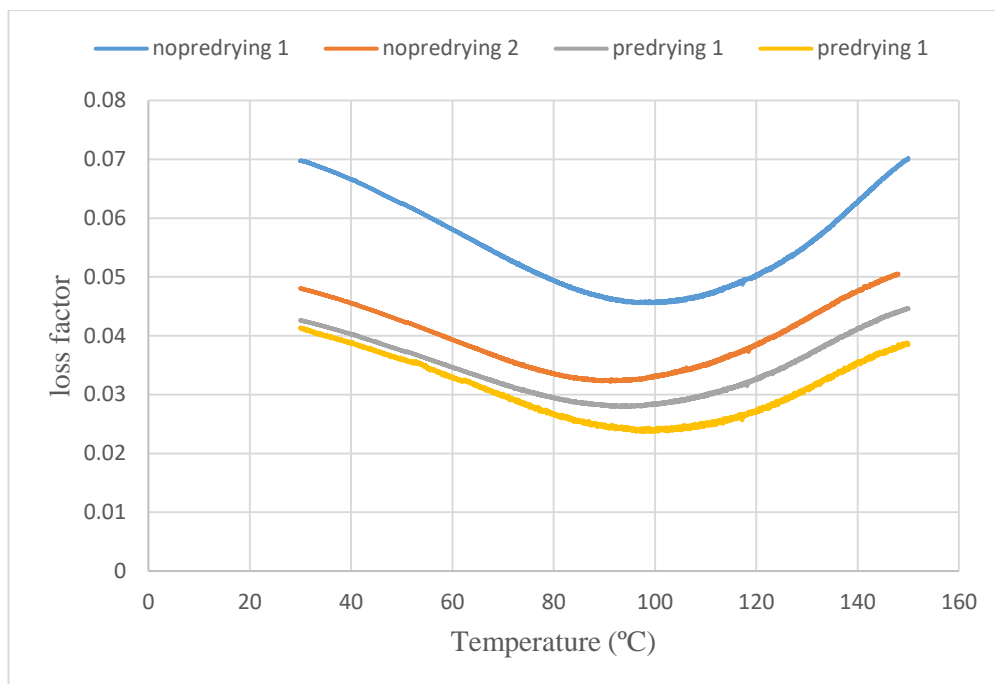
Figure 6-24 Real component of complex permittivity vs. temperature
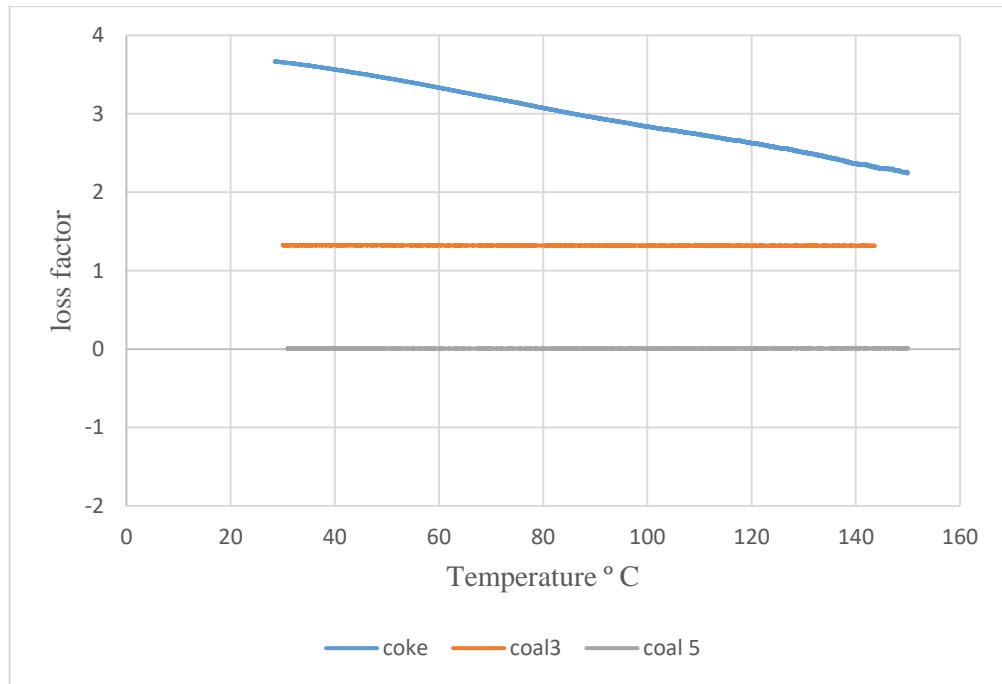
Figure 6-25 Imaginary component of complex permittivity vs. temperature

6.5 Cavity system for dielectric measurements of saturated AC

One of the most important technologies used to reduce the climate change is Carbon dioxide capture and storage (CCS), as the coal is main raw-material for energy production. In coal post-combustion capture technology, CO_2 is separated from a diluted flue gas stream which contains normally around 12-15% CO_2, at ambient pressure and at temperatures of 40-100°C. There is a need for new adsorption technologies that have a high operating flexibility and low costs. Additionally, effective techniques for regeneration systems are required for ensuring multiple reuse of adsorbent materials and reducing energy consumption [115-117].

There are two main methods for desorption in laboratory and industrial applications: Pressure Swing Adsorption (PSA) and Temperature Swing Adsorption (TSA). The difference between both technologies is the method for regeneration of the adsorbent after the adsorption process. In PSA applications, the pressure of the bed is reduced, whereas in TSA, the temperature is raised while pressure is maintained approximately constant [118-120].

Activated carbons are one class of carbonaceous adsorbents that use CO_2 capture, due to their wide availability, low cost, high thermal stability and low sensitivity to moisture [118, 119, 121].

In these experiments, activated carbon in the form of granular manufactured by Cabot Corporation was used. The size of the particles of AC was around 210-595μm, and the surface area was 1513.9 m²/g and pore diameter about 1.2 nm [15]; particles were dried in a lab oven at 110 °C for 12 h and stored in a desiccator before using in the relevant experiments.

The same granular AC samples were crushed as previously into fine powders (section 4.3). The adsorption of water vapour was done in a very simple way by putting the sample close to boiling water for ten minutes, then performing the microwave characterization using the same cavity system and laboratory oven. Experiments were conducted using the same system as illustrated in Figure 6-3. The complex permittivity of the water-saturated samples were measured over the temperature range of 30ºC -150ºC, and the results are illustrated in Figure **6-26** and Figure **6-27**. The dielectric constant decreases considerably between 80ºC and 150ºC, correlated to the expected drying of the sample. The associated dielectric loss factor of the water-saturated, granular AC is shown in Figure **6-27** and this also decreases with temperature.

To attempt to saturate the AC samples with carbon dioxide, granular activated carbon (GCN3070) was filled in quartz tubes, with glass wool frits used at both ends of the quartz tube to support the AC samples. First, 5g samples of granular AC were dried in the laboratory oven at 110ºC for 2 hours. Next, a CO_2 stream was passed through the sample at room temperature and atmospheric pressure for 1 hour, at a flow rate of 1 litre/min. Two granular AC samples were measured using cavity resonator system using the TM_{010} mode at 2.498GHz.
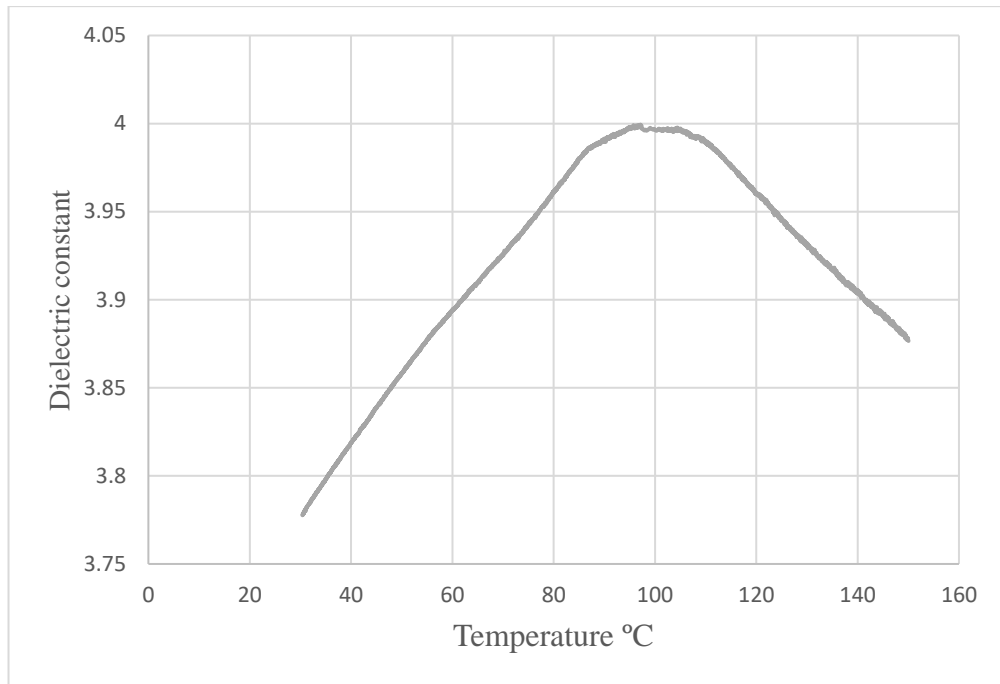
Figure 6-26 Real component of complex permittivity of AC sample saturated with water
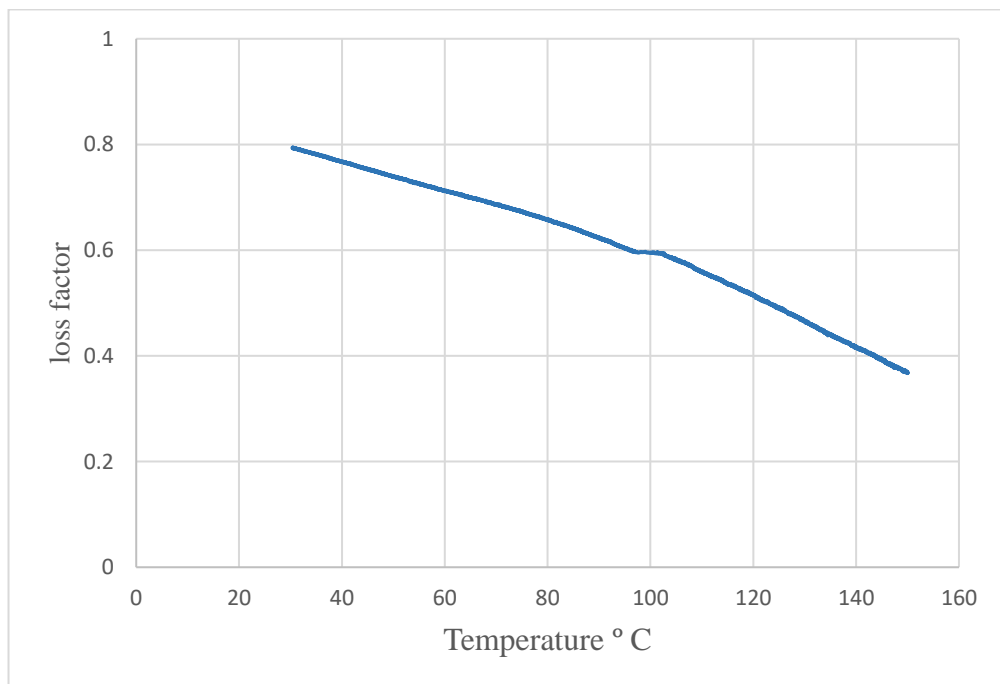
Figure 6-27 Imaginary component of complex permittivity of AC sample saturated with water

Figure 6.28 and Figure 6-29 show the time-dependent dielectric constant and dielectric loss factor of two granular AC carbon samples. The changes in dielectric constant and loss factor of both samples are small, implying little desorption of CO_2 at room temperature, even for the highly porous structure of AC.
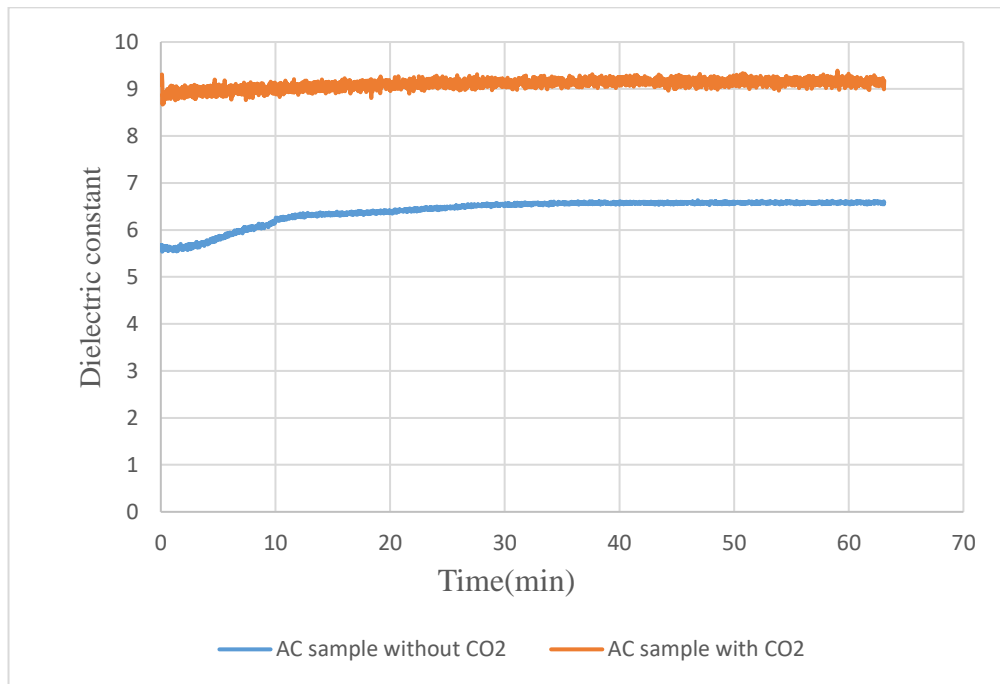
Figure 6-28 Real component of complex permittivity of AC sample saturated with CO_2
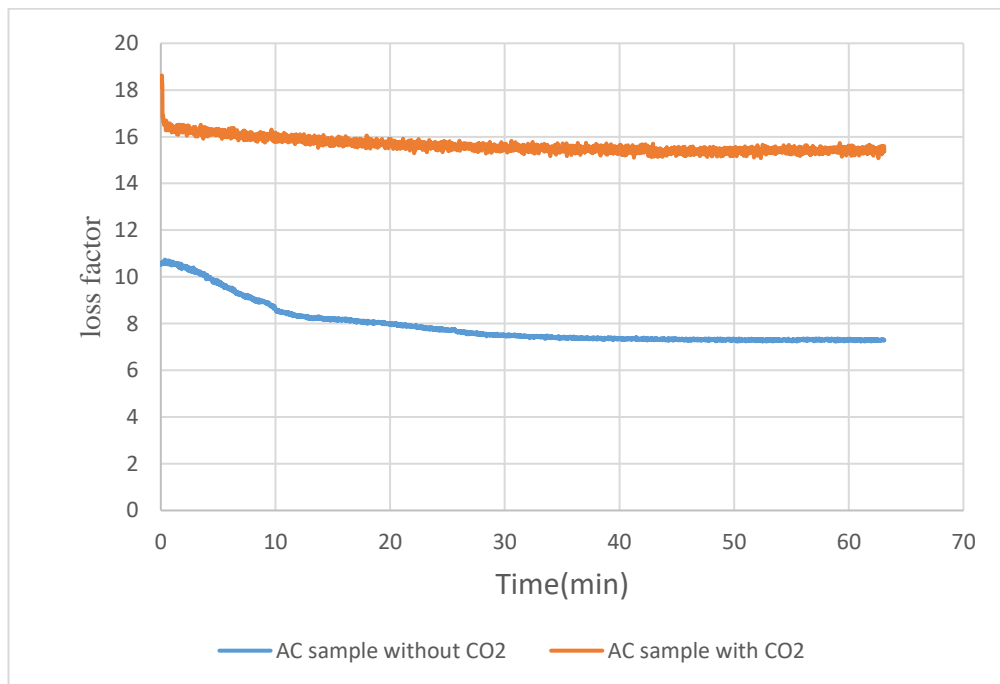
Figure 6-29 Imaginary component of complex permittivity of AC sample saturated with CO_2

6.6 Conclusion

In this chapter the potential for the use of microwave cavity techniques for the measurement of the temperature-dependent dielectric properties of activated carbons and carbonaceous materials contained in BFD at microwave frequencies are presented. The TM_{310} mode was used as a nodal mode for temperature correction of the TM_{010} measurements. The dielectric properties of both groups of carbons were measured within the temperature range between 30ºC and 150ºC. Measurements were recorded using a LabVIEW program. The measurements show that the dielectric constant variations with temperature for most samples exhibit a significant decrease between 80ºC and 150ºC, except for the coke sample, whose dielectric constant increases with temperature. This decrease in the dielectric constant might be related to the drying of the samples, as moisture removal would decrease both dielectric constant and loss factor.

The measurements of activated carbons have high practical relevance in the use of cavity perturbation as a means of characterising the dielectric properties prior to (or simultaneous with) the use of microwave heating in order to regeneration exhausted activated carbon. Additionally, the results demonstrate the potential for this technique to differentiate the carbonaceous materials contained in BFD at different temperatures in order to combine the microwave system with blast furnace to allowing the real-time monitoring of complex permittivity of coal, char, and coke in BFD.

Finally, it is worth noting that the sudden change in dielectric properties of activated carbons when undergoing microwave characterisation, associated with explosive ejection of the powder samples, is not seen in the BFD materials. This uniqueness to activated samples, with their large surface areas and porous nature, is currently unexplained, but has been observed for the first time in this thesis. It is worth noting that this effect only occurs when microwaves are applied. Similar experiments on the same samples heating to the same temperatures with just the oven (and no microwaves applied) show no such ejection. This is consistent with the lack of changes observed in the thermogravimetric data of Figure 6-20. The microwave power levels for the cavity perturbation experiments here are very low, at 0 dBm (i.e. 1 mW rms). For them to have such a dramatic effect implies an extreme microwave coupling to an explosive phenomenon which may have important consequences for the use of microwaves in the regeneration of such samples when used, for example, in carbon dioxide capture.

Chapter 7 Conclusion and future work

This chapter summarises the main conclusions, discusses the relevant challenges that have been faced during the research, and finally provides suggestions for future work and possible improvements that can be implemented. This thesis has focused on using microwave techniques in characterizing and differentiating types of carbons. In this respect, two groups of carbonaceous materials have been characterized.

7.1   Literature Survey:

Chapter 2 gives a survey of the properties and applications of activated carbon materials, blast carbon materials contained in furnace dust. The initial proposal of this research is to design and build microwave cavity system and broadband coaxial probe applicator to measure dielectric properties of these materials, in order to characterize and differentiate these materials over range of frequencies and under temperature range between 30ºC and 150ºC.

7.2   Analysis: Microwave Systems Principles

Chapter 3 gives an explanation on the microwave cavity system and how they work. The relevant equations for the microwave cavity perturbation method are presented, with an original expression for the theoretical bandwidth for TM modes. A variety of different modes with different frequencies have been identified for measuring the frequency dependent dielectric properties. A circuit model is also presented which is important for understanding how to take measurements. Additionally, Principles and design of the coaxial probe system are presented, with details of the chosen model which used to extract complex permittivity from the measured data.

7.3   Experiments

Chapter 4 The microwave cavity system in this chapter has been shown to have high measurement accuracy for both carbon groups. Even when the samples are from the

same materials treated differently such as samples AC2 and AC3, the system are capable of differentiate the samples.

Chapter 5 This study shows that multi-mode microwave cavity can be used to estimate the microwave dielectric properties of carbons contained in BFD at the discrete set of resonant frequencies in the 2 to 10 GHz range. TM modes were used. Moreover, broadband measurements of dielectric properties of both carbon groups were presented and the results show that both the multimode cavity and open-ended coaxial probe methods are appropriate to be used as test methods for identifying and differentiating the different types of carbons based on the frequency dependence of their dielectric properties.

Chapter 6 gives an explanation of how to use microwave cavity resonator to measure the temperature dependent dielectric properties of samples. A procedure for the correction of systematic temperature fluctuations using higher order cylindrical modes is detailed. Analytically, the temperature dependent resonant frequency and bandwidth of all modes are linked, respectively, through the thermal expansion coefficient and the coefficient of resistivity. In practice, offsets in these coefficients exist across the modes. The relationship between each of the modes, however, is constant and thus this procedure should only be used to remove systematic fluctuations in the conducted experiment.

7.4   Characterization of activated carbon materials

The dielectric complex permittivity of activated carbons has been measured using both microwave cavity and coaxial probe techniques to represent and quantify the differences between different AC materials that have been produced from different precursors and had different treatments.

7.5   Characterization of types of carbon contained in BFD

Microwave cavity and coaxial probe techniques have been used for measuring the dielectric complex permittivity of carbonaceous materials contained in BFD. This characterization of these materials is required to differentiate the different forms of carbonaceous materials from the raw materials coke and coal. The differentiation of

these types of carbons in the blast furnace dust is important to quantify the utilization of coal injected in the furnace and determine the efficiency of coal injection.

7.6   Further Work

In this research, attempts have been made to comprehensive characterization of different types of carbons by measuring the change in complex permittivity with frequency and temperature. With regard to the activated carbon materials, more microwave heating experiments are suggested to regenerate or recycle the loaded activated carbons.

7.6.1   Microwave regeneration of saturated activated carbons

In order to try to develop microwave system to regeneration of activated carbons, a cylindrical cavity at lower centre frequency has already been designed using COMSOL Multiphysics software shown in Figure **7-1**. The cavity is designed to have its TM_{010} mode at a frequency of 900 MHz and TM_{010} mode, so the cavity's inner radius should be 128 mm. A mode chart is used to choose an appropriate length of cavity based on the ratio $\left(2a/d\right)^2$ to ensure that there is no interference between the TM_{010} mode and TE_{111}; this results in the cavity's inner height being chosen to be 200 mm. It should be noted that 900 MHz is an ISM frequency, at which there are a number of cost-effective power amplifiers for generation of high microwave powers up to 1 kW. The larger cavity volume permits larger sample volumes, in this case up to a few cm^3, depending on the loss factor of the samples.

The cavity is constructed from three parts: cavity body, the bottom lid and the side piece to place the coupling connector. Aluminium is chosen for the cavity's metal, since it is easy to machine, cheap and has low mass compared with copper, even though the Q factor is only sacrificed by about 25%.
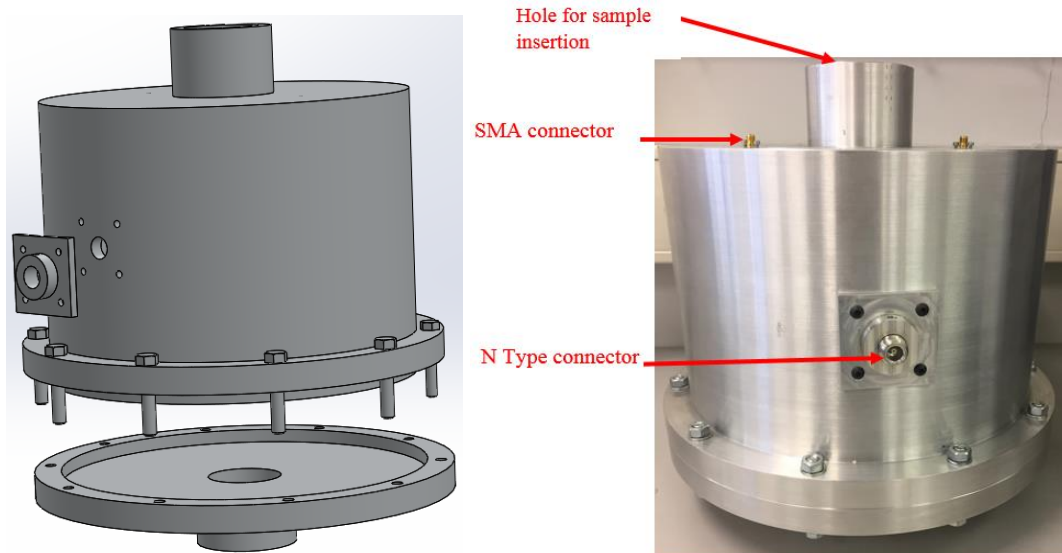
Figure 7-1 the large aluminium cylindrical cavity resonator.

The coupling loop is designed on the middle of the side of cylindrical metal wall, and it is shown in **Figure 7-1**. The radius of coupling loop in the simulations is 5 mm and the radius of the coupling loop in the practice is 25 mm. There are two types of coupling used; SMA connectors at the top of the cavity allow cavity perturbations in the usual way, to study dielectric properties of a sample; the side-wall N connector allows high power to be pumped into the cavity, so that in principle samples can be simultaneously heated and characterized.

7.6.2   Electric fields distribution

Figure **7-2** shows the electric field distribution for the TM_{010} mode in this large cylindrical cavity, including the 5 cm diameter sample hole which acts as a microwave choke. These are calculated and plotted using COMSOL software. The intensity of electric field decreases from the cavity centre to the boundary walls, where it is reduced to zero.
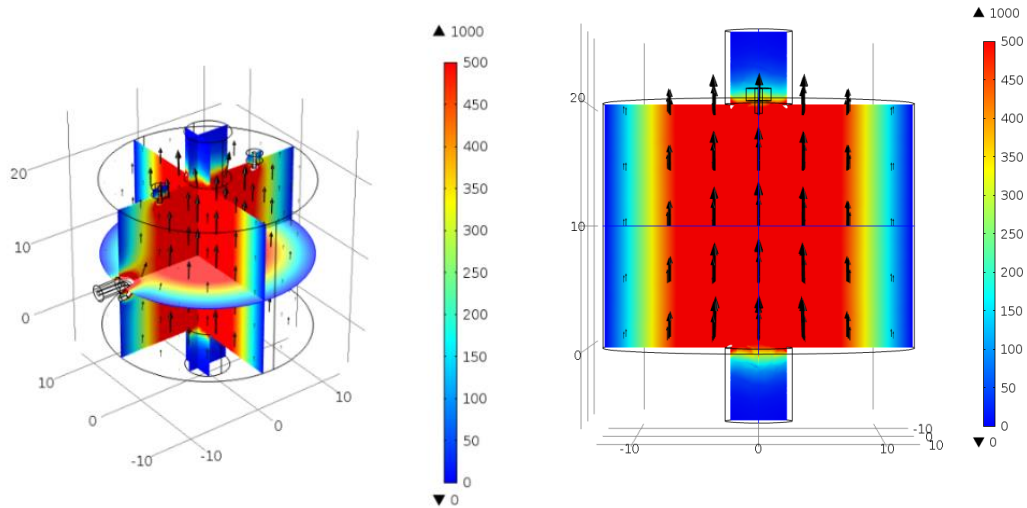
Figure 7-2 Electric field distribution of a 900MHz cavity operating in the TM_{010} mode

7.6.3 Microwave excitation system

A high power system was designed to deliver high power microwave at both frequencies of 2.45 GHz and 900 MHz, for both small and large cavities used in this thesis. Figure 7.3 illustrates a circuit diagram of the system. It consists of a microwave generator which provides an rms output at a power level of 1mW to the input of the high power amplifier for cavity excitation. The system set up for experiments is shown in **Figure 7-3** and **Figure 7-4**.
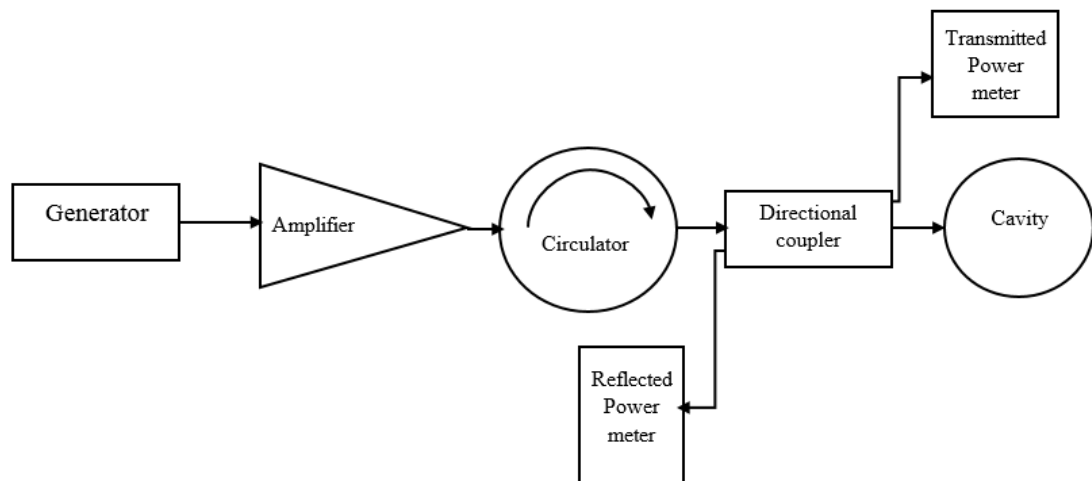
Figure 7-3 Schematic of the whole microwaving system using the large cavity
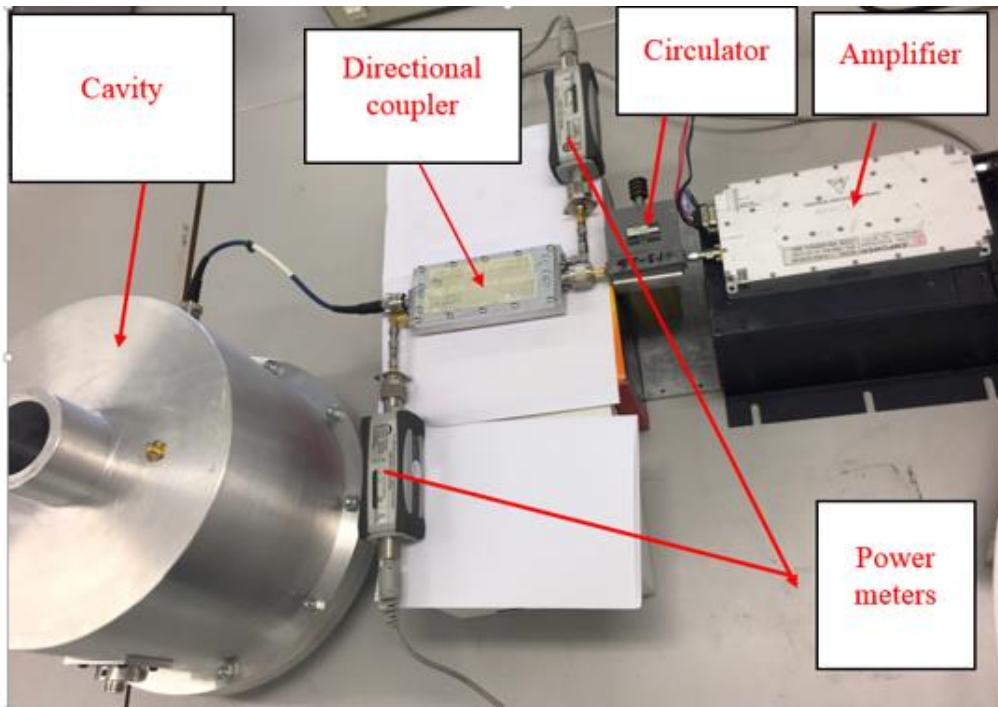
Figure 7-4 System set up ready for measurement

APPENDIX A Durometer Conversion Chart

MR MECHANICAL RUBBER

Durometer* Conversion Chart

Approximate Hardness Value
(to be used as a guide)

Type	Extra Soft / Soft (Chewing Gum)			Medium Soft (Pencil Eraser)			Medium Hard (Windshield Wiper Blade)							Hard (Skate Wheel)			Extra Hard (Bowling Ball)		
Shore A Rubber, Soft Plastic & Polyurethane		10	15	20	25	30	35	40	45	50	55	60	65	70	75	80	85	90	95	100
Shore B** Rigid Rubber				6	12	17	22	27	32	37	42	47	51	56	62	66	71	76	81	85
Shore C** Rubber & Plastic					9	12	14	17	20	24	28	32	37	42	47	52	59	70	77
Shore D Hard Rubber & Plastic					6	7	8	10	12	14	16	19	22	25	29	33	39	46	58
Shore O** Soft Rubber	8	14	21	28	35	42	48	53	57	61	65	69	72	75	79	84			

Type	Soft (Slice of Bread)				Med. Soft (Seat Cushion)			Med. Firm (Mouse Pad)						Firm (Tennis Ball)	
Shore OO Sponge	45	55	62	70	76	80	83	86	88	90	91	93	94	95	97	98

Type	Very Soft (Slice of Bread)	Extra Soft (Pillow)	Soft (Mattress)	Firm (Tennis Ball)	Extra Firm (Styrofoam Cup)	Very Firm (Life Preserver)
Density Foam	0 - 2 PSI 0 - 14 kPa	2 - 5 PSI 14 - 34 kPa	5 - 9 PSI 34 - 62 kPa	9 - 13 PSI 62 - 89 kPa	13 - 16.5 PSI 89 - 114 kPa	16.5+ PSI 114+ kPa

*Durometer is the standard for hardness measurement of rubber, plastic, sponge & non-metallic material.

** Not commonly used

www.mechanicalrubber.com

137

APPENDIX B Published paper 1

https://pubs.acs.org/doi/pdf/10.1021/acs.langmuir.6b02013

New Routes to Functionalize Carbon Black for Polypropylene Nanocomposites

Céline Shepherd,[†] Emina Hadzifejzovic,[†] Fatma Shkal,[§] Kerstin Jurkschat,[‡] Jonathan Moghal,[‡] Emily M. Parker,[†] Montree Sawangphruk,[∥] Daniel R. Slocombe,[§] John S. Foord,[†] and Mark G. Moloney*,[†]

[†]Department of Chemistry, Chemistry Research Laboratory, University of Oxford, Mansfield Road, Oxford OX1 3TA, United Kingdom

[‡]Department of Materials, University of Oxford, Parks Road, OX1 3PH Oxford, United Kingdom

[§]School of Engineering, Cardiff University, The Queen's Buildings, The Parade, Cardiff CF24 3AA, United Kingdom

[∥]Department of Chemical and Biomolecular Engineering, School of Energy Science and Technology, Vidyasirimedhi Institute of Science and Technology, Rayong 21210, Thailand

S *Supporting Information*

ABSTRACT: Methods for chemical surface functionalization for carbon black (CB) nanoparticles were studied to produce (CB)/polypropylene (PP) nanocomposites with superior electrical and thermal properties. Nanoparticle dispersion is known to directly control the extent to which nanocomposites maximize the unique attributes of their nanoscale fillers. As a result, tailored nanoparticle surface chemistry is a widely utilized method to enhance the interfacial interactions between nanoparticles and polymer matrices, assisting improved filler dispersion. In this work, a rapid chemical functionalization approach using a number of diarylcarbene derivatives, followed by the azo-coupling of substituted diazonium salts, for the covalent introduction of selected functional groups to the CB surface, is reported. Characterization of the modified CB by XPS, TGA, CHN, and ATR-IR collectively confirmed surface functionalization, estimating surface grafting densities of the order of 10^{13} and 10^{14} molecules/cm^2. Nanocomposites, synthesized by solvent mixing PP with pristine and modified CB, demonstrated macroscopic property changes as a result of the nanoparticle surface functionalization. Pronounced improvements were observed for PP nanocomposites prepared with a dodecyl-terminated diaryl functionalized CB, in which TEM analysis established improved nanofiller dispersion owing to the enhanced CB-PP interfacial interactions in the nanocomposite. Observed dielectric relaxation responses at 20 wt % loading and a reduced percolation threshold realized conductivities of 1.19×10^{-4} S cm^{-1} at 10 wt %, compared to 2.62×10^{-15} S cm^{-1} for pristine CB/PP nanocomposites at the same filler loading. In addition, thermal properties signify an increase in the number of nucleation sites by the raised degree of crystallinity as well as increased melting and crystallization temperatures.
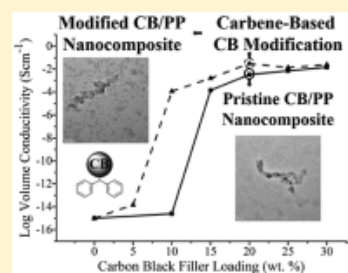
■ INTRODUCTION

Nanocomposites exploit the unique properties of both nanomaterials and polymers and are emerging as an important class of multifunctional materials with superior electrical,[1] thermal,[2] mechanical,[3] optical,[4] and antibacterial[5] functionalities. Nanocomposites therefore exhibit substantial potential for applications in electrical, automotive, and aerospace industries.

It is widely acknowledged that polymer nanocomposite properties are dependent upon a multitude of factors. First, the method used to prepare the nanocomposite will directly influence the interfacial interactions between the nanofiller and polymer matrix. Typically, nanocomposites are prepared by melt compounding, solvent blending, or in situ polymerization methods.[6,7] Second, the chemistry of the selected polymer, including its polarity, degree of crystallinity, and viscosity, all contribute to the control of the overall nanocomposite properties.[8] Equally, the surface area, specific surface chemistry, porosity, aspect ratio, and morphology of the selected nanofiller will further dictate the performance of the polymer nanocomposites.[9] In particular, a key property of CB in nanocomposite technology is the "structure" of the CB. This term describes the size and shape of the CB aggregates, which are defined units of fused primary CB nanoparticles. It is the presence of CB aggregates in polymer nanocomposites which enables electrical conductivity at lower loadings than are otherwise predicted for a system with separate primary spherical particles.[10] However, attractive van der Waals interactions between aggregates and poor compatibility of the filler with the polymer matrix promotes the formation of CB

Scheme 1. Route A Synthesis and Two-Step CB Surface Modification[a]

[a]**Conditions:** (i) NH$_2$NH$_2$.H$_2$O, EtOH, reflux, 72 h; (ii) HgO$_2$, KOH, EtOH, RT, overnight; (iii) 120 °C; (iv) Soak in EtOH 5 °C, overnight. Diazonium salts 3a-b synthesized from corresponding amines by reaction with isoamyl nitrite, HBF$_4$, EtOH at 0 °C, 1 h.

Scheme 2. Route A Synthesis of Diazonium Salts for Diazonium Coupling onto Prefunctionalized CB_2[a]
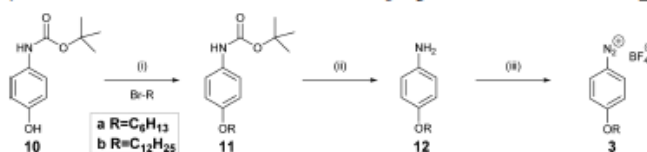
[a]**Conditions:** (i) MeCN, K$_2$CO$_3$ reflux; (ii) TFA:DCM 1:6; (iii) isoamyl nitrite, HBF$_4$, EtOH at 0 °C, 1 h.

Scheme 3. Route B Synthesis and One-Step CB Surface Modification[a]
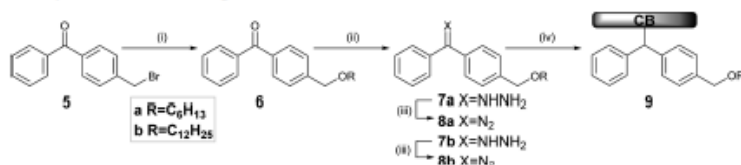
[a]**Conditions:** (i) NaH, ROH, THF, Stir, 18 h; (ii) NH$_2$NH$_2$.H$_2$O, EtOH, reflux, 18 h; (iii) MnO$_2$, KOH, MeOH, RT, overnight; (iv) 120 °C.

superagglomerates. This is unfavorable for higher performance nanocomposites as high filler loadings are required to achieve electrical conductivity in the polymer nanocomposite, compromising the attractive innate mechanical and processability properties of the original polymer.[11]

Particle functionalization has therefore been employed as a versatile and useful strategy in nanocomposite technology, both for the improvement of the filler-matrix interfacial interactions as well as the inhibition of unfavorable aggregate agglomeration, thereby improving the dispersion of the nanofiller.[12] In the study reported here-in, nanocomposites prepared using polypropylene (PP), selected as a widely used commodity thermoplastic, and carbon black (CB), a convenient, inexpensive conductive amorphous carbon nanofiller, were explored to determine if chemical surface functionalization can lead to enhanced electrical and thermal nanocomposite properties. CB was modified using diarylcarbene derivatives with different substitutions to tailor the surface chemistry of the nanofiller. Previously, diarylcarbene derivatives have provided a direct, versatile method for the irreversible introduction of desired functionality into materials. Examples include the surface modification of single walled carbon nanotubes (SWCNTs),[13] fullerenes,[14] hydrogen-terminated diamond,[15] and silica[16] as well as a comprehensive range of polymers.[17,18] This approach permits changes to the surface chemistry, which allows for the introduction of color,[19] biocidal activity,[20] biocompatibility,[21] as

well as wettability.[22] We have used two diarylcarbene functionalization approaches to modify CB nanoparticles: Route A used a two-step approach to introduce detectable nitrogen functionality as well as steric-stabilizing hexyl and dodecyl hydrocarbon chains to the surface. Route B used a one-step approach as a target synthesis for the direct introduction of a hydrocarbon-terminated diaryl unit onto the CB. Subsequently, Route B modified CB/PP nanocomposites were prepared to investigate the effect of the CB chemical functionalization upon the interfacial interactions in the polymer matrix and any concomitant altered macroscopic properties.

■ EXPERIMENTAL SECTION

Materials. Commercial Monarch CB (CB, M 430) was supplied from Cabot Corporation (Billerica, MA). The CB possessed a primary particle size of 27 ± 10 nm diameter, density 1.1–1.9 g/cm^3 (manufacturer's data), and a BET surface area 72.5 m^2/g. Commercial grade polypropylene (PP, 2440TC polypropylene copolymer with ethylene as comonomer, MFI 55 g/10 min) was provided by IRPC Ltd., Thailand. All other reagents were used as supplied from Alfa Aesar Chemicals Ltd., Sigma-Aldrich Chemicals and Lancaster Chemicals Ltd.

Nanoparticle Functionalization. CB nanoparticles were functionalized in Route A using diaryldiazo derivatives followed by a diazonium coupling reaction (Scheme 1).

Route A used bis(4-(dimethylamino)phenyl)diazomethane as a first step to functionalize the CB to produce modified **CB_2**. This

139

diaryldiazo compound was prepared from the commercially available Michler's ketone in a two-step synthesis, via conversion to the hydrazine product, as previously reported.[18] For the modification step, diazo 1c was dissolved in Et₂O and sonicated with addition of the CB nanoparticles, after which solvent evaporation in vacuo afforded the diazo compound physisorbed onto the CB surface. Thermal decomposition of the labile diazo precursor generated the transient carbene and dinitrogen, and the in situ generated carbene irreversibly modified the CB surface. When cool, the modified CB nanoparticles were washed thoroughly with acetone (500 mL) and dried for 1 h in vacuo. The surface of modified **CB_2** was further manipulated using diazonium coupling reactions by treatment with hydrocarbon-terminated diazonium salts 3a−b (Scheme 2).

The diazonium salts 3a−b were prepared by reaction of *tert*-butyl-(4-(hexyloxy)phenyl) carbamate 10 with the required alkyl bromides followed by BOC removal, to generate the aniline products, 12a−b. Reaction with isoamylnitrite in tetrafluoroboric acid produced the corresponding diazonium salts and their presence was confirmed using the H-acid test.[17] **CB_2** was added to the in situ generated diazonium salts solutions and the mixture left overnight before washing with acetone and drying in vacuo, to generate two-step modified **CB_4a** and **CB_4b**, possessing terminal hexyl and dodecyl groups, respectively.

Route B (Scheme 3) permitted the introduction of the steric stabilizing alkyl chains in a four-step synthesis, using a more direct route by a single diazo modification to functionalize the CB nanoparticles.

Williamson ether reaction with 4-bromomethylbenzophenone and hexanol or dodecanol generated hydrocarbon-terminated diaryl ketocompounds 6a−b and following treatment with hydrazine monohydrate, afforded the subsequent hydrazone derivatives 7a−b. Oxidation with manganese dioxide produced the target diazo compounds, which were reacted with CB to give functionalized **CB_9a** and **CB_9b**, that is, with hexyl and dodecyl terminating groups, respectively. Detailed preparation and characterization data of the synthesis of the diazo compounds and diazonium salts is included in the Supporting Information.

Nanoparticle Characterization. Thermogravemetric analysis (TGA) and differential scanning calorimetry (DSC) was conducted using a PerkinElmer Simultaneous Thermal Analyzer, STA6000. Experiments were performed under nitrogen and samples (~12 mg) were loaded in an alumina preconditioned pan. For carbene insertion analysis, the sample was heated at a ramp rate of 10 °C min⁻¹ and a sigmoidal baseline was used to evaluate the reaction enthalpy. For nanoparticle analysis, samples were heated from 30−850 °C at a ramp rate of 20 °C min⁻¹.

Combustion analysis (CHN) of 5 mg samples was conducted by MEDAC Ltd.

X-ray photoelectron spectroscopy (XPS) samples were prepared in a pellet press and affixed to the sample stub using double-sided carbon tape. Analysis was performed using a VG - Escalab X-ray Photoelectron Spectrometer VGX900 using Al Kα radiation with an energy of 1486.6 eV at an operating pressure <1 × 10⁻⁸ mBar. The Pass Energy was set at 50 eV for the wide scan of the sample and 20 eV for scans of specific areas: C 1s, N 1s, and O 1s. Casa XPS peak fitting software was used to analyze spectra and a reference charge correction of 284.5 eV for C 1s used.[23] The area under the elemental peaks and standard sensitivity factors (C, 1; O, 2.93; N, 1.8)[24] were used to calculate relative percentage elemental abundance within the surface and near-surface sampling depth of the XPS.

Attenuated total reflectance-infrared spectroscopy (ATR-IR) was conducted using a Bio-Rad FTS-6000 Fourier Transform Infrared Spectrometer fitted with DuraSamplIR Diamond ATR accessory. Nanoparticle samples were screwed into position using the compression tip on the diamond accessory and the spectra collected with a resolution of 0.25 cm⁻¹ from 6000−700 cm⁻¹ as the sum of 256 scans.

BET Brunauer-Emmett-Teller (BET) surface area analysis was performed at −195.9 °C by nitrogen sorption experiments using a Micromeritics Tristar II PLUS surface area and pore size analyzer.

Before analysis, samples (~0.8 g) were heated at 200 °C overnight using a Micromeritics VacPrep 061 sample degas system.

Nanocomposite Preparation and Processing. Nanocomposite samples were prepared by solvent mixing methods, adapted from general procedures in the literature.[25−27] PP pellets (0.15 g) were dissolved in toluene (10 mL) under reflux (130 °C) for 30 min. Subsequently, pristine and modified CB at 10, 15, 20, 25, and 30 wt % of PP were added in a hot suspension in toluene (2 mL) to the dissolved PP in toluene. Following 10 min stirring, the PP/CB suspension was sonicated for 30 min in an ultrasonic bath and dried in vacuo. For TEM and dielectric analysis, nanocomposite samples were pressed into films (15 and 50 μm, respectively) using a Specac Film Maker. The selected steel spacer was fitted between two optically polished platens, which held the nanocomposite sample between aluminum foil sheets. Heat and pressure treatment at 170 °C and 0.5 Torr was followed by cooling before removal for analysis.

Samples for conductivity measurements were prepared by compression molding into plaques (1 × 1 × 0.1 cm³) using a hot press (200−190 °C) for 30 min, at a final pressure of 0.5 T.

Nanocomposite Characterization. Nanocomposite plaques were silver pasted[28] on each pair of parallel sides, and the sheet resistance was measured by the two-point probe method using a Keithley Electrometer 617. For highly resistive samples ($R > 10^9$), the bias voltage (20 V) was applied and the resistance calculated from the voltage-current ratio. Dielectric analysis was performed using a PNA-L Vector Network Analyzer N5232 and a flat coaxial reflectance probe with a 1.6 mm aperture. Prepared nanocomposite films (50 μm) were held in place using a PTFE stub to ensure good contact between the probe and samples. The diameter of the center conductor of the coaxial probe was 0.3 mm and the diameter of the outer conductor was 1.6 mm. The samples were each measured more than 50 times, at different positions of the film, in the frequency range 10 MHz to 10 GHz at room temperature.

TEM Samples were prepared from nanocomposite films (15 μm) and imbedded in epoxy for imaging, low to high magnification. Experiments were conducted on a JEOL 2010 analytical TEM, with a LaB6 electron gun operable between 80 and 200 kV. The TEM has a resolution of 0.19 nm, an electron probe size down to 0.5 nm and a maximum specimen tilt of ±10 degrees along both axes. It is equipped with an Oxford Instruments LZ5 windowless energy dispersive X-ray spectrometer (EDS) controlled by INCA.

Differential scanning calorimetry (DSC) was conducted using PerkinElmer Simultaneous Thermal Analyzer, STA6000. For nanocomposite analysis, the samples under nitrogen were subjected to a heating run (30−250 °C), to remove the thermal history, followed by a cooling cycle (250−30 °C), and then heated beyond the decomposition of PP (30−850 °C), at a ramp rate of 20 °C min⁻¹.

RESULTS AND DISCUSSION

Modified CB Characterization. Surface analysis was performed to evaluate the success of the chemical functionalization routes used to modify the CB nanoparticles. Samples prepared by Route A include **CB_2**, directly modified by carbene insertion, and **CB_4a** and **CB_4b**, modified by the two-step process of carbene insertion followed by azo-coupling of diazonium salts terminated with hexyl and dodecyl groups, respectively. Route B prepared samples include **CB_9a** and **CB_9b**, modified by one-step carbene insertion reactions of diaryldiazo complexes terminated in hexyl and dodecyl groups, respectively.

X-ray Photoelectron Spectroscopy (XPS) of Pristine and Modified CB. The main features on the wide spectrum of pristine CB include a dominant C 1s photoemission peak at ~285 eV binding energy and a small O 1s peak at ~532 eV binding energy. The relative elemental abundances which were found are included in Table 1.

Table 1. Chemical percentage composition by XPS and CHN

sample	XPS (%)			CHN (%)		
	C	N	O	C	N	H
pristine CB	98.4	n.d.[a]	1.6	96.5	<0.1[b]	1.2
CB_2	96.5	1.4	2.1	95.3	0.8	1.2
CB_4a	92.7	0.4	6.9	95.2	0.4	0.9
CB_4b	91.8	1.1	7.1	91.8	0.9	1.6
CB_9a	94.4	n.d.	5.6	96.7	<0.1	1.4
CB_9b	97.0	n.d.	3.0	96.2	0.3	1.6

[a]n.d., not detected; the N 1s peak could not be observed by XPS.
[b]The measurable detection limit of CHN is <0.1% N.

Oxygenated functionalities are a characteristic surface component of many types of CB and carboxylic, lactonic and phenolic groups are reported to be present on the CB used in this work.[29] On this basis, reaction at the surface with diarylcarbene might be expected to lead to the formation of benzhydryl esters and ethers along with C−C and C−H insertion products. Overall, minor changes were observed between the C 1s and O 1s regions present on the pristine CB and modified CBs, as detailed in the Supporting Information. The XPS clearly identified the presence of nitrogen species, which were introduced to the CB surface following the Route A functionalization procedure. In contrast, N 1s features were not detected on pristine CB or Route B functionalized CB, as would be expected.

In detail, one-step Route A functionalized nanoparticle CB_2 displays a notable feature in the N 1s region at 399.9 eV binding energy (Figure 1), owing to the NMe$_2$ group, present on the precursor diazo 1c, and now present on the CB surface.
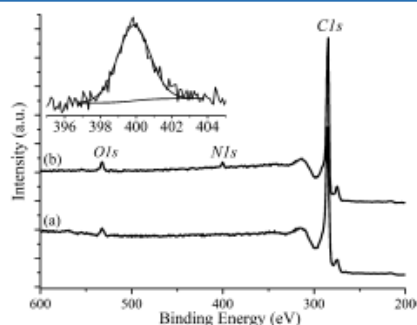
Figure 1. XPS survey scan of (a) pristine CB and (b) modified CB_2 (inset shows the high resolution scan of the N 1s region.).

Two-step Route A modified CB_4a and CB_4b each display a N 1s peak at 400.3 and 400.6 eV binding energies, respectively, which can be attributed to the NMe$_2$ and additional N=N functionality present on the modified surface, consistent with detected azo-linkages reported elsewhere.[16] It is likely that there is some variation of functionality that can be introduced as a monolayer coverage to the surface during the two-step functionalization procedure for CB_4a−b, and some possibilities are shown in Scheme 4.

Some areas of the CB surface may remain unchanged following exposure to the diazonium salt solution, retaining the
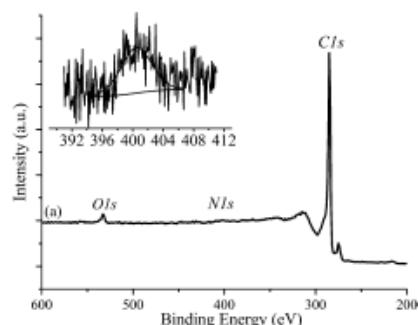
Figure 2. XPS survey scan of (a) modified CB_2 following treatment by thermal analysis (inset shows the high resolution scan of the N 1s region.).

Scheme 4. Potential Functionalized Surface CB_4a-b Following the Two-Step Carbene Insertion and Diazonium Coupling Reactions[a]

[a](a) Unsuccessful diazonium coupling reaction (same surface as CB_2); (b) single azo-coupling to a single aromatic ring on CB_2; (c) dual azo-coupling to both aromatic rings on CB_2; (d) azo-coupling directly to the CB surface; (e) C−C linkage to CB surface.

surface of CB_2 (Scheme 4a) or the unmodified CB surface. Otherwise, the diazonium coupling step is expected to occur at one or both of the rings on CB_2, due to the electron donating effect from each of the NMe$_2$ groups present, to give single or dual insertion products (Scheme 4b,c). Additionally, direct azo-coupling to CB (Scheme 4d), by reaction directed from phenolic groups present on the graphitic surface, has been reported[25] as well as C−C linkage (Scheme 4e) initiated by the reduction of diazonium cations by the graphitic surface.[30,31] However, for both instances, as the reaction with the diazonium salt is the second step onto prefunctionalized CB_2, it is expected any direct linkages to the CB surface to be minimal.

TGA-DSC Thermal Analysis of Pristine and Modified CB. The carbene insertion reaction to generate CB_9a was followed by thermal analysis (STA) (Figure 3), using a sample of CB coated with diazo 8a. The diazo decomposition reaction was readily observed by the exothermic peak on the DSC thermogram, which shows a reaction enthalpy of −45.6 J/g

141
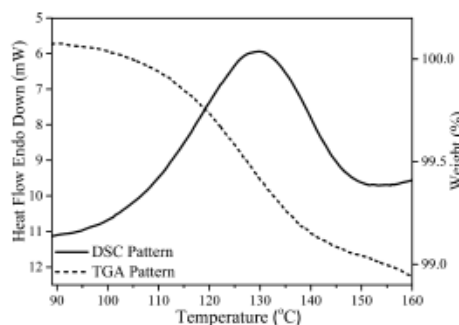
Figure 3. STA analysis of **CB_9a** surface modification reaction under nitrogen flow.

with an extrapolated peak onset at 107.9 °C and peak decomposition temperature at 129.2 °C. Additionally, the TGA thermogram indicated initial weight loss of the sample begins at ~90 °C and plateaus at ~160 °C, with a total weight loss of 0.165 mg (1.13%), which can be attributed to the loss of N_2 upon generation of the reactive carbene species, corresponding to a maximum conversion of the diazo compound to diarylcarbene of 33%.[32,33]

Further analysis of the functionalized CB by thermogravimetric analysis (TGA) (Figure 4) indicates the thermal stability of the modification and affords the opportunity to directly estimate the surface loading from the determined mass losses (Table 2).
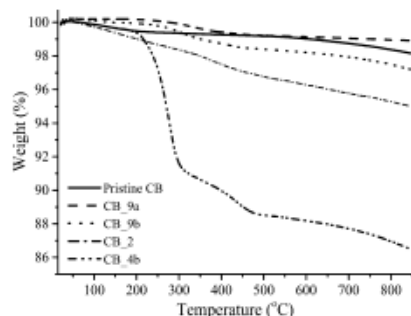
Figure 4. Thermogravimetric analysis of pristine and covalent modified CB under nitrogen flow.

The pristine and modified CB samples showed a similar weight loss, 0.3−1.0%, in the temperature range 30−200 °C, due to degassing and volatilization of water or residual solvents.[34] Alternatively, in the 200−500 °C temperature range, Figure 4 shows the significant weight loss for the functionalized CB samples compared to pristine CB and this is attributed to the thermal decomposition, or cleavage, of the covalent modifications. One-step weight loss with onset decomposition temperatures in the range 255−326 °C is observed for the majority of the modified CB samples and is in agreement with reported thermal stability of similar covalent bound moieties on carbon-based substrates.[13,35] In addition,

CB_4b presents a two-step weight loss, with onset temperatures of 237.1 and 403.5 °C, respectively. This result strongly indicates the success of the two-step reaction following the procedure with diazonium salts, either by azo-coupling to the **CB_2** modification or directly to the CB surface. Subsequently, above 500 °C to the end of the TGA run, ~850 °C, a small similar weight loss can be observed for all the CB samples and generally this can be ascribed to the loss of appreciable nongraphitic fractions present on the CB.[36] To confirm total removal of the modifications following thermal treatment, XPS analysis was performed to **CB_2** retrieved after TGA analysis. Figure 2 indicates the loss of the nitrogen species by the survey scan, although it is not fully lost, indicated by the small N 1s peak, 0.9% relative elemental abundance (Figure 2, insert). It is therefore evident that some of the surface modification survives the thermal treatment. Nonetheless, the percentage weight loss of modified CB can be compared to pristine CB during the thermal program (30−800 °C), and taking into account the known surface modifier present and the experimental BET surface area of CB (72.5 m^2/g), an estimate of number of molecules present on CB can be calculated (Table 2).

TGA analysis therefore estimates the surface loading to be in the range of 2.4×10^{13} to 1.3×10^{14} molecules/cm^2, a comparable result to previous work using diaryldiazo modifications.[16] It can be noted that Route A modified **CB_4b** displays the highest loading of 1.3×10^{14} molecules/cm^2, indicating the superior efficiency of the two-step carbene and diazonium modification procedure. Further, the TGA data from **CB_4b** can be used to assess if single or dual azo-coupling, or direct insertion to the CB surface, to the premodified **CB_2** is taking place (Scheme 4a−e). From the calculated surface loading by TGA of 1.0×10^{14} molecules/cm^2 for CB_2 (Table 2), the expected weight loss of **CB_4b** can be estimated at 4.5×10^{-4} g and 6.9×10^{-4} g for single or dual insertion products, respectively. The measured weight loss of **CB_4b** by TGA was 8.7×10^{-4} g, suggesting that the dual insertion modification mechanism predominates for the prefunctionalized **CB_2**.

Combustion Analysis (CHN). Further qualitative evidence by CHN confirmed the presence of nitrogen following surface modification (Table 1). Modified CB, **CB_2**, **CB_4a**, and **CB_4b** all show the presence of nitrogen, which is consistent with the N-label functionality introduced in Route A. Furthermore, surface coverage estimates can be extracted from the CHN results (Table 2), assuming a monolayer surface coverage of the experimentally determined CB BET surface area (72.5 m^2/g). CHN estimates the surface loadings on CB to be in the range of 4.0×10^{13} to 1.9×10^{14} molecules/cm^2. These results are in good agreement with the TGA estimated surface coverage, and within the same order of magnitude. Additionally, it should be noted that nitrogen was also detected on **CB_9b** by CHN analysis, however this is expected due to contamination as it was not detected by XPS analysis, which has otherwise demonstrated a higher degree of sensitivity.

ATR-IR Spectra. ATR-IR analysis of the two-step modified **CB_4b** (Figure 5) with the highest surface modification, further established the introduction of new functionality compared to pristine CB.

Characteristic C−H symmetric and asymmetry bending bands were identified at v 2916 cm^{-1} and v 2849 cm^{-1}, respectively, presumably from the introduction of the dodecyl hydrocarbon chain added in the diazonium coupling step. Further, a stretching band at v 1514 cm^{-1} corresponded to

Table 2. TGA and CHN Analysis and Loading Calculations of Pristine and Modified CB

	TGA					CHN[b]	
	TGA weight loss (%)			surface loading[a]		surface loading[a]	
sample	30–200 (°C)	200–500 (°C)	500–800 (°C)	mol/g	molecules/cm²	mol/g	molecules/cm²
pristine CB	0.5	0.3	0.8	n.c.[e]	n.c.	n.c.	n.c.
CB_2	1.0	2.3	1.4	1.2×10^{-4}	1.0×10^{14}	2.3×10^{-4}	1.9×10^{14}
CB_4a[d]	n.m.[c]	n.m.	n.m.	n.c.	n.c.	4.8×10^{-5}	4.0×10^{13}
CB_4b[d]	0.7	10.9	1.6	1.6×10^{-5}	1.3×10^{14}	1.1×10^{-4}	9.0×10^{13}
CB_9a	0.7	1.9	1.4	8.5×10^{-5}	7.1×10^{13}	n.c.	n.c.
CB_9b	0.3	1.5	0.9	2.9×10^{-4}	2.4×10^{13}	n.c.	n.c.

[a]Assumes monolayer surface coverage of the experimentally determined BET CB surface area, 72.5 m²/g. [b]CHN surface loadings calculated from detected nitrogen content present on modified CB. [c]n.m., not measured; TGA was not performed for sample CB_4a. [d]Calculation assumes surface functionalization following the two-step procedure gives the dual azo-coupled product, as shown in Scheme 4c. [e]n.c., not calculated; surface loading could not be calculated.
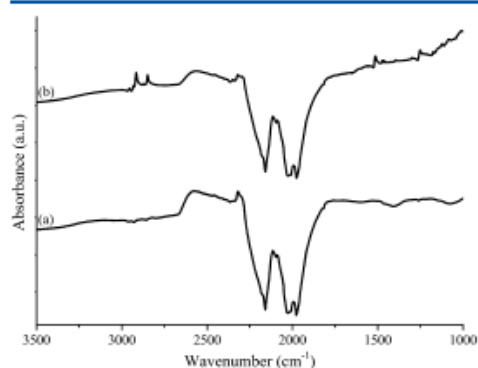
Figure 5. ATR-IR spectra of (a) pristine CB and (b) modified CB_4b.

aromatic C=C and can be attributed to the benzene rings, and an aryl alkyl asymmetric stretch can be observed at v 1251 cm⁻¹ from the introduced C—O—C functionality in the diazonium coupling reaction, all of which are not observed for pristine CB. Unfortunately, the *trans* azo N=N stretching vibration in the 1400–1500 cm⁻¹ region is typically rendered inactive on the IR spectrum[37] and therefore, as expected, was not observed. The presence of functional groups for the other modified one-step and two-step CB samples could not be detected, presumably as result of being below the sensitivity limit for the ATR-IR instrument. In addition, CB as a substrate is known to be difficult for ATR-IR spectroscopy, as it is an effective absorber

and its high refractive index is also close to that of the diamond accessory.[38]

In summary, modified CB from Route A provided direct evidence of the introduction of nitrogen onto the CB nanoparticle surface and that surface functionalization by carbene and diazonium coupling reactions was successful. Next, Route B modified nanoparticles permits optimization of the functionalization method with a one-step approach for the introduction of steric stabilizing functional groups the CB surface. With this achieved, the potential of Route B modified CB samples for the improvement of polypropylene nanocomposites was investigated.

Nanocomposite Preparation and Characterization. With modified CB nanoparticles in hand, polymer nanocomposites were prepared. Accordingly, PP was combined with pristine CB and covalently modified Route B, **CB_9a** and **CB_9b**, at varying filler additions, 10–30 wt % of PP. The volume conductivity of the resulting nanocomposites was then evaluated. Further analysis by dielectric analysis, TEM and STA was additionally carried out on selected nanocomposite samples.

Volume Resistance–Conductivity Percolation Curves. Improved electrical conductivity was a key aim of this study since it provides an indication on the nanoscale of the altered filler–filler and filler–polymer interfacial interactions following filler functionalization. The addition of conductive carbon-based fillers dispersed in insulating polymers, such as PP, induces electrical conductivity at a critical filler concentration, termed the percolation threshold.[39] Before this point, upon addition of the nanofiller into the polymer matrix, the level of electrical conductivity rises gradually from the original polymer matrix. At the percolation threshold, the formation of
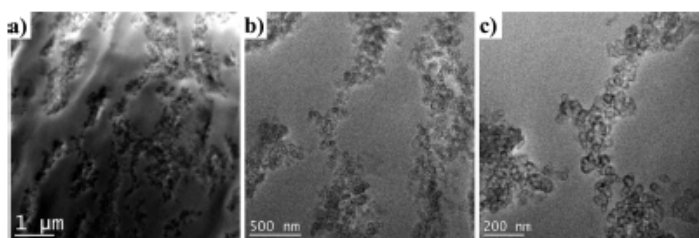
Figure 6. TEM images of pristine CB/PP at (a) 1 μm, (b) 500 nm, and (c) 200 nm resolution.

continuous three-dimensional networks permits the passage of electrons through the nanocomposite, resulting in a significant increase in conductivity over a small range of nanofiller addition into the system.[40,41] The formation of conductive networks can be seen in the TEM images of pristine CB in PP at 30 wt % in Figure 6.

After the critical concentration has been reached, continued filler addition leads to a gradual increase in the conductivity measurements as the nanocomposite sample approaches the peak electrical conductivity of the filler.

The volume conductivities, as calculated from the measured sheet resistance of the pristine and modified CB/PP nanocomposite samples, are presented in Figure 7 as a function of filler loading. Full details, including repeat experiments demonstrating the reproducibility of the measurements, are included in the Supporting Information.
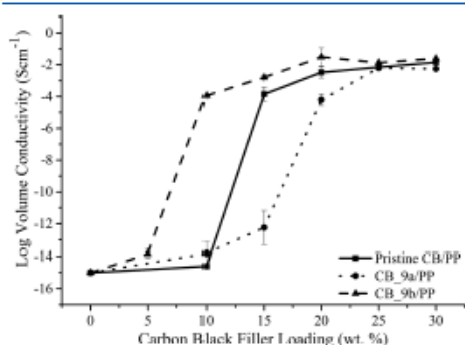
Figure 7. Logarithm of the volume electrical conductivity of pristine and modified CB/PP nanocomposites as a function of CB nanofiller loading.

The electrical conductivity of the pristine CB/PP nanocomposites increased significantly in the region from 10 to 20 wt % filler loading, with a percolation threshold starting to be reached around 15 wt % with a conductivity in the order of 4.66×10^{-4} S cm^{-1}. The high loading required to induce electrical conductivity is expected due to the low aspect ratio and low structure CB which was used,[42] and this result is consistent with previous work on similar nanocomposite systems.[43] The **CB_9a**/PP prepared nanocomposites, in which CB was covalently modified with a terminal hexyl chain, required an increased critical concentration of ~20 wt % for the initial achievement of conductive three-dimensional networks in PP. This result indicates that the presence of even one polar ether group in the short side chain modifying group leads to an increased electrical percolation threshold, consistent with poor CB-PP matrix compatibilisation in the nanocomposite.

By contrast, **CB_9b**/PP, in which the CB functionalization is terminated by a dodecyl chain, displayed high electrical conductivity at reduced filler loadings. Top conductivities of 2.51×10^{-1} S cm^{-1} were observed, and the percolation threshold was beginning to be realized near 10 wt % loading with a conductivity of 1.19×10^{-4} S cm^{-1} (Figure 7). This result is likely due to favorable steric stabilization from the modification hindering CB agglomeration of aggregates, and assisted compatibilisation between the functionalized CB and PP matrix. This reveals that the terminal dodecyl chain present

on **CB_9b**, compared to hexyl terminated modification on **CB_9a**, is a viable nanoparticle modification for the production of nanocomposites with improved properties. It is important to note here that the difference between the two covalently modified nanoparticles is unlikely to be as a result of the surface loading of the modifiers, as they were similar, with values of 7.1×10^{13} and 2.4×10^{13} molecules/cm^2 for **CB_9a** and **CB_9b**, respectively, as estimated by TGA.

Additionally, the volume conductivity was measured across both sides of the compressed molded nanocomposite plaques, permitting estimation of the error bars in Figure 7. The bidirectional analysis indicated an excellent level of sample homogeneity for the dodecyl modified **CB_9b** but a poorer level for the hexyl modified **CB_9a**, especially at a lower filler concentration, consistent with greater agglomeration in the system.

Dielectric Analysis. Altered percolation thresholds of carbon-based polymer nanocomposites have been shown to exhibit promising dielectric properties, for example in electromagnetic interference (EMI) shielding applications.[44] Further, testing nanocomposite samples close to the percolation threshold can provide information about the conductive mechanism of the nanocomposite samples.[45] Figure 8 displays
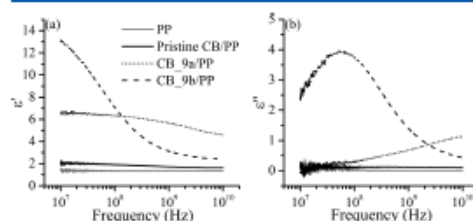
Figure 8. (a) Real part (ε') and (b) the imaginary part (ε'') of the complex permittivity as a function of frequency, averaged over 50 repeat measurements at different points, of pure PP and pristine CB/PP, **CB_9a**/PP, and **CB_9b**/PP nanocomposite film samples (15 μm), at 20 wt % loading in the range 10 MHz to 10 GHz.

the real (ε') and imaginary (ε'') parts of the complex permittivity as a function of frequency of pure PP and pristine CB/PP, **CB_9a**/PP, and **CB_9b**/PP nanocomposite samples at 20 wt % loading in the range 10 MHz to 10 GHz.

For the real part (ε') of the complex permittivity, which represents the capacity for electric energy storage,[46] pure PP displays a frequency independent response at a value of 1.3 and pristine CB/PP a low frequency dependent response at 1.8. Modified CB nanocomposite samples, **CB_9a**/PP and **CB_9b**/PP, both display dielectric relaxation responses as the frequency is increased, indicating changed CB-CB and CB-PP interfacial interactions following the covalent modifications. In detail, **CB_9a**/PP displays an increased real permittivity of 6.5 at lower frequency measurements, reducing to 4.7 at the highest frequency recorded. In a similar trend, sample **CB_9b**/PP displays the greatest increase of real permittivity of 13.2 at lower frequency measurements, leveling to 2.4 at the highest frequency recorded. The imaginary part (ε'') of the complex permittivity is related to the energy dissipation, accounting for conductive and relaxation effects of the nanocomposite sample.[47] Similar to the real permittivity results, PP demonstrates a frequency independent response at a value of 0.03 and pristine CB/PP a flat low frequency dependent

144
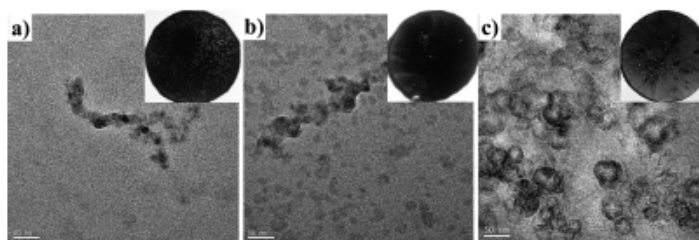
Figure 9. TEM micrographs for (a) pristine CB/PP, (b) **CB_9b**/PP, (c) **CB_9a**/PP nanocomposites at a loading of 20 wt % at 50 nm. Inset shows the nanocomposite films (15 μm) used for the analysis.

response at 0.1, both exhibiting nonconductive behavior at this frequency range. **CB_9b**/PP displayed a typical dielectric relaxation response with a maximal value $\sim 1 \times 10^8$ Hz while **CB_9a**/PP demonstrated a weaker dielectric response, which has shifted toward higher frequencies $\sim 1 \times 10^{10}$ Hz.

The observed frequency dependence, notably larger for **CB_9b**/PP compared to **CB_9a**/PP, is indicative of the conducting features of nanocomposites with increasing percolative correlation length as the percolation threshold is approached.[48,49] At this measured loading, therefore, the electrical conductivity is influenced by interfiller tunnelling.[49] The observed frequency dependence is a result of the Maxwell−Wagner−Sillars effect, common to highly inhomogeneous systems such as nanocomposites comprising of conductive fillers embedded in an insulating polymer matrix.[50] In the presence of an alternating current, interfacial polarization can be induced at the interface between adjacent conductive CB clusters embedded in the PP matrix, resulting in a system of nanocapacitors, whereby the CB filler aggregates act as nanoelectrodes and the PP matrix as nanodielectrics.[27,51] The frequency dependent response of CB nanocomposites is largely directed by the CB loading and dispersion as well as the interfacial polarization effects.[52,53] Additionally, the surface chemistry of the filler, in this case the covalent modifications, can also have a direct effect on the electron tunnelling mechanism between adjacent CB clusters in the PP matrix, as demonstrated by these results as well as in other systems.[54] In detail, as the sample is subjected to the alternating current, at lower frequencies interfacial polarization follows the change in the electric field and maximal interfacial polarization is obtained. As the frequency is increased, the alternating electrical field becomes too fast to induce polarization effects, leading to dielectric relaxation and a reduced contribution to the real permittivity.[42] In the imaginary part of the complex permittivity, there is a corresponding relaxation response, associated with induced oscillating interfacial polarizations.[27] The greater frequency dependence upon the **CB_9b**/PP sample indicates a more dispersed filler structure in this nanocomposite sample, with more nanocapacitors present concomitant with a greater polarization density.[28] On the other hand, the reduced frequency dependence of the **CB_9a**/PP sample is indicative of a more aggregated structure following the hexyl terminated CB surface functionalization.

As with the DC conductivity results, the variance of the repeat dielectric measurements (>50 times) at different points on the nanocomposite films provides further evidence of the uniformity of the CB filler dispersion. The wide range of relaxation peaks observed for **CB_9a**/PP, included in the Supporting Information, further suggests that the dispersion is highly nonuniform over the length scale of the measurement (the probe has a 1.6 mm aperture). By contrast, the repeat relaxation peaks for **CB_9b**/PP are more regular as a result of better dispersion and uniformity of the sample across measurement length scales.

It should be noted that microwave frequency dielectric measurements such as these reveal a great deal of useful information about connectivity, microstructure and electrodynamics in mixtures.[55−57] As demonstrated in the results in Figure 8, major differences between percolative conduction in modified samples and in pristine samples are exposed; these are properties that DC measurements are unable to reveal. For 20 wt % loading at DC, percolation is well established and values of conductivity are similar for all samples, but at microwave frequencies it is clear that charge dynamics are very different for the modified and pristine samples. While the DC conductive pathways of the pristine CB/PP composite are indeed well established at 20 wt % loading, the microwave measurements do not probe the macroscopic DC conductivity in this sample. There is a small frequency dependence of the pristine sample rising to an effective microwave permittivity value similar to that of PTFE at lower frequencies, unlike the frequency independent response of the PP sample, and this is entirely as expected. For the **CB_9a**/PP and **CB_9b**/PP samples, there is an increased frequency dependence because of the modified connectivity. However, this is not shown in the DC measurements, which, for any given loading value, provide limited information about conduction mechanisms. The large frequency dependence exhibited in the modified samples highlights the different conduction mechanisms associated with their modified connectivity.

Morphological Characterization. TEM micrographs and thin films (15 μm) of the pristine and modified CB/PP nanocomposites (Figure 9) provide a visual indication of the altered dispersion of the CB nanofiller in the region of the percolation threshold.

Pristine CB displays a large isolated agglomerate in the polymer matrix and modified **CB_9a** also displays CB agglomerates and additionally visibly clustered PP. This further indicates the poor filler−polymer compatibilities and equally the unhindered attractive filler−filler interactions following the hexyl-terminated nanoparticle functionalization. However, for modified **CB_9b**, good nanofiller dispersion in PP can be observed by the TEM image. A small agglomerate, or part of a conductive nanoparticle network is visible, and furthermore small dispersed CB aggregates are distributed across the TEM micrograph in accordance with the reported superior

conductivity results. This result further indicates that covalent modified **CB_9b** has improved the compatibilisation between the filler and PP matrix.

Nanocomposite Thermal Properties. The melting and crystallization behavior of the pure PP and modified CB/PP nanocomposites, extracted from the DSC runs in non-

Table 3. Thermal Properties and Degree of Crystallinity of PP and Prepared Pristine and Covalent Modified CB_9a/PP and CB_9b/PP Nanocomposites

sample	CB loading (%)	$T_{oc}{}^{a}$ (°C)	$T_{c}{}^{b}$ (°C)	$T_{m}{}^{c}$ (°C)	$\Delta H_{m}{}^{d}$ (J/g)	$X_{C}{}^{e}$ (%)
pure PP	0	127.6	122.9	163.2	71.1	34
pristine CB/PP	10	128.9	124.1	161.9	66.5	36
	15	125.1	119.9	164.2	61.6	36
	20	132.5	125.5	165.5	59.4	36
	25	131.5	123.8	165.1	60.0	39
	30	133.8	126.6	166.0	59.2	41
CB_9a/PP	10	121.3	115.8	162.5	57.7	31
	15	125.2	117.4	166.2	57.8	33
	20	126.3	120.7	163.7	57.3	35
	25	127.7	121.2	165.8	56.8	37
	30	129.1	121.7	167.4	54.8	38
CB_9b/PP	10	133.3	126.7	165.7	67.3	36
	15	127.8	122.8	163.7	62.7	34
	20	134.0	127.3	166.9	62.2	38
	25	132.1	124.7	165.6	60.4	39
	30	133.9	126.5	166.2	59.6	41

$^{a}T_{oc}$, onset crystallization temperature. $^{b}T_{c}$, peak crystallization temperature. $^{c}T_{m}$, peak melting temperature (second melting cycle). $^{d}\Delta H_{m}$, enthalpy of melting (second melting cycle). $^{e}X_{C}$, degree of crystallinity.

isothermal conditions, are reported in Table 3. The determined degree of crystallinity (X_{C}) was calculated as follows:

$$X_{C} = \frac{H_{m}}{(1-x)H_{0}} \times 100$$

where H_{m} is the sample melting enthalpy, as measured by DSC, H_{0} is the melting enthalpy of 100% crystalline PP, which is reported to be 207.1 J/g,[58,59] and x is the weight fraction of CB present in the nanocomposite.[60]

As a function of filler content, an increased nucleation efficiency of all the nanocomposite systems is indicated by the general increase in T_{oc}, T_{c}, and calculated degree of crystallinity. Although CB nanoparticles are known to collect in the amorphous regions of semicrystalline polymers like PP, they can influence the crystalline structure.[61] Accordingly, nanofillers can act as heterogeneous nucleation sites, initiating nucleation at higher temperatures closer to the melting temperature[62] resulting in smaller, less uniform spherulites.[63] As a result, this can increase the rate and degree of crystallinity when a filler is embedded in the polymer matrix of nanocomposites.[48,64] Comparison of the samples at equal filler loading permits further consideration of the changes to the nucleation ability of the CB filler following surface modification. Once more, these changes can be attributed to changes in the filler-filler interfacial interactions as well as polymer-filler interfacial interactions, controlling the filler dispersion, and importantly provides an indication of the mechanical properties changes, such as the modulus and toughness, of the polymer nanocomposite.[65]

Figure 10 displays the cooling and Figure 11 the melting thermograms of the pristine and the modified CB/PP nanocomposites at 20 wt % loading.
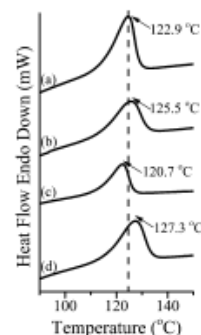
Figure 10. DSC cooling thermograms of (a) pure PP, (b) pristine CB/PP, (c) **CB_9a/PP**, and (d) **CB_9b/PP** nanocomposites at 20 wt % filler loading.
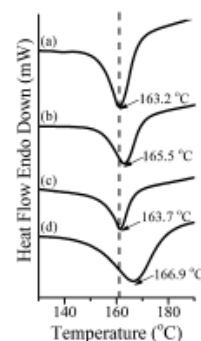
Figure 11. DSC melting thermograms (second heating cycle) of (a) pure PP, (b) pristine CB/PP, (c) **CB_9a/PP**, and (d) **CB_9b/PP** nanocomposites at 20 wt % filler loading.

It is evident from the T_{c} values that a similar trend to the conductivity measurements can be observed. **CB_9b/PP** shows the largest T_{c} increase compared to pure PP by ~4 °C, which can be compared to an increase of ~2 °C for pristine CB/PP. While only a small change, this result further supports improved filler dispersion following modification, which is directing an increased number of nucleation sites present at the same filler loading. Conversely, the T_{c} of **CB_9a** is lower than pristine CB/PP by ~5 °C, and is also lower than pure PP by ~2 °C. This further supports the evidence of the poor compatibility and poor dispersion of this hexyl-terminated CB modification with PP. Figure 11 also reveals a similar trend for the T_{m} values, with the most dispersed system, **CB_9b/PP**, showing the highest melting temperature. Raised T_{m} values following filler addition is indicative of decreased lamellar thickness in a more ordered PP matrix and is observed due to the increased nucleation ability of the most dispersed **CB_9b/PP** system.[66]

146

With regards to the degree of crystallinity results, it can be observed that at low filler additions of 10 and 15 wt %, **CB_9a**/PP nanocomposite displayed low X_C values of 31% and 33%, respectively. It is worth noting that this is lower than the X_C of pure PP, 34%, and this result can be attributed to the presence of large CB agglomerates which may be restricting PP chain movement as well as hindering effective polymer chain packing.[65] Finally, above 20 wt % filler loading of **CB_9a**/PP, the X_C of the nanocomposite surpasses pure PP, with an eventual X_C of 38% at maximum loading. Pristine CB/PP and **CB_9b**/PP nanocomposites both immediately display increased X_C compared to pure PP, with the **CB_9b**/PP nanocomposite displaying a notably higher degree of crystallinity at 20 wt % loading, a result again indicative of the nucleation capability of this modified CB filler. Finally, it is evident that the reported degree of crystallinity (Table 3) follows a similar trend to the nanocomposite conductivity measurements (Figure 7). Previous studies have also found corresponding results between the nucleation effect of filler nanoparticles and the conductivity measurements above the percolation threshold.[67]

CONCLUSIONS

In summary, the use of two covalent approaches for the tailored functionalization of CB nanoparticles for polymer nanocomposite applications has been clearly demonstrated. Route A used a two-step approach, involving carbene insertion followed by diazonium coupling reactions, to introduce an N-label terminated by hexyl and dodecyl hydrocarbon chains to the CB surface. Route B applied the same carbene functionalization technology in an optimized one-step approach, in which the CB was directly modified with a tailored hexyl and dodecyl terminated diaryl complex. Direct evidence of the altered surface chemistry of CB, including the introduction of nitrogen functionality, was found by TGA, CHN, XPS, ATR-IR analysis, and grafting densities estimated to be in the order of 10^{13} and 10^{14} molecules/cm^2 for the modified samples.

The application of modified **CB_9a–b** for use in PP nanocomposites was investigated. The macroscopic property changes in the resulting CB/PP nanocomposites further indicate the changed CB surface chemistry and altered CB-CB and CB-PP interfacial interactions following the carbene functionalization approach. Interestingly, the hexyl-terminated covalent Route B modification of **CB_9a** resulted in an increased percolation threshold compared to pristine CB/PP nanocomposites, indicating increased CB agglomeration in the nanocomposite system. TEM micrographs, dielectric analysis and STA data further corroborated this result. We attribute this effect might be a result of the modification reducing the CB-PP compatibility, or equally enhancement of the CB filler–filler interactions, or a combination of the two effects, leading to aggregated, poorly dispersed and distributed CB in the PP matrix. On the other hand, TEM micrographs of dodecyl terminated Route B modified **CB_9b** visibly demonstrated improved dispersion of CB aggregates and reduced CB agglomerate formation. Correlation with STA data illustrated increased crystallization temperatures following CB modification, and indicated an increased number of nucleation sites owing to separated and dispersed CB aggregates present in the nanocomposite. Correspondingly, enhanced dielectric and electrical properties were observed. The electrical percolation threshold of the covalent modified **CB_9b**/PP was reduced to

~10 wt % filler addition, almost half the required filler loading to achieve conductivity for pristine CB/PP nanocomposites. Finally, this versatile carbene CB modification strategy highlights the potential of tailored nanoparticle functionalization in the pursuit of superior, multifunctional nanocomposites.

ASSOCIATED CONTENT

ⓢ Supporting Information

The Supporting Information is available free of charge on the ACS Publications website at DOI: 10.1021/acs.langmuir.6b02013.

> Detailed synthesis procedures of the organic compounds including compound spectra, XPS analysis of the C 1s and O 1s regions of pristine and modified CB, raw XPS, ATR-IR, BET, CHN and TGA data of pristine and modified CB, TGA and CHN surface loading calculations of modified CB, and raw CB/PP nanocomposite conductivity, dielectric and STA data. (PDF)

AUTHOR INFORMATION

Corresponding Author
*E-mail: Mark.moloney@chem.ox.ac.uk.

Notes

ACKNOWLEDGMENTS

REFERENCES

(1) Zhang, W.; Dehghani-Sanij, A. A.; Blackburn, R. S. Carbon based conductive polymer composites. *J. Mater. Sci.* **2007**, *42* (10), 3408–3418.

(2) Wen, X.; Wang, Y.; Gong, J.; Liu, J.; Tian, N.; Wang, Y.; Jiang, Z.; Qiu, J.; Tang, T. Thermal and flammability properties of polypropylene/carbon black nanocomposites. *Polym. Degrad. Stab.* **2012**, *97* (5), 793–801.

(3) Tjong, S. C. Structural and mechanical properties of polymer nanocomposites. *Mater. Sci. Eng., R* **2006**, *53* (3–4), 73–197.

(4) Ritzhaupt-Kleissl, E.; Boehm, J.; Hausselt, J.; Hanemann, T. Thermoplastic polymer nanocomposites for applications in optical devices. *Mater. Sci. Eng., C* **2006**, *26* (5–7), 1067–1071.

(5) Diez-Pascual, A. M.; Diez-Vicente, A. L. Development of Nanocomposites Reinforced with Carboxylated Poly(ether ether ketone) Grafted to Zinc Oxide with Superior Antibacterial Properties. *ACS Appl. Mater. Interfaces* **2014**, *6* (5), 3729–3741.

(6) Huang, S.; Wang, M.; Liu, T.; Zhang, W.-D.; Tjiu, W. C.; He, C.; Lu, X. Morphology, thermal, and rheological behavior of nylon 11/multi-walled carbon nanotube nanocomposites prepared by melt compounding. *Polym. Eng. Sci.* **2009**, *49* (6), 1063–1068.

(7) Gulrez, S. K. H.; Ali Mohsin, M. E.; Shaikh, H.; Anis, A.; Pulose, A. M.; Yadav, M. K.; Qua, E. H. P.; Al-Zahrani, S. M., A review on electrically conductive polypropylene and polyethylene. *Polym. Compos.* **2014**, *35*, (5), 900–914.10.1002/pc.22734

(8) Tchoudakov, R.; Breuer, O.; Narkis, M.; Siegmann, A. Conductive polymer blends with low carbon black loading: Polypropylene/polyamide. *Polym. Eng. Sci.* **1996**, *36* (10), 1336–1346.

(9) Medalia, A. I.; Heckman, F. A. Morphology of aggregates—II. Size and shape factors of carbon black aggregates from electron microscopy. *Carbon* **1969**, *7* (5), 567–582.

147

(10) Kost, J.; Narkis, M.; Foux, A. Resistivity Behavior of Carbon-Black-Filled Silicone-Rubber in Cyclic Loading Experiments. *J. Appl. Polym. Sci.* **1984**, *29* (12), 3937–3946.

(11) Narkis, M.; Lidor, G.; Vaxman, A.; Zuri, L. New injection moldable ESD compounds based on very low carbon black loadings. *Electrical Overstress/Electrostatic Discharge Symposium Proceedings - 1998* **1998**, 1–9.

(12) Moniruzzaman, M.; Winey, K. L. Polymer nanocomposites containing carbon nanotubes. *Macromolecules* **2006**, *39* (16), 5194–5205.

(13) Luksirikul, P.; Ballesteros, B.; Tobias, G.; Moloney, M. G.; Green, M. L. H. Sidewall functionalisation of carbon nanotubes by addition of diarylcarbene derivatives. *J. Mater. Chem.* **2011**, *21* (47), 19080–19085.

(14) Luksirikul, P.; Ballesteros, B.; Tobias, G.; Moloney, M. G.; Green, M. L. H. pH-triggered release of materials from single-walled carbon nanotubes using dimethylamino-functionalized fullerenes as removable "corks". *Carbon* **2010**, *48* (7), 1912–1917.

(15) Wang, H.; Griffiths, J. P.; Egdell, R. G.; Moloney, M. G.; Foord, J. S. Chemical functionalization of diamond surfaces by reaction with diaryl carbenes. *Langmuir* **2008**, *24* (3), 862–868.

(16) Leonard, D.; Moloney, M. G.; Thompson, C. Chemical modification of materials by reaction with diaryl diazomethanes. *Tetrahedron Lett.* **2009**, *50* (26), 3499–3502.

(17) Choong, C.; Foord, J. S.; Griffiths, J. P.; Parker, E. M.; Luo, B. W.; Bora, M.; Moloney, M. G. Post-polymerisation modification of surface chemical functionality and its effect on protein binding. *New J. Chem.* **2012**, *36* (5), 1187–1200.

(18) Bagwell, C. L.; Leonard, D. M. L.; Griffiths, J.-P.; Moloney, M. G.; Stratton, N. J.; Travers, D. P. Post-Polymerization Modification of Materials using Diaryldiazomethanes: Changes to Surface Macroscopic Properties. *Macromol. React. Eng.* **2014**, *8* (2), 170–180.

(19) Awenat, K. M.; Davis, P. J.; Moloney, M. G. A chemical method for the convenient surface functionalisation of polymers. *Chem. Commun.* **2005**, *8*, 990–992.

(20) Griffiths, J. P.; Maliha, B.; Moloney, M. G.; Thompson, A. L.; Hussain, I. Surface Functional Polymers by Post-Polymerization Modification using Diarylcarbenes: Introduction, Release and Regeneration of Hydrogen Peroxide and Bactericidal Activity. *Langmuir* **2010**, *26* (17), 14142–14153.

(21) Choong, C.; Griffiths, J. P.; Moloney, M. G.; Triffitt, J. Direct introduction of phosphonate by the surface modification of polymers enhances biocompatibility. *React. Funct. Polym.* **2009**, *69* (2), 77–85.

(22) Griffiths, J.-P.; Leonard, D. M. L.; Moloney, M. G.; Stratton, N. J. Control of wetting behavior using post-polymerization modifications of surface chemical functionality. *J. Mol. Eng. Mater.* **2013**, *01* (01), 1250002.

(23) Toupin, M.; Belanger, D. Thermal stability study of aryl modified carbon black by in situ generated diazonium salt. *J. Phys. Chem. C* **2007**, *111* (14), 5394–5401.

(24) Su, F.; Poh, C. K.; Chen, J. S.; Xu, G.; Wang, D.; Li, Q.; Lin, J.; Lou, X. W. Nitrogen-containing microporous carbon nanospheres with improved capacitive properties. *Energy Environ. Sci.* **2011**, *4* (3), 717–724.

(25) Gulrez, S. K. H.; Ali Mohsin, M. E.; Shaikh, H.; Anis, A.; Pulose, A. M.; Yadav, M. K.; Qua, E. H. P.; Al-Zahrani, S. M. A review on electrically conductive polypropylene and polyethylene. *Polym. Compos.* **2014**, *35* (5), 900–914.

(26) Zhang, K.; Park, B.-J.; Fang, F.-F.; Choi, H. J. Sonochemical preparation of polymer nanocomposites. *Molecules* **2009**, *14* (6), 2095–2110.

(27) Arjmand, M.; Sundararaj, U. Broadband dielectric properties of multiwalled carbon nanotube/polystyrene composites. *Polym. Eng. Sci.* **2015**, *55* (1), 173–179.

(28) Ma, P.-C.; Liu, M.-Y.; Zhang, H.; Wang, S.-Q.; Wang, R.; Wang, K.; Wong, Y.-K.; Tang, B.-Z.; Hong, S.-H.; Paik, K.-W.; Kim, J.-K. Enhanced Electrical Conductivity of Nanocomposites Containing Hybrid Fillers of Carbon Nanotubes and Carbon Black. *ACS Appl. Mater. Interfaces* **2009**, *1* (5), 1090–1096.

(29) Panchompoo, J.; Aldous, L.; Compton, R. G. Size-effects in the chemical modification of carbon black nanoparticles with 4-nitroaniline. *New J. Chem.* **2010**, *34* (11), 2643–2653.

(30) Toupin, M.; Bélanger, D. Spontaneous Functionalization of Carbon Black by Reaction with 4-Nitrophenyldiazonium Cations. *Langmuir* **2008**, *24* (5), 1910–1917.

(31) Belmont, J. A.; Amici, R. M.; Galloway, C. P. Carbon black reacted with diazonium salts and products. In Google Patents: 1996.

(32) Shin, S. H.; Cizmeciyan, D.; Keating, A. E.; Khan, S. I.; Garcia-Garibay, M. A. Control of Carbene Reactivity by Crystals. A Highly Selective 1,2-H Shift in the Solid-to-Solid Reaction of 1-(4′-Biphenylyl)-2-phenyldiazopropane to (Z)-1-(4′-Biphenylyl)-2-phenylpropene. *J. Am. Chem. Soc.* **1997**, *119* (8), 1859–1868.

(33) Zawadiak, J.; Hefczyc, B.; Janeczek, H.; Kowalczuk, M. Synthesis and thermal properties of azo-peroxyesters. *Monatsh. Chem.* **2009**, *140* (3), 303–308.

(34) Toupin, M.; Belanger, D. Spontaneous functionalization of carbon black by reaction with 4-nitrophenyldiazonium cations. *Langmuir* **2008**, *24* (5), 1910–1917.

(35) Dyke, C. A.; Stewart, M. P.; Tour, J. M. Separation of Single-Walled Carbon Nanotubes on Silica Gel. Materials Morphology and Raman Excitation Wavelength Affect Data Interpretation. *J. Am. Chem. Soc.* **2005**, *127* (12), 4497–4509.

(36) Borah, D.; Satokawa, S.; Kato, S.; Kojima, T. Characterization of chemically modified carbon black for sorption application. *Appl. Surf. Sci.* **2008**, *254* (10), 3049–3056.

(37) Silverstein, R. M.; Webster, F. X.; Kiemle, D. J. *Spectrometric Identification of Organic Compounds.* 7th ed.; John Wiley & Sons: New York, 2005.

(38) Wilhelm, P. Applications of FT-IR microscopy with materials analyses. *Micron* **1996**, *27* (5), 341–344.

(39) Stauffer, D. *Introduction of Percolation Theory*; Talyor and Francis: London, 1985.

(40) Potschke, P.; Fornes, T. D.; Paul, D. R. Rheological behavior of multiwalled carbon nanotube/polycarbonate composites. *Polymer* **2002**, *43* (11), 3247–3255.

(41) Potts, J. R.; Dreyer, D. R.; Bielawski, C. W.; Ruoff, R. S. Graphene-based polymer nanocomposites. *Polymer* **2011**, *52* (1), 5–25.

(42) Sui, G.; Jana, S.; Zhong, W. H.; Fuqua, M. A.; Ulven, C. A. Dielectric properties and conductivity of carbon nanofiber/semicrystalline polymer composites. *Acta Mater.* **2008**, *56* (10), 2381–2388.

(43) Li, Y.; Wang, S.; Zhang, Y.; Zhang, Y. Electrical properties and morphology of polypropylene/epoxy/glass fiber composites filled with carbon black. *J. Appl. Polym. Sci.* **2005**, *98* (3), 1142–1149.

(44) Yousefi, N.; Sun, X. Y.; Lin, X. Y.; Shen, X.; Jia, J. J.; Zhang, B.; Tang, B. Z.; Chan, M. S.; Kim, J. K. Highly Aligned Graphene/Polymer Nanocomposites with Excellent Dielectric Properties for High-Performance Electromagnetic Interference Shielding. *Adv. Mater.* **2014**, *26* (31), 5480–5487.

(45) Li, Y. C.; Li, R. K. Y.; Tjong, S. C. Frequency and Temperature Dependences of Dielectric Dispersion and Electrical Properties of Polyvinylidene Fluoride/Expanded Graphite Composites. *J. Nanomater.* **2010**, *2010*, 1–10.

(46) Dang, Z. M.; Shehzad, K.; Zha, J. W.; Mujahid, A.; Hussain, T.; Nie, J.; Shi, C. Y. Complementary percolation characteristics of carbon fillers based electrically percolative thermoplastic elastomer composites. *Compos. Sci. Technol.* **2011**, *72* (1), 28–35.

(47) Qing, Y. C.; Zhou, W. C.; Jia, S.; Luo, F.; Zhu, D. M. Electromagnetic and microwave absorption properties of carbonyl iron and carbon fiber filled epoxy/silicone resin coatings. *Appl. Phys. A: Mater. Sci. Process.* **2010**, *100* (4), 1177–1181.

(48) Logakis, E.; Pollatos, E.; Pandis, C.; Peoglos, V.; Zuburtikudis, I.; Delides, C. G.; Vatalis, A.; Gjoka, M.; Syskakis, E.; Viras, K.; Pissis, P. Structure–property relationships in isotactic polypropylene/multiwalled carbon nanotubes nanocomposites. *Compos. Sci. Technol.* **2010**, *70* (2), 328–335.

(49) Yu, C. R.; Wu, D. M.; Liu, Y.; Qiao, H.; Yu, Z. Z.; Dasari, A.; Du, X. S.; Mai, Y. W. Electrical and dielectric properties of polypropylene nanocomposites based on carbon nanotubes and barium titanate nanoparticles. *Compos. Sci. Technol.* **2011**, *71* (15), 1706−1712.

(50) Yacubowicz, J.; Narkis, M. Dielectric Behavior of Carbon-Black Filled Polymer Composites. *Polym. Eng. Sci.* **1986**, *26* (22), 1568−1573.

(51) Dang, Z. M.; Yao, S. H.; Yuan, J. K.; Bai, J. B. Tailored Dielectric Properties based on Microstructure Change in BaTiO3-Carbon Nanotube/Polyvinylidene Fluoride Three-Phase Nanocomposites. *J. Phys. Chem. C* **2010**, *114* (31), 13204−13209.

(52) Jianwen, X.; Wong, M.; Wong, C. P. In Super high dielectric constant carbon black-filled polymer composites as integral capacitor dielectrics. *2004 54th Electronic Components and Technology Conference*, Electronic Components and Technology Conference, 2004. Proceedings. 54th, 1−4 June 2004, 2004; pp 536−541, Vol. 1.10.1109/ ECTC.2004.1319391

(53) Song, Y.; Noh, T. W.; Lee, S. I.; Gaines, J. R. Experimental-Study of the 3-Dimensional Ac Conductivity and Dielectric-Constant of a Conductor-Insulator Composite near the Percolation-Threshold. *Phys. Rev. B: Condens. Matter Mater. Phys.* **1986**, *33* (2), 904−908.

(54) Xu, H. P.; Dang, Z. M.; Jiang, M. J.; Yao, S. H.; Bai, J. Enhanced dielectric properties and positive temperature coefficient effect in the binary polymer composites with surface modified carbon black. *J. Mater. Chem.* **2008**, *18* (2), 229−234.

(55) Youngs, I. J.; Bowler, N.; Lymer, K. P.; Hussain, S. Dielectric relaxation in metal-coated particles: the dramatic role of nano-scale coatings. *J. Phys. D: Appl. Phys.* **2005**, *38* (2), 188.

(56) Brosseau, C.; Bourbigot, C.; Beroual, A.; Queffelec, P.; Mest, Y. L.; Loaec, J. In Dielectric and microstructure properties of polymer carbon-black composites *Conference Record of the 1996 IEEE International Symposium on Electrical Insulation*, Conference Record of the 1996 IEEE International Symposium on Electrical Insulation, 16−19 Jun 1996; pp 850−853, Vol. 2.10.1109/ELINSL.1996.549475

(57) Hotta, M.; Hayashi, M.; Lanagan, M. T.; Agrawal, D. K.; Nagata, K. Complex Permittivity of Graphite, Carbon Black and Coal Powders in the Ranges of X-band Frequencies (8.2 to 12.4 GHz) and between 1 and 10 GHz. *ISIJ Int.* **2011**, *51* (11), 1766−1772.

(58) Wunderlich, B. *Thermal Analysis*; Academic Press: New York, 1990.

(59) Li, Y.; Sundararaj, U. Comparative study on electrical properties of copper nanowire/polypropylene and carbon nanotube/polypropylene composites. *AIChE J.* **2015**, *61* (1), 296−303.

(60) Zhang, H.; Zhang, Z. Impact behaviour of polypropylene filled with multi-walled carbon nanotubes. *Eur. Polym. J.* **2007**, *43* (8), 3197−3207.

(61) Mucha, M.; Marszalek, J.; Fidrych, A. Crystallization of isotactic polypropylene containing carbon black as a filler. *Polymer* **2000**, *41* (11), 4137−4142.

(62) Bikiaris, D. Microstructure and Properties of Polypropylene/ Carbon Nanotube Nanocomposites. *Materials* **2010**, *3* (4), 2884−2946.

(63) Vassiliou, A.; Bikiaris, D.; Chrissafis, K.; Paraskevopoulos, K. M.; Stavrev, S. Y.; Docoslis, A. Nanocomposites of isotactic polypropylene with carbon nanoparticles exhibiting enhanced stiffness, thermal stability and gas barrier properties. *Compos. Sci. Technol.* **2008**, *68* (3−4), 933−943.

(64) Assouline, E.; Lustiger, A.; Barber, A. H.; Cooper, C. A.; Klein, E.; Wachtel, E.; Wagner, H. D. Nucleation ability of multiwall carbon nanotubes in polypropylene composites. *J. Polym. Sci., Part B: Polym. Phys.* **2003**, *41* (5), 520−527.

(65) Manchado, M. A. L.; Valentini, L.; Biagiotti, J.; Kenny, J. M. Thermal and mechanical properties of single-walled carbon nanotubes−polypropylene composites prepared by melt processing. *Carbon* **2005**, *43* (7), 1499−1505.

(66) Chrissafis, K.; Paraskevopoulos, K. M.; Stavrev, S. Y.; Docoslis, A.; Vassiliou, A.; Bikiaris, D. N. Characterization and thermal degradation mechanism of isotactic polypropylene/carbon black nanocomposites. *Thermochim. Acta* **2007**, *465* (1−2), 6−17.

(67) Li, Y. F.; Zhu, J. H.; Wei, S. Y.; Ryu, J. E.; Wang, Q.; Sun, L. Y.; Guo, Z. H. Poly(propylene) Nanocomposites Containing Various Carbon Nanostructures. *Macromol. Chem. Phys.* **2011**, *212* (22), 2429−2438.

149

References

1. Prapuchanay, E., N. Puangngernmak, and S. Chalermwisutkul. *A single mode cylindrical microwave cavity for heating applications of liquid material*. in *Electrical Engineering/Electronics, Computer, Telecommunications and Information Technology (ECTI-CON), 2012 9th International Conference on*. 2012. IEEE.

2. Pozar, D.M., *Microwave engineering*. 4th ed. ed. 2012: Hoboken, N.J. : Wiley.

3. McDougall, G., *The physical nature and manufacture of activated carbon.* Journal of the South African institute of mining and metallurgy, 1991. **91**(4): p. 109-120.

4. Al-Qodah, Z. and R. Shawabkah, *Production and characterization of granular activated carbon from activated sludge.* Brazilian Journal of Chemical Engineering, 2009. **26**(1): p. 127-136.

5. Stewart, M.L. and J. Stencel, *Treatment of Activated Carbons for Densification.* PREPRINTS OF PAPERS-AMERICAN CHEMICAL SOCIETY DIVISION FUEL CHEMISTRY, 1993. **38**: p. 408-408.

6. Menéndez, J., et al., *Microwave heating processes involving carbon materials.* Fuel Processing Technology, 2010. **91**(1): p. 1-8.

7. Dias, J.M., et al., *Waste materials for activated carbon preparation and its use in aqueous-phase treatment: a review.* Journal of Environmental Management, 2007. **85**(4): p. 833-846.

8. Chronopoulos, T., et al., *CO 2 desorption via microwave heating for post-combustion carbon capture.* Microporous and Mesoporous Materials, 2014. **197**: p. 288-290.

9. Ania, C., et al., *Effect of microwave and conventional regeneration on the microporous and mesoporous network and on the adsorptive capacity of activated carbons.* Microporous and Mesoporous Materials, 2005. **85**(1): p. 7-15.

10. Hesas, R.H., et al., *Preparation and characterization of activated carbon from apple waste by microwave-assisted phosphoric acid activation: application in methylene blue adsorption.* BioResources, 2013. **8**(2): p. 2950-2966.

11. Ania, C., et al., *Microwave-induced regeneration of activated carbons polluted with phenol. A comparison with conventional thermal regeneration.* Carbon, 2004. **42**(7): p. 1383-1387.

12. Qiu, Y. and M. Hawley. *Composite material processing in a single mode cavity with variable frequency microwaves*. in *12th International Conference on Composite Materials. Paris, France*. 1999.

13. Menendez-Diaz, J. and I. Martin-Gullon, *Types of carbon adsorbents and their production.* Interface Science and Technology, 2006. **7**: p. 1-47.

14. Atwater, J. and R. Wheeler Jr, *Microwave permittivity and dielectric relaxation of a high surface area activated carbon.* Applied Physics A, 2004. **79**(1): p. 125-129.

15. Chronopoulos, T., et al., *CO2 desorption via microwave heating for post-combustion carbon capture.* Microporous and Mesoporous Materials, 2014. **197**: p. 288-290.

16. YAĞŞİ, N.U., *Production and Characterization of Activated Carbon from Apricot Stones*, in *The Department of Chemical Engineering*. 2004, The Middle East Technical University. p. 114.

17. Harris, P.J., Z. Liu, and K. Suenaga, *Imaging the atomic structure of activated carbon.* Journal of Physics: Condensed Matter, 2008. **20**(36): p. 362201.

18. Rouquerol, J., et al., *Recommendations for the characterization of porous solids (Technical Report).* Pure and Applied Chemistry, 1994. **66**(8): p. 1739-1758.

19. Warhurst, A.M., G.L. McConnachie, and S.J. Pollard, *Characterisation and applications of activated carbon produced from Moringa oleifera seed husks by single-step steam pyrolysis.* Water Research, 1997. **31**(4): p. 759-766.

20. White, R.J., et al., *Tuneable porous carbonaceous materials from renewable resources.* Chemical Society Reviews, 2009. **38**(12): p. 3401-3418.

21. Atwater, J.E. and R.R. Wheeler, *Complex permittivities and dielectric relaxation of granular activated carbons at microwave frequencies between 0.2 and 26 GHz.* Carbon, 2003. **41**(9): p. 1801-1807.

22. Hotta, M., et al., *Complex permittivity of graphite, carbon black and coal powders in the ranges of X-band frequencies (8.2 to 12.4 GHz) and between 1 and 10 GHz.* ISIJ international, 2011. **51**(11): p. 1766-1772.

23. Yang, Y., et al., *Characterizing Adsorption Performance of Granular Activated Carbon with Permittivity.* Materials, 2017. **10**(3): p. 269.

24. Al-Sehemi, A.G., et al., *Effect of Activated Carbons on the Dielectric and Microwave Properties of Natural Rubber Based Composites.* Materials Research, 2017. **20**(5): p. 1211-1220.

25. Ab Jabal, S.N., Y.B. Seok, and W.F. Hoon, *Carbon composition, surface porosities and dielectric properties of coconut shell powder and coconut shell activated carbon composites.* Journal of Engineering and Applied Sciences 2016. **11(6)**.

26. He, C.L., et al., *Calorimetry Study of Microwave Absorption of Some Solid Materials.* Journal of Microwave Power and Electromagnetic Energy, 2013. **47**(4): p. 251-261.

27. Motasemi, F., et al., *Microwave dielectric characterization of switchgrass for bioenergy and biofuel.* Fuel, 2014. **124**: p. 151-157.

28. Omorogie, M.O., J.O. Babalola, and E.I. Unuabonah, *Regeneration strategies for spent solid matrices used in adsorption of organic pollutants from surface water: a critical review.* Desalination and Water Treatment, 2016. **57**(2): p. 518-544.

29. Ania, C.O., et al., *Microwave-assisted regeneration of activated carbons loaded with pharmaceuticals.* Water Res, 2007. **41**(15): p. 3299-306.

30. Bradshaw, S., E.V. Wyk, and J.d. Swardt, *Preliminary economic assessment of microwave regeneration of activated carbon for the carbon in pulp process.* Journal of microwave power and electromagnetic energy, 1997. **32**(3): p. 131-144.

31. Ng, K., et al., *Carbon type differentiation technique for diagnosing pulverised coal injection efficiency.* Ironmaking & Steelmaking, 2016. **43**(3): p. 214-219.

32. Gray, R. and K. Devanney, *Coke carbon forms: microscopic classification and industrial applications.* International Journal of Coal Geology, 1986. **6**(3): p. 277-297.

33. Lundgren, M., *Blast furnace coke properties and the influence on off-gas dust*. 2010, Luleå tekniska universitet.

34. Geerdes, M., R. Chaigneau, and I. Kurunov, *Modern Blast Furnace Ironmaking: An Introduction (2015)*. 2015: Ios Press.

35. Zhong, Y., et al., *Structural Characterization of Carbon in Blast Furnace Flue Dust and Its Reactivity in Combustion.* Energy & Fuels, 2017. **31**(8): p. 8415-8422.

36. Marland, S., A. Merchant, and N. Rowson, *Dielectric properties of coal.* Fuel, 2001. **80**(13): p. 1839-1849.

37. Snoeyink, V.L. and W.J. Weber, *The surface chemistry of active carbon; a discussion of structure and surface functional groups.* Environmental Science & Technology, 1967. **1**(3): p. 228-234.

38. Leblanc, J.L., *Rubber–filler interactions and rheological properties in filled compounds.* Progress in polymer science, 2002. **27**(4): p. 627-687.

39. Barroso-Bogeat, A., et al., *Activated carbon surface chemistry: Changes upon impregnation with Al (III), Fe (III) and Zn (II)-metal oxide catalyst precursors from NO3– aqueous solutions.* Arabian Journal of Chemistry, 2016.

40. Figueiredo, J.L., *Functionalization of porous carbons for catalytic applications.* Journal of Materials Chemistry A, 2013. **1**(33): p. 9351-9364.

41. Boehm, H.P., *Surface oxides on carbon and their analysis: a critical assessment.* Carbon, 2002. **40**(2): p. 145-149.

42. Peschel, G., *Carbon-carbon bonds: hybridization.* Obtained online from: http://www. physik. fu-berlin. de/einrichtungen/ag/ag-reich/lehre/Archiv/ss2011/docs/Gina_Peschel-Handout. pdf, published on, 2011. **5**(5).

43. Cuenca, J.A., *Characterisation of powders using microwave cavity perturbation*. PhD thesis, Cardiff University, 2015.

44. Sheen, J., *Comparisons of microwave dielectric property measurements by transmission/reflection techniques and resonance techniques.* Measurement Science and Technology, 2009. **20**(4): p. 042001.

45. Krupka, J., *Frequency domain complex permittivity measurements at microwave frequencies.* Measurement Science and Technology, 2006. **17**(6): p. R55.

46. Singh, D.P., et al., *Microwave cavity technique to study the dielectric response in 4'-n-Heptyl-4-biphenyl nematic liquid crystal at 20.900 GHz and 29.867 GHz.* Measurement, 2011. **44**(4): p. 605-610.

47. Jha, S.N., et al., *Measurement techniques and application of electrical properties for nondestructive quality evaluation of foods—a review.* Journal of food science and technology, 2011. **48**(4): p. 387-411.

48. Note, A.A., *Agilent Basics of Measuring the Dielectric Properties of Materials.* Agilent Literature Number, 2006.

49. Saeed, K., et al., *Planar microwave sensors for complex permittivity characterization of materials and their applications*, in *Applied Measurement Systems*. 2012, InTech.

50. Venkatesh, M. and G. Raghavan, *An overview of dielectric properties measuring techniques.* Canadian biosystems engineering, 2005. **47**(7): p. 15-30.

51. Al-Hartomy, O.A., et al., *Effect of matrix chemical nature on the properties of composites for microwave absorbers.* Polymer-Plastics Technology and Engineering, 2013. **52**(11): p. 1113-1121.

52. Stuchly, M., *Dielectric properties of biological substances-Tabulated.* J. Microwave Power, 1997. **15**(1): p. 39-43.

53. Rytting, D., *Network analyzer error models and calibration methods.* White Paper, September, 1998.

54. Reinecke, T., et al., *Open-ended coaxial probe for the quantification of edema in human brain tissue.* Sensors and Actuators B: Chemical, 2014. **204**: p. 763-769.

55. Salema, A.A., et al., *Dielectric properties and microwave heating of oil palm biomass and biochar.* Industrial Crops and Products, 2013. **50**: p. 366-374.

56. Tripathi, M., et al., *Effect of microwave frequency on dielectric properties of oil palm shell (OPS) and OPS char synthesized by microwave pyrolysis of OPS.* Journal of Analytical and Applied Pyrolysis, 2015. **112**: p. 306-312.

57. Tereshchenko, O., F.J.K. Buesink, and F.B.J. Leferink. *An overview of the techniques for measuring the dielectric properties of materials*. in *General Assembly and Scientific Symposium, 2011 XXXth URSI*. 2011. IEEE.

58. Fan, W., et al., *Dielectric properties of coals in the low-terahertz frequency region.* Fuel, 2015. **162**: p. 294-304.

59. Sklavounos AH, Barker NS. Liquid-permittivity measurements using a rigorously modeled overmoded cavity resonator. IEEE Transactions on Microwave Theory and Techniques. 2014 Jun;62(6):1363-72.

60. Thuery J. Microwaves: industrial, scientific, and medical applications. Artech House on Demand; 1992.

61.	Orfanidis, A.P., G.A. Kyriacou, and J.N. Sahalos, *Numerical analysis of cylindrical cavities used for microwave heating, employing the mode matching technique.* PIERS Online, 2007. **3**(8): p. 1228-1231.

62.	Kashyap, R.S., Waveguide resonators. *Term paper report, Dept. of Electrical Engineering, Indian Institute of Technology, Bombay*..

63.	Che, W., et al. *Permittivity measurement of biological materials with improved microwave cavity perturbation technique*. in *Microwave Conference, 2008. EuMC 2008. 38th European*. 2008. IEEE.

64.	Li, X. and Jiang, Y., 2010. Design of a Cylindrical Cavity Resonator for Measurements of Electrical Properties of Dielectric Materials.

65.	Levcheva, V. and S. Ivanov, *Application of TE011 mode cylindrical resonator for complex permittivity estimation of dielectric materials.* Bulg. J. Phys, 2005. **32**(2): p. 147-158.

66.	Salema, A.A., et al., *Microwave dielectric properties of Malaysian palm oil and agricultural industrial biomass and biochar during pyrolysis process.* Fuel Processing Technology, 2017. **166**: p. 164-173.

67.	Motasemi, F., A.A. Salema, and M.T. Afzal, *Dielectric characterization of corn stover for microwave processing technology.* Fuel Processing Technology, 2015. **131**: p. 370-375.

68.	Motasemi, F., M.T. Afzal, and A.A. Salema, *Microwave dielectric characterization of hay during pyrolysis.* Industrial Crops and Products, 2014. **61**: p. 492-498.

69.	Al-Harahsheh, M., et al., *Dielectric properties of Jordanian oil shales.* Fuel Processing Technology, 2009. **90**(10): p. 1259-1264.

70.	Krupka, J., et al., *Uncertainty of complex permittivity measurements by split-post dielectric resonator technique.* Journal of the European Ceramic Society, 2001. **21**(15): p. 2673-2676.

71.	Chen, F., et al., *Effect of Cavity Dimensions on TE01δ Mode Resonance in Split-Post Dielectric Resonator Techniques.* Journal of Electromagnetic Analysis and Applications, 2012. **4**(09): p. 358.

72.	Givot, B., J. Krupka, and K. Derzakowski. *Split-post dielectric resonator for complex permittivity measurements at 20-25 GHz*. in *Microwaves, Radar and Wireless Communications, 2002. MIKON-2002. 14th International Conference on*. 2002. IEEE.

73.	Semouchkina E, Cao W, Mittra R. Modeling of microwave ring resonators using the finite-difference time-domain method (FDTD). microwave and optical technology letters. 2000 Mar 20;24(6):392-6..

74.	Heinola, J.-M., et al., *Investigation of Using the Harmonics of a Microstrip Ring Resonator Structure on Determination of Dielectric Properties.*

75.	Waldron, I.J., *Ring Resonator Method for Dielectric Permittivity Measurements of Foams*. 2006, Worcester Polytechnic Institute.

76.	Abduljabar, A.A., *Compact microwave microfluidic sensors and applicator*. 2016, Cardiff University.

77.	Abduljabar, A.A., et al., *Novel microwave microfluidic sensor using a microstrip split-ring resonator.* IEEE Transactions on Microwave Theory and Techniques, 2014. **62**(3): p. 679-688.

78.	Sklavounos, A.H. and N.S. Barker, *Liquid-Permittivity Measurements Using a Rigorously Modeled Overmoded Cavity Resonator.* Ieee Transactions on Microwave Theory and Techniques, 2014. **62**(6): p. 1363-1372.

79.	Banerjee, G., *Electrical and electronics engineering materials*. 2014: PHI Learning Pvt. Ltd.

80.	Vander Vorst, A., A. Rosen, and Y. Kotsuka, *RF/microwave interaction with biological tissues*. Vol. 181. 2006: John Wiley & Sons.

81. Von Hippel, A.R. and A.S. Labounsky, *Dielectric Materials and Applications*. 1995: Artech House.

82. Ulaby, F.T. and U. Ravaioli, *Fundamentals of Applied Electromagnetics, 7/E*. 2015: Pearson Education.

83. Klein, O., et al., *Microwave cavity perturbation technique: part I: principles.* International Journal of Infrared and Millimeter Waves, 1993. **14**(12): p. 2423-2457.

84. Metaxas, A.a. and R.J. Meredith, *Industrial microwave heating*. IEEE Power Engineering Vol. 1. 1983, London, UK: Peter Peregrinus.

85. Meredith, R.J., *Engineers' handbook of industrial microwave heating*. IEEE Power 1998, London, UK: Iet.

86. Nowak, D., *The Impact of Microwave Penetration Depth on the Process of Heating the Moulding Sand with Sodium Silicate.* Archives of Foundry Engineering, 2017. **17**(4): p. 115-118.

87. Orfanidis, S.J., *Electromagnetic waves and antennas*. 2002: Rutgers University New Brunswick, NJ.

88. Grant, E.H., R. Sheppard, and G. South, *Dielectric behaviour of biological molecules in solution*. Monographs on physical biochemistry. 1978, Oxford: Clarendon Press.

89. *Polar molecules. By P. Debye, Ph.D., Pp. 172. New York: Chemical Catalog Co., Inc., 1929.* Journal of the Society of Chemical Industry, 1929. **48**(43): p. 1036-1037.

90. Chen, L.-F., et al., *Microwave electronics: measurement and materials characterization*. 2004: John Wiley & Sons.

91. Wilson, I., C. Schramm, and J. Kinzer, *High Q resonant cavities for microwave testing.* Bell System Technical Journal, 1946. **25**(3): p. 408-434.

92. Donovan, S., et al., *Microwave cavity perturbation technique: Part II: Experimental scheme.* International Journal of Infrared and Millimeter Waves, 1993. **14**(12): p. 2459-2487.

93. Nyfors, E.G., *Cylindrical microwave resonator sensors for measuring materials under flow*. 2000: Helsinki University of Technology.

94. Gardiol, F.E., *Introduction to microwaves*. 1984: Dedham, Mass. : Artech House.

95. Raveendranath, U., S.B. Kumar, and K.T. Mathew, *Improved loaded quality factor of cavity resonators with cross iris coupling.* Iete Technical Review, 1999. **16**(5-6): p. 481-485.

96. Balmus, S., et al., *The cavity perturbation method for the measurement of the relative dielectric permitivity in the microwave range.* Journal of optoelectronics and advanced materials, 2006. **8**(3): p. 971.

97. Li, X. and Y. Jiang, *Design of a Cylindrical Cavity Resonator for Measurements of Electrical Properties of Dielectric Materials*. 2010, University of Gävle: Sweden.

98. Waldron, R., *Perturbation theory of resonant cavities.* Proceedings of the IEE-Part C: Monographs, 1960. **107**(12): p. 272-274.

99. Mehdizadeh, M., *Microwave/RF applicators and probes: for material heating, sensing, and plasma generation*. 2015: William Andrew.

100. Li, S., C. Akyel, and R.G. Bosisio, *Precise Calculations and Measurements on the Complex Dielectric Constant of Lossy Materials Using TM/sub 010/Cavity Perturbation Techniques.* IEEE Transactions on Microwave Theory and Techniques, 1981. **29**(10): p. 1041-1048.

101. Zajíček, R., J. Vrba, and K. Novotný, *Evaluation of a Reflection Method on an Open-Ended Coaxial Line and its Use in Dielectric Measurements.* Acta Polytechnica, 2006. **46**(5).

102. Grant, J., et al., *In vivo dielectric properties of human skin from 50 MHz to 2.0 GHz.* Physics in Medicine & Biology, 1988. **33**(5): p. 607.

103. Cuenca, J.A., et al., *Investigating the broadband microwave absorption of nanodiamond impurities.* IEEE Transactions on Microwave Theory and Techniques, 2015. **63**(12): p. 4110-4118.

104. Porch, A., et al., *Microwave treatment in oil refining.* Applied Petrochemical Research, 2012. **2**(1-2): p. 37-44.

105. Stuchly, M.A. and S.S. Stuchly, *Equivalent circuit of an open-ended coaxial line in a lossy dielectric.* IEEE Transactions on instrumentation and Measurement, 1982. **1001**(2): p. 116-119.

106. Gabriel, C., T. Chan, and E. Grant, *Admittance models for open ended coaxial probes and their place in dielectric spectroscopy.* Physics in medicine and biology, 1994. **39**(12): p. 2183.

107. Zheng, H. and C.E. Smith, *Permittivity measurements using a short open-ended coaxial line probe.* IEEE Microwave and Guided Wave Letters, 1991. **1**(11): p. 337-339.

108. Bussey, H. and A. Estin, *Errors in dielectric measurements due to a sample insertion hole in a cavity.* IRE Transactions on microwave Theory and Techniques, 1960. **8**(6): p. 650-653.

109. Shkal, F., et al., *Microwave Characterization of Activated Carbons.* Journal of Computer and Communications, 2017. **6**(01): p. 112.

110. Slocombe, D., *The electrical properties of transparent conducting oxide composites*, PhD thesis, Cardiff University, 2012.

111. Cuenca, J.A., D.R. Slocombe, and A. Porch, *Temperature Correction for Cylindrical Cavity Perturbation Measurements.* IEEE Transactions on Microwave Theory and Techniques, 2017. **65**(6): p. 2153-2161.

112. Cuenca, J.A., D.R. Slocombe, and A. Porch, *Temperature Correction for Cylindrical Cavity Perturbation Measurements.*

113. Plaza, M.G., et al., *Ammoxidation of carbon materials for CO2 capture.* Applied Surface Science, 2010. **256**(22): p. 6843-6849.

114. Pevida, C., et al., *Surface modification of activated carbons for CO2 capture.* Applied Surface Science, 2008. **254**(22): p. 7165-7172.

115. Council, W., *World energy resources, 2013 survey: summary.* Report. World Energy Council, 2013.

116. Wang, M., et al., *Post-combustion CO2 capture with chemical absorption: a state-of-the-art review.* Chemical Engineering Research and Design, 2011. **89**(9): p. 1609-1624.

117. Balsamo, M., et al., *CO2 adsorption onto synthetic activated carbon: Kinetic, thermodynamic and regeneration studies.* Separation and Purification Technology, 2013. **116**: p. 214-221.

118. Chronopoulos, T., et al., *Utilisation of microwave energy for CO2 desorption in post-combustion carbon capture using solid sorbents.* Energy Procedia, 2014. **63**: p. 2109-2115.

119. Plaza, M.G., et al., *Post-combustion CO2 capture with a commercial activated carbon: comparison of different regeneration strategies.* Chemical Engineering Journal, 2010. **163**(1-2): p. 41-47.

120. Chronopoulos, T., *CO2 desorption via microwave heating for post-combustion carbon capture.* Microporous and Mesoporous Materials, 2014(197): p. 288–290.

121. Yu, C.-H., C.-H. Huang, and C.-S. Tan, *A review of CO2 capture by absorption and adsorption.* Aerosol Air Qual. Res, 2012. **12**(5): p. 745-769.